THÈSE

Pour l'obtention du grade de

DOCTEUR DE L'ÉCOLE NATIONALE SUPÉRIEURE DE MÉCANIQUE ET D'AÉROTECHNIQUE

(Diplôme National – Arrêté du 25 mai 2016 modifié par l'arrêté du 26 Août 2022)

École Doctorale :
Mathématiques, Informatique, Matériaux, Mécanique, Energétique (MIMME)

Secteur de Recherche :
Énergétique, Thermique, Combustion

Experimental analysis of cyclic ignition strategies for pistonless constant-volume combustion

---

Présentée par :

Choomanee RUNNOO

Sous la direction de : **Marc BELLENOUE**
Co-encadrants : **Bastien BOUST** et **Quentin MICHALSKI**

Soutenue le 8 avril 2026 devant la Commission d'Examen

JURY

Rapporteurs :		
Razi NALIM	Full Professor	Université de Purdue, USA
Philippe GUIBERT	Professeur des Universités	ESTACA, France
Membres du jury :		
Guillaume VANHOVE	Professeur des Universités	Université de Lille, France
Antonio ANDREINI	Assistant Professor	Université de Florence, Italie
Quentin MICHALSKI	Research Fellow	RMIT University, Australia
Bastien BOUST	Ingénieur de recherche	Institut PPRIME, France
Marc BELLENOUE	Professeur des Universités	ISAE-ENSMA, France

Acknowledgement

Je tiens tout d'abord à remercier Prof. Philippe Guibert et Prof. Razi Nalim d'avoir accepté de rapporter ce manuscrit de thèse. Plus généralement, je remercie l'ensemble du jury, Prof. Antonio Andreini et Prof. Guillaume Vanhove, pour leurs remarques pertinentes ainsi que pour les échanges enrichissants que nous avons eus à l'issue de ma soutenance.

J'adresse également un immense merci à Christine Roussel, qui m'a accompagné depuis mon premier CSI jusqu'à la fin de cette aventure. Merci pour ta bienveillance, tes encouragements et tes retours toujours constructifs sur mes travaux, lors des congrès comme lors des CSI. Tes mots ont souvent eu un impact considérable sur moi.

Un immense merci, à la hauteur de leur investissement, à mes encadrants Marc, Bastien et Quentin. Nos nombreuses discussions m'ont été d'une aide précieuse tout au long de cette thèse. Je vous suis également très reconnaissante pour tout ce que vous m'avez appris dans vos domaines de spécialité respectifs. Malgré des emplois du temps particulièrement chargés, vous avez toujours trouvé du temps pour m'accompagner et répondre à mes questions.

Une thèse est aussi l'occasion de découvrir le monde de la recherche dans toute sa richesse. Marc, tu as énormément contribué à cette découverte et je t'en remercie sincèrement. Merci de m'avoir donné l'opportunité de présenter mes travaux lors de congrès nationaux et internationaux et d'échanger avec de nombreux chercheurs. Au-delà de l'apport scientifique et du développement de mes capacités de communication, ces expériences m'ont permis de vivre des moments que je n'oublierai jamais. Ton engagement dans la recherche comme dans la vie publique m'impressionne et m'amène à réfléchir à mes propres engagements pour la suite.

Bastien, je te remercie infiniment pour l'énorme travail que tu réalises. Grâce à toi, j'ai pu travailler tout au long de cette thèse avec des outils robustes et performants. J'admire ta rigueur, ta méthode et ton expertise. Si j'atteins un jour un niveau d'excellence comparable au tien dans un domaine, j'aimerais conserver la même humilité et la même approche que toi.

Quentin, merci pour toute l'aide que tu m'as apportée, notamment sur les aspects numériques. Tu as toujours été disponible et prêt à aider, malgré le décalage horaire. Ton soutien a été précieux tout au long de cette thèse.

L'administration française n'est jamais simple, en particulier pour les étudiants internationaux. Je tiens donc à remercier Marie-Cannelle, Emmanuelle Kari, Céline Portran, Maggy Souriseau ainsi que Mme Carouge pour leur aide, leur disponibilité et les éclaircissements qu'elles m'ont apportés dans mes nombreuses démarches administratives.

Une thèse ne repose pas uniquement sur l'encadrement scientifique. J'ai également bénéficié de l'aide précieuse de nombreuses personnes sur les aspects techniques, notamment Alain, Émilien et Redouane.

Je remercie également les doctorants, spécialement ceux avec qui j'ai partagé le bureau et l'ensemble du personnel des équipes CT et FTC. Je n'oublie évidemment pas les doctorants du projet INSPIRE: merci d'avoir rendu cette aventure aussi mémorable.

Je souhaite aussi remercier le personnel du SUAPS (Nicolas Hayer, Nicolas Becker, Christophe, Milène, Vincent, Capucine et Caroline Samson) que j'ai eu le plaisir de côtoyer depuis janvier 2024. Merci pour l'organisation des séjours et pour toutes les belles rencontres que vos activités m'ont permis de faire avec des étudiants des autres facultés de l'Université de Poitiers.

À mes amis, qui ont toujours été présents malgré la distance: Jean-David, Nicolas Pironnet, Roshan, Junjie, Anna, Surya et Titouan. Merci pour votre soutien indéfectible au fil des années.

Enfin, je remercie ma famille, à plus de 9 000 kilomètres d'ici, pour son amour, sa confiance et son soutien constant.

Je dédie ce travail à mon grand-père et à mon oncle, que j'ai perdus au cours de cette thèse. Je ne serais pas arrivée jusqu'ici sans vous.

Publications associated with this research

Article

1. **C. Runnoo**, Q. Michalski, B. Boust et M. Bellenoue, “Cyclic spark-ignition versus self-ignition phenomena in Constant Volume Combustor,” *Flow, Turbulence and Combust* ,116, 24 ,2026. DOI: 10.1007/s10494-025-00725-9

Conference Proceedings

1. **C. Runnoo**, B. Boust, M. Bellenoue, et Q. Michalski, “Time-resolved PIV investigation of spark-ignition and self-ignition combustion in a Constant Volume Combustion Chamber”, *AIAA Scitech Forum*, American Institute of Aeronautics and Astronautics Inc (AIAA), 2026. DOI: 10.2514/6.2026-1034

2. **C. Runnoo**, B. Boust, M. Bellenoue, et Q. Michalski, “Characterization of Re-Ignition Events in Constant Volume Combustion”, AIAA Scitech Forum, American Institute of Aeronautics and Astronautics Inc (AIAA), 2025. DOI:10.2514/6.2025-1180

3. **C. Runnoo**, Q. Michalski, B. Boust et M. Bellenoue, “Cyclic Re-Ignition Phenomena in Constant Volume Combustors”, 8th International Conference on Jets, Wakes and Separated Flows (ICJWSF), 2024.

4. **C. Runnoo**, Q. Michalski, B. Boust et M. Bellenoue, “Cyclic Re-Ignition Phenomena in Pressure-Gain Constant Volume Combustors”, 13th International Workshop on Detonation for Propulsion (IWDP), 2024.

Nomenclature

ACARE	Advisory Council for Aviation Research and Innovation in Europe
BPR	Bypass ratio
CV2	Constant Volume Combustion Vessel
CVC	Constant Volume Combustion
dt air	cycle to cycle air intake duration
dt ex	cycle to cycle exhaust duration
dt fuel	cycle to cycle fuel intake duration
ICE	internal combustion engine
OER	Overall Equivalence Ratio
OPR	Overall pressure ratio
Pacc	Pressure inside the combustion chamber
PDE	Pulse detonation engine
$P_{initial}$	Initial pressure, determined from the pressure evolution inside the chamber
Pex	exhaust pressure
Pexp	Experimental pressure inside the combustion chamber
PIV	Particle image velocimetry
P_{max}	Peak pressure, determined from the pressure evolution inside the chamber
Pnum	0D/1D simulated pressure inside the combustion chamber
SAF	Sustainable aviation fuel
SEC	Shockless explosion combustion
RBG	Residual burnt gases
RDE	Rotating detonation engine
RIS	Self-ignition sequence success
t_{comb}	Combustion duration
tign	cycle to cycle spark-ignition timing
tex	cycle to cycle exhaust timing
p_{RIS}	self-ignition sequence success probability

Table of contents

List of figures

List of tables

Chapter 1: Introduction

1.1 Background and aim

Over the past few decades, the aviation industry has undergone significant changes and advancements, leading to a revolution in air travel. One of the key developments which have contributed to this revolution is the introduction of jet engines. First introduced in the 1950s, they enabled faster and more attractive air travel. Replacing older propeller piston-engines, they allowed airplanes to fly higher and faster making long-distance air travel more practical and cost-effective. However, faster air travel also came with significant environmental impacts. In 2021, the air travel accounted for 2% of the global CO_2 emissions. While 2% may seem relatively small percentage, in absolute terms, it can translate to roughly 915 million tons of CO_2 emissions per year as reported by the Intergovernmental Panel on Climate Change (IPCC) [1]. Additionally, aviation emissions exert a disproportionate influence on climate change, as they are released at high altitude, amplifying their overall warming effect. This contribution is expected to grow up to 3% by 2050[2] as air travel demand rises.

To solve this complex and contentious issue, the Advisory Council for Aviation Research and Innovation in Europe (ACARE) has set ambitious targets to decrease CO_2 emissions by 75% by 2050, relative to aircraft emissions levels recorded in 2000 [3]. Although the numerical targets and their distribution have evolved over time, the main conclusion remains the same: improving aircraft efficiency, engine efficiency, use of sustainable aviation fuel (SAF) and air traffic management are the key contributors to emission reduction.

Engine efficiency improvements can be achieved through **propulsive** or **thermal efficiency** enhancements. Propulsive efficiency is improved by optimizing engine design and increasing the bypass ratio (BPR), which enhances the conversion of fuel energy into thrust. Thermal efficiency can be raised by increasing the overall pressure ratio (OPR), which improves air compression and energy extraction in the turbine, or by modifying the thermodynamic cycle to allow higher turbine inlet temperature (TET) and more efficient combustion. Together, these changes enable engines to generate more power while consuming less fuel. However, improvements in OPR and TET are constrained by size, weight and material limitations and current designs have largely plateaued [4].

At the same time, there is renewed interest in pushing the thermodynamic efficiency of gas turbines beyond current limits. Efficiency in conventional gas turbines is primarily constrained by thermal losses, which depend on OPR, TET and aerodynamic inefficiencies.

One promising avenue rethinks the combustion process itself. Traditional gas turbines operate with isobaric combustion, which, although mechanically simple, generates substantial thermodynamic losses. Exergy analyses of the Brayton cycle indicate that the combustion chamber accounts for most of the irreversibility and efficiency losses in the system. As early recognized by Francois H. Reynst [5], combustion at constant pressure entails a significant entropy increase and thus a waste of available energy. Consequently, it is within the combustion process and the architecture of fuel utilization that the greatest potential lies for achieving the next leap in gas turbine efficiency, as the dominant source of entropy generation in existing engines originates from combustion. Therefore, exploring the optimization of an alternative combustion cycle presents a promising avenue for reducing entropy production and enhancing overall efficiency.

In this context, the INSPIRE (INSpiring Pressure gain combustion Integration, Research and Education) program, a Marie Skłodowska-Curie Innovative Training Network (ITN) project, brings together a consortium of universities, research laboratories and industries, to investigate the most promising Pressure Gain Combustion (PGC) solutions, namely Constant-Volume Combustion (CVC) and Rotating Detonation Engines (RDE), on an innovative integrated level. The research presented in this manuscript is conducted within the Work Package 2 (WP2 in Figure 1-1).

Figure 1-1. Structure of the project INSPIRE (https://inspire.cerfacs.fr/en/home/).

The experimental reference configuration is the CV2 chamber (Constant Volume Combustion Vessel). This test rig was previously developed within the CAPA Chair, an ANR–SAFRAN Tech–MBDA France collaborative research program led by the Pprime Institute to study fundamental aspects involved in constant volume combustor [6] but without the technological constraints imposed by the retained technology of the intake and exhaust valves of real engine combustors.

1.2 Thesis structure

This work is organized in five chapters.

Chapter 1 introduces the research topic, presents the background and context and explains the motivation for exploring alternative combustion cycles for aerospace applications.

Chapter 2 reviews the fundamental concepts of pressure-gain combustion, an alternative combustion cycle. It also provides a state-of-the-art overview and limitations of spark-ignition strategies in Constant-Volume Combustion, one type of pressure-gain combustion. Additionally, it examines the potential of liquid self-ignition strategies and outlines the objectives of the present study.

Chapter 3 describes the experimental setup, diagnostic techniques and analysis methodology. It also presents the in-house 0D/1D model used to estimate parameters that are difficult to measure directly within the setup for more in-depth analysis of combustion process as well as wall heat losses during a cycle.

Chapter 4 presents a detailed reference case for the spark-ignition strategy and analyses the parametric studies conducted using the methodology analysis described in Chapter 3.

Chapter 5 explains the mechanisms leading to self-ignition within the experimental setup and provides a detailed reference case. It also discusses the parametric studies performed to evaluate the sensitivity of this ignition strategy.

The manuscript concludes with a summary of the main findings and offers perspectives for future research.

Chapter 2: State-of-the-art

2.1 Alternative combustion cycles

In thermal engines, different combustion modes can be considered: constant-pressure, constant-volume and detonative combustion. In aviation, conventional gas turbines operate under constant-pressure combustion, characteristic of the Brayton cycle. Constant-volume combustion, based on the Humphrey cycle, is typically representative of piston engines cycles. Both constant-pressure and constant-volume modes involve deflagrative combustion, meaning a subsonic combustion wave driven by chemical reactions and the transport of species and energy between burnt and unburnt gases [7].In contrast, detonation, a detonative combustion, associated with the Fickett-Jacobs cycle, features a combustion wave that propagates through the mixture at supersonic speed. A comparative illustration of the various thermodynamics cycles is presented in the P-V diagram in Figure 2-1.

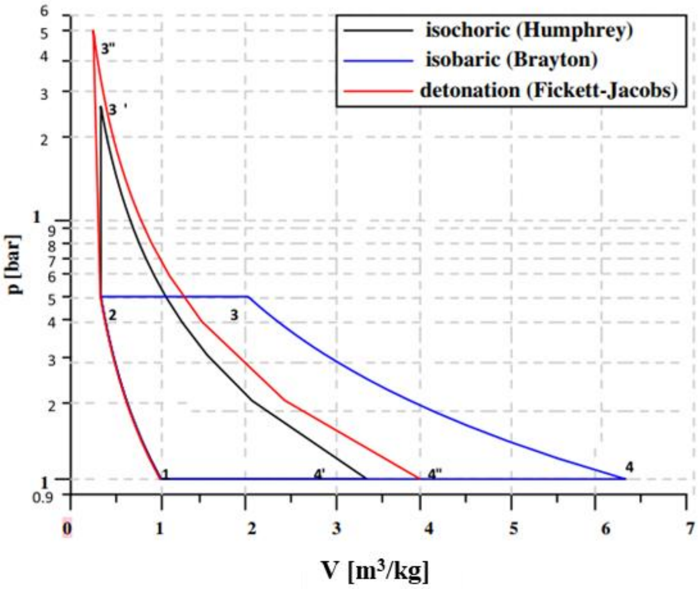

Figure 2-1. Comparison of Brayton-Joule Humphrey and Fickett-Jacobs thermodynamic cycles[8]

In the isobaric Brayton-Joule cycle, heat addition through deflagration leads primarily to an increase in volume, though in practice the pressure may slightly decrease during the process [8].In the isochoric Humphrey cycle, heat addition at constant volume results in a rise in pressure. The largest pressure increases, accompanied by a reduction in specific volume, occurs when heat is released under detonation conditions, as described by the Fickett-Jacobs model.

The theoretical efficiency of these thermodynamic cycles can be expressed by the following relations:

- Brayton-Joule cycle:

$$\eta = 1 - \frac{1}{\left(\frac{p_2}{p_1}\right)^{\frac{k-1}{k}}} \qquad \text{Equation 2-1}$$

- Humphrey (isochoric) cycle:

$$\eta = 1 - k \cdot \frac{T_1}{T_2} \cdot \frac{\left(\frac{T_{3'}}{T_2}\right)^{\frac{1}{k}} - 1}{\left(\frac{T_{3'}}{T_2}\right) - 1} \qquad \text{Equation 2-2}$$

- Fickett-Jacobs (detonative) cycle:

$$\eta = 1 - k \frac{1}{\left(\frac{p_2}{p_1}\right)^{\frac{k-1}{k}}} \frac{\left(\frac{T_{3''}}{T_2}\right)^{\frac{1}{k}} - 1}{\left(\frac{T_{3''}}{T_2}\right) - 1} \qquad \text{Equation 2-3}$$

Where η is the thermal thermal efficiency of the cycle, p_1 is the initial pressure, p_2 is the pressure after compression, k is the specific heat ratio, T_1 is the initial temperature before compression, T_2 is the temperature after isentropic compression, $T_3{}'$ is the temperature after isochoric heat addition and T_3" is the temperature after detonation.

The ideal efficiencies of these thermodynamic cycles were compared for three fuels at an initial compression ratio of 5[14] and 30 as summarized in Table 2-1. The comparison is based on data from [14], where compression and expansion are assumed adiabatic.

Table 2-1. Efficiency comparison across fuels and thermodynamic cycles for an initial compression ratio of 5 [9] and 30.

Fuel	**Brayton (%)**	**Humphrey (%)**	**Fickett-Jacobs (%)**
Pressure ratio	5 - 30	5 - 30	5 - 30
Hydrogen (H_2)	36.9 - 62.1	54.3 - 68.0	59.3 - 71.5
Methane (CH_4)	31.4 - 53.7	50.5 - 61.0	53.2 - 65.2
Acetylene (C_2H_2)	36.9 - 62.1	54.1 - 67.5	61.4 - 70.8

The cycle efficiency, in terms of specific fuel consumption, improves by around 9.5 – 47.1% for hydrogen, 13.6 – 60.8% for methane and 8.7 – 46.6% for acetylene when using the Humphrey cycle compared to the conventional Brayton cycle. This notable gain in thermodynamic performance remains one of the main motivations for ongoing research into pressure-gain combustion for energy conversion and propulsion applications.

2.2 Pressure Gain Combustion

The term *Pressure Gain Combustion* (PGC) regroups all combustion processes that produce a net pressure increase during combustion and is therefore of significant interest for propulsion applications. Unlike conventional constant-pressure combustion, PGC is an inherently unsteady process (illustrated in blue in Figure 2-2) in which gas expansion during heat release is constrained, causing a rise in stagnation pressure and enabling work extraction as the flow expands back to its initial pressure. Unlike steady combustion, which always involves a loss in stagnation pressure, unsteady combustors can generate a net pressure rise. This pressure gain allows the PGC concept to replace conventional steady-flow combustors and potentially reduce or eliminate some costly stages of the high-pressure compressor and turbine.

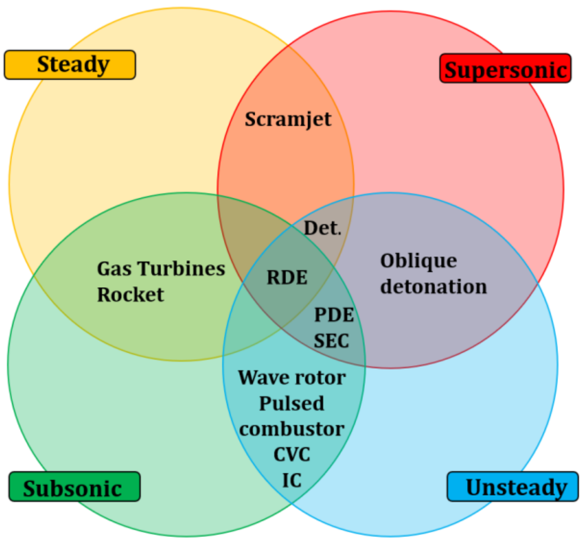

Figure 2-2 Classifications of most common engines (adapted from [10])

To capitalize on these benefits, efforts have focused on replacing conventional pressure-loss combustors with pressure-gain designs to enhance engine thermal efficiency and consequently increase power or thrust. As illustrated schematically in Figure 2-2, for a turbofan engine, the PGC replaces the steady-flow combustor and may also enable the elimination of some costly stages in the high-pressure compressor and turbine.

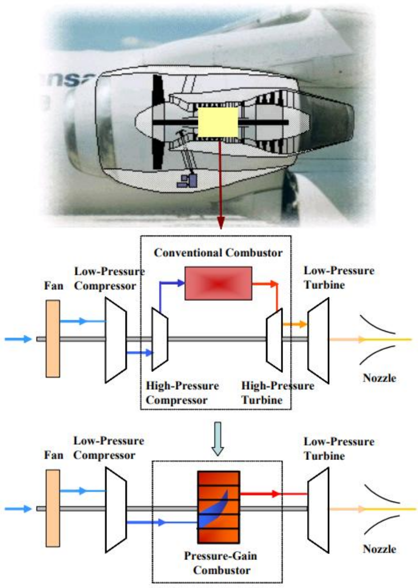

Figure 2-3 Concept of pressure-gain combustion engine [11]

The potential efficiency gains and design advantages of PGC depend on meeting specific operational requirements.

2.2.1 Conditions to achieve PGC

To achieve the benefits of PGC, the system must satisfy several key requirements [12]:

1. Combustion must occur at constant volume.

2. The formation of strong shock waves and the associated losses must be avoided.

3. No moving parts should be present in the main airflow path, ensuring simplicity and operational reliability.

Having established these operational requirements, it is instructive to examine the historical development of PGC, illustrating how early limitations drove successive innovations, with each generation of designs addressing the drawbacks of its predecessors. The following subsection provides a historical overview of PGC concepts, followed by a discussion of more recent advancements and ongoing research.

2.2.2 Some history and evolution of PGC

2.2.2.1 Pulsed Detonation Engine

Pulsed detonation engines (PDEs) are one of the early concepts investigated to for achieve pressure gain combustion in propulsion applications. Research on this topic has been carried out since the beginning of 1940s and continues today [12]. They are the class of detonative propulsion systems that have attracted the most attention over the past 25 years [8]. A typical PDE consists of a sufficiently long tube filled with a fresh fuel–oxidizer mixture and ignited by a powerful energy source.

Recently, PDEs have gained attention as potential alternatives to rockets and gas turbine propulsion systems. Air-breathing PDEs, in particular, offer the advantage of significantly higher specific impulse compared to traditional rockets, while also utilizing atmospheric air[13].

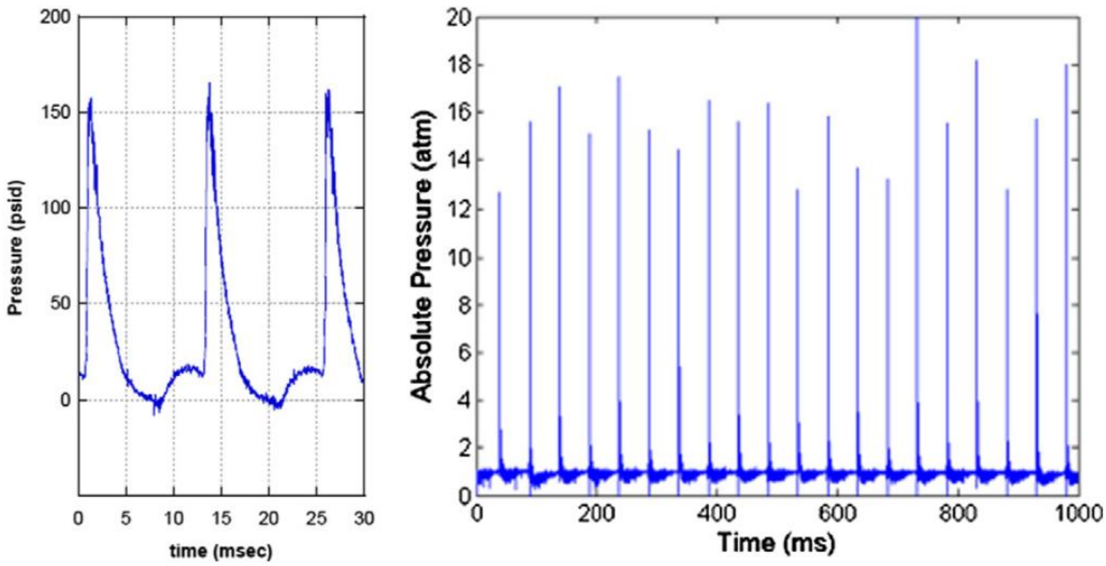

Figure 2-4 Typical pressure signals of a simple PDE system [8]

2.2.2.1.1 Advantages of PDE

Pulsed-detonation-engines are compact and capable of generating thrust levels comparable to larger conventional gas turbines. Furthermore, PDEs are being explored as possible combustion chambers within gas turbines, where their ability to produce a pressure rise during combustion could lead to notable improvements in specific fuel consumption.

2.2.2.1.2 Challenges of PDE

The most extensively studied approach of pulsed detonation combustion uses rapidly traveling detonation waves to approximate constant volume combustion. However, these detonation waves come with several drawbacks. Before a detonation can be established, the flame must accelerate through a deflagration-to-detonation transition (DDT) process, which requires a certain distance and time. In this region, combustion remains relatively slow and therefore does not strictly correspond to constant-volume heat release.

Once initiated, the detonation wave generates very sharp and high pressure peaks, which can impose severe mechanical loads on downstream components such as turbines. In addition, the flow behind the detonation front contains a significant amount of kinetic energy. Because this kinetic energy cannot be fully recovered as useful work, part of it is lost, reducing the overall efficiency of the system.

To mitigate some of these issues, the concept of the rotating detonation engine was introduced[12].

2.2.2.2 Rotating Detonation Engine

Rotating detonation engines (RDEs), as a form of PGC, can be applied to various types of propulsion systems, including rockets, ramjets, turbines and combined-cycle engines. More recently, in the United States, dedicated programs such as Vulcan-1 and Vulcan-2 have been launched to investigate the integration of constant volume combustion systems into jet propulsion, with a particular focus on detonation-based propulsion.

The rotating detonation engine operates by sustaining a continuously propagating detonation within a cylindrical combustion chamber [8]. In this type of engine, a continuous detonation wave travels inside an annular chamber. Fresh fuel-air mixture is continuously injected to sustain the rotating detonation[12].

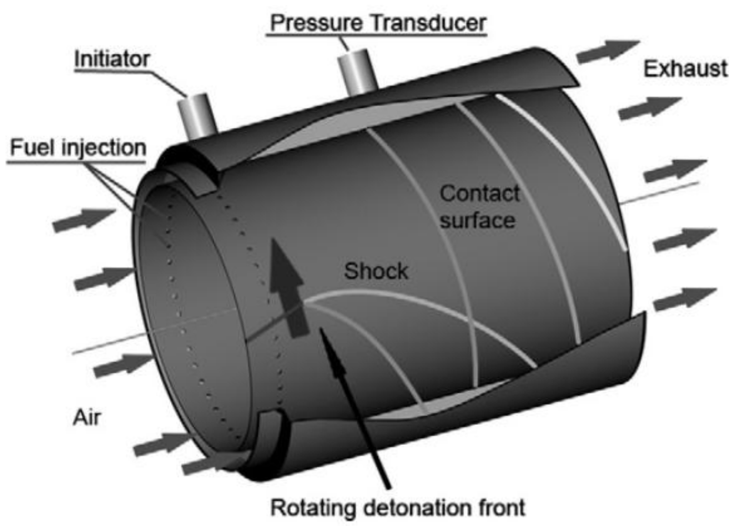

Figure 2-5. Schematic diagram of a detonation chamber used in RDE research [8]

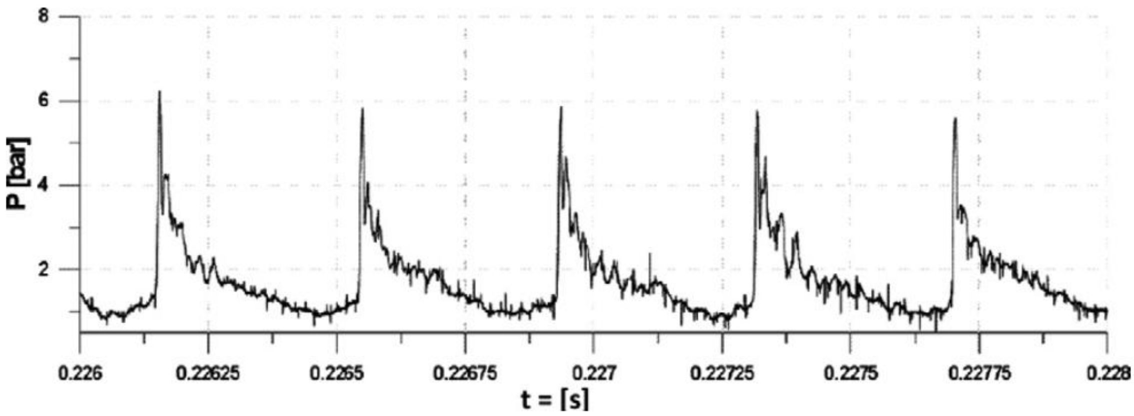

Figure 2-6. Typical pressure measurements of a stable continuous rotating detonation in a research chamber[8].

2.2.2.2.1 Advantages associated with rotating detonation engine

The detonation process can, under ideal conditions, lead to theoretically higher combustion temperatures and potentially lower entropy generation compared to conventional deflagrative combustion, depending on the system configuration. This results in a gain in thermal efficiency often exceeding 20%, potentially enabling substantial improvements in the specific impulse of rocket engines[14], [15]. Since detonation waves remain confined within an annular chamber, energy losses associated with wave discharge are limited, contributing to efficient energy utilization and stable operation. In addition, RDEs can operate over a relatively wide range of conditions and with different fuel–oxidizer mixtures, making them suitable for both rocket and air-breathing propulsion applications.

2.2.2.2.2 Challenges associated with rotating detonation engine

Despite their promising performance, RDEs still face several important challenges. A stable operation requires a continuous and well-mixed fuel–air supply; any inhomogeneity in the mixture can disturb or even extinguish the detonation wave. In addition, the presence of strong shock waves inside the chamber leads to mechanical stresses and unavoidable losses. The continuous rotation of the detonation wave also generates high thermal loads, particularly near the turbine inlet, which complicates cooling and overall engine integration. Furthermore, pressure losses in the feeding system must remain limited, otherwise the expected pressure-gain benefit can be reduced[8], [15], [11], [12] [16]

Because of these integration and operational constraints, the wave rotor concept was introduced as an alternative.

2.2.2.3 Wave Rotor

Wave rotors are unsteady-flow devices that transfer energy through pressure waves, using sequences of compression and expansion to exchange energy directly between fluids. This mechanism allows for rapid pressure variations and high tolerance to transient peaks in pressure and temperature.

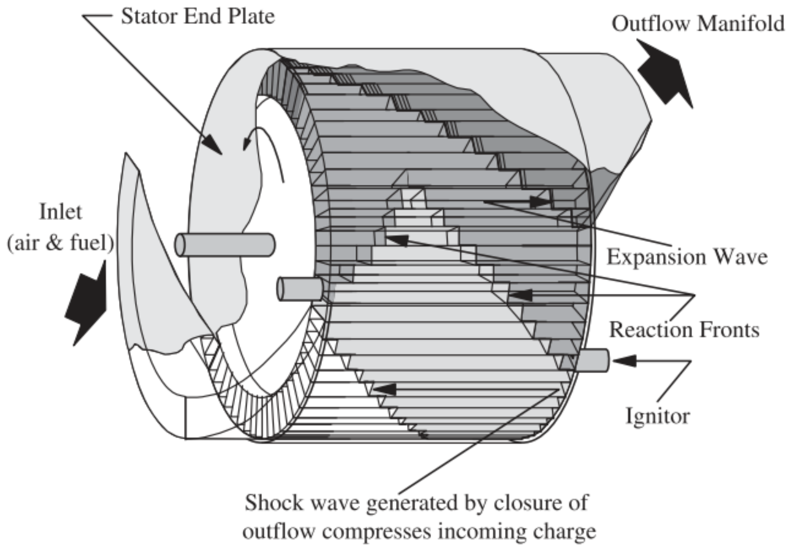

Figure 2-7 Details of a wave rotor [17]

The concept evolved from early twentieth-century pressure-exchange ideas, but practical progress became possible only after advances in unsteady fluid mechanics during and after World War II[18]. Between 1949 and 1967, Jendrassik [19], [20]conducted foundational work on integrating wave rotors as high-pressure topping stages in aircraft engines. In the mid-1960s, Rolls-Royce explored the use of wave rotor combustion in turbofan engines, predicting a 14 % reduction in specific fuel consumption (SFC) at sea level and 10 % at Mach 0.8 cruise at 35 000 ft[13].

Research intensified[18] in the 1990s, particularly through NASA studies demonstrating the feasibility of combustion within wave rotor channels, including both deflagrative and detonative modes. At the same time, ONERA examined integration into various gas-turbine configurations while accounting for realistic system losses.

2.2.2.3.1 Advantages of wave rotor[12],[18],[11],[16],[17]

Wave rotors offer a practical pathway to pressure-gain combustion. By using pressure waves in mechanically closed or quasi-closed channels, they can approach constant-volume combustion without relying on strong detonation shocks. The rotating passages also act as self-timed valves, enabling near-steady inflow and outflow without complex mechanical valve systems. Integration into existing gas-turbine architectures is possible with relatively limited layout modifications and experimental prototypes have validated the fundamental operating principles. Advances in unsteady CFD and combustion modelling have further improved understanding and predictive capabilities.

2.2.2.3.2 Challenges associated with wave rotor

Despite these advantages, significant challenges remain. The presence of rotating components in the hot-gas path introduces mechanical and thermal constraints, particularly regarding sealing and cooling of the rotating barrel. Uneven thermal loading can lead to deformation and reduced durability. Combustion occurs under highly unsteady conditions, involving complex wave–flame interactions that are not fully captured by conventional combustion models. Ignition control, stability and scaling to higher pressure ratios remain open research questions.

While the wave rotor offers shock-free pressure-gain combustion, its reliance on moving parts in the hot gas path and the associated cooling challenges highlight the need for alternative approaches. The Shockless Explosion Combustion (SEC) concept, proposed by Bobusch et al[21]., addresses these limitations by achieving near-constant-volume combustion without shock waves and without any moving components in the main airflow path.

2.2.2.4 Shockless Explosion Combustion

Shockless Explosion Combustion [12][22][23][24], derived from the pulsejet concept, is a cyclic constant-volume combustion process designed to achieve pressure-gain conditions while avoiding the losses associated with strong shock waves and moving components. The process relies on a periodic combustion cycle that establishes a standing pressure wave inside the combustion tube. Combustion occurs in phase with this wave, increasing the pressure at the inlet and enabling pressure-gain combustion.

Although SEC operates cyclically, similar to pulsed detonation combustion, it does not rely on detonation waves. Instead, it exploits thermodynamic and mixture properties to generate a gradual pressure rise, thereby approaching near-constant-volume combustion without producing strong shocks. The combustion cycle of an SEC combustor consists of four distinct stages, each contributing to maintaining the pressure wave and achieving efficient combustion. The main phases of the SEC cycle are illustrated in Figure 2-8.

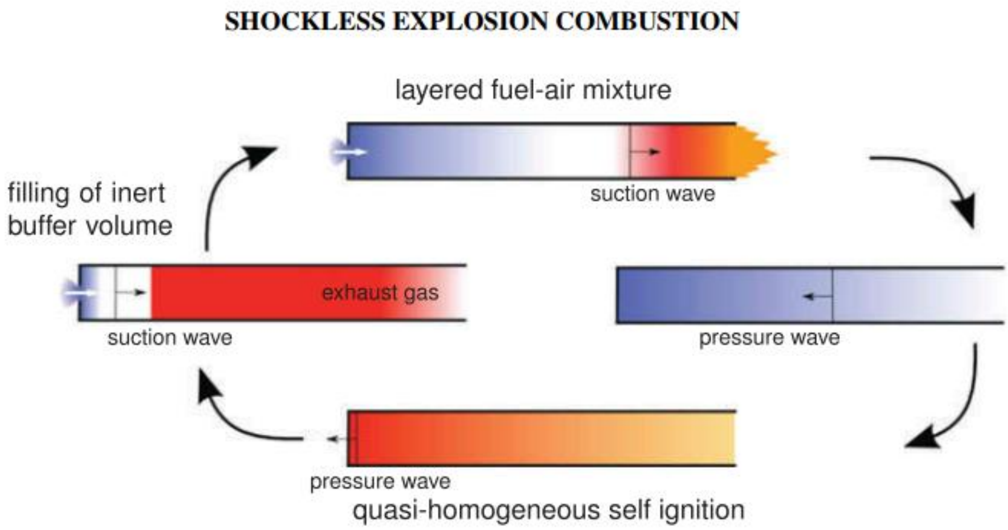

Figure 2-8 Stages of the shockless explosion combustion process[12]

2.2.2.4.1 Advantages of SEC

A key advantage of SEC is the reduction of shock-related losses and mechanical stress. Unlike detonation-based systems, it avoids large kinetic-energy losses behind a detonation front, which cannot be fully recovered by the turbine. It also eliminates losses associated with the deflagration-to-detonation transition (DDT), including the need for high ignition energy and the non-ideal combustion that occurs during flame acceleration.

2.2.2.4.2 Challenges associated with SEC [23], [24]

Despite these advantages, several challenges remain. Reliable and homogeneous fuel–air mixing is critical, as fuel is injected into hot compressed air and must be rapidly distributed to prevent local hot spots. High operating frequencies also require fast and durable valve systems capable of handling hot flows, which currently represents a technological limitation. In addition, preventing premature auto-ignition under high-pressure and high-temperature conditions requires precise control of the thermodynamic state inside the chamber.

Building on the principles and operational features of SEC, focus now shifts to constant-volume combustion (CVC). CVC offers enhanced combustion control, improved stability and higher thermodynamic efficiency by employing a mechanically closed chamber that maintains steady, constant-volume conditions. Unlike SEC, which relies on cyclic pressure waves and periodic combustion that can introduce fluctuations, CVC delivers more consistent pressure gain and allows easier integration into practical propulsion systems.

2.2.2.5 Constant Volume Combustion

2.2.2.5.1 Reciprocating Internal Combustion Engines

The reciprocating internal combustion engine (ICE) remains the most well-studied and recognized practical application of constant-volume combustion. Owing to more than a century of research and industrial development, its thermomechanical behavior is well characterized and extensively documented[25].

An ICE typically consists of a crankshaft connected to a piston (see Figure 2-9) through a connecting rod, converting the reciprocating motion of the piston into rotational motion. The piston moves between the top dead center (TDC) and bottom dead center (BDC), forming a combustion chamber enclosed by the piston crown and the cylinder liner. Intake and exhaust valves regulate the flow of fresh charge and exhaust gases, while piston rings ensure proper sealing during operation.

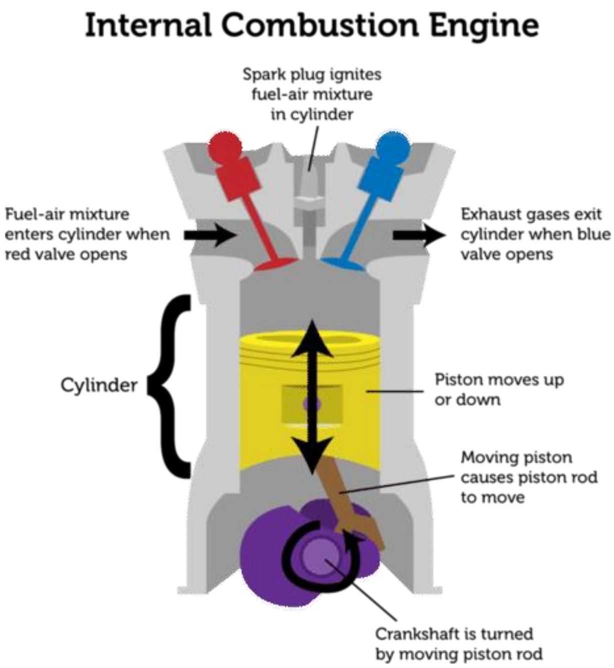

Figure 2-9 Schematic diagram of an internal combustion engine

The combustion process in spark-ignition engines follows four main phases (see Figure 2-10):

1. Intake phase - The piston descends from TDC, drawing in an air–fuel mixture through the intake valve.

2. Compression phase - The piston ascends, compressing the trapped mixture to increase pressure and temperature.

3. Combustion and expansion (power) phase - Near the end of compression, ignition occurs, rapidly increasing pressure and driving the piston downward to produce useful work.

4. Exhaust phase - Burned gases are expelled as the piston returns upward.

Depending on whether these phases occur in one or two crankshaft revolutions, the engine operates on a two-stroke or four-stroke cycle. Two-stroke engines complete combustion twice as often as four-stroke engines, yielding higher specific power but lower efficiency due to incomplete scavenging.

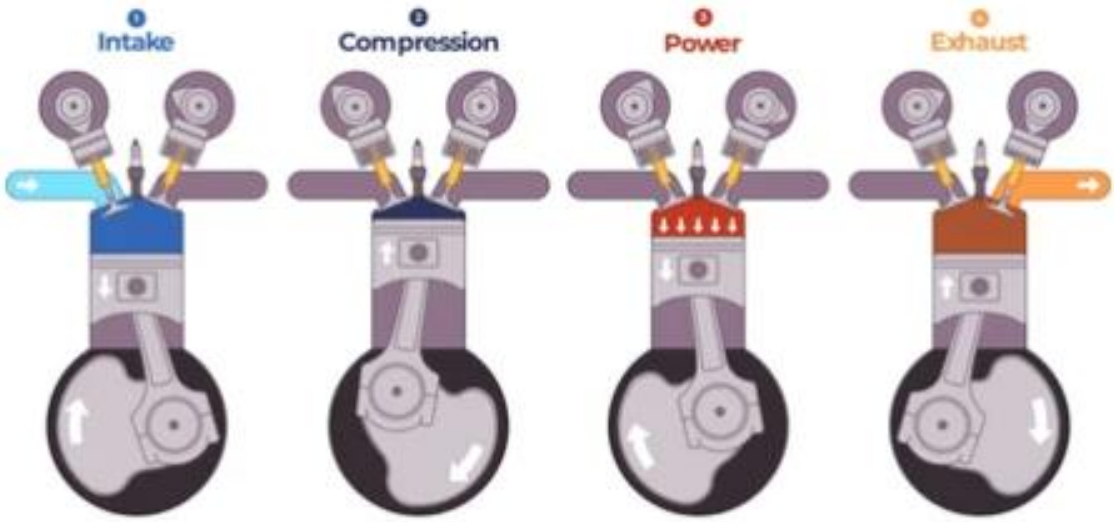

Figure 2-10. Operation of a spark-ignited combustion cycle

In theory, assuming constant-volume combustion, the thermodynamic behavior of such engines follows the Otto cycle. However, in practice, combustion is not perfectly isochoric due to finite flame propagation time. The efficiency of the Otto and related Humphrey cycles increases with higher compression ratios.

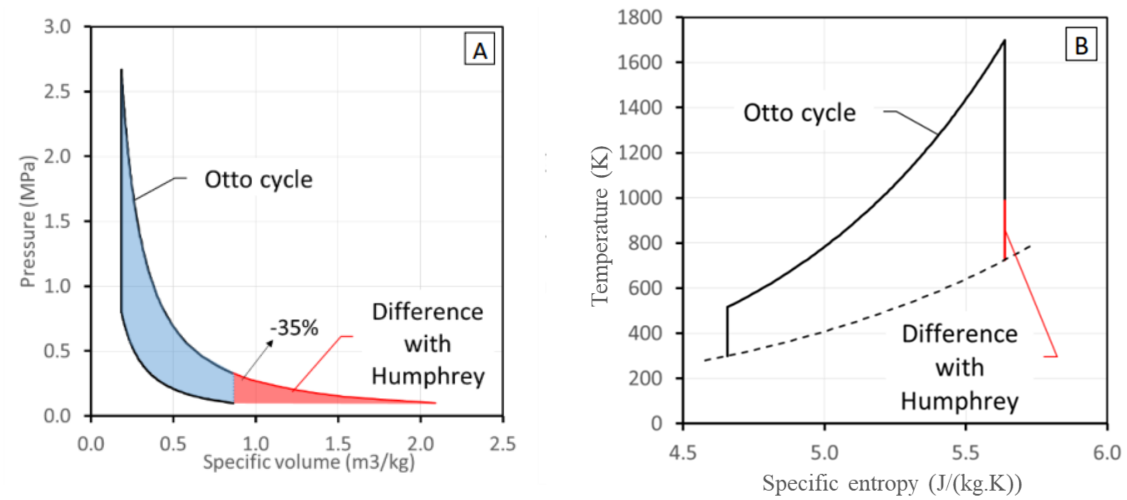

Figure 2-11 A. Pressure–specific volume diagram of an Otto cycle, highlighting the differences compared with an Atkinson–Humphrey cycle/Miller cycle. B. Temperature–entropy diagram corresponding to Cycle A [6].

Beyond its direct thermodynamic effect, a higher compression ratio also improves the combustion process itself. The adiabatic compression enhances the combustion process in two key ways: it accelerates fuel evaporation and increases flame propagation speed. By the end of compression, the temperature can rise by roughly a factor of 2 [6]. Since the vapor pressure of a liquid increases exponentially with temperature, even a moderate temperature increase greatly promotes vaporization, shortening the time required to form a combustible mixture.

Flame propagation also benefits from this temperature rise. To first order, the turbulent flame speed scales with the laminar (fundamental) flame speed. For a lean isooctane–air mixture, the laminar flame speed increases approximately with the square of temperature and decreases with pressure to about the power of 1/5 [26]. Under adiabatic compression ($\gamma \approx 1.35$), this results in a flame speed that scales roughly with the compression ratio to the power of 2/5. In the configuration shown in Figure 2-11(OPR = 8.1), the flame speed is thus increased by about a factor of 2.3, leading to a further reduction in combustion duration.

The reciprocating internal combustion engine offers clear advantages in terms of maturity and reliability. However, it presents several limitations when considered for air-breathing propulsion. From a thermodynamic point of view, the Otto cycle remains imperfect. At the end of the expansion stroke, a non-negligible residual pressure remains in the cylinder. This unrecovered pressure represents lost work, which limits the overall cycle efficiency.

For propulsion applications, the limitations are even more significant. A reciprocating engine delivers power in a discontinuous manner, with cyclic combustion and mechanical motion. The presence of pistons imposes constraints on maximum rotational speed, due to piston inertia and mean piston velocity limits. In addition, sealing requirements, friction losses and mechanical stresses reduce the power-to-weight and power-to-volume ratios. These factors become critical in aerospace propulsion, where compactness, high specific power and continuous flow are essential.

For air-breathing propulsion systems in particular, removing the piston allows higher rotational speeds, smoother flow and improved power density. Eliminating reciprocating parts also reduces friction losses and mechanical constraints. For these reasons, several patents and research efforts have proposed piston-less architectures aimed at overcoming the intrinsic mechanical and thermodynamic limitations of reciprocating internal combustion engines presented in the next section.

2.2.2.5.2 Patent review and analysis of patented technological solutions: Evolution of CVC in industry

While engine development in the automotive sector pursued solutions suited to ICE, industry efforts in the early 20th century also explored how CVC could be applied to turbine-based propulsion. The first industrial attempt to implement this concept was made by Hans Holzwarth in 1905. His gas turbine operated through combustion in sealed vessels, generating the pressure rise required to drive the turbine without any compressor stage, achieving an overall efficiency of about 13%[27]. Despite demonstrating the feasibility of the concept, the design faced significant technical limitations[28]. The combustion chamber and turbine blades were exposed to severe thermal loads and the valve system required for cyclic operation proved difficult to control reliably. These persistent issues hindered further development and as compressor technology rapidly improved and constant pressure combustion systems emerged as less complex, constant volume combustion gas turbines were gradually replaced in industrial applications.

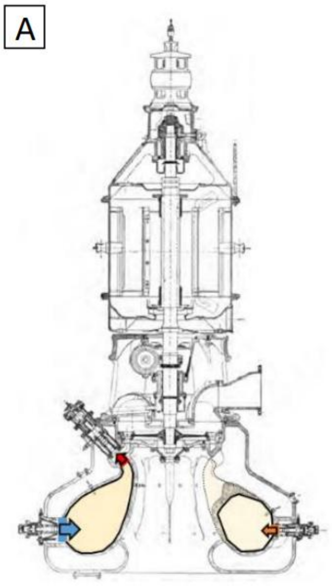

Figure 2-12 The Holzwarth constant volume combustion gas engine [27]

C.A.L. Bosco (1948) [29]presents a gas turbine configuration featuring twelve constant-volume combustion chambers (CVCC) arranged circumferentially around a rotary distributor (Figure 2-13). The distributor is equipped with ports that sequentially admit compressed air and discharge the combustion products. Air enters radially, while the exhaust flow is directed axially toward the turbine. A common exhaust plenum connects the chambers, its volume being sized to condition the pressure and temperature of the burned gases so that they remain compatible with the thermomechanical limits of the turbine.

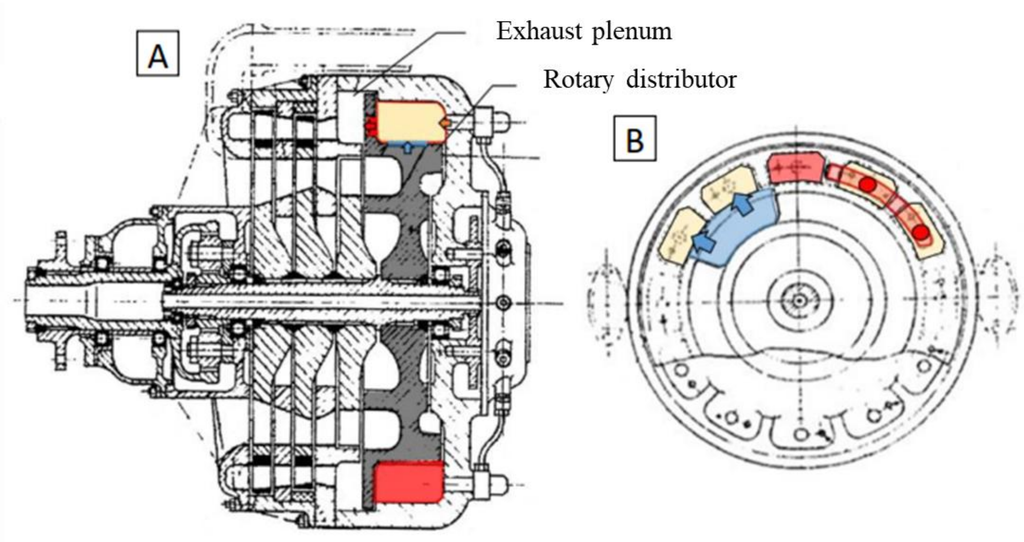

Figure 2-13 C.A.L. Bosco CVC Turbomachinery Architecture (adapted from [29] [6] A: Sectional view of the system, illustrating the CVCC in the fully open position (top) and fully closed position (bottom).B: Sectional view of the rotary distributor, showing the circumferential

arrangement of the combustion chambers and the distributor ports controlling chamber opening and gas exchange.

P. Canarelli (1955)[30] (Figure 2-14 A-C) presents a three-chamber gas turbine with an elliptical cylindrical configuration, where the air intake is positioned opposite the exhaust. The timing of the chamber openings is controlled by a rotating distributor composed of two discs at the ends of the chambers. The rotation of the discs is slowed via an epicyclic gear train and is synchronized with the main shaft.

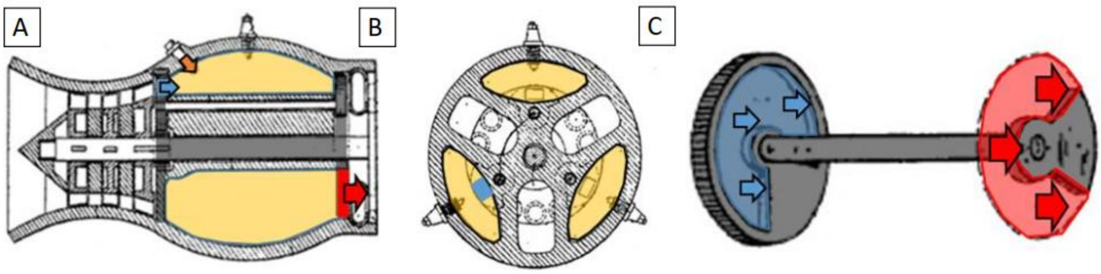

Figure 2-14 CVC Turbomachine Architecture by P. Canarelli (adapted from [30] [6]
A: Sectional view of the system, showing the CVCC fully open at the top and fully closed at the bottom. B: Sectional view of the rotary distributor, illustrating the arrangement of the combustion chambers and the distributor ports controlling chamber openings. C: Detailed isolated view of the rotary distributor.

E. Guenther (1960)[31] (Figure 2-15) describes a similar concept scaled up to fifteen chambers. In this design, the distributor features three sets of ports arranged at 120° intervals. Some ports allow the burnt gases to flow directly into the turbine for expansion, while others redirect the exhaust radially to mix with the incoming scavenging air, thereby promoting dilution and improving combustion control.

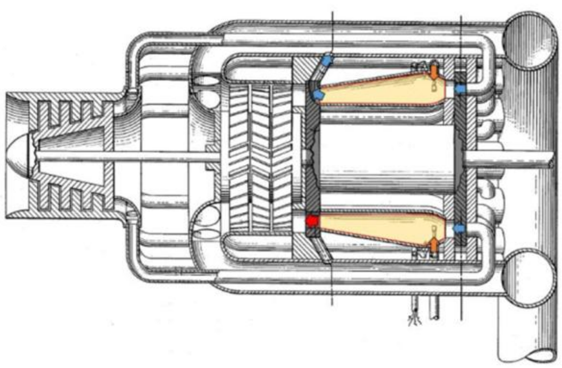

Figure 2-15 Sectional View of the CVCC by E. Guenther (adapted from[31][6]

In 1948, Kadenacy[32] proposed equipment based on a constant-volume explosive combustion gas turbine. This device produced high-pressure or high-velocity gases suitable for jet propulsion. The chambers were supplied with fuel and compressed air and ignition occurred either automatically or through dedicated ignition systems. The design included inlet and outlet openings aligned on opposite sides of the chamber wall, controlled by two rotors. Notably, during the filling process, the generation of pressure waves enabled the system to attain chamber pressures exceeding the inlet pressure, even in the absence of combustion. This was achieved by admitting gas at super-atmospheric pressure under high pressure inlet conditions, trapping it in the chamber at a pressure at least 1.5 times that of the incoming gas.

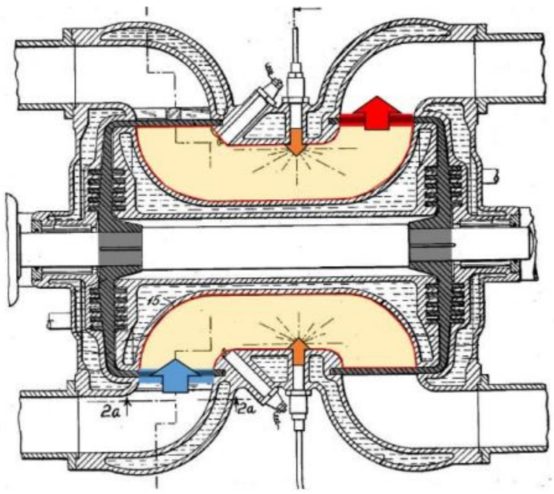

Figure 2-16 Cutaway view of the CVCC architecture by Kadenacy[32][6]

The designs proposed by A.G. Forsyth (1941)[33]and J. Semery (1980)[34] feature combustion chambers in which the intake and exhaust are controlled by valves. In Forsyth's design, the valves are actuated hydraulically, while in Semery's design, valve operation is driven by cams linked to the compressor shaft (Figure 2-16).

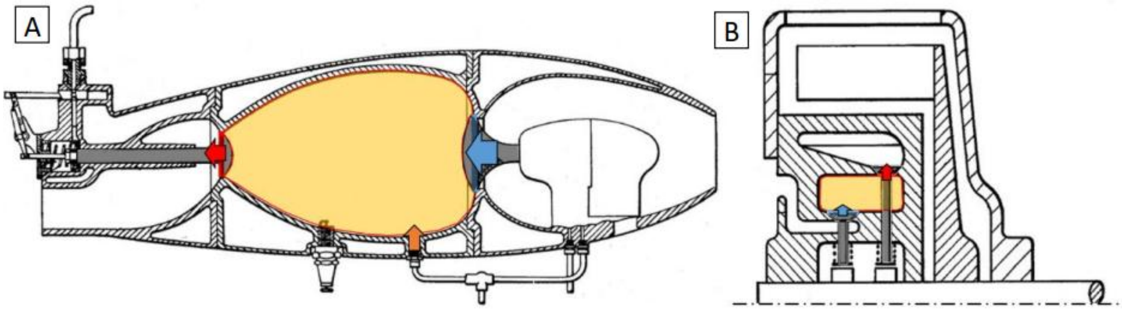

Figure 2-17 A: Sectional view of the CVCC by A.G. Forsyth (adapted from [33] [6] B: Sectional view of the CVCC by J. Semery (adapted from [34]) [6].

W. V. Taylor (1968) [35]describes a rotary distributor device where the rotor fills three-quarters of the chamber. The intake and exhaust manifolds are fixed, while the rotor with 20 chambers rotates at 2000 rpm (33 Hz). The design is similar to a low-aspect-ratio wave rotor. A notable feature is a regenerator that uses a heat exchanger to recover part of the residual enthalpy from the turbine exhaust gases and transfer it to the intake air, improving thermal efficiency.

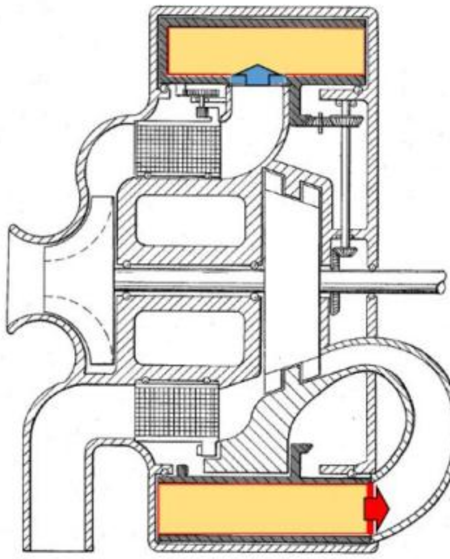

Figure 2-18 Sectional View of the CVCC device by W. V. Taylor (adapted from [35] [6])

More recently, the constant-volume combustion concept has been revisited by the European engine group SAFRAN. B. Robic [36], at Safran Aircraft Engines, describes a chamber with a linear intake and exhaust arrangement, controlled by a system of rotating spheres with perforations. This approach is conceptually similar to earlier designs to B.G. Macarez[37] (2001), which employs a rotating throttle. G. Taliercio [38]and C.N.H. Viguier (2016), at

Safran Helicopter Engines, propose a rotary distributor turbine in which the gas inlet and outlet are radial and positioned opposite each other (Figure 2-19).

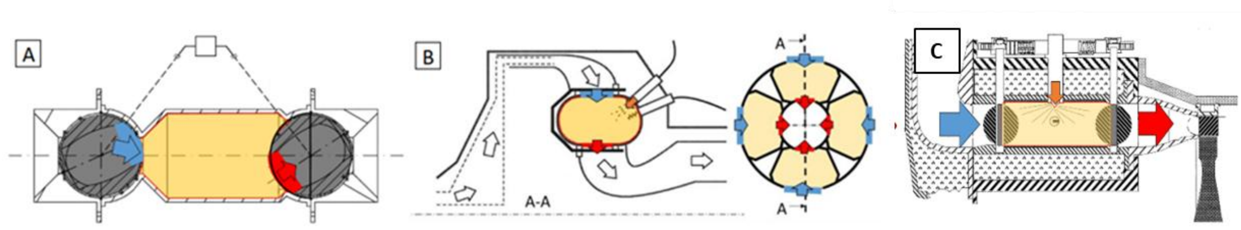

Figure 2-19 A: Cutaway view of Robic's CVCC concept [36]. B: Sectional views of the CVCC design by Taliercio and Viguier[38]C: Sectional view of Macarez's CVCC design [37]

In 2016, Leyko[39], [40] patented a combustion module for turbine engines in collaboration with SafranTech. The design targets constant-volume combustion for aircraft engines such as turbojets, turboprops and open-rotor configurations (see Figure 2-20).

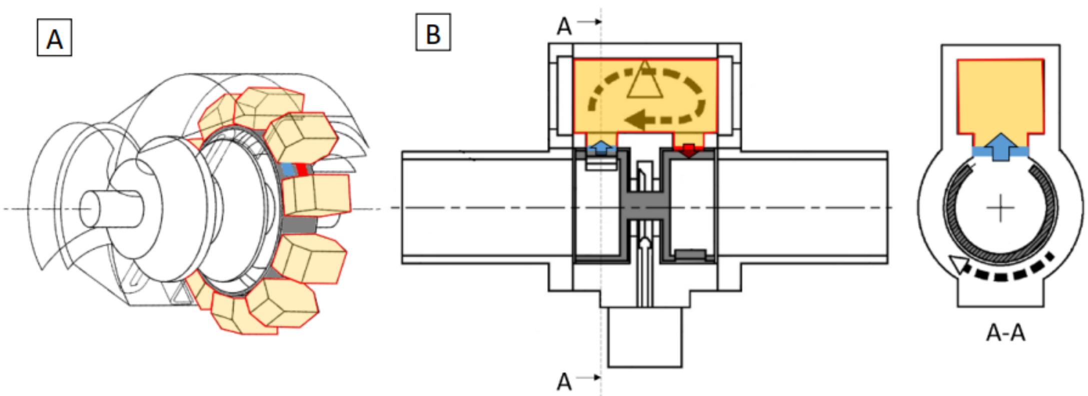

Figure 2-20 A: Conceptual view of a turboshaft engine integrated with 10 isochoric combustion chambers (Leyko, 2016 [39], [40] B: Sectional views of a simplified configuration illustrating the operation of the coaxial radial rotary distributor.

Conventional ignition in such chambers relies on a spark igniter, which requires careful synchronization across multiple chambers and results in a complex ignition system. To improve energy efficiency, the patent proposes linking the outlets of two chambers with ducts to create back pressure, thereby increasing the mixture density. Additional ducts between the inlets of two chambers allow the transfer of burnt gases or compounding gases, improving the compression level in the following chamber before fuel injection, without disturbing ignition. In the absence of a spark igniter, the system may instead introduce hot burnt gases directly into the constant-volume chamber, triggering combustion due to their elevated temperature.

Despite the industrial difficulties that prevented early constant-volume combustion systems from reaching maturity, interest in CVC technologies persisted because of their potential performance advantages for aeroengines. Early performance [3] estimates suggested that, if the technical challenges could be overcome, CVC could offer meaningful improvements over conventional Brayton-cycle propulsion. In particular, the higher pressure rise achievable through CVC was predicted to reduce SFC, with studies indicating up to a 5% [13]improvement at supersonic cruise conditions compared to a conventional Brayton cycle engine. These prospective gains (illustrated in Figure 2-21) provided a strong incentive for renewed investigation beyond industrial prototypes. As a result, research efforts gradually shifted from early engineering trials to more systematic academic studies aimed at understanding the underlying physics of CVC and identifying pathways toward practical implementation.

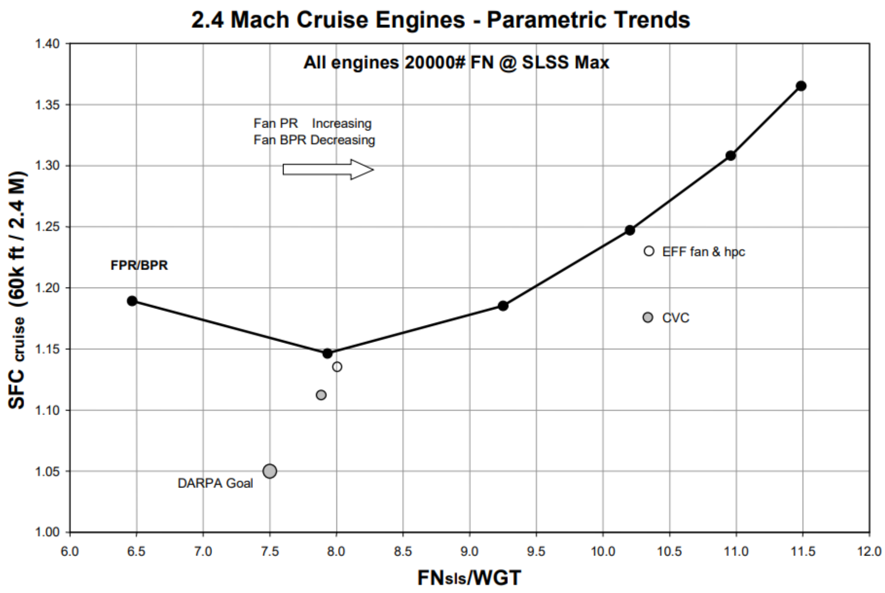

Figure 2-21. Impacts on SFC due to component efficiency improvements[13]

2.2.2.5.3 Fundamental research of pistonless CVC

Fundamental research on pistonless CVC remains limited and is mainly conducted by a small number of research groups, mainly in France and Italy. The University of Florence [41], [42]exploit an approximate constant-volume combustion (a-CVC) set-up, with the absence of the exhaust valve in collaboration with Finno-Exergy as well as a 1D model of a deflagration-based pressure-gain concept inspired by pistonless ICE. Politecnico di Milano[28] proposed thermodynamic numerical tools. PPrime Institute conducts both experimental investigations, using two dedicated test benches (CVC and CV2) [43], [44] and complementary numerical studies. Politecnico di Torino[45] has addressed system-level integration of the CVC test bench at PPrime. CERFACS also focused on LES investigations[46] [47]of CVC setup. Overall, the available literature is scarce, which makes detailed comparison between studies difficult and highlights the need for further fundamental investigations.

2.2.2.5.3.1 CVC facility at PPRIME

The constant-volume combustion chamber shown in Figure 2-22 Constant Volume Combustion setup was developed and installed in the combustion laboratory of the Pprime Institute (Poitiers, France) as part of the RAPID project Thermoreacteur [46]. The system is composed of a combustion chamber equipped with rotating valves that control the intake and exhaust phases. This configuration was investigated experimentally by Boust et al. [48][49] Michalski [43]and numerically by Labarrere et al. [46]. The primary objective of the project was to demonstrate the feasibility of operating an isochoric combustor at high frequencies, a key requirement for propulsion applications. Tests were conducted over a broad range of operating frequencies and it was observed that above approximately 40 Hz, the combustion duration became too long to ensure complete heat release, leading to stronger cycle-to-cycle variations.

Gallis et al. [45], [50], [51]developed a 0-D/1-D model of the CVC configuration using GT-Power. As the software is originally intended for piston internal combustion engines, it was adapted to represent the motionless chamber of the CVC. The model incorporated parametrized discharge coefficients, a modified burning rate formulation and a heat transfer model. The experimental data from PPrime were used both as boundary conditions and as validation data for the numerical simulations. The predicted pressure fluctuations showed reasonable agreement with the measurements. A complementary 3D[50] numerical study of the exhaust system was also carried out.

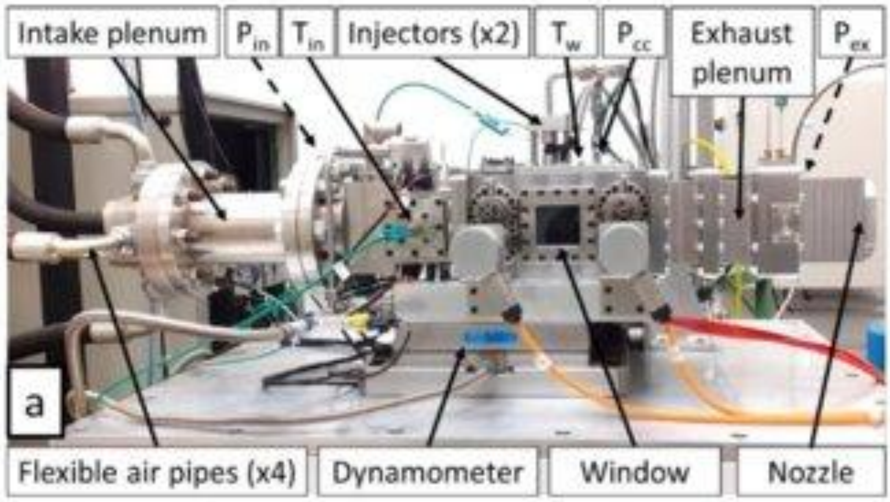

Figure 2-22 Constant Volume Combustion setup

2.2.2.5.3.2 Constant Volume Combustion Vessel (CV2)

Another pistonless combustor was designed to overcome the main technological limitations of the abovementioned setup, such as restricted modularity, limited optical access and valve sealing. Developed by Michalski (2019) [6]at Pprime, the CV2 setup[1] (Figure 2-23) enables full optical access and optimal modularity for fundamental, canonical CVC investigations. Michalski (2019) carried out both experimental and numerical investigations from the CV2 set-up.

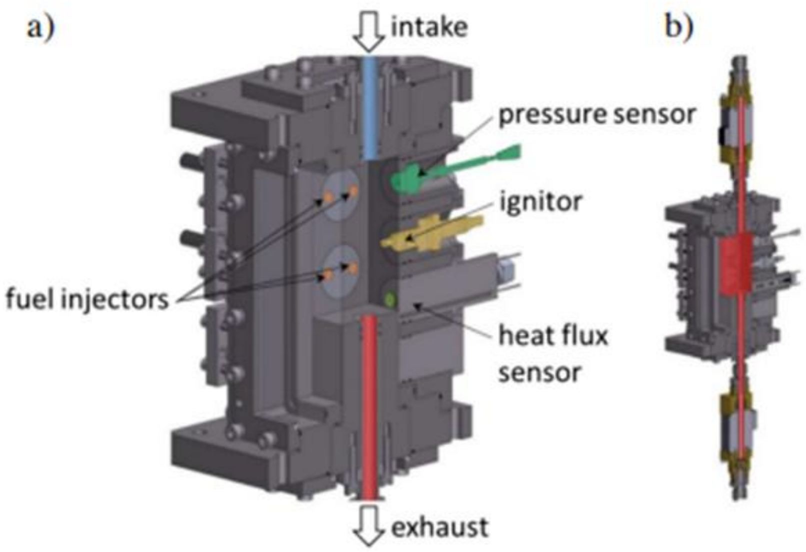

Figure 2-23. (a) CV2 combustor details. (b) The entire inner volume of the chamber (red).

In parallel with these experimental developments, Bonneau et al. (2022) [52]proposed a dedicated Large Eddy Simulation (LES) framework for CV2 that couples a simplified flamelet-type turbulent combustion model with a reduced thermochemical database exploiting self-similar laminar flame structures and a wall-law formulation tailored to the strong cyclic variations of heat transfer in the chamber. This low-cost strategy was designed to simulate sequences of many cycles with realistic intake and exhaust mass-flow histories, while still reproducing the measured pressure and wall-heat-flux signals and capturing the role of residual burnt gases in the mixture evolution. By adjusting a limited set of modelling parameters (air and exhaust mass, sub-grid segregation rate and wall-heat-loss coefficient), the framework achieves good agreement with CV2 experiments over up to ten consecutive cycles and provides access to three-dimensional fields of velocity, mixture fraction and temperature throughout injection, combustion and exhaust.

More recently, Detomaso (2023)[47] studied turbulent flame propagation in the CV2 numerically using LES. His work examined the effects of stretched and thickened flame modes across multiple spark-ignition cycles. Building on numerical strategies previously applied to afterburner simulations[53] the methodology was adapted for CVC applications, including approaches to track carbon dioxide and water vapor within the flammable mixture.

Together, these numerical studies show that CV2 can be used not only as an experimental platform but also as a reference configuration for LES-based investigations of cyclic constant-volume combustion. In the following, the discussion focuses on how different parameters (for example velocity-field, residual-gas dilution, ignition strategy, cycle-to-cycle variability) control spark-ignition regime in pistonless CVCs.

2.3 Spark-ignition combustion in pistonless CVCs

In pistonless chambers such as the CVC and CV2 test rigs, all cycle-to-cycle variability originates from the aerodynamic field established during intake and from the properties of the residual burnt gases trapped after exhaust, since there is no piston-driven compression to restructure the flow before ignition. Compared to four-stroke engines where compression amplifies and spatially reorganizes in-cylinder turbulence, turbulence in CVCs decays freely once the intake valve closes and the chamber is at constant volume. Therefore, the ignition event and subsequent flame propagation are constrained to a relatively narrow time window[48], [54].

2.3.1 Velocity field at ignition and ignition probability

Time-resolved PIV measurements on both the original CVC chamber [48]and the CV2 [55]vessel show that the intake jet generates large coherent vortices and intense shear layers, which then rapidly break down into smaller-scale turbulence as the valve closes. In the CVC chamber, Labarrere et al. (2016)[46] showed through joint experiments and LES that local velocity at spark timing and residual gas fraction were the dominant drivers of cycle variability, with cycles starting above ~30 m/s at the plug systematically misfiring even with powerful sparks.

In CV2, the intake phase reaches bulk velocities of the order of 250-300 m/s near peak mass flow rate, but after valve closure the mean velocity near the spark plug decays from tens of m/s to a few m/s over roughly 10 ms. For late ignition timings (e.g. $t_{ign} \approx 32.5$ ms in CV2), Michalski reports low local velocities around 2 m/s in the spark region and a 100% kernel propagation success rate with very small cycle-to-cycle dispersion in peak pressure and combustion duration.

At earlier ignition timings, the residual flow is more structured and velocities at the plug are significantly higher, which degrades ignition reliability. In the CVC set up, Boust et al[48]. observed that when the spark is located in a high-speed stream, ignition probability drops sharply once the local velocity magnitude exceeds about 20–25 m/s, even though the turbulent fluctuation level u' can be higher in other regions where ignition statistics are more favorable. Complementing these results, De Jesus Vieira et al. [56]measured minimum ignition energy (MIE) directly in the TUMBLE-2 chamber with grid-generated isotropic turbulence, finding that average velocities around 35-40 m/s in the gap region raise required spark energy by nearly 6x under 10% dilution compared to quiescent conditions.

In CV2, under stoichiometric propane/air conditions, a statistical analysis of PIV and pressure data led Michalski [54]to define a "limit velocity", V_{lim}, based on the cumulative distribution of local speed near the plug: diluted cycles with OER = 1.0 and ~21% RBG dilution exhibit a characteristic limit $V_{lim} \approx 9.3$m/s, above which the misfire rate increases strongly. When the overall equivalence ratio is reduced to 0.6 at similar dilution, the characteristic velocity shrinks to $V_{lim} \approx 2.4$m/s, consistent with the reduced chemical reactivity near the lean flammability limit.

A key implication is that, for given mixture composition and RBG dilution, the average ignition success rate can be predicted from the local velocity statistics: ignition probability essentially equals the probability for the instantaneous velocity at the plug to fall below Vlim, so any change in intake strategy, valve phasing or operating frequency that modifies the velocity probability density function (PDF) directly shifts the stable operating window. This view is consistent with the earlier CVC work of Boust et al.[48], who also linked ignition probability to local flow speed more than to global turbulence intensity and with LES studies[52] [54]which confirm that, at the CV2 ignition location, equivalence ratio fluctuations at ignition scale are relatively small in the operating range of interest.

It should be noted, however, that LES predictions of instantaneous velocity fields can exhibit sensitivity to initial and boundary conditions, which may affect quantitative reproducibility while generally preserving statistical trends. In addition, while velocity is used here as a practical indicator, other flow quantities such as local strain rate are also accessible from LES and may provide a more direct measure of the aerodynamic constraints on flame kernel survival. However, these quantities were not explicitly analyzed in the present context, and velocity remains a convenient and widely used proxy.

2.3.2 Operating frequency

Operating frequency adds another layer of constraint. On the original CVC setup, Boust [48]showed that increasing the cycle frequency from 25 to 40–60 Hz reduces the available mixing time and shortens the constant-volume phase, while the turbulence level at ignition does not scale linearly with frequency; beyond a certain point, the flame cannot fully consume the charge before the exhaust opens, so maximum pressure drops and incomplete combustion appears. In CV2, Michalski [54], [57] reports similar behaviour: earlier ignition timings are required to reach higher effective frequencies, but these timings coincide with higher velocities and stronger shear at the plug, leading to increased misfire rates unless the spark energy or position is adapted.

2.3.3 Residual burned gases dilution

Because there is no dedicated scavenging in CV2, every successful combustion cycle leaves a fraction of hot products in the chamber; the fresh air and fuel are injected on top of this residual mass, so the mixture at ignition is always partially diluted by RBG except for "primary" cycles following a misfire or a non-reactive purge. 0D analyses by Michalski [55]indicate that, depending on exhaust back-pressure and wall temperature, RBG mass fractions at ignition typically range from about 15–40% by mass in liquid n-decane/air operation, with corresponding residual temperatures on the order of 500–600 K at low wall temperature and significantly higher when the walls approach realistic combustor temperatures [54], [57].

In gaseous propane operation, this dilution directly affects both maximum combustion pressure and flame propagation time. For stoichiometric OER = 1.0 in CV2, "secondary" cycles diluted by ~21% RBG exhibit longer ignition-kernel development times t0–10 and longer overall combustion durations $t_{10–90}$, where these intervals correspond to the time required for the normalized pressure rise (used as a proxy for heat release) to increase from 0% to 10% and from 10% to 90%, respectively. In contrast, primary cycles igniting in nearly undiluted fresh mixture reach higher peak pressures, while diluted cycles exhibit lower peak pressures due to the reduced density jump across combustion. At leaner overall mixtures (OER ≈ 0.6), dilution still sits around 20%, but the combined effect of lower reactivity and a lower limit velocity produces ignition success rates of order 30–50% depending on phasing[54].

In liquid-fuel operation, residual gas properties are controlled mainly via exhaust back-pressure and wall temperature. Increasing the exhaust pressure from ~0.07 MPa up to ~0.21 MPa raises the trapped RBG mass and its temperature, increasing dilution from roughly 16% to nearly 40% and stretching combustion durations by about a factor 2.5‑3 between the least and most diluted cases. The higher dilution reduces flame speed and moves more heat release towards the end of the constant-volume window, which tightens the allowed ignition timing range if the exhaust schedule is kept fixed. Raising the wall temperature towards 1000 K reduces cooling of the residual gases during exhaust, so that at a given back-pressure the trapped mass is lower but hotter; 0D extrapolations [57]show higher initial gas temperatures at ignition and lower dilution, which should favour faster combustion but also increase the risk of auto-ignition in subsequent cycles.

2.3.4 Cycle-to-cycle variability and LES insights

Both experimental pressure traces and optical diagnostics on CV and CV2 reveal significant cycle-to-cycle dispersion in maximum pressure, combustion duration and even in whether a given cycle fires or misfires, especially in the regimes with early ignition and high dilution. Primary cycles typically achieve higher peak pressures and shorter burning times than secondary ones at identical command signals, because they start from lower dilution and higher density; secondary cycles inherit the RBG field of the previous cycle and are more sensitive to its spatial inhomogeneities. Misfired diluted cycles act as an effective scavenging pulse, resetting the chamber to almost fresh conditions for the next ignition attempt and thereby intermittently restoring high-pressure cycles[52],[48],[54],[43].

LES have been developed specifically [52], [55]for CV2 to complement these measurements and to explore how initial and boundary conditions propagate across many cycles. In stable operating points, LES reproduces the measured pressure and wall-heat-flux signals over sequences of several cycles with reasonable accuracy and confirms that: (i) mixing during intake is efficient enough to yield a nearly premixed field at the ignition scale for the conditions used in ignition-stability studies; (ii) hot RBG pockets persist in recirculation zones during the intake, providing potential self-ignition kernels if their temperature and composition cross auto-ignition thresholds; and (iii) local scalar and velocity histories at the plug are crucial to determine whether a given spark leads to a growing flame kernel or to quenching. These numerical results also highlight the sensitivity of cycle-to-cycle variability to small changes in injected and exhausted mass, wall-heat-loss modelling and spark-kernel parametrization, which is consistent with the experimental observation that small drifts in tank pressure or valve response can change the balance between primary, secondary and self-ignited cycles.

Overall, previous work on CV and CV2 suggests that cyclic spark ignition of liquid or gaseous fuels in pistonless CVCs is controlled by a limited set of strongly coupled parameters: local velocity statistics at the plug (and the associated limit velocity, V_{lim}), mixture composition at ignition (equivalence ratio and RBG dilution), wall temperature and exhaust back-pressure (through their control of RBG mass and temperature) and the imposed cycle frequency and ignition phasing. For a given fuel and spark system, reliable cyclic ignition requires operating within a window where, at the chosen ignition timing, (i) the probability for the local velocity to remain below V_{lim} is high, (ii) the mixture remains within a relatively narrow band of equivalence ratio that keeps V_{lim} compatible with the available aerodynamic conditions and (iii) the combination of dilution and turbulence intensity still allows the flame to consume most of the charge before the exhaust opens.

Outside this window, misfires, incomplete combustion and/or self-ignition events become more frequent and the system exhibits pronounced cycle-to-cycle variations that are undesirable for propulsion applications but can be exploited, as in Michalski's work, to probe ignition mechanisms and to design alternative ignition strategies based on controlled residual-gas-triggered auto-ignition. At high dilution levels, this behaviour becomes more pronounced. Some cycles experience slow combustion which promote a higher residual temperature leading to self-ignition events in the next cycle. Furthermore, achieving the power density required for flight demands high cycle frequencies, which limit mixing time and require more sophisticated spark-ignition strategies [43], [58]. In these regimes, controlled self-ignition could offer a viable alternative ignition mechanism, with residual burnt gases providing a potential pathway. Michalski [6] performed a preliminary study to path the way on ignition of liquid fuels by hot residual gases for self-ignition processes in n-decane/air mixtures.

2.4 Liquid-fuel self-ignition in aeroengine applications

Self-ignition is the phenomenon where a fuel-air mixture ignites spontaneously without an external ignition source, driven solely by elevated temperature and/or pressure. This occurs when the mixture reaches its self-ignition temperature, allowing the chemical reaction to proceed without a spark or flame. This phenomenon is central to many combustion systems: under controlled conditions, it can enhance thermal efficiency and contribute to stable combustion, but if uncontrolled, it may also lead to detrimental effects such as engine knock and component degradation. The onset of self-ignition is influenced by several factors, including air temperature, pressure, fuel properties and the presence of residual hot gases. Higher residual gas temperatures and elevated flow rates further promote this phenomenon[59].

Self-ignition is particularly relevant in gas-turbine aeroengines, which typically operate with fuel-lean, direct-injection combustors designed for conventional kerosene-based fuels. Compared to gaseous fuels such as natural gas, kerosene exhibits significantly shorter auto-ignition delay times under similar thermodynamic conditions[60], making it more prone to spontaneous ignition at high temperatures and high pressures. Aeroengines operate at overall pressure ratios on the order of 40–45[61], conditions that favor high thermodynamic efficiency but also increase the likelihood of self-ignition in regions where fuel and air mix before combustion. Understanding self-ignition behavior is therefore essential for predicting ignition dynamics, defining safe operability limits and designing next-generation combustors that must function under increasingly challenging conditions.

Several studies have examined liquid-fuel self-ignition under conditions representative of turbine operation. Giusti et al.[62] investigated the self-ignition characteristics of isolated kerosene droplets in vitiated air, focusing on the influence of dilution with hot combustion products. Their results showed that increasing dilution reduces the auto-ignition delay, primarily due to the elevated temperature of the surrounding gases. Complementary numerical work by Fredrich et al. [63]further explored kerosene self-ignition in aeroengine environments, confirming that reduced dilution levels lead to longer ignition delays. Their study also highlighted the strong sensitivity of ignition behavior to droplet size: small initial droplet diameters ignite only at sufficiently high pressures, while a reduction in initial fuel temperature mainly acts to extend both the self-ignition delay and the total evaporation time.

Hinkeldey et al. [64] extended this understanding by studying the self-ignition and combustion of kerosene and heptane sprays in a premixing duct across temperatures from 750 to 1100 K. Their results revealed the formation of multiple, spatially separated ignition kernels, indicating that spray self-ignition cannot be represented by a single droplet model and instead requires a more comprehensive description of multiphase and spatially distributed processes.

In aeroengine applications, research on liquid-fuel self-ignition has primarily focused on preventing uncontrolled ignition. This focus stems from the wide range of pressures, temperatures and flow rates encountered in flight, which demand reliable and predictable combustion behavior over the entire operating envelope. However, when self-ignition can be deliberately triggered and controlled, it may offer performance benefits in alternative combustion modes[61]. CVC allows a means to regulate the self-ignition phenomenon and harness it for beneficial purposes.

At present, the behavior of kerosene in the CVC conditions remains undocumented as current turbine engines do not operate in this mode[3]. Beyond the work of Michalski, there is a dearth of information regarding self-ignition resulting from direct liquid injection fuel in pistonless CVC systems. This lack of data highlights the need to better understand and control liquid-fuel self-ignition within constant volume combustion configurations for aeroengine applications. Existing self-ignition studies are almost exclusively tied to the conventional Brayton cycle, leaving a significant gap in knowledge for the more efficient Humphrey cycle. Addressing this gap is essential, as mastering self-ignition in CVC systems offers the potential for higher thermal efficiency and reduced soot emissions, ultimately improving overall aeroengine performance.

Despite numerous experimental and numerical investigations of kerosene and surrogate auto-ignition, systematic parametric studies of self-ignition under CVC-relevant conditions (pressure, temperature, equivalence ratio and dilution) are still missing. In this context, the present thesis aims to provide such a parametric characterization for liquid fuels in a pistonless constant-volume combustor and to clarify how the ignition timing, hot residual gases and operating frequency control the onset of self-ignition.

2.5 Objectives of the thesis

This thesis addresses the critical gap in understanding and controlling liquid-fuel combustion initiated by spark or by self-ignition under CVC conditions for air-breathing propulsion. While previous studies have primarily focused on spark-ignition, mainly with gaseous fuel, data on direct liquid injection remain scarce. The main objective of this work is to investigate liquid-fuel combustion in an airbreathing CVC combustor and ultimately make its occurrence controllable in spark-ignition as well as self-ignition.

The key contributions of this thesis can be synthesized as follows:

1. Experimental investigation of liquid-fuel spark-ignition in a pistonless CVC system

Using the CV2 setup, the thesis systematically examines how flow conditions, mixture dilution, residual burnt gases and ignition strategies influence spark-ignition stability.

2. Experimental study of parameters enabling self-ignition in pistonless CVC systems

The research identifies the conditions that trigger self-ignition and explores how these parameters can be controlled to achieve reliable and repeatable ignition.

3. 0D/1D modeling of the CV2 setup

A 0D/1D numerical model, initially developed for gaseous spark ignition, is adapted to simulate liquid-fuel spark ignition and self-ignition, providing access to key parameters that are difficult to measure experimentally.

4. Assessment of overall combustion efficiency

The thesis evaluates the efficiency of both spark ignition and controlled self-ignition, quantifying the potential advantages of self-ignition in terms of energy conversion.

5. Potential industrial application of self-ignition in aeroengines

The study explores the use of self-ignition in multi-chamber configurations for future aircraft engines, demonstrating its potential relevance for high-efficiency propulsion systems.

Through these contributions, the thesis advances both fundamental understanding and the practical control of liquid-fuel ignition in CVC systems, addressing a key limitation in the development of next-generation aeroengine technologies.

Chapter 3: CV2: an experimental cyclic constant-volume combustion device and its reduced order model

3.1 Introduction

This chapter is dedicated to the presentation of the materials used to perform the study, most of which have been adapted to our specific case. The chapter is divided into three parts: the description of the experimental setup (CV2), the experimental diagnostics and the 0D/1D model used for physical analysis.

The first part presents the CV2 assembly, the characterization of boundary conditions and the digital analysis tools employed. In the second section dedicated to experimental diagnostics, both physical sensors and optical diagnostics of the setup are described in detail.

In the last section, a 0D/1D model adapted in this framework to direct liquid fuel injection and to self-ignition configuration is detailed. This physical simulation code allows to predict the behavior of CVC successive cycles and to interpret and analyze experimental results, thus providing information and parameters that could not be measured directly. Finally, the coupling methodology enables a comprehensive characterization of a reference case (detailed in Chapter 4:): a spark-ignited cycle of liquid n-heptane directly injected in air. This reference case provides the foundation for achieving the objectives related to self-ignition, which are addressed in Chapter 5: .

3.2 Description of the CV2 setup

The CV2 setup (Figure 3-1) also known as Constant-Volume Combustion Vessel is an experimental test rig designed to reproduce pistonless cyclic constant-volume combustion at PPrime Institute. The modular design of CV2 allows for multiple geometrical arrangements (linear, corner, stagnation point), corresponding to several patents [36], [39], [40]. In this manuscript, the study is limited to the linear configuration of the system [65]. The main systems of this pistonless setup include the combustion chamber, intake and exhaust systems. These systems are described in detail in the following subsections.

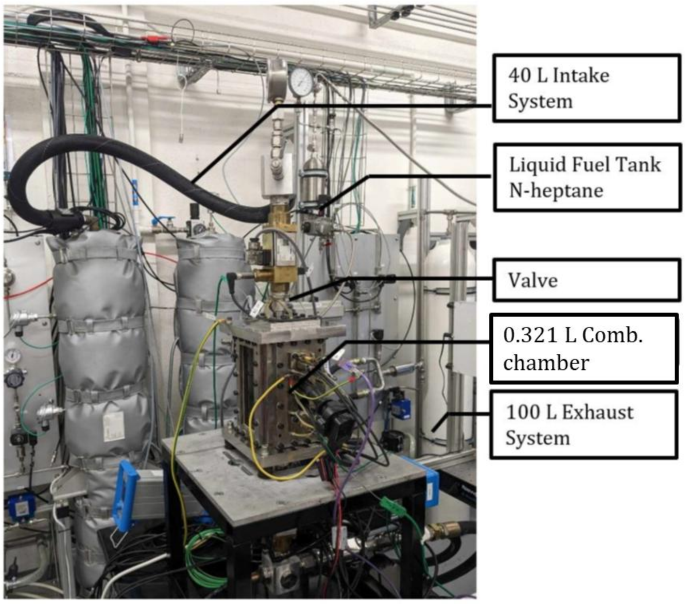

Figure 3-1. CV2 set up at PPrime Institute

3.3 Introduction

The aviation sector faces increasing scrutiny due to CO_2 emissions associated with rapid air travel, motivating initiatives such as ACARE to set ambitious reduction targets. The optimized propulsive efficiency of conventional aircraft engines underscores the need for alternative combustion strategies capable of further improving their overall thermal performance. Pressure Gain Combustion emerges as a promising solution.

The chapter discusses about efficiency gains of PGC through the Humphrey cycle, based on constant-volume combustion and the Fickett-Jacobs cycle, based on detonative combustion, over the Brayton cycle (constant-pressure combustion), which is currently used in aeroengines. The conditions required to achieve PGC are then outlined, followed by a historical review of pressure gain combustion technologies, highlighting the advantages and drawbacks that shaped their evolution.

Focus then shifts to a detailed state-of-the-art of constant-volume combustion (CVC) systems, where issues such as self-ignition, scavenging and ignition control arise. Particular attention is given to pistonless combustion chamber configurations, which provide a basis for identifying critical research gaps. This progression ultimately sets the foundation for examining self-ignition as a potential ignition strategy for achieving stable, high-efficiency operation in piston-less constant-volume combustion.

3.3.1 Description of the combustion chamber

3.3.1.1 Volume of the combustion chamber

The combustion chamber is a single rectangular chamber, machined from stainless steel (17-4 PH) with internal dimensions of 100 × 50 × 50 mm (represented as the rectangular optically accessible nominal volume in blue in Figure 3-2). The whole system is manufactured and assembled with reduced tolerances and mechanical clearances so as to minimize the volumes of the crevices (dead volumes represented red and labelled as crevices in Figure 3-2). The tubular volume (intrinsic to the valves represented in green in Figure 3-2 and volumes of the crevices of the chamber have extensive thermodynamic properties which must be measured or estimated at best to ensure the fidelity of the simulations, of the properties of intake (temperature, pressure) and of combustion (unburnt gases in the crevices). Fresh gases are compressed in the cavities close to the wall and in particular in the assembly gaps. This amount of unburnt gas is directly involved in the degradation of combustion efficiency (final combustion pressure) and must therefore be correctly estimated via the volumes of crevices.

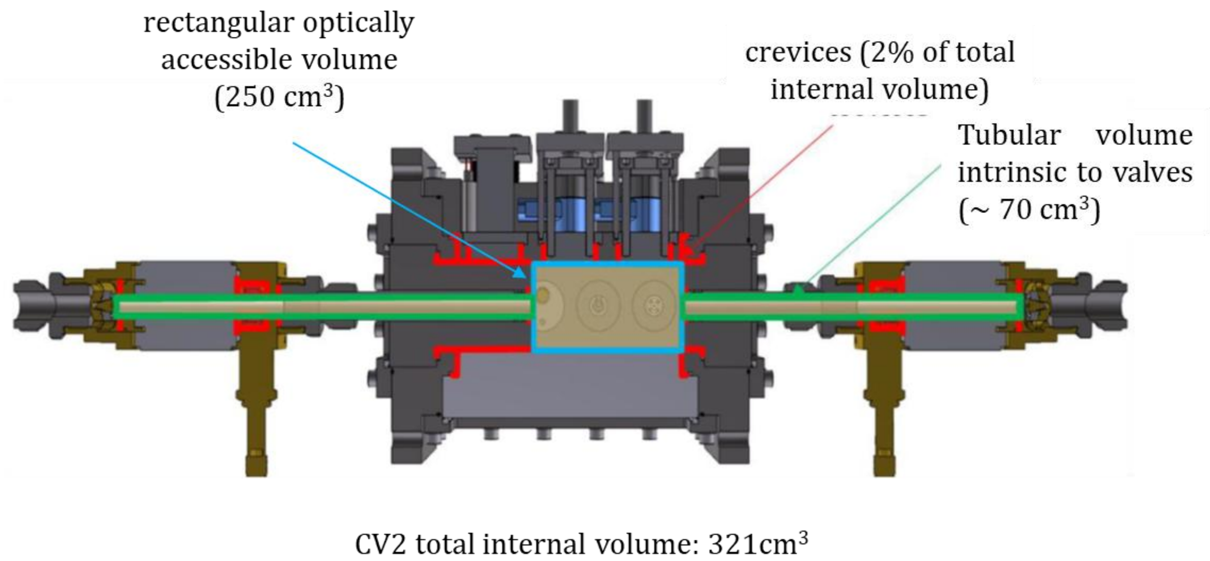

Figure 3-2 Sectional view of the combustion chamber in a linear configuration. The total internal volume represented in yellow is the sum of the rectangular optically accessible nominal volume in blue, the volumes of the crevices represented in red and the tubular volume intrinsic to the valves represented in green.

The internal volume is sealed at several points. On flanges and inserts, sealing is ensured by O-rings (FKM Viton) so as to minimize the volumes of crevices. The volume of the crevices is estimated by measuring the assembly clearances (cross-checking of measurements with shims and a caliper) and represents 2% of the total volume. The total internal volume of the combustion chamber is thus 0.3214±0.0017 L (uncertainty of 0.5 %).

3.3.1.2 Diagnostics of the combustion chamber

The combustion chamber features wide, shoulder-mounted windows made from 7980 KrF UV silica, allowing full optical access to the internal parallelepiped volume. Hence, it enables chemiluminescence visualization from excited chemical radicals during combustion (such as CH* or OH*). The chamber also includes different sensors for temperature and pressure diagnostics, as well as unsteady wall heat flux measurement (cf. Figure 3-3).

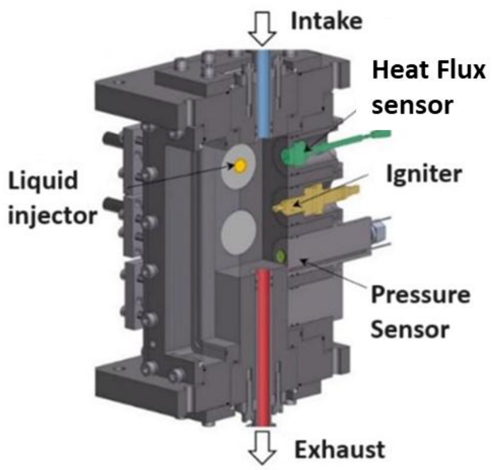

Figure 3-3 Visual of the combustion chamber

A flush-mounted spark plug installed in the chamber wall is used to ignite the mixture and initiate combustion propagation. A flush-mounted configuration limits geometric flow perturbation and ensures that ignition occurs under well-defined local aerodynamic conditions. In addition, placing the spark plug flush to the wall helps reduce its thermal exposure compared to the middle of the chamber, since conductive heat transfer to the chamber wall is stronger in the near-wall region, limiting excessive heating of the igniter. In this reference scenario, combustion begins under controlled initial conditions: pressure and temperature are set in advance and the valves remain closed. The combustion chamber temperature is maintained at 130 °C using proportional-integral-derivative (PID) controllers and thermocouples on the internal chamber walls.

3.3.2 Description of the intake system

3.3.2.1 Air intake system

The air intake system is connected to the combustion chamber through electro-valves. A single COAX MK10 fast solenoid valve controls the air intake.

This setup enables filling two tanks of 20 L with hot air.

The temperature of the air tanks is maintained at 150 °C using thermocouples associated with PID-controlled heaters. Air intake tanks are linked to the fast solenoid valve by a 1.5 m connecting hose with a 16 mm internal diameter (cf. Figure 3-4), also heated and regulated to 150 °C.

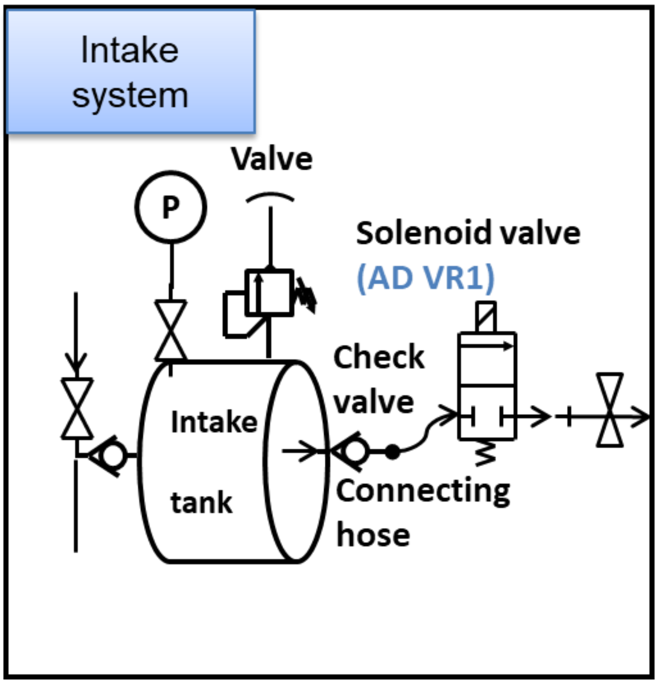

Figure 3-4 Schema of the air intake system

The inlet volume is charged to a desired pressure (usually 10 bar) higher than the chamber pressure so that, given the valve cross-sections, the resulting mass flow rate achieves the target to control the equivalence ratio. This volume is comprised of connecting pipes from the panel, the main tank and the connecting hose. The characterization of the air intake system is annexed in Appendix A.

3.3.2.2 Fuel Intake System

Liquid fuel is pressurized inside an injection tank up to 100 bar (n-heptane under N_2). The liquid fuel injector used in this study is a Bosch HDEV-5.1 (as seen in Figure 3-5). Based on the injector characteristics and the pressure in combustion chamber at injection time, the pressure in the fuel tank is set to 100 bar. The characterization of the fuel injection systems is annexed in Appendix B.

With modification implemented during the study, the setup operates over 10 to 20 cycles, enabling precise measurement of injected air and fuel mass. From the characterization of the intake systems, the Equivalence Ratio can be controlled, enabling fine tuning over the experimental conditions further described in section 3.4.2.

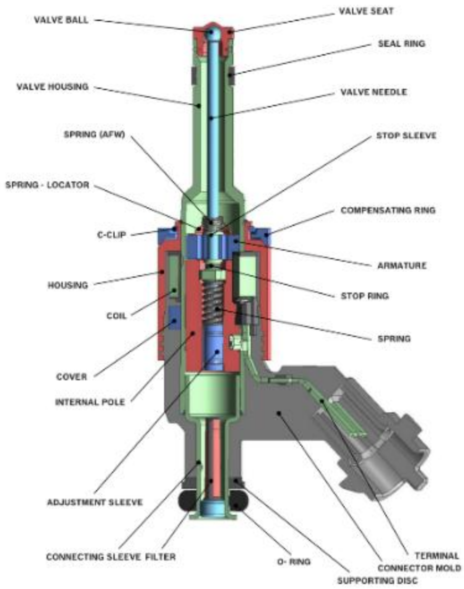

Figure 3-5. Bosch HDEV-5.1, liquid injector used in CV2

3.3.3 Description of the exhaust system

The exhaust system is connected to the combustion chamber through an electro-valve. A COAX MK10 fast solenoid valve controls the exhaust phase during operation. It uses two 50 L tanks connected by 16 mm internal diameter piping. The main tank connects to the exhaust valve through a non-insulated hose, 1.5 m long, with a 16 mm internal diameter. Between the exhaust valve and the exhaust tanks, a lambda probe allows to evaluate the mean equivalence ratio of exhaust gas (see description § 3.4.2).

The main components and their subsystems are characterized to ensure the proper operation of the test bench (see APPENDIX A-C).

3.3.4 Physical sensors and data acquisition system

Data acquisition and bench control are managed by a National Instruments PXIe-8820 controller. It operates a fast acquisition card (PXIe-6363) at 100 kHz per channel and a slower acquisition card (PXI-6224) at 10 kHz per channel.

The chamber is fitted with two pressure sensors for combustion pressure measurement. A piezoresistive sensor (Kistler 4049B) records absolute pressure signals up to 20 bar, with a mechanical limit of 30 bar (natural frequency of 60 kHz). A piezoelectric sensor (Kistler 6067C) is added to capture the high-frequency pressure variations (up to 90 kHz) and resolve peaks that exceed the 20 bar limit of the piezoresistive sensor 4049B.

The specifications of all the bench sensors used to measure additional parameters during the combustion process are organized into four functional categories: pressure sensors, temperature sensors, position measurements and gas composition measurement, as shown across Table 3-1 - Table 3-4. These data are subsequently used for diagnostics and analysis.

Table 3-1 Pressure sensors

Measurement Point	Sensor Type	Model & Make	Accuracy	Bandwidth
Gage chamber pressure (Pdcc)	Piezoelectric transducer	Kistler 6067C	±25 mbar	90 kHz
Absolute chamber pressure (Pacc)	Piezoresistive transducer	Kistler 4049B	±60 mbar	60 kHz
Absolute inlet tank pressure (Prad)	Piezoresistive transducer	Druck PTX 5072	±16 mbar	3.5 kHz
Absolute exhaust tank pressure (Pex)	Piezoresistive transducer	Druck PTX 5072	±10 mbar	3.5 kHz
Exhaust line pressure (Ple)	Piezoresistive transducer	Kistler 4049B	±60 mbar	60 kHz

Table 3-2 Temperature and Heat Flux Sensor

Measurement Point	Sensor Type	Specification	Accuracy	Recording frequency
Local wall temperature in chamber (Tw)	K-type thermocouple	Insulated sheathed Φ 1.5 mm	±1.5 °C	100 kHz
Local wall heat flux in chamber (Tw)	E-type thermocouple	Nanmac E12-3	±1 ° C	100 kHz

Table 3-3 Valve position Measurements

Measurement Point	Sensor Type	Model & Make	Bandwidth
Valve position (Afc)	Inductive proximity sensor	Balluff BHS005P	400 Hz
Valve position (Efc)	Inductive proximity sensor	Balluff BHS005P	400 Hz

Table 3-4 Exhaust gas composition measurement

Measurement Point	Sensor Type	Model & Make	Bandwidth
Exhaust oxygen concentration (λ)	Lambda probe	Bosch LSU 4.9	<10 Hz

An in-house–developed interface enables remote control of all systems and actuators via a computer connected to the controller over Ethernet. The CV2 device is designed for a limited number of operating cycles, with the air reservoir allowing up to 24 cycles per series. This limitation arises from the cumulative pressure drop in the air tank during successive cycles, which typically reaches around 10%.

Before operation, the user programs a fully configurable cycle chronogram inserted in the interface that includes the parameters stated in Table 3-5.

Table 3-5 Parameters adjusted for a configurable cycle chronogram

Parameters adjusted	Units
Number of cycles	-
Time period of a cycle	ms
Cycle to cycle air injection timing (tair)	ms
Cycle to cycle air injection duration (dt air)	ms
Cycle to cycle fuel injection timing (tfuel)	ms
Cycle to cycle fuel injection duration (dt fuel)	ms
Ignition timing (tign)	ms
Cycle to cycle exhaust timing (tex)	ms
Cycle to cycle exhaust duration (dt ex)	ms

This flexibility allows rapid adjustment of actuator timings, to vary, for example, air, fuel or exhaust intake timing. The complete sequence is preloaded into the machine prior to firing. Once triggered, the controller executes the sequence and records dynamic acquisition channels for later analysis. An example of a typical chronogram of the different phases for a sequence is given below in Figure 3-6:

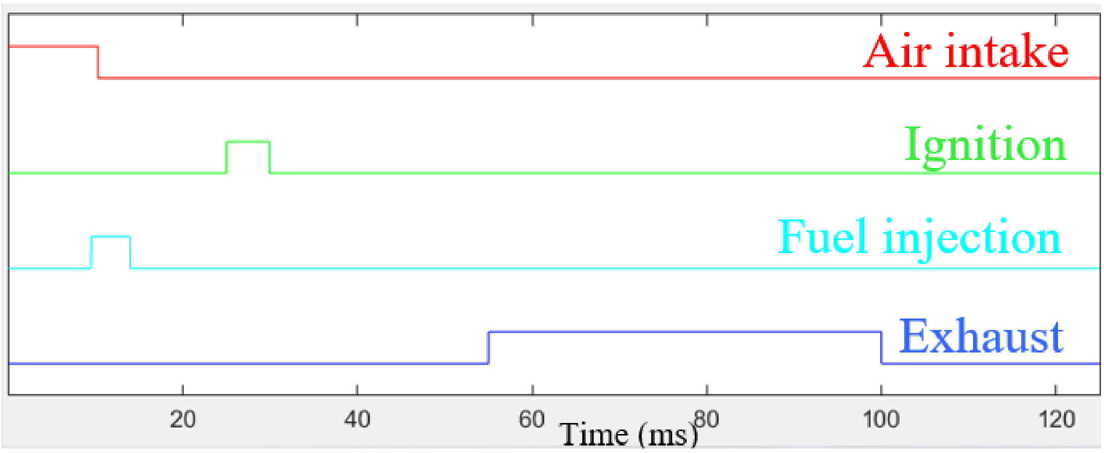

Figure 3-6 Chronogram of a sequence sample

3.3.5 Protocol and configuration operating conditions

3.3.5.1 Limits and settings of operating conditions

The chamber is designed to operate at a maximum combustion pressure of approximately 40 bar, placing strong constraints on valves, portholes and certain flanges. Consequently, the maximum initial pressure considered for combustion is 5 bar. The actual initial pressure achieved results from a compromise between the target cycle time, filling times and the corresponding exhaust pressure (cf Figure 3-7). To ensure accurate mass-balance measurements in the reservoirs, no scavenging of the system is performed during the study.

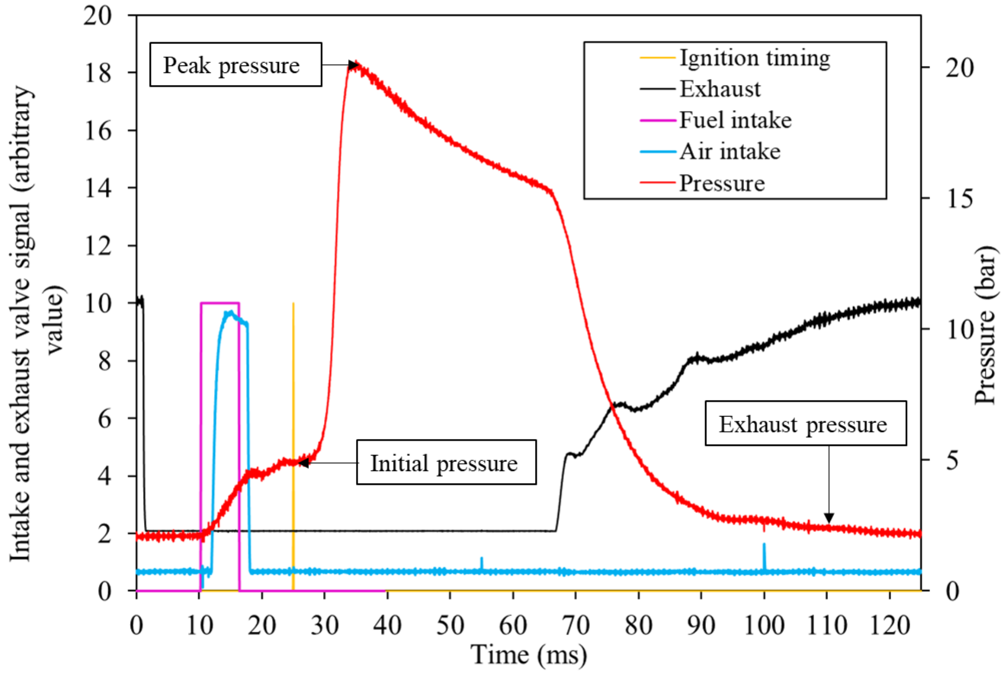

Figure 3-7 Pressure evolution (represented in red) inside the CV2 chamber of the reference spark-ignition cycle with valve timings

To define an operating point, the intake duration (i.e., injected mass) is first adjusted over several sequences to reach the desired initial pressure. During inert cycles, no spark ignition is applied, so only air is injected to characterize the filling dynamics. When the valve is fully open, the pressure rise during an inert admission phase of the cycle is roughly 200 mbar per millisecond of additional opening. The equivalence ratio (ER) of the cycle is initially estimated through preliminary calculations and then adjusted by comparing the lambda probe readings and fine-tuning the injector opening duration. The effective ER is later recalculated during post-processing (see Chapter 3.4.2) by accounting for pressure drops in the tanks. Exhaust duration and overall cycle time are also adjusted to balance the pressure between the chamber and the exhaust tank. In this work, a lambda probe is used to verify equivalence ratio previously determined from air and fuel mass flow rate measurements. The reliability of the measurements is ensured through redundancy.

In reactive cycles, dilution with residual burnt gases from a previous cycle can affect the initial pressure of subsequent fillings. Therefore, adjustments are necessary to restore the initial pressure achieved during inert cycles, often requiring a reduction of intake time by approximately 0.5 to 1.0 ms.

3.3.5.2 Protocol for a spark-ignition test

For this initial study, the initial pressure is limited to a maximum of 4.5 bar for a fresh cycle (air tank pressure: 10 bar and the air intake valve opening duration of 11 ms), with an exhaust pressure of approximately 2 bar (cf. Figure 3-7). This controls the peak combustion pressure and allows the use of the Pacc absolute sensor for dynamic pressure measurements.

With the current air valves, higher injected mass requires longer exhaust and cycle times. These conditions form the reference case.

3.3.5.3 Acquisition Protocol

The setup is controlled remotely from a separate room via a computer connected to the controller, enabling manual operation of all actuators, including valves, injectors and vacuum pumps. Before performing acquisition sequences, the actuators are systematically checked: first manually (by verifying audible opening noise and visible spark) and then during an inert sequence with settings equivalent to those planned for the reactive sequences.

3.3.5.4 Test preparation procedure

Before a test, the air tank and hose are heated to 150 °C and the combustion chamber to 130 °C. This step typically takes up to four hours. Once these temperatures are reached, the following steps are performed:

1. (Optional) The chamber is evacuated to a vacuum (<10 mbar) using a vacuum pump connected to the exhaust tank, with the exhaust valve open. This step removes water vapor that can condense on the chamber walls.

2. The exhaust tank and the chamber are filled with compressed air up to the test set pressure (typically 1, 1.5, 2 bar).

3. Critical cycle parameters are checked visually via the chronogram display and the boundary conditions (temperatures and pressures).

4. Pressures are adjusted if necessary, for example by modifying the duration of the air intake (from 2.5 bar to 4.5 bar).

5. Firing parameters are preloaded into the controller (parameters stated in Table 3-5).

6. The test is initiated.

7. Data are recorded for analysis. An example of the pressure evolution of a sequence of 20 cycles is presented in Figure 3-8.

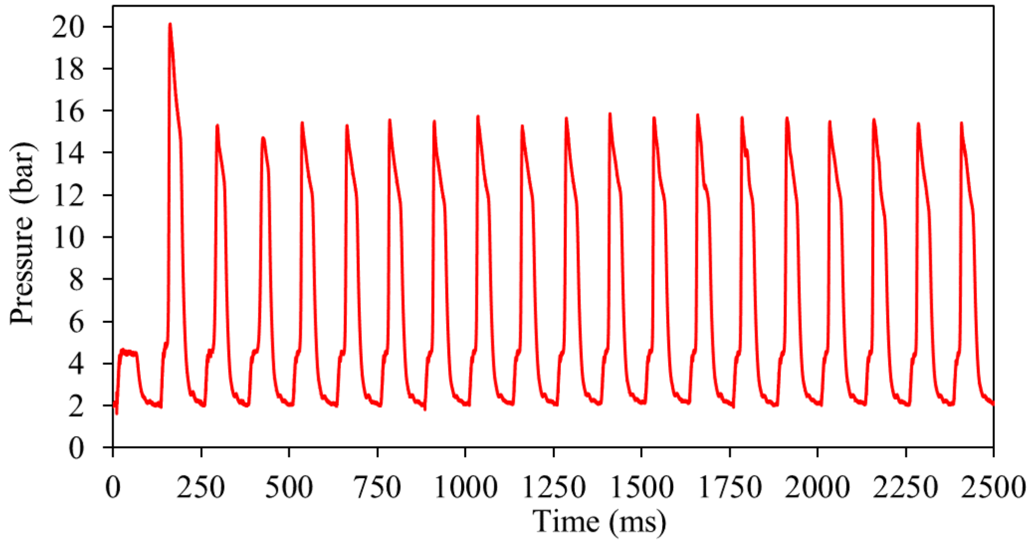

Figure 3-8 Pressure evolution for a sequence of 20 cycles with an initial pressure at 4.5 bar and an exhaust pressure at 2 bar

3.4 Experimental diagnostic

3.4.1 Pressure Analysis for Combustion Characterization

Pressure signals are deemed as a reliable indicator of the flame propagation due to their capacity to capture the dynamics ranging from the early kernel development to the flame-wall interactions at the end of combustion. Therefore, the evolution of the absolute pressure inside the combustion chamber is recorded (see the typical time evolution of the chamber pressure during a spark-ignited cycle in Figure 3-9). This pressure evolution allows us to visually represent the constant volume combustion cycle.

Unlike a piston engine, the piston-less spark-ignited CVC cycle has only three phases: intake, constant volume combustion and cooling and exhaust. These three phases are represented in Figure 3-9. The intake phase (highlighted in blue) where air and fuel are injected into the chamber containing residual burned gas of the previous cycle. The liquid fuel used in this study is n-heptane. The combustion phase in orange, represented by the large pressure increase, is initiated by a spark-plug. Once the flame reaches the chamber wall and combustion ended, a cooling phase can be observed as seen in the purple phase. By optimizing the cycle timing, this cooling phase can be eliminated to shorten the total cycle duration. The green phase represents the exhaust phase. Further explanation of how this pressure data is analyzed is described next.

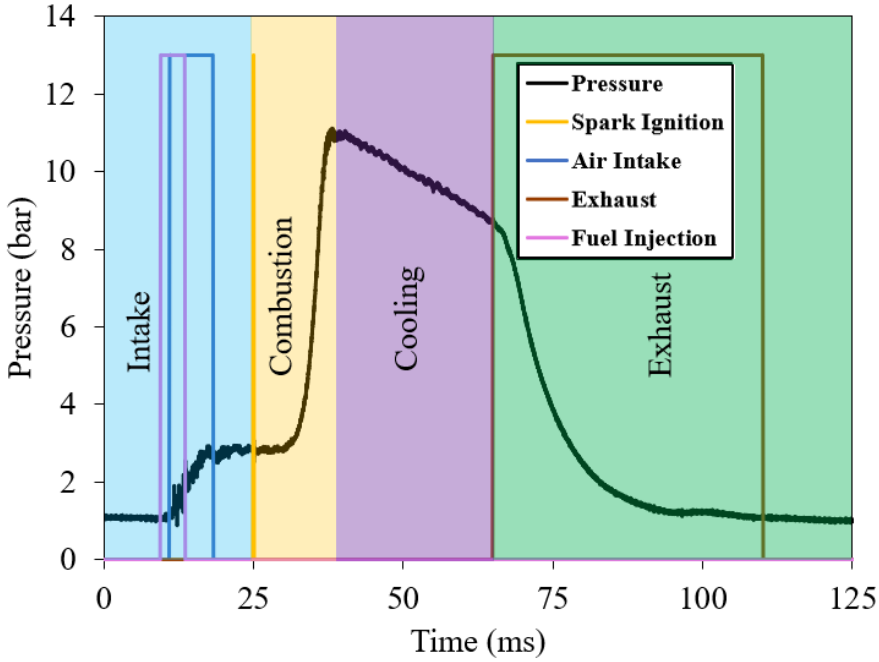

Figure 3-9 Typical pressure evolution in the combustion chamber of one spark-ignition cycle (conditions: Targeted OER = 0.9; initial pressure = 3.5 bar; Pex = 1 bar)

3.4.1.1 Pressure ratio

The initial pressure, $P_{initial}$ and peak pressure, P_{max} identified on Figure 3-10, can be determined from the evolution of pressure signal. This allows the calculation of the pressure ratio as shown below.

$$Pressure\ Ratio = \frac{P_{max}}{P_{initial}} \qquad \text{Equation 3-1}$$

Where, $P_{initial}$ is the pressure at the instant when the spark is ignited for a spark-ignited cycle.

For a self-ignited cycle, it represents the pressure at the instant when air is first injected in the combustion chamber. P_{max} for both type of cycles, is the peak pressure.

3.4.1.2 Combustion duration

To systematically investigate combustion duration, t_{comb}, the pressure signal is evaluated as a key indicator of the combustion heat release. The pressure rise in the combustion process is characterized by assigning an initial combustion heat release of 0% to $P_{initial}$ and a maximum heat release of 100% to the peak pressure, P_{max}.

The combustion process can be divided into several successive stages:

1) Ignition kernel generation:

The ignition kernel is generated by the spark discharge, occurring at nearly constant pressure.

2) Ignition kernel development:

The flame kernel begins to grow and the pressure increases slightly, typically between 5% and 10% [6]of the total pressure rise (P_{max} - $P_{initial}$).

3) Flame propagation phase**:**

The flame propagates through the mixture and the corresponding heat released at constant volume generates the main pressure increase.

4) Wall-flame interaction and end of combustion:

The flame interacts with the chamber walls, marking the end of combustion. During this last stage, the pressure reaches approximately 90–95% [6]of the total pressure rise.

The transition times between stages 2-3 and 3-4 are determined by identifying when the pressure rise reaches 5% or 10% of the total pressure increase (P_{max} - $P_{initial}$) and when it reaches 90% or 95% of the maximum increase. The time interval between these limits provides an estimation of the combustion duration.

In the present study, the 10% and 90% thresholds are selected to characterise the combustion process for a spark-ignition cycle (as seen on Figure 3-10). For the self-ignition cycle, since there is no distinct ignition kernel generation or development phase, the combustion duration is defined between 0% and 100% of the pressure rise (cf. Figure 3-10).

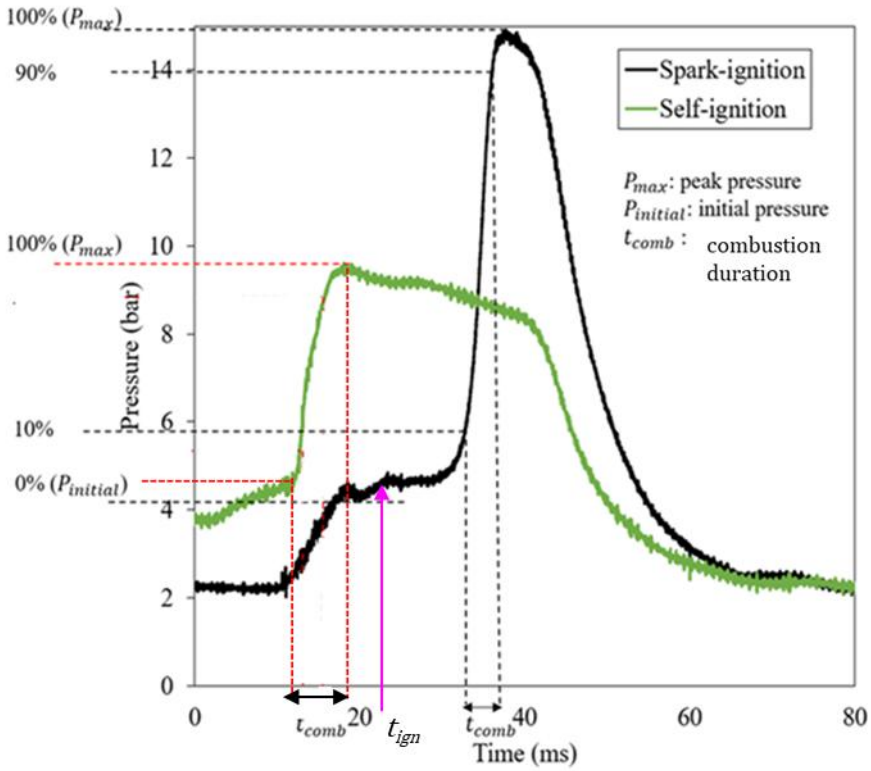

Figure 3-10 Illustration of the pressure signal for a spark-ignited with a spark-ignited timing at 25 ms and a self-ignition cycle

3.4.1.3 Maximum dP/dt

The maximum pressure rise rate $(dP/dt)_{max}$, associated to the so-called "combustion rate", is also evaluated. To ensure reliable estimation and reduce noise sensitivity, the pressure signal is first filtered before differentiation.

For the spark-ignition cycle and self-ignition cycle represented in Figure 3-10, a median filter of width 50, corresponding to 0.5 ms is applied to the pressure signal prior to calculating *dP/dt*. The pressure derivative is then smoothed using a Savitzky–Golay filter with a polynomial order of 3 and a window size of 21 points. The half-window size is therefore equal to 10 points. A target temporal resolution of 0.2 ms is maintained for the determination of the maximum *dP/dt*.

The $(dP/dt)_{max}$ is determined within the 10–90% interval for the spark-ignition cycle and within the 0–100% interval of the total pressure rise for the self-ignition cycle, in order to ensure consistency with the combustion duration. Figure 3-11 shows the pressure-time evolution and the corresponding *dP/dt* temporal evolution during the combustion phase for a typical spark-ignited cycle (Figure 3-11 (i)) and a self-ignited cycle (Figure 3-11 (ii)).

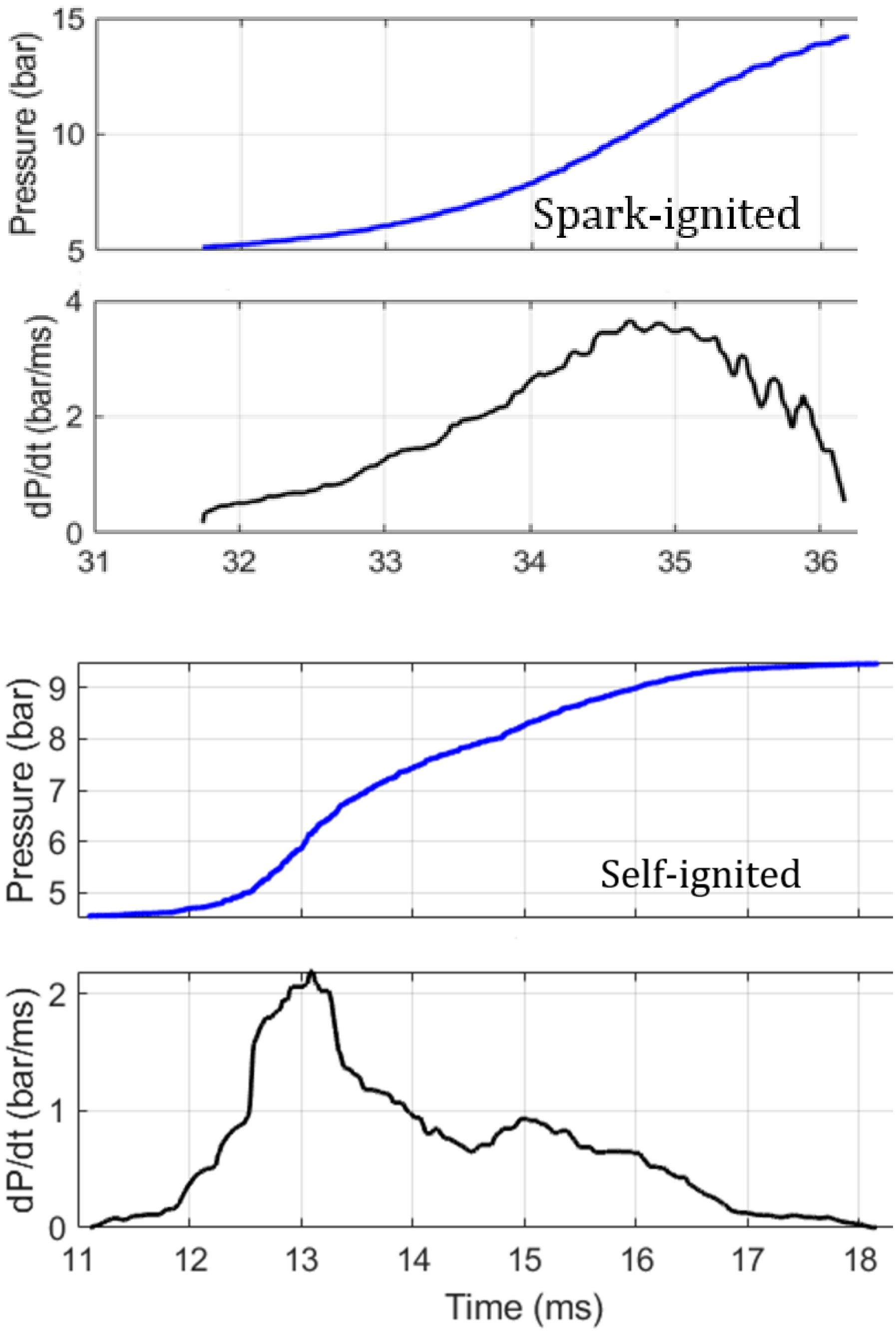

(i)

(ii)

Figure 3-11 Pressure evolution and the corresponding dP/dt temporal evolution during the combustion phase for a spark-ignited cycle (i) and a self-ignited cycle (ii).

3.4.2 Equivalence ratio

Following the comprehensive characterization of the air intake system (APPENDIX A) and fuel injection system (APPENDIX B), accurate prediction of the Equivalence Ratio (ER) becomes feasible, enabling precise control of experimental conditions. To perform a spark-ignition test at a desired ER, since the air intake duration is fixed, hence the corresponding mass of air intake, it is possible to determine the appropriate fuel injection duration and corresponding mass through the following equations:

The molar mass of the alkane (n-heptane) and air under stoichiometric conditions is determined from the balanced reaction equation, given by Equation 3-2:

$$C_nH_{2n+2} + \frac{1}{0.21}\frac{3n+1}{2}(0.21O_2 + 0.79N_2) \rightarrow nCO_2 + (n+1)\mathrm{H_2O} \qquad \text{Equation 3-2}$$

where n is the number of carbon in the alkane.

The stoichiometric dilution, D_{st} is then found:

$$D_{\mathrm{st}} = \frac{m_{\mathrm{air}}}{m_{\mathrm{alkane}}}\bigg|_{st} \qquad \text{Equation 3-3}$$

where m_{air} is the mass of air and m_{alkane} is the mass of alkane respectively.

The dilution D is then found using the following equation:

$$D = \frac{D_{st}}{ER} \qquad \text{Equation 3-4}$$

Where D is the dilution, D_{st} is the stoichiometric dilution and ER is the equivalence ratio.

The mass of alkane injected is found using the equation:

$$m_{alkane} = \frac{m_{air}}{D} \qquad \text{Equation 3-5}$$

where D is the dilution, m_{air} is the mass of air and m_{alcane} is the mass of alkane respectively.

Once the mass of the alkane is found, the corresponding liquid fuel injection time is extrapolated.

3.4.2.1 Overall Equivalence Ratio

Direct measurement of the Overall Equivalence Ratio (OER) within the combustion chamber is difficult. However, the mass of air and fuel can be easily determined. For the liquid fuel, the value is obtained from the mass flow from an *a priori* calibration of the liquid injection system (cf. Appendix C: Characterization of the exhaust system).

For air, the mass is determined by analyzing the pressure drop in the air intake tank following each cycle, as illustrated in cycle Figure 3-12.

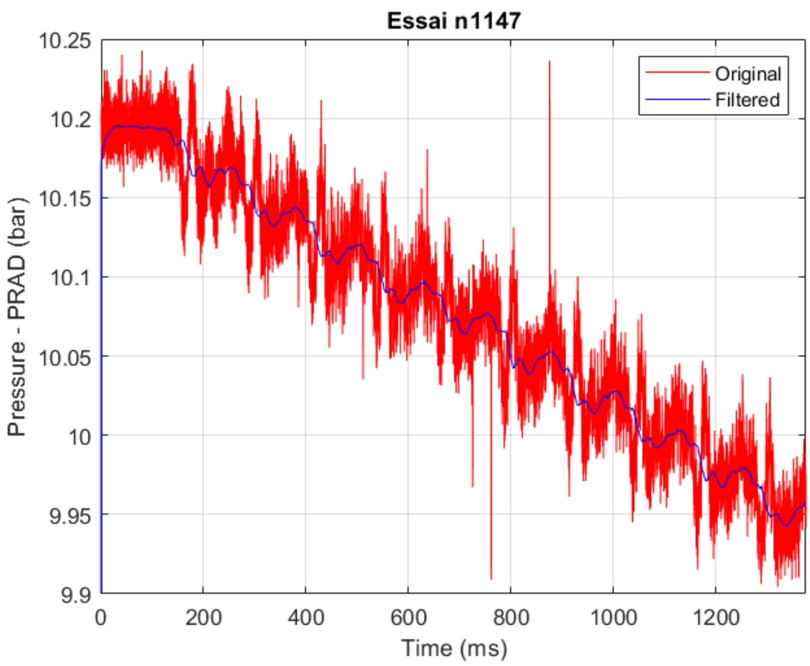

Figure 3-12 Pressure drop in the air intake tank after each cycle

The mass corresponding to this pressure drop is calculated using the following equations. The assumptions considered are that (i) the cycles are isentropic and (ii) the air mixture in the tank behaves as a perfect gas.

$$m = \rho \times V \quad => \Delta m = \Delta(\rho V) \qquad \text{Equation 3-6}$$

Using Laplace Law:

$$PV^{\gamma} = C_1 P\rho^{-\gamma} = C_2 \qquad \text{Equation 3-7}$$

Differentiating gives the isentropic flow equation (for compressible flow):

$$\frac{\Delta P}{P} = \gamma \frac{\Delta \rho}{\rho} \qquad \text{Equation 3-8}$$

With $P = \rho \mathrm{rT}$;

$$\therefore \frac{\Delta P}{\gamma \mathrm{rT}} = \Delta\rho \qquad \text{Equation 3-9}$$

Replacing $\mathrm{r} = \frac{\mathrm{R}}{\mathrm{M}}$ and $\Delta\rho = \frac{\Delta m}{V}$, while taking into consideration that the air injection system operates at constant volume:

$$\Delta m = \frac{1}{\gamma}\frac{M\Delta PV}{RT} \qquad \text{Equation 3-10}$$

Where, Δm is the mass variation of air in kg, γ is the ratio of the heat capacities of the air contained in the tank, M is the molar mass of air in kg/mol, T is the initial pressure at each cycle, V is the volume of the air tanks in m^3, ΔP is the change in pressure between two cycles (in Pa) and R is the molar gas constant.

After finding the corresponding mass loss in the intake tank, OER can be found using Equation 3-3 to Equation 3-5.

3.4.2.2 Equivalence ratio via oxygen sensor measurement

A lambda probe is an electrochemical sensor designed for real-time use in motor vehicles. It measures the oxygen content in exhaust gases, even under harsh conditions (temperatures up to 930°C and pressures up to 2.5 bar). In automotive systems, it plays a key role in managing and adjusting fuel injection based on the exhaust's oxygen concentration. In the latest wideband sensor models, it is possible to obtain precise, quantitative oxygen readings. These measurements rely on regulating the ionic flow of O_2^- through a ceramic membrane. The feedback-controlled current (ip) keeps the oxygen level in the sensor's measurement chamber constant and aligned with stoichiometric conditions. At stoichiometry, this measurement current drops to zero.

Such a probe is mounted just downstream of the exhaust valve. A control unit (SKYNAM LSU 49-5V) manages the sensor and outputs a 0–5 V analog signal, calibrated for atmospheric pressure (1013 mbar) and a fuel mixture modeled as C_nH_{2n} with a stoichiometric air-fuel ratio of 14.7. To enhance the response time, especially by increasing the ceramic's gas diffusivity, the sensor is heated to around 780°C. Its response time typically falls between 50 and 100 ms, fast enough for the timing needs of combustion cycles and sequence-based measurements in the setup.

This probe is mainly used in experiments where fuel injection is pre-calibrated (i.e., injector opening time is mapped to injected fuel mass) prior to combustion measurements. The lambda sensor provides continuous monitoring of the air–fuel ratio during the tests, allowing verification that the mixture remains within the desired operating conditions.

3.4.3 Wall heat flux

A surface-type E thermocouple sensor (Nanmac E12-3) is mounted flush with the chamber wall to locally measure the unsteady wall heat flux. This heat flux sensor is suitable for studying unsteady flame-wall interactions [66]. The chamber wall and the sensor are both made of stainless steel to avoid altering the local thermal properties of the wall. The sensor is an eroding thermocouple, equipped with three layers of very thin (0.0002-inch thickness) electrical insulators and two layers (0.0015/0.002 thickness) of thermocouple alloy ribbon (see Figure 3-13(a)).

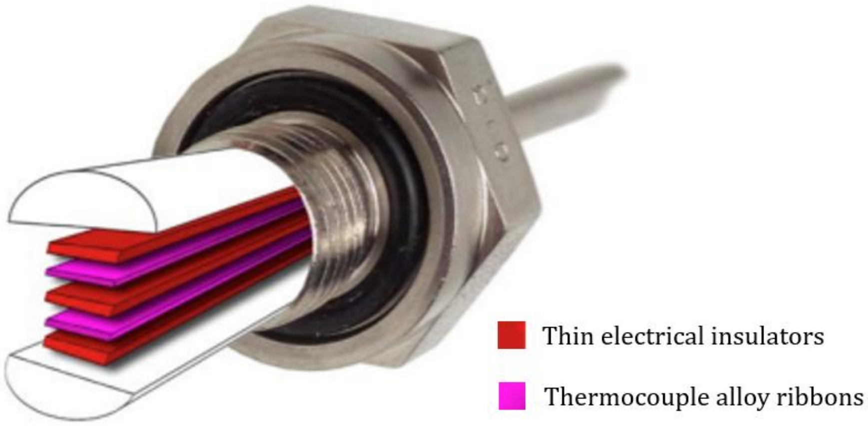

(a) Nanmac “Eroding” Thermocouple

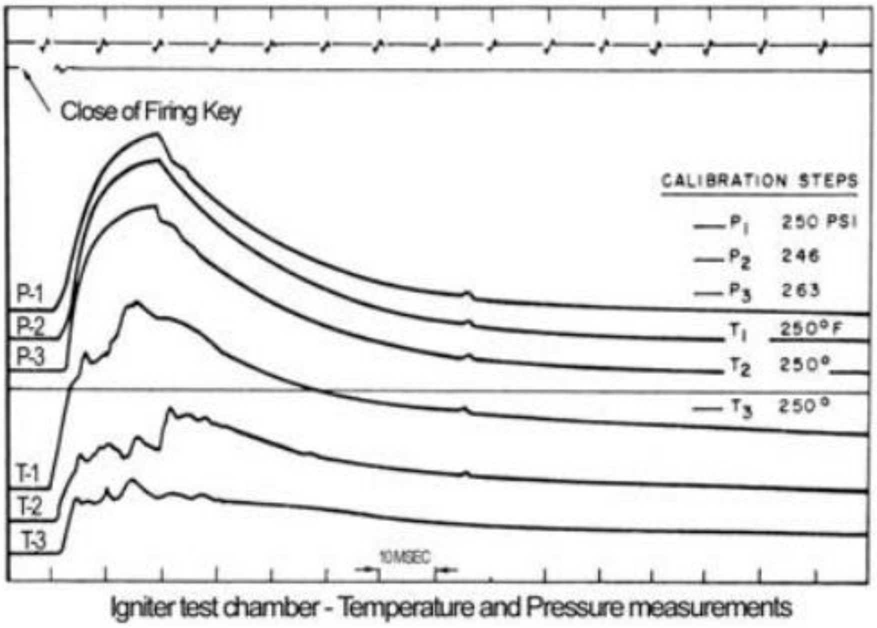

(b) Igniter test chamber: Measured temperature and pressure response

Figure 3-13 Nanmac “Eroding” Thermocouple [67], [68]

This thermocouple responds within microseconds and for extreme operating conditions up of temperatures up to 2300 °C and pressures up to 25,000 psi [67]. The instantaneous temperature recording sharp thermal effects can be demonstrated from a study in Figure 3-13(b)[68].

The wall heat flux density Q is obtained by solving the temperature T using the Duhamel Integral:

$$Q = \sqrt{\frac{k\rho \cdot C_p}{\pi}} \int_{\tau=0}^{t} \frac{\partial T(\tau)}{\partial \tau} \cdot \frac{d\tau}{\sqrt{t-\tau}} \qquad \text{Equation 3-11}$$

Where Q: Wall heat flux (W/m^2), T is the measured wall temperature, t is the current time and τ is the integration variable. The parameter k is the thermal conductivity, ρ is the density and C_p is the specific heat capacity of the thermocouple material.

Figure 3-14 presents the temporal evolution of the wall heat flux for a spark-ignited cycle, calculated from the wall temperature, along with the wall temperature and pressure in the chamber.

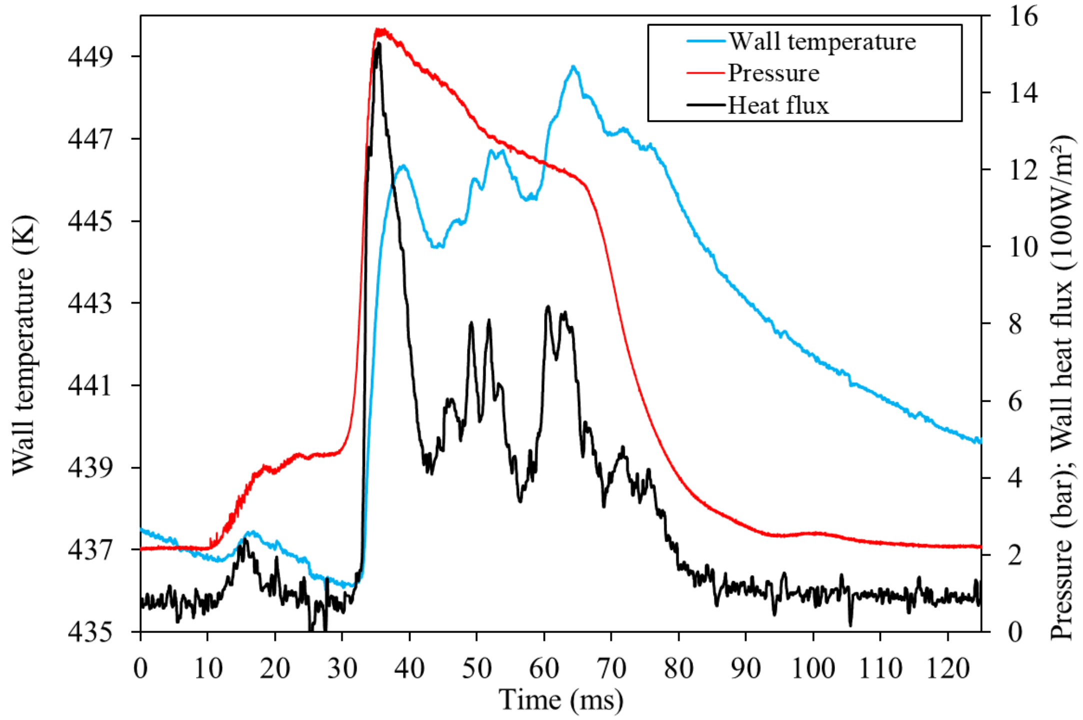

Figure 3-14 Temporal evolution of pressure in the chamber, wall temperature and the derived wall heat flux.

3.4.4 PIV measurements for chamber flow characterization

To gain deeper insight into the rapid combustion phase associated with the two types of cycles, it is essential to understand how internal flow structures influence mixing dynamics, ignition and flame propagation. In this context, PIV provides a powerful, non-intrusive technique to visualize and quantify the flow field. Applying PIV to both spark-ignited and self-ignited cycles enables direct comparison of intake flow behavior and its role in initiating combustion.

3.4.4.1 PIV acquisition

In this technique, tracer particles are introduced into the flow and a dual-cavity laser produces two closely spaced light pulses to illuminate them within a thin planar section of the chamber. A high-resolution camera, placed at right angles to the laser sheet (see Figure 3-15(ii)), records two consecutive images of the illuminated particles.

The delay between the two pulses, *dt* (either 8 µs or 25 µs), is adjusted according to the expected flow velocity so that the particles move about 3–5 pixels between frames. This displacement provides reliable velocity measurements while preserving strong correlations between image pairs. Cross-correlation analysis of the images yields particle displacements, which, combined with *dt* and the optical setup, give instantaneous velocity vectors.

The system uses a MESA PIV laser (532 nm) together with a high-speed Photron SA-Z camera, allowing sampling at up to 20 kHz of velocity fields. In this arrangement, each laser fires at 20 kHz and the camera operates at 40 kHz, enabling double-frame capture for each PIV measurement. Data acquisition and processing are carried out with LaVision software (v10.2.1).

Managed with a La Vision PTU controller, the PIV setup provides the tomographic visualizations of the chamber flow and full-cycle PIV sequences under both inert and reactive operation, with an acquisition frequency of 10 kHz. The camera and lasers are triggered just after the filling phase began, ensuring suitable particle density for measurement under reactive conditions.

The laser sheet thickness, determined with photosensitive paper, is 4–5 mm. This thickness reduces errors from out-of-plane particle motion induced by 3D flow motion. To improve the signal-to-noise ratio, the chamber walls are coated with high-temperature black paint to suppress light reflections. Consistent seeding density is maintained by fully emptying and refilling the air tank after every three measurement runs.

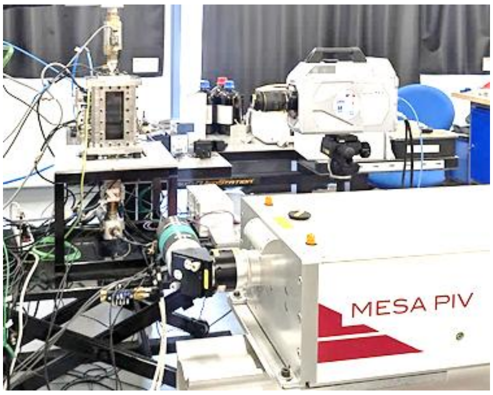

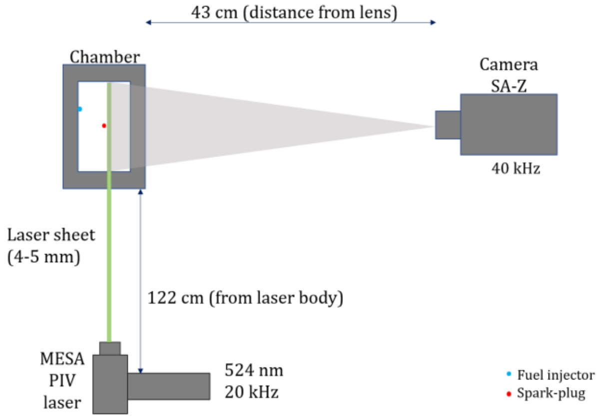

(i) Picture of the PIV assembly (ii) Schematic view of the PIV layout

Figure 3-15 PIV assembly and schematic layout

3.4.4.2 Seeding Particles

A LaVision seeder is used to generate aerosol particles from Shell Ondina 917 oil, which are introduced into the air tank. The droplets have a mean diameter of approximately 200 nm. The response time of the seeding particles, τ_p , defined as the characteristic time needed for a particle to adapt to a sudden change in flow velocity, was calculated using the Stokes model:

$$\tau_p = d_p^2 \frac{\rho_p}{18\mu} \qquad \text{Equation 3-12}$$

Where d_p is the particle diameter, ρ_p the particle density and μ the dynamic viscosity of the air. At 130 °C, with μ=2.27×10−5 Pa·s and ρ_p=854 kg/m^3 for Shell Ondina 917 oil, the chosen particle size provided adequate response (τ_p = 0.084 μs) characteristics for resolving the chamber flow dynamics.

During operation, chamber velocities ranged from 0 to 300 m/s and remained subsonic during the filling phase. The characteristic turbulent structures, estimated from cross-correlation, varied from millimeter-scale eddies during intake down to sub-millimeter scales, below the spatial resolution of the PIV system.

3.4.4.3 Data Processing

Flow tomographic images were analyzed using Davis software (version 10.2.1). The raw images were of sufficient quality to be processed directly without additional filtering. To isolate the flow field and suppress artifacts from boundary reflections, a mask was applied.

Velocity vectors were calculated with a multi-pass cross-correlation approach. The procedure began with a 64 × 64-pixel interrogation window, followed by a 32 × 32-pixel pass and concluded with three passes at 24 × 24 pixels with 50% overlap. This adaptive refinement improved accuracy in strongly directional regions, such as the intake jet and yielded a final spatial resolution of 2.20 mm per vector.

Uncertainty in the PIV measurements, arising from cross-correlation, was estimated at 0.1–0.5 pixels, corresponding to a velocity uncertainty of 0.37–1.83 m/s. The exact value depended on seeding density, correlation quality, inter-pulse timing, signal-to-noise ratio and interrogation window size. Given the large volume of data generated by high-speed PIV, a post-processing tool is developed in MATLAB to automate the analysis.

3.4.4.4 Analysis of mean and turbulent flow fields

In this thesis, the velocity field is analyzed using a cycle-resolved approach followed by an ensemble-averaging approach[69]. The 2D PIV measurements provide instantaneous two-component velocity fields U(x,y,t,c)=(u,v), where t denotes the time within the cycle and c the cycle index.

Following Reynolds decomposition, the instantaneous velocity field U is separated into a mean component, U_{mean_t} and a fluctuating component, $\mathrm{U}_{\mathrm{fluc}}$.

$$\mathrm{U}(x,y,t,c) = \mathrm{U}_{mean\_t}(x,y,t,c) + \mathrm{U}_{fluc}(x,y,t,c) \qquad \text{Equation 3-13}$$

A mean sliding velocity, U_{mean_t}, is calculated for each cycle and for each time t using the cycle-resolved computation method. The time window size, N_t, is chosen so that the typical time scale separating the mean and fluctuating flow fields is 1 ms (cut-off frequency = 1 kHz).

$$\mathrm{U}_{mean_t}(x,y,t,c) = \frac{1}{N_t}\sum_{\tau=1}^{N_t} \mathrm{U}(x,y,t+\tau,c) \qquad \text{Equation 3-14}$$

The cycle-resolved fluctuating velocity field is then obtained by subtracting the mean velocity field:

$$\mathrm{U}_{\mathrm{fluc}}(x,y,t,c) = \mathrm{U}(x,y,t,c) - \mathrm{U}_{mean\_t}(x,y,t,c) \qquad \text{Equation 3-15}$$

To separate large-scale coherent motion from small-scale turbulence, the fluctuating field is decomposed into two contributions. A bulk-flow component, denoted U_{BF}, is obtained by applying a local spatial moving average to the fluctuating velocity field. This operation extracts slowly varying, large-scale flow structures.

The spatial window size, $N_{x=} N_y$, is chosen so that the typical spatial scale separating the low and high frequency flow fields is 7 mm. This value is smaller than, but of the same order as, the inlet valve diameter (12 mm), which sets the characteristic size of the largest flow structures during intake. The selected cutoff scale therefore removes the large-scale motion while retaining the smaller-scale turbulent fluctuations.

The high-frequency component, denoted U_{HF} , is defined as:

$$U_{HF}(x,y,t,c) = U_{fluc}(x,y,t,c) - U_{BF}(x,y,t,c) \qquad \text{Equation 3-16}$$

and is identified with the turbulent velocity fluctuations while the low frequency component, U_{BF} , is associated to cycle-to-cycle variations and large flow structures.

The instantaneous velocity field can therefore be written as:

$$U(x,y,t,c) = U_{mean\_t}(x,y,t,c) + U_{BF}(x,y,t,c) + U_{HF}(x,y,t,c) \qquad \text{Equation 3-17}$$

In this formulation, U_{mean_t} describes the mean velocity, U_{BF} represents large-scale coherent fluctuations and U_{HF} corresponds to turbulence. This decomposition forms the basis for the subsequent analysis of turbulence intensity, turbulent kinetic energy and the interaction between aerodynamics and combustion. Figure 3-16 shows the velocity fields U, U_{mean_t}, U_{BF} and U_{HF} at 25.3 ms for a spark-ignited cycle corresponding to the spark timing.

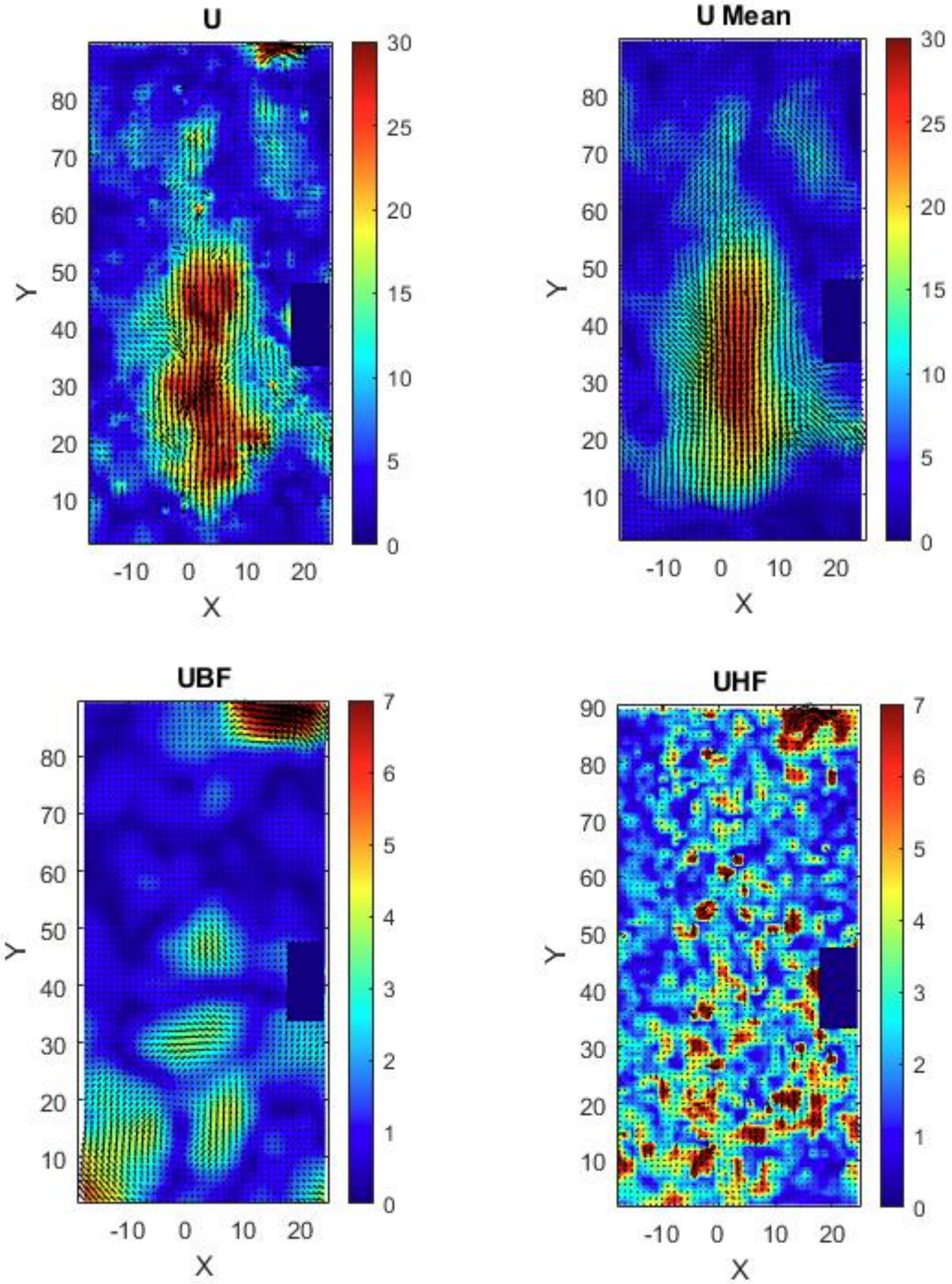

Figure 3-16 Velocity field of the U, Umean_t, UBF and UHF for a spark-ignited cycle (Test 1607 - cycle 6) at 25.3 ms

The equations and method described above (Equation 3-13-Equation 3-17) used to resolve the velocity field applied to one cycle are replicated for each secondary cycle of the sequence. An ensemble-average method is applied to compute U_{mean_t} and U_{HF}, namely the mean velocity and the turbulent fluctuation.

3.4.5 Chemiluminescence Analysis

Chemiluminescence imaging is used in this thesis as a diagnostic to characterize combustion. A high-speed color camera (Phantom V310) first records broadband emission from the whole visible spectrum. This view gives general information on the flame behavior and helps distinguish rich and lean cycles by highlighting soot radiation, visible in yellow (cf Figure 3-17).

To obtain species-specific information, a second high-speed camera (Photron SA5) captures filtered chemiluminescence from two radicals: OH* at 306 nm and CH* at 430 nm. These radicals were chosen because they trace different flame regions. CH* emission marks the reaction front and thus shows the flame kernel development, while OH* appears in high-temperature zones and in hot burnt gases that still contain this radical. Together, they provide complementary information on flame propagation and post-flame regions.

Both filtered recordings are made at 1000 frames per second with a resolution of 640 × 1024 pixels. This frame rate represents a compromise between temporal resolution and light sensitivity. At higher frame rates, the shorter exposure time per frame significantly weakens the chemiluminescence signal. To maintain adequate brightness under these conditions, a high-speed gated image intensifier (Hamamatsu C10880 series) is mounted in front of the Photron camera. The intensifier operates synchronously with the camera to amplify the weak optical emission of combustion radicals.

The methodology used to analyze the chemiluminescence data is based on frame-by-frame intensity integration. For each recorded image, all pixel values are summed to obtain a single representative intensity for that frame. The temporal evolution of this global signal provides an indication of the combustion process over time. In the case of OH*, this evolution is used to determine the onset and progression of combustion, consistently with previous findings[70] showing that OH* emission correlates with the heat release rate. The same analysis is performed for CH* images under identical conditions. The exposure time is adjusted to capture the weak emission during spark-ignited cycles, though this can occasionally lead to partial saturation in the following self-ignition cycles. Figure 3-17 shows chemiluminescence from a preparatory spark-ignited cycle (left) and self-ignited cycle (right) at maximum pressure. The filtered OH* emissions from the Photron camera (grayscale) are compared with broadband emission from the Phantom color camera.

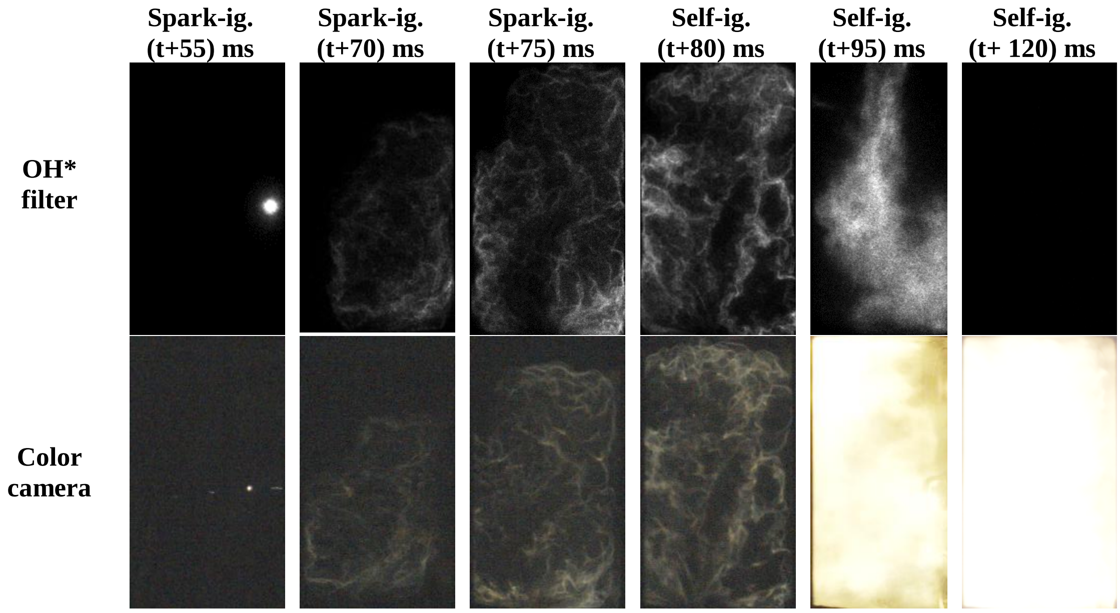

Figure 3-17 Comparison of radical emission at maximum pressure of a preparatory spark-ignited (from t+55 ms to t+75 ms) and self-ignited cycle (from t+80 ms to t+120 ms) obtained from the OH*-filtered and broadband imaging

3.5 1-D model for cycle analysis

To complement the experimental work, a 1-D model of the CV2 setup, originally developed by Q. Michalski for gaseous spark-ignition cycles [6]is modified and is used to simulate physical phenomena involved and to estimate parameters that cannot be measured experimentally. The model has been refined in this study to simulate both liquid spark-ignition and liquid self-ignition, thereby broadening its applicability across various combustion regimes.

3.5.1 Description and purpose of the OD/1-D analysis model

The 0D/1-D model provides a simplified yet physically representative model of a constant-volume combustion chamber, capturing the key thermodynamic processes that govern its operation. In such systems, the primary extensive variables defining the internal state are the mass of the working fluid and its internal energy. Establishing well-defined boundary conditions (detailed in section 3.5.3) enables the determination of the flow rates entering and leaving the chamber. When the composition of the working fluid remains unchanged during transfer phases, the thermodynamic state can be fully described using only two variables. In this framework, the "1-D" formulation does not refer to a spatial dimension, but rather to a reduced-order description of combustion evolution in time. It can be seen as a one-dimensional representation in time of the combustion propagation. The approach is based on a combustion progress variable, with the flame surface area assumed approximately constant.

Experimentally, the most accessible parameters are the injected mass (estimated from pressure variations in the supply reservoir and calibration of the fuel injector) and the transient pressure inside the chamber. Heat transfer plays a critical role throughout the operating cycle, affecting the fluid temperature and, in turn, the pressure level. In practice, filling is neither perfectly adiabatic nor perfectly isothermal, as a portion of the input energy is invariably lost through heat exchange with the chamber walls.

Direct measurement of transient temperature under such conditions presents significant challenges and is typically limited to local measurements. The flow's high kinetic energy and short timescales render conventional thermocouples ineffective. Optical diagnostic methods such as PLIF [71], CARS or LITGS, though capable of providing the required data, are difficult to implement at this stage due to their complexity and resource demands.

The governing equations ensure mass and energy conservation in each control volume, thereby conserving the total mass within each subsystem. Inter-enclosure flows are controlled by time-dependent actuator laws, which dictate the exchange dynamics between connected volumes as seen in Figure 3-18. Some model parameters are adjusted to achieve agreement with the measured pressure traces, providing a consistent framework for validating the underlying physical hypotheses and assessing the accuracy of the governing assumptions.

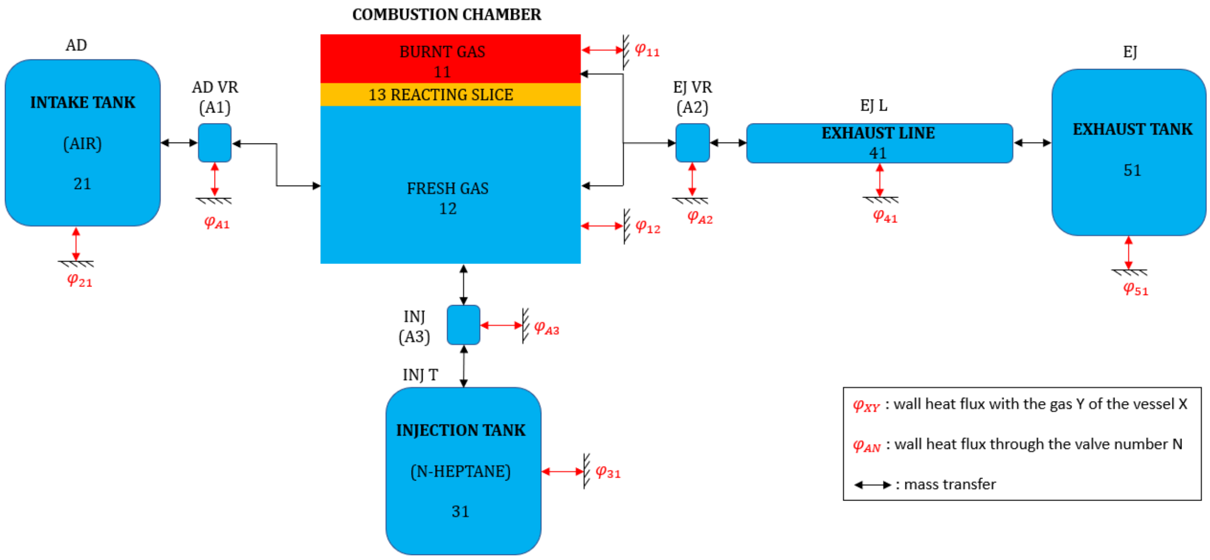

Figure 3-18 Flowchart of the systems and subsystems of the developed 1-D model adapted from [6]

Building on this modeling framework, the next sections describe the main physical processes governing the chamber's thermodynamic behavior. These include the heat and mass exchanges with the surroundings, heat transfer modeling and combustion modeling to represent the energy release within the chamber. Together, these elements form the foundation for accurately reproducing the mass and energy evolution throughout the different phases.

3.5.1.1 Heat and mass exchanges

The 0D/1D analysis applies the conservation equations for mass and energy. When reactions are excluded, for instance, in the tanks or during transfer phases into the chamber, these equations reduce to form Equation 3-18 and Equation 3-19. Integration is performed across all enclosures of CV2, ensuring conservation of the total mass. The reservoir volumes correspond to the experimental measurements reported in Section C. Each enclosure X is connected to one or more enclosures Y_N through actuators, whose opening laws are prescribed.

$$\frac{dm_X}{dt} = \dot{m}_{\text{in}} - \dot{m}_{\text{out}} \qquad \text{Equation 3-18}$$

$$\frac{dE_X}{dt} = h_{\text{in}}\,\dot{m}_{\text{in}} - h_X \dot{m}_{\text{out}} + \varphi_X \qquad \text{Equation 3-19}$$

Here, $\dot{m}_{\text{in}}$ and $\dot{m}_{\text{out}}$ denote the instantaneous mass flows entering and leaving volume X, h is the specific enthalpy of the exchanged flows and φ_X represents the integral of the heat flux transferred to the walls of volume X. The exhaust line is modelled as a fixed volume of 50 cm^3, estimated from the hose and connection volumes and is assumed to remain permanently open to the exhaust. The exchanged mass flows, $\dot{m}_{\text{in}}$ and $\dot{m}_{\text{out}}$, are determined from the pressure ratio between the connected gas volumes.

$$\frac{p_2}{p_1} \geq \left(\frac{2}{\gamma_1+1}\right)^{\frac{\gamma_1}{\gamma_1-1}} \qquad \dot{m}_{1\to 2} = c_d \frac{p_1 S}{\sqrt{T_1 R/M_1}} \left(\frac{p_2}{p_1}\right)^{1/\gamma_1} \sqrt{\frac{2\gamma_1}{\gamma_1-1}\left(1-\left(\frac{p_2}{p_1}\right)^{\frac{\gamma_1-1}{\gamma_1}}\right)}$$

$$\frac{p_2}{p_1} \leq \left(\frac{2}{\gamma_1+1}\right)^{\frac{\gamma_1}{\gamma_1-1}} \leq 1 \qquad \dot{m}_{1\to 2} = c_d \frac{p_1 S}{\sqrt{T_1 R/M_1}} \sqrt{\gamma_1} \left(\frac{2}{\gamma_1+1}\right)^{\frac{\gamma_1+1}{2(\gamma_1-1)}}$$

Equation 3-20

For an exchange between a volume X and a volume Y, the index “1” refers to the volume at the higher pressure, in which case $\dot{m}_{1\to 2} \geq 0$. *S(t)* denotes the actuator opening section law (valves or injectors) governing the exchange. The discharge coefficient c_d is assumed constant and is calibrated a single time so that the simulated reservoir pressure signals match the experimental measurements. This calibrated value remains unchanged from cycle to cycle.

3.5.1.2 Heat transfer modelling

Heat transfer through the walls of the tanks and chamber is represented by the corresponding heat fluxes and is described by an overall convection model applied to each volume:

$$\varphi_W = h \cdot S \cdot (T_w - T) \qquad \text{Equation 3-21}$$

where φ_W is the instantaneous heat flux (W), T is the temperature of the gas (K) and T_w is the wall temperature (K), assumed constant in both tanks and the chamber during a test.

The forced convection coefficient at the chamber walls, h, is evaluated using the empirical correlation proposed by Hohenberg (1980)[72], which is widely applied in internal combustion engine studies and is expressed as follows:

$$h_{eff} = \alpha \cdot h = \alpha \cdot 130 \cdot V_{cc}^{-0.06} \cdot p^{0.8} \cdot T^{-0.4} \cdot (v + 1.4)^{0.8} \qquad \text{Equation 3-22}$$

Here, V is the chamber volume (m^3), T the gas temperature (K), p the pressure (MPa) and v the gas velocity (m/s) and h is homogeneous to $W/m^2/K$. While piston speed is often used as the velocity term in such correlations, in this work, v is computed as the average velocity derived from the instantaneous mass flow rate, gas density and the cross-sectional area of the considered volume. This formulation allows heat transfer to be directly linked to the thermodynamic state of the gas. The coefficient α, which varies over different phases of the cycle, is introduced to fine-tune the heat exchange behavior in accordance with the specifics of the setup.

During injection, the temperature drop in the tanks is limited, on the order of a few degrees, so the assumption of isothermal walls is valid for the reservoirs. In the chamber, the cumulative temperature rise is less than 20 K (≈5%) for an initially hot state (130 °C). Compared with the burnt gas temperatures (above 1500 K), where most of the exchanges occur, the relative difference is negligible (< 3%) for these hot flows. Therefore, the assumption of isothermal walls for the chamber is also justified.

Heat exchanges are also considered at the actuators (valves or injectors). The flow accelerates significantly through the reduced passage sections, which can lead to notable heat transfer. These heat exchanges, φ_S, are modeled using a coefficient α (ranging from 0 to 1) as follows:

$$\varphi_S = \alpha\left(\hat{h}(T_S) - \hat{h}(T)\right) \qquad \text{Equation 3-23}$$

Here, $\hat{h}(T_S)$ is the sensible enthalpy of the gas at the actuator reference temperature T_S and $\hat{h}(T)$ is the sensible enthalpy of the gas at the stagnation temperature (T). A value of (α = 0) corresponds to an adiabatic transfer, while (α = 1) implies that the fluid leaves the actuator at the actuator temperature.

The heat exchanges, representing a loss of internal energy, are computed simultaneously with the internal energy variations associated with mass transfers. The chamber is divided into several distinct gas volumes, reflecting the structure of the chosen combustion model. The procedure for calculating mass exchanges within the chamber is described in the following section.

3.5.1.3 Combustion modelling

The constant-volume combustion process is described using the sliced-combustion method ([54]). This method is particularly suitable for chambers where acoustic effects are negligible. The constant-volume chamber (V) is divided into three distinct zones: a fresh-gas volume (V_f), which consists of residual burned gas of the previous cycle mixed with the fresh air and fuel; a burning slice (V_r) and a burnt-gas volume (V_b) (see combustion chamber section of Figure 3-18). Because the flame propagates at largely subsonic speeds and pressure equilibrates quickly, the pressure is uniform throughout the chamber at any instant:

$$V = V_f + V_b + V_r \qquad \text{Equation 3-24}$$

Before the reaction begins, the entire chamber is filled with fresh gas, consisting of residual burned gas of the previous cycle mixed with fresh air and fuel, ($V_f = V;\ V_b = V_r = 0$) (case (i) in Figure 3-19). The apparent flame propagation speed v_F is updated each time step so that the modeled combustion duration matches the cycle measurement. The propagation distance is constrained between 0 and $(V - V_u)/S$, where S is the chamber cross-section (50 mm × 50 mm) and V_u is a quenching volume representing permanently unburnt gas. The instantaneous flame propagation speed is given by:

$$\mathrm{v_F(t)} = \frac{1}{\mathrm{S}}\frac{\mathrm{V_f(t) - V_u}}{\mathrm{t_f - t}} \qquad \text{Equation 3-25}$$

where t_f is the measured combustion end time. This 1D calculation can be extended to different cycle conditions. For this, the flame speed v_F can be replaced by a model that includes the laminar flame speed and corrections for turbulence and gas expansion; these corrections can be estimated beforehand using tools such as Cantera.

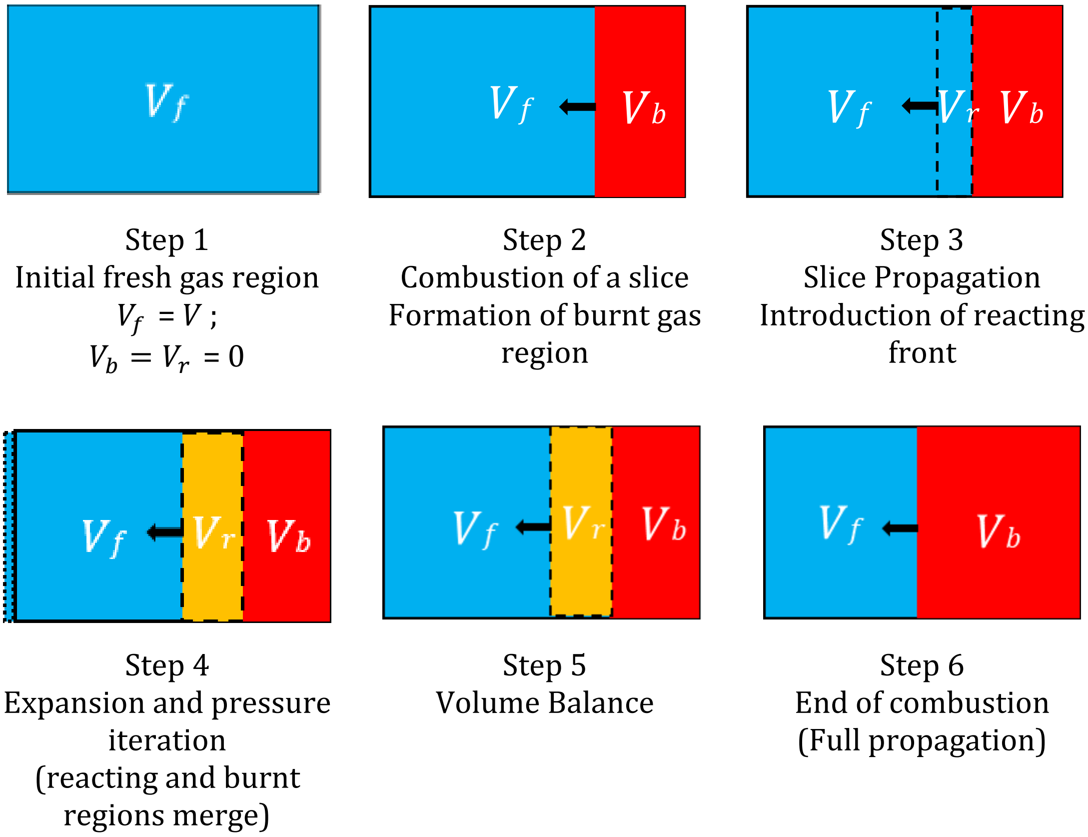

Figure 3-19 Stages of the sliced-combustion model

The steps of the sliced-combustion model can therefore be described as (see Figure 3-19):

Step 1: Fresh gas region

The sliced-combustion process begins with the chamber entirely filled with fresh, unburned mixture. A thin gas layer adjacent to the ignition side is selected as the first slice to undergo combustion. At this stage no combustion has yet occurred, no reaction products exist and no equilibrium assumption is applied, the chamber contains only the fresh-gas sub-volume and no pressure or volume redistribution is required.

Step 2: Combustion of a fresh slice and formation of a burnt slice

Once the flame is initiated, the first thin slice of fresh mixture undergoes chemical conversion. The reaction products are assumed to reach isobaric, isenthalpic thermochemical equilibrium. The same assumption is used to compute adiabatic (isenthalpic) flame temperatures. This provides a consistent thermodynamic basis for computing the state of the burnt gas. Because this equilibrium treatment neglects finite-rate chemical kinetics, the model cannot capture kinetically controlled species such as NO_x, which form over much shorter timescales than those represented by equilibrium thermochemistry.

Step 3: Flame front propagation and appearance of the reacting flame front

As the flame propagates into the fresh mixture, a reacting zone forms between the unburned and fully burned regions, resulting in three sub-volumes: fresh gas, reacting front and burnt gas.

Step 4: Density drop, thermal expansion and pressure iteration

When the flame front passes through a slice, the local gas density drops sharply due to temperature rise, causing an immediate volume expansion of that slice. This rapid expansion makes the total computed volume (as in Equation 3-24) temporarily exceed the actual chamber volume. The pressure rise then follows from heat release and confinement within the fixed chamber geometry.

Step 5: Volume balance

An iterative isentropic compression is therefore applied across all non-empty sub-volumes until the total volume satisfies the chamber-volume constraint within a strict tolerance ($\varepsilon < 10^{-16}$). This step captures the coupling between heat release, thermal expansion and pressure rise. A root-finding algorithm is used to enforce this adiabatic recompression.

Step 6: Merging of burnt gases and combustion end

The newly burnt slice is then merged with all the burnt gases. At combustion end:

$$\begin{aligned} t &= t_f \\ V_f &= V_u \end{aligned} \qquad \text{Equation 3-26}$$

The remaining fresh gas is treated as unburnt, mainly due to quenching at walls. In premixed or partially premixed conditions, the mixture may reach the walls and the flame can propagate there; however, flame-wall interaction strongly modifies thermal diffusion and leads to quenching. Quenching distances depend on geometry (frontal, lateral, cavity) and mixture conditions. For high-pressure hydrocarbon-air mixtures, they are typically on the order of 100 μm[73]. The quenching volume is estimated as this distance multiplied by the chamber wall area. In the present apparatus, the parietal quenching volume is about 1% of the chamber volume (≈3.2 cm^3), of which ≈0.8% (≈2.5 cm^3) lies inside the chamber and the remainder in the tubing. After combustion finishes, gases are compressed and expelled through the assembly (≈2% of the total volume). Clearances are small enough to prevent flame propagation through them (which would otherwise quench and burn the confined mixture); that trapped mixture is therefore considered unburnt. Before the exhaust and the next intake, the fresh and burnt gases are mixed and the chamber is treated as filled with fresh gas again:

$$V_b = V_r = 0 \qquad \text{Equation 3-27}$$

Heat and mass exchanges between gas sub-volumes are handled in the same framework as combustion. Mass and heat transfers are treated as enthalpy exchanges: changes in composition and internal energy alter the subsystem temperatures and volumes. Similar to the reactive slice expanding during flame passage, any sub-volume expands or contracts depending on the net exchange. After each exchange step, the pressure change is computed by iterating an isentropic compression across the sub-volumes until the chamber volume constraint is satisfied.

Combustion is handled with logic steps; the combustion ends when the fresh gas volume is equal to the specified quenching volume. Self-ignition cycles are thus cycles for which the combustion persists across cycles and during which fresh gases are injected and their mass and volume in the chamber increases meanwhile the combustion process from the previous cycle is on-going.

Because each actuator (valve, injector, etc.) is connected to a single non-empty sub-volume, the gaseous subset concept limits mass exchange pathways: an actuator can only draw from the sub-volume to which it is coupled. For example, the intake valve is coupled to the fresh-gas sub-volume and the exhaust valve to the burnt-gas sub-volume.

3.5.2 Model assumptions

For ease of reference, the main hypotheses governing the 0D/1D model, fully described in Section 3.5.1, are summarized below in Table 3-6.

Table 3-6 Main hypotheses adopted in the 0D/1D code

Hypothesis	Physical mechanism	Affected equations
Ideal gas behavior	Equation of state: relates p, ρ, T, R and V	Equation 3-9
Mass and energy conservation	Isochoric process: conservation of total mass and energy within controlled volume	Equation 3-18 - Equation 3-19
Wall heat transfer	Forced convection: using the Hohenberg [72] correlation	Equation 3-22

3.5.3 Description of the boundary conditions

Boundary conditions are derived directly from experimental measurements to refine model parameters and ensure consistency with observed pressure trends. The Cantera library is employed for fluid modeling and for computing thermodynamic and transport properties while MATLAB is used for post-processing experimental data and for integrating the 1-D model. The Cantera library also enables the direct use of calculated compositions in routines for determining key reactive properties of the mixture, such as fundamental flame speed and auto-ignition delay. To ensure computational efficiency without compromising the accuracy of pressure and temperature predictions, the simulations are based on a reduced set of chemical species. In addition to the primary fuel (n-C_7H_{16}) and oxidizer mixture (O_2/N_2), the following species are included: H_2, H, O, OH, H_2O, HO_2, H_2O_2, C, CH, CH_2, $CH_2(S)$, CH_3, CH_4, CO, CO_2, HCO, CH_2O, CH_2OH, CH_3O, CH_3OH, C_2H, C_2H_2, C_2H_3, C_2H_4, C_2H_5, C_2H_6, HCCO, CH_2CO, HCCOH, N, NH, NH_2, NH_3, NNH, NO, NO_2, N_2O, HNO, CN, HCN, H_2CN, HCNN, HCNO, HOCN, HNCO, NCO, Ar, C_3H_7, C_3H_8, CH_2CHO and CH_3CHO. Including all species from the GRI3.0 mechanism (53 species) would substantially increase simulation times, often to tens of minutes, while providing only negligible improvements in the predicted pressure and temperature.

To accurately capture the dynamics of the constant-volume combustion chamber, boundary conditions are defined through the operation of the rapid valves (A1, A2, A3 shown in Figure 3-18), which constitute the main control elements of the experimental setup. These valves regulate the timing and magnitude of the mass flows entering and leaving the chamber. Based on transient experimental measurements, such as pressure variations in the supply reservoir and combustion chamber pressure, the mass flow rates are imposed as dynamic boundary constraints within the model. It is assumed that the working fluid composition remains unchanged during transfer phases, allowing the thermodynamic state at the boundaries to be fully described by two variables, typically pressure and temperature or internal energy. Heat transfer at the boundaries, particularly during filling and emptying phases, is considered to account for energy exchange with the walls of fluid actuators (valves, injector), reflecting more realistic system behavior. These carefully defined boundary conditions ensure that the 0D/1D model represents the experimental system's physical interactions effectively, providing a solid basis for simulating mass and energy balances and validating against observed pressure signals.

Table 3-7. List of coefficients used for the boundary conditions

Coefficient	Description
C_{dA1}	Discharge coefficient of the inlet valve (air)
C_{dA2}	Discharge coefficient of exhaust valve
C_{dA3}	Discharge coefficient of fuel injector
C_{dA4}	Discharge coefficient of the exhaust line
α_{A1}	Heat transfer coefficient governing rate of enthalpy exchange through inlet valve
α_{A2}	Heat transfer coefficient governing rate of enthalpy exchange through exhaust valve
α_{A3}	Heat transfer coefficient governing rate of enthalpy exchange through the fuel injector
α_{A4}	Heat transfer coefficient governing rate of enthalpy exchange through the exhaust line
k	Wall heat transfer coefficient in the different phases

The boundary conditions coefficients are briefly stated in Table 3-7, together with the phases in which they are applied. They are adjusted during the validation process. However, once defined, each value is kept constant throughout all cycles for both spark-ignition and self-ignition cases to ensure consistency in the simulation.

3.5.4 Model validation

As stated in section 3.5.1, the purpose of the 0D/1D model is to enable a physical interpretation of the experimental data by reproducing the pressure signals recorded in the reservoirs and the combustion chamber. This process facilitates the estimation of unmeasured properties such as burned gas temperature and dilution by residual burnt gas of the previous cycle. To accomplish this, the mass exchange parameters (flow coefficient C_d) and thermal exchange parameters (wall heat transfer coefficient k and actuator heat transfer coefficient α) in the three different phases are iteratively adjusted following the procedure outlined in Figure 3-20. The validations of the parameters of these three phases are described in the succeeding sub-sections (3.5.4.1-3.5.4.3).

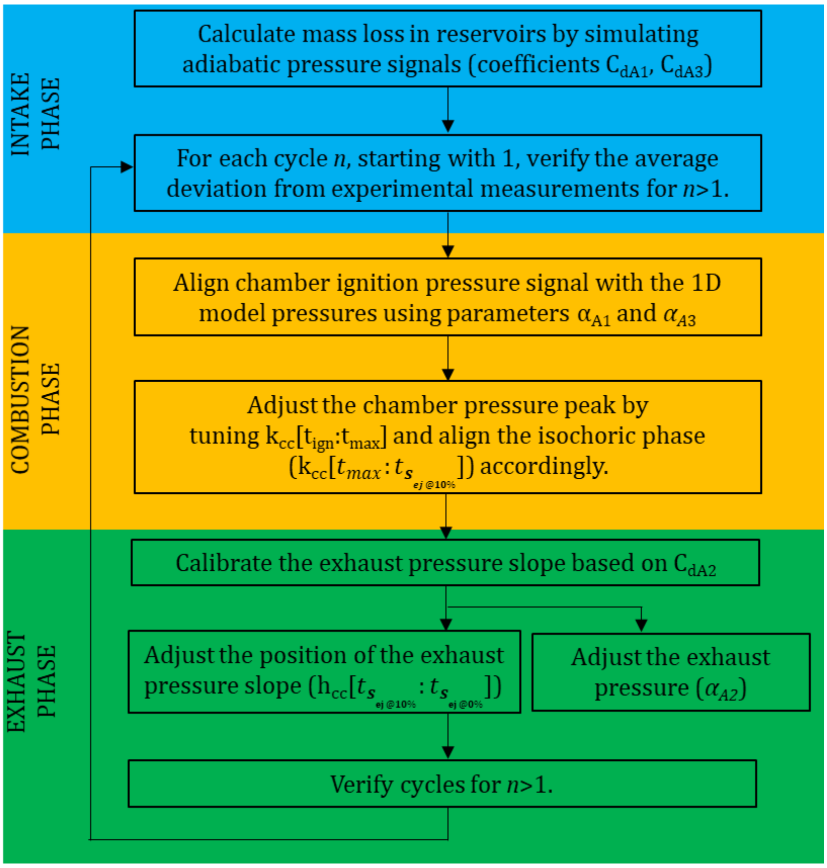

Figure 3-20 Flowchart illustrating the adjustment of model variables to achieve agreement between 0D/1D pressure signals and experimental pressure measurements. The index CC denotes the combustion chamber and A(N) refers to the three actuators shown in Figure 3-18.

3.5.4.1 Intake phase

The validation of the air intake phase is done through mass transfer analysis from the air tank reservoir by comparing the simulated value and the experimental values. The simulated value is fitted using the flow coefficient C_{dA1} for air and C_{dA3} for fuel. These values are assumed constant during the intake phase. However, this assumption is questionable during air valve opening and closure transients due to dynamic flow effects.

To ensure that the mass and energy balances are accurate, it is essential that the intake system is correctly replicated and validated. To verify that mass and energy are conserved by the numerical integration, heat exchange coefficients (k and α) are set to zero. With this configuration, the entire system (comprising the reservoirs and the chamber) is sealed, ensuring that total internal energy and total mass remain constant throughout integration, regardless of time step or algorithm. The results confirm that mass is indeed conserved, with discrepancies due to small numerical errors, with relative variation on the order of 10^{-16}. For very small-time steps, the code's conservation of energy is confirmed, with internal energy differences similarly reduced to numerical noise. To balance computational efficiency and accuracy, a time step of 100 microseconds is chosen, which keeps the total simulation time below five minutes for a full sequence (at 8 Hz) and ensures that energy errors remain negligible over 20 cycles.

The air flow coefficients, representing the valves and injectors, are calibrated so that the simulated pressure profiles (in red) align closely with experimental measurements (in blue) as seen in Figure 3-21. Because the pressure ratios during intake produce choked flow, those flow coefficients are kept constant. For each cycle, the theoretical mass injected is computed using sonic flow conditions as the reference. The actual flow coefficient is derived as the ratio of mass measured from experimental pressure signals to the ideal sonic mass calculated for that cycle.

Slight pressure changes during injection (acoustic effects from transients) cause a small average error between calculated and experimental masses (calculated using Equation 3-10), as shown in Table 3-8. Since the first cycle likely fails to open properly due to rapid valve limits, it is excluded from the results. Table 3-8 therefore lists the mean and standard deviation from cycles 2 to 20. The air intake model agreed closely with the experimental data, with deviations of less than 1%.

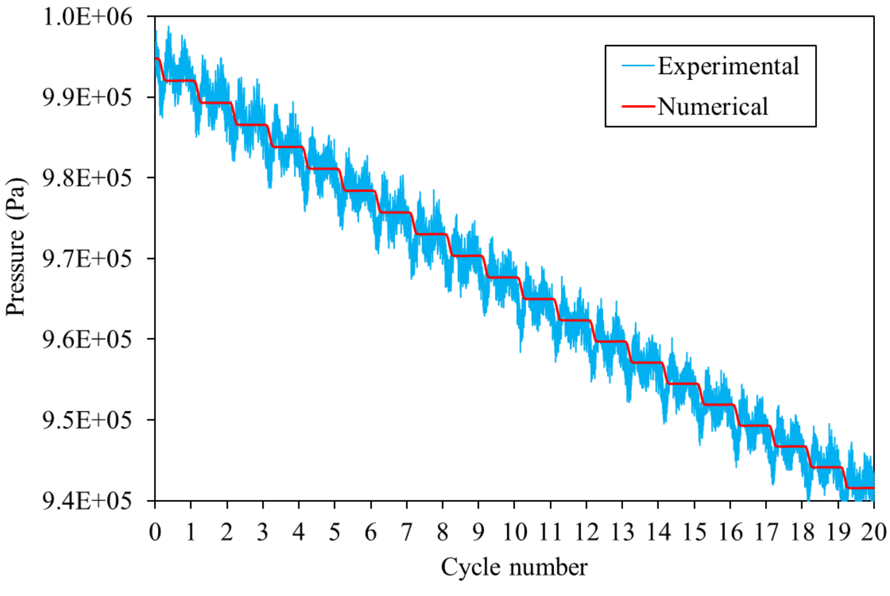

Figure 3-21 Experimental and numerical air intake pressure

Table 3-8 Comparison of experimental and simulated air mass injected per cycle

	Experimental	Numerical
Mass of air lost per cycle (mg/cycle)	630.8 ± 41.3	627.2 ± 13.2
Average mass flow rate of air (g/s)	57.34 ± 3.75	57.01 ± 1.20

For the fuel injection system, it is numerically assumed that the mass of fuel injected from cycle to cycle remains constant and this value is imposed.

The intake valve temperature is adjusted according to thermocouple measurements performed during the experimental tests (150 °C) and the exchange coefficient α_{A1} is set to 1. The intake phases of the cycles, up to spark-ignition (t_{ign} = 35 ms), are generally well reproduced and the ignition pressures are accurately captured, with an average difference below 1% over the 19 cycles. The signal is very well reproduced for the secondary cycles as illustrated by cycles 1 (C1) to 4 (C4) of the typical spark-ignition case (Test 1672) shown in Figure 3-22). Having adjusted and validated the intake parameters, the next phase of interest is the combustion phase.

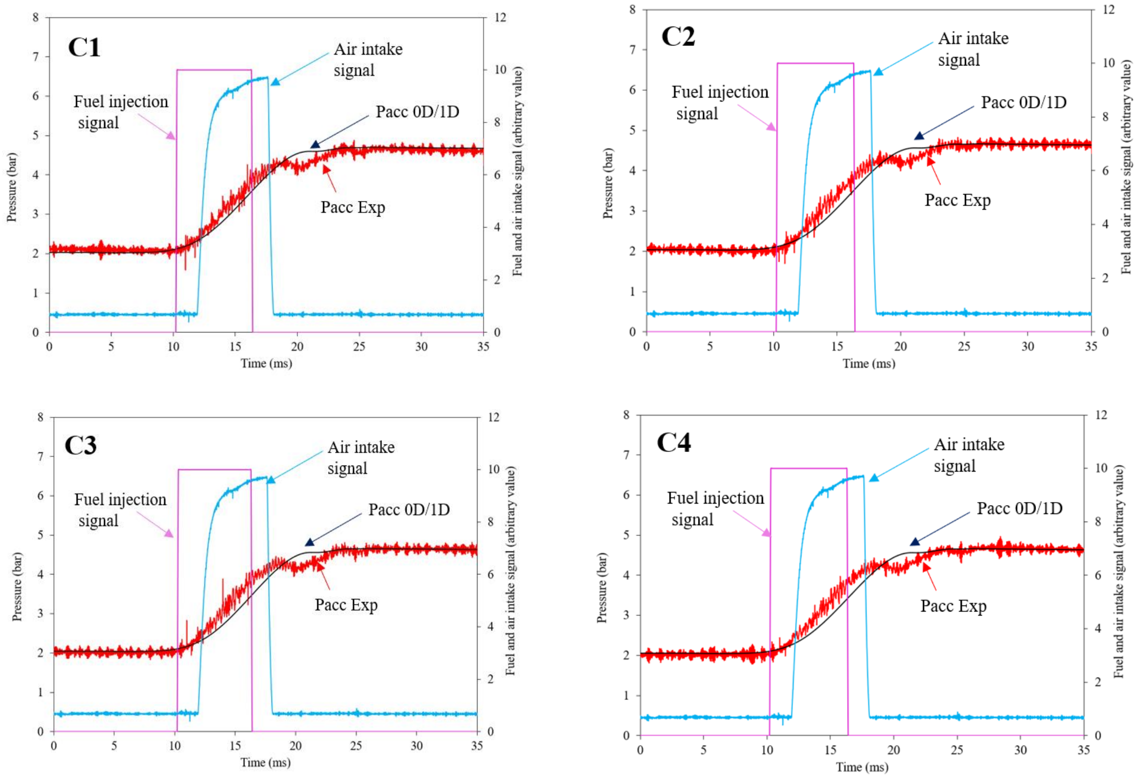

Figure 3-22 Comparison of experimental and 0D/1D pressure signals from cycles 1 to 4 during the intake phase of the cycle until ignition (0-35 ms). Test 1672 – n-heptane/air.

3.5.4.2 Combustion phase

The shape of the combustion pressure profile obtained from the simulation results is directly governed by the flame surface consumption rate imposed in the model. In the present case, because the flame surface area is assumed to be constant, which results in a relatively monotonic pressure evolution. To ensure consistency between the 0D/1D model and the experimental measurements, the combustion duration is adjusted so that the simulated pressure profile matches the experimental one. In practice, this approach approximates the experimental combustion pressure trace as a quasi-linear profile. Hence, the experimental ignition instant is not used as a reference point. This is because, during the initial stages of ignition, the ignition kernel undergoes a spherical propagation, a phenomenon that is poorly represented by the simplified 0D/1D model, which in return used the sliced-combustion method. Instead, the reference point is defined as the intersection between the tangent drawn at the inflection point of the experimental pressure signal (shown in Figure 3-23) and the initial chamber pressure (shown in green).

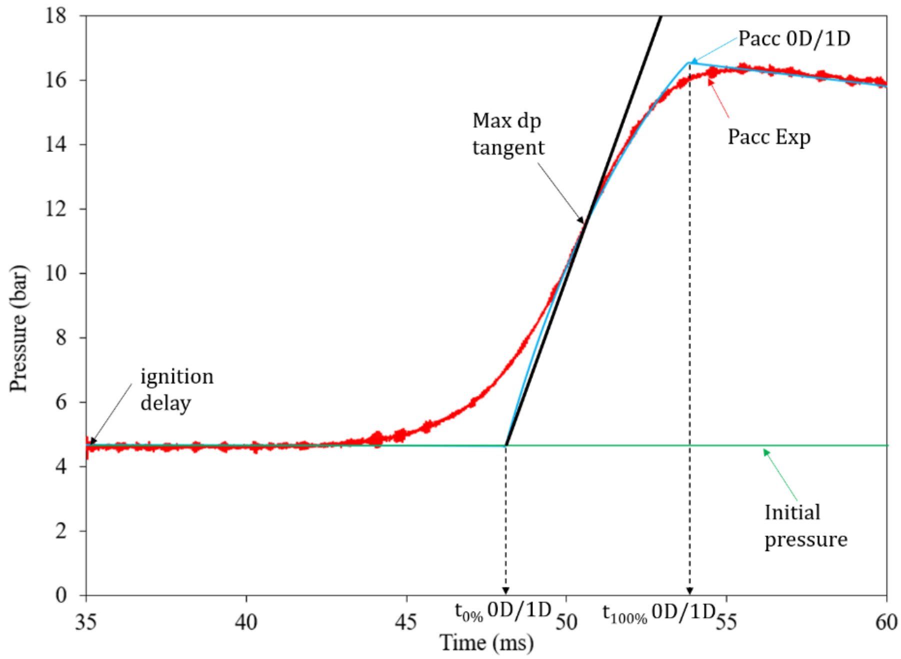

Figure 3-23 Comparison of experimental and simulated pressure signals for cycle 1 during the combustion phase. Test 1672 – n-heptane/air.

Once the combustion duration is imposed, the only remaining parameter available to adjust the pressure peak amplitude is the chamber flow adjustment coefficient, denoted k. This coefficient is kept constant and identical for all cycles, which may explain the discrepancies observed on a case-by-case basis. Nevertheless, the mean relative deviation between the simulated and experimental maximum pressures remains low, on the order of 1%.

A sequence of 10 successive cycles of the typical spark-ignition test (Test 1672) is illustrated in Figure 3-24 to visually show the deviation between the simulated and experimental pressure.

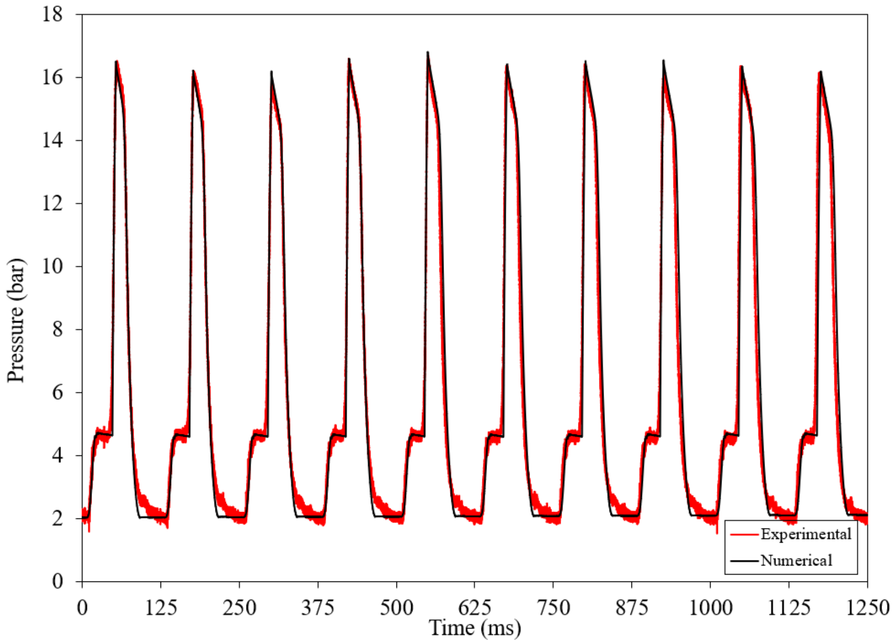

Figure 3-24 Comparison of experimental and simulated pressure signals for a sequence of 10 cycles

3.5.4.3 Exhaust phase

The exhaust valve opening timing is defined a priori. An isochoric cooling phase occurs after the peak combustion pressure, followed by the exhaust phase. During this phase, the flow coefficient is adjusted to reproduce the pressure decrease observed experimentally in the chamber. The coefficient is set to ensure correct recovery of the final pressure. The agreement between the simulated and experimental pressure profiles is satisfactory, as illustrated in Figure 3-25. It is to be noted that the flow coefficient of the exhaust valve, C_{dA2}, is defined using a static equivalent, whereas in reality, the behavior is static leading to small differences in the numerical cycle.

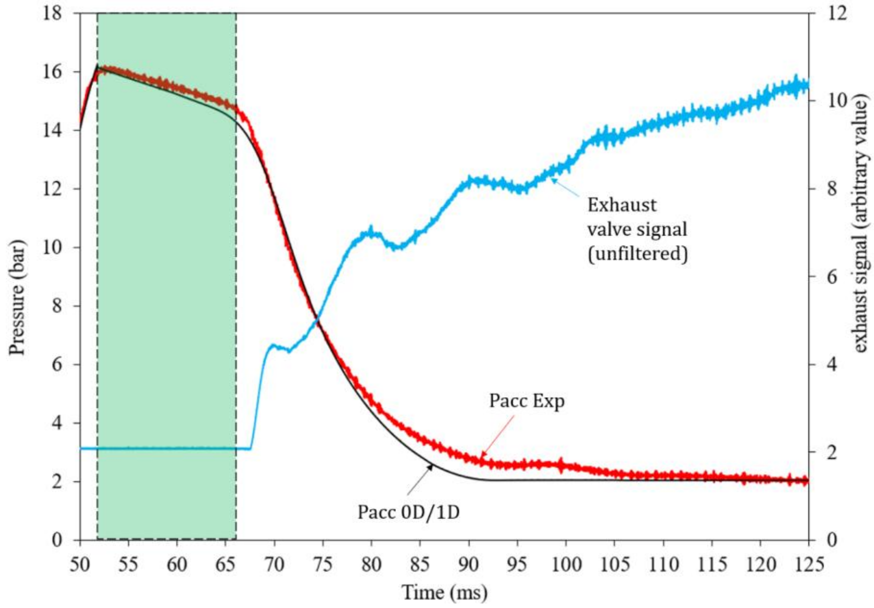

Figure 3-25 Comparison of experimental and simulated pressure signals for cycle 2 during the Isochoric (highlighted in green) and exhaust phase. Test 1672 – n-heptane/air

The calculation of the chamber exhaust mass flow rate depends on the exhaust backpressure at the valve seat, which must therefore be accurately represented. The exhaust process is more complex than the intake process, since the flow is not choked over the entire exhaust phase and the exhaust gases, which contain water vapor, may partially condense within the exhaust system. The boundary condition between the exhaust line and the exhaust tank is fixed. The exhaust flow coefficient and the heat transfer coefficient at the exhaust valve are adjusted to reproduce the pressure signal measured downstream of the valve.

The heat transfer coefficient during combustion, denoted k_{cc}, is assumed to be identical for all cycles. This assumption may lead to cycle-to-cycle variations in the quality of agreement between the experimental pressure signals and the 0D/1D simulations. To quantify this effect, the root-mean-square (RMS) deviation between the experimental and simulated pressure traces is computed for each cycle.

3.5.5 Simulation-derived parameters

The simulation code identifies hard-to-measure physical parameters such as residual gas dilution, gas temperature and wall heat losses. These are evaluated by tracking mass and energy exchanges across systems.

3.5.5.1 Residual burnt gas dilution

In the present model, residual burnt gas dilution is evaluated on a cycle-to-cycle basis using the species composition stored in the combustion chamber at the end of each cycle. Species are tracked with Cantera (massFractions, m, gasSet), hence it can be computed directly.

It is to be noted that at the start of cycle N+1, the chamber content is a mixture of fresh intake gases (air + possibly injected fuel) and RBG from cycle N that did not leave through the exhaust.

The methodology of measuring residual burnt gas dilution from the code is described thoroughly as follows:

1. **Identification of tracer species**

Residual burned gas is defined as the fraction of combustion products that remain in the chamber after the exhaust process. To quantify this, species that are not present in the fresh mixture but are robust indicators of burnt gases are selected. In the present study, carbon dioxide (CO_2), water vapor (H_2O) and carbon monoxide (CO) are used as tracers. CO_2 and H_2O are the stable, major products of complete hydrocarbon combustion. CO is included to trace incomplete oxidation, which is particularly relevant under fuel-rich or transient conditions. These three species provide a reliable measure of the mass fraction of burnt gases in the chamber.

2. **Residual gas quantity at the end of cycle N**

At the end of each cycle, the chamber mass fractions are extracted from the simulation. The residual gas fraction is defined as the sum of the mass fractions of the tracer species:

$$Y_{\mathrm{RBG}}(N) = Y_{\mathrm{CO_2}}(N) + Y_{\mathrm{H_2O}}(N) + Y_{\mathrm{CO}}(N) \qquad \text{Equation 3-28}$$

Where Y_{RBG} is the mass fraction of the residual burnt species.

The corresponding residual mass is then obtained as:

$$m_{\mathrm{RBG}}(N) = Y_{\mathrm{RBG}}(N) \cdot m_{\mathrm{chamber}}\,(N) \qquad \text{Equation 3-29}$$

where $m_{\mathrm{chamber}}\,(N)$ is the total mass trapped in the chamber at the end of cycle N.

3. **Dilution for the next cycle (cycle N+1)**

The dilution that affects cycle N+1 is then defined as the ratio between the residual gas mass carried over from cycle N and the total chamber mass at the beginning of cycle N+1:

$$\mathrm{Dilution}_{N+1} = \frac{m_{\mathrm{RBG}}(N)}{m_{\mathrm{total}}(N+1)} \qquad \text{Equation 3-30}$$

Where $m_{\mathrm{RBG}}(N)$ is the mass of burnt species (mass of tracer species) remaining at the end of cycle N (after exhaust) and $m_{\mathrm{total}}(N+1)$ is the total chamber mass calculated after the intake process of cycle N+1 (residual + new fresh mixture)

3.5.5.2 Heat loss

Since the numerical model incorporates a time-resolved energy balance, it enables an accurate estimation of energy losses occurring during the different phases of the cycle. This approach allows a detailed analysis of each phase of the cycle, with the associated losses quantified using the 0D/1D model.

The distinct phases of a typical spark-ignition cycle are illustrated in Figure 3-26. Intake-related losses are denoted by A, while B represents the losses associated with combustion and unburnt gases. The heat losses occurring during the isochoric cooling phase are identified as C and D corresponds to the exhaust-related losses.

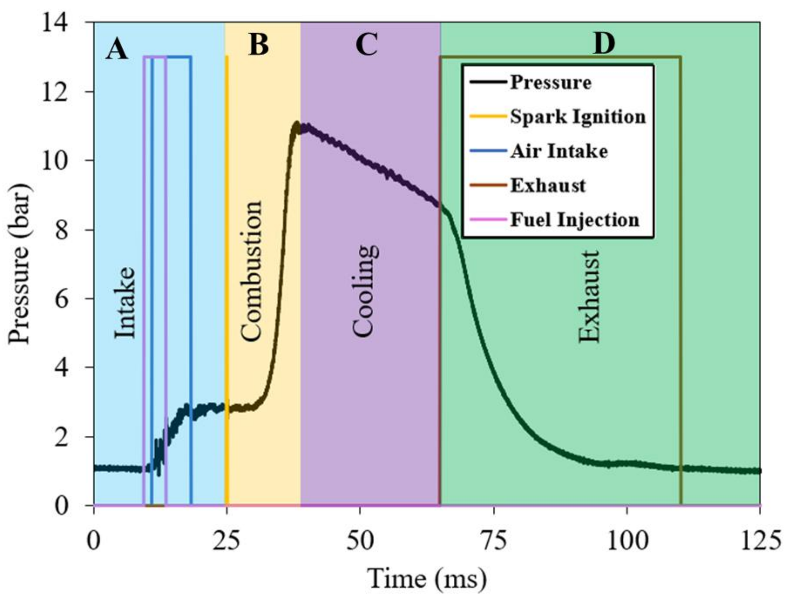

Figure 3-26 Distinct phases to estimate energy losses of a typical spark-ignited cycle

The 1D analysis performed on each cycle allows the establishment of a total energy balance within the combustion chamber. The total energy lost during a cycle, Q, for a lean mixture, is normalized by the energy associated with the injected fuel mass m_f, defined as:

$$Q_f = m_f I_p \qquad \text{Equation 3-31}$$

where I_p is the lower heating value of the fuel.

The overall energy losses are decomposed into two contributions: the energy exchanged with the chamber walls, Q_w, and the losses due to unburnt fuel, $\widehat{m}_i$, linked to flame quenching at the walls. The integral of the wall heat loss is reset at the beginning of each cycle, corresponding to the start of the intake phase (time t_a). At any time t during the cycle, the normalized wall heat loss can therefore be expressed as:

$$\widehat{Q}_w = \frac{S_{cc}}{m_f I_p} \int_{t_a}^{t} q_{w,0D}(t) \mathrm{d}t \qquad \text{Equation 3-32}$$

where $q_{w,0D}$ (W/m^2) is the wall heat flux predicted by the 0D model and S_{cc} (m^2) is the combustion chamber surface area.

3.6 Conclusion to this chapter

This chapter has presented the materials and methods used throughout the study. The chapter is organized into two main parts: the description of the experimental setup and diagnostics of the CV2 system and the 0D/1D modeling framework employed for phenomenological analysis.

The first part detailed the CV2 assembly. Boundary conditions are carefully controlled using intake and exhaust volumes, which allows precise control of the injected masses, calculation of the equivalence ratio in the chamber and regulation of the exhaust backpressure. All relevant parameters (such as air intake system) are finely characterized and the associated uncertainties are quantified. This detailed knowledge is essential for the development of the 0D/1D modeling framework presented in this work and it facilitates the subsequent analysis of physical processes. The experimental diagnostics section described both physical sensors and optical measurement techniques, providing a comprehensive understanding of the experimental capabilities and limitations.

The 0D/1D model, adapted for direct liquid fuel injection configurations, is presented in the second part. This model enables the prediction of cyclic behavior in the combustion chamber, offering insights into quantities that are difficult or impossible to measure directly. Importantly, the 0D/1D model has been validated for all key phases (intake, combustion and exhaust) of the spark-ignition cycle, ensuring the reliability of the predicted mass, energy and pressure evolutions.

In the next chapter, the methodology coupling the experimental data with the simulation framework will be applied to a reference spark-ignited cycle case of directly injected n-heptane in air. This reference case provides the foundation for the study of self-ignition phenomena, which will be addressed in detail in Chapter 5. Overall, the tools and methods presented in this chapter offer a robust framework for analyzing combustion cycles and interpreting experimental results with high confidence.

Chapter 4: Liquid spark-ignited cyclic CVC

4.1 Introduction

The present chapter introduces reference conditions using liquid n-heptane injection in the CV2 setup. In the aerospace context, fuels are predominantly stored and supplied in liquid form due to their high energy density and compatibility with compact onboard storage systems. In the CV2 facility, the use of liquid fuel offers several advantages. It enables injection at elevated pressure (100 bar), as a result, the injected mass flow rate is hardly sensitive to variations in chamber pressure compared to gaseous injectors. Improved control, repeatability of the injection process and representativeness of operating conditions relevant to aerospace propulsion systems can eventually be studied.

The objective of this chapter is to identify opportunities for optimizing the combustion cycle and to assess the thermodynamic efficiency of the constant-volume combustion process under conditions representative of aeronautical applications.

4.2 Presentation and analysis of a typical spark-ignition sequence using liquid n-heptane injection

4.2.1 Spark-ignition sequence presentation

The CV2 facility is designed with a highly modular architecture, enabling a wide range of geometric configurations to be implemented. This flexibility allows the study of combustion under constant-volume cyclic conditions representative of those imagined for aeronautical applications[39], [40]. In our experimental approach, particular attention is paid to the control of initial and boundary conditions throughout the experiments. Several diagnostic tools and analysis methods, such as pressure measurements, 0D/1D thermodynamic analysis, PIV and OH*/CH* chemiluminescence, are implemented to investigate both the thermodynamic and aerodynamic behavior of the unsteady reactive flow at play during a cyclic CVC sequence.

The initial characterization of both the experimental setup and the associated post-processing methodologies is carried out using direct injection of liquid n-heptane for spark-ignition cycles. This preliminary phase made it possible to establish and validate all measurement techniques used to characterize the initial and boundary conditions over an entire sequence of several cycles (see Figure 4-1).

In addition, it provided a detailed understanding of the physic occurring during each phase of a sequence and within an individual cycle. The experimental sequence examined in this chapter has been thoroughly characterized and is intended to serve as a reference case for subsequent numerical simulations.

A large number of parameters must be set and adjusted to achieve a stable cyclic configuration. A reference case (Test 1576) is selected based on these stability conditions. The operating conditions for this reference case are summarized in Table 4-1 and the resulting sequence obtained under these conditions is shown in Figure 4-1.

Table 4-1 Operating conditions for the reference cyclic configuration (Test 1576)

dt air (ms)	dt fuel (ms)	tign (ms)	tex (ms)	dt ex (ms)	Pex (bar)	Period (ms)
11	5	25	55	45	2	125

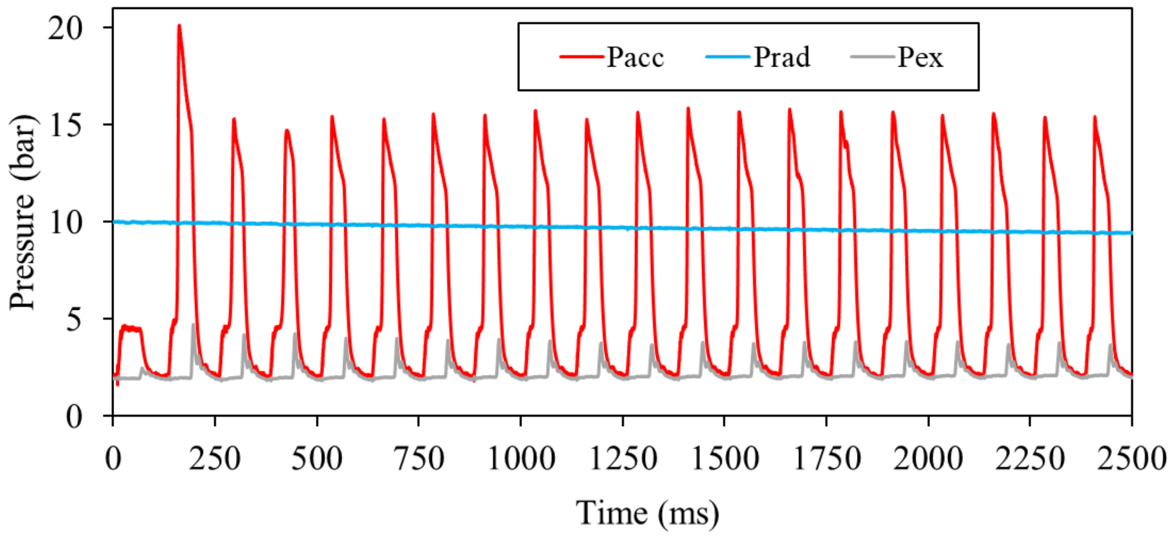

Figure 4-1Experimental signals of the pressure in tanks and chamber over a sequence of 20 cycles in the reference configuration

This characterization is performed at a nominal operating point, defined in accordance with the facility specifications. The reference sequence consists of 20 cycles. In this configuration, the OER targeted is equal to 0.9. The initial chamber pressure, controlled by air intake opening duration, is 4.49 ± 0.05 bar, corresponding to a variation of approximately 1.1%. The initial exhaust pressure is fixed at 2.0 bar and the effective exhaust volume is 100 L. During the exhaust phase of the cycles, an instantaneous increase in exhaust pressure is observed at the pressure gauge location (just downstream of the exhaust valve). This pressure rise is associated with unsteady choked flow at the fast exhaust valve. Under these conditions, the ratio between the upstream pressure Pacc and the exhaust pressure Pex consistently exceeds 1.8. As a result, the variations in exhaust pressure do not affect the exhaust process.

Examination of the in-chamber pressure signal over the 20 cycles highlights three distinct cycles/stages within the sequence:

- Cycle 1 initial conditions differs from the others for several reasons. The chamber is initially filled with air and the first valve opening is both slower and shorter, resulting in a reduced amount of air being injected into the chamber. The OER of this first cycle is thus not well controlled and may lie outside the flammability limits. This likely explains why, despite the presence of a spark, combustion rarely occurs during the first cycle.
- Cycle 2 follows this unburned first cycle. The residual gases present before fresh gas filling thus consist mainly of fresh air/n-heptane mixed with a low-temperature n-heptane-air mixture of previous cycle. This cycle is referred to as *primary cycle* as it lacks dilution from hot residual burned gas from the previous combustion cycle. Primary cycle reaches higher maximum pressure because mixture is only composed of unburned mixture allowing complete combustion, unlike diluted cycles where hot residuals reduce the quantity of initial unburned in the chamber that lower peak pressure.
- Cycles 3 to 20 are consecutive burning cycles, referred to as *diluted cycles* or *secondary cycles*. Prior to the filling phase of these cycles, the chamber contains burned gases in which the n-heptane fraction is negligible, primarily originating from unburned fuel, if any. After filling, the fresh gases are partially diluted by previous cycle residual burned gas influencing all the combustion process along the cycle. Under these reference conditions, ignition is induced at 25 ms and the ignition success rate for the secondary cycles is 100%, indicating a stable operating configuration.

The 0D/1D model introduced in Chapter 3.5 allows the determination of overall properties that could not be easily measured such as density and average temperature during each cycle of a sequence (cf. Figure 4-2). From the evolution of density, the constant-volume phases can be clearly identified, corresponding to the periods between mass transfer events, during which the combustion process occurs.

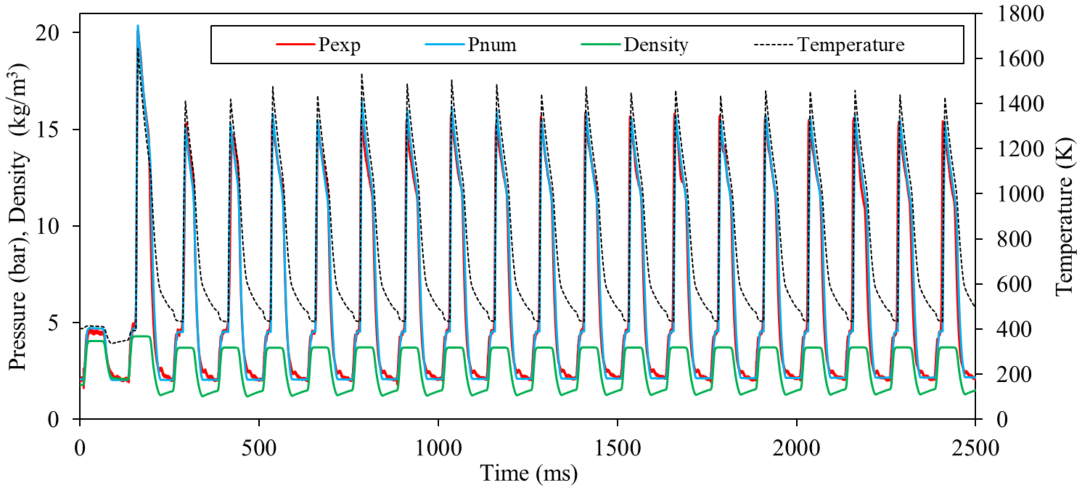

Figure 4-2 0D/1D pressure representation of the reference test and its associated density (0D) and temperature (0D).

In the next section, statistical indicators, such as mean and standard deviation, are computed from the pressure traces across the ensemble of cycles to analyze the spark-ignition cycles.

4.2.2 Spark-ignition cycle analysis

The reference spark-ignition cycles are analysed following the methodology described in section 3.4. Pressure, wall heat flux, chemiluminescence and PIV analyses are performed on the secondary cycles under the reference conditions. Pressure analysis is particularly important for parametric studies, as it provides quantitative information on heat release and stability. In contrast, chemiluminescence reveals combustion reaction dynamics while PIV shows chamber flow structure, together giving a more fundamental understanding of the cycle. The pressure evolution of a spark-ignition cycle and its corresponding intake and exhaust signals of the reference case is shown in Figure 4-3.

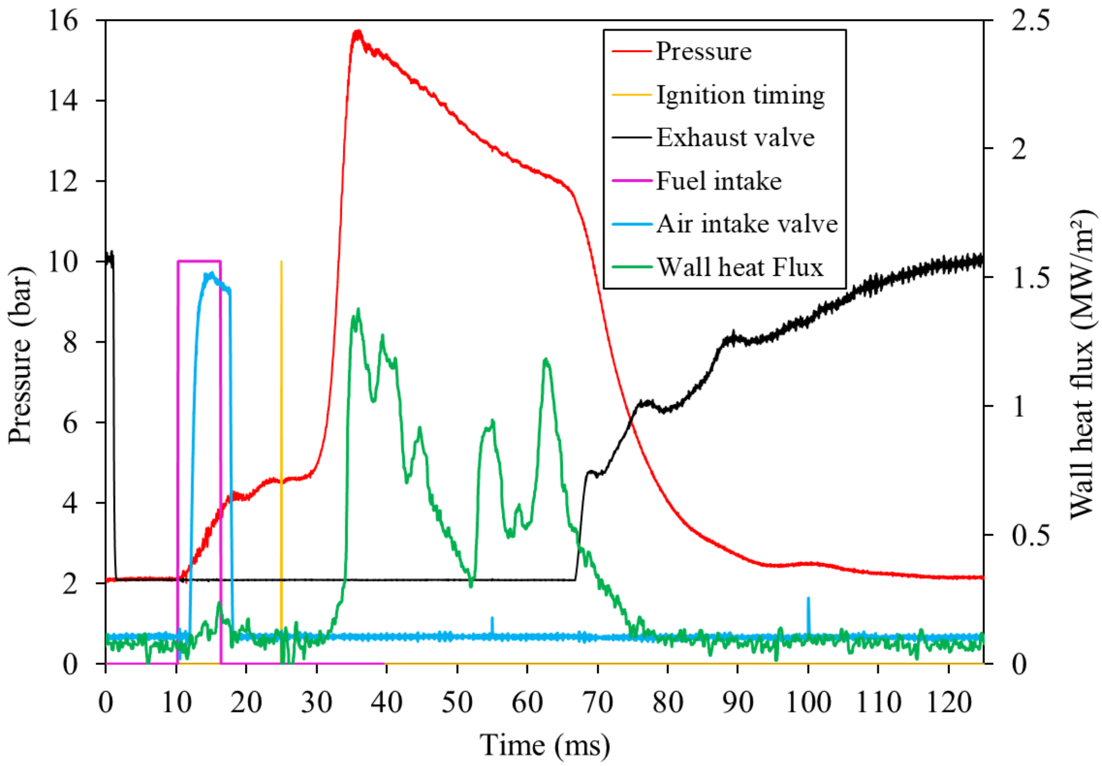

Figure 4-3 Presentation of a spark-ignition cycle (reference case – cycle 11) and its corresponding intake and exhaust valve signals.

While some parameters are directly relevant for specific parametric studies, others serve as a basis for global comparison like OER. These results therefore establish a baseline for the different parameters; however, their main value lies in illustrating their influence on other parameters, as further explored in section 4.3.

4.2.2.1 Pressure analysis

The overall mean and standard deviation of key parameters obtained from the pressure analysis over the sequence of the 18 secondary cycles is summarized in Table 4-2. Figure 4-4 shows the 18 superposed secondary pressure cycles and their corresponding wall heat flux.

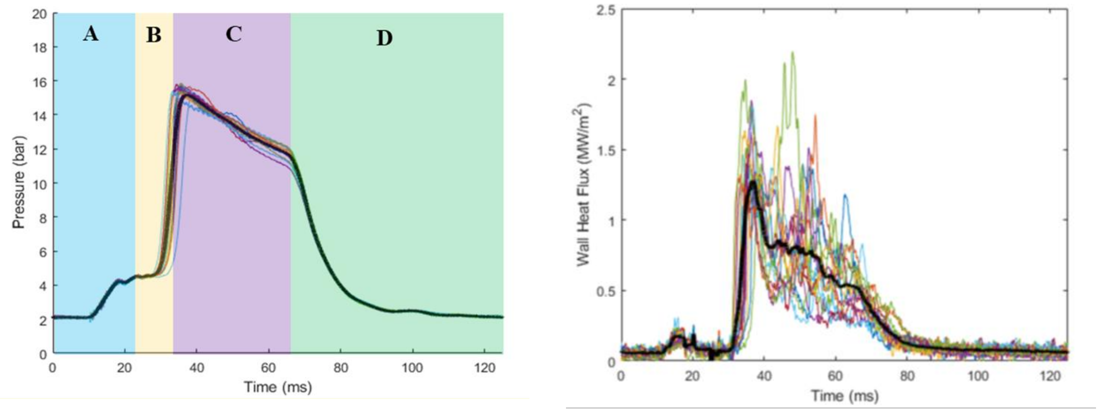

Figure 4-4 Superposed traces of combustion pressure (on the left) and wall heat flux (on the right) for secondary cycles of the reference spark-ignition case. Bold black line: the mean pressure and mean wall heat flux

Table 4-2 Overall mean and standard deviation of key parameters over the sequence for 18 cycles for the reference case

Parameters	
From experiment:	
OER	$0.95 \pm 0.06_{6.3\%}$
Initial pressure (bar)	$4.49 \pm 0.05_{1.1\%}$
Maximum pressure (bar)	$15.51 \pm 0.25_{1.6\%}$
Pressure ratio	$3.46 \pm 0.06_{1.7\%}$
$t_{comb,10\%-90\%}$ (ms)	$3.79 \pm 1.17_{30.8\%}$
Maximum dP/dt (bar/ms)	$3.51 \pm 0.66_{18.8\%}$
Maximum wall heat flux (MW/m^2)	$1.53 \pm 0.16_{10.5\%}$
From simulation:	
RBG Dilution (%)	$21.9 \pm 0.6_{2.7\%}$

The pressure analysis gives an OER (see section 3.3.2.13.4.2.1) is of 0.95, indicating near-stoichiometric or slightly lean mixture. The small cycle-to-cycle variation in OER (±0.06) shows that the mixture in the intake phase (A) is consistent from one cycle to another. A study on the effect of OER on cycle stability and combustion duration will be discussed in section 4.3.1.2 and 4.3.1.3.

Peak pressure reaches 15.51 ± 0.25 bar. The low standard deviation (~1.6%) indicates stable peak pressure across cycles. This stability is mainly due to the OER being near stoichiometric conditions. The effect of OER on the peak pressure will be further discussed in section 4.3.3.1. The corresponding pressure ratio is 3.46 ± 0.06.

Combustion duration, defined as the interval for 10%–90% of energy release (see section 3.4.1.2), is measured at 3.79 ± 1.17 ms for an ignition timing of 25 ms. This large variability (~30%) may be related to the increased sensitivity of slower flames to turbulence, spark location and remaining mixture inhomogeneity in the combustion phase (B). Michalski [54]performed a similar test at the same time frequency using the CV2 set-up with propane-air at stoichiometric conditions and 21% RBG dilution. The initial pressure was 3.3 bar and the exhaust pressure was at 1 bar. The tests were carried out at two different ignition timings at 19.0 ms and 32.5 ms. He reported combustion duration (10%-90%) of the secondary cycles to be 2.9 ± 0.6 and 4.3 ± 0.5 at those two different ignition timings.

The maximum pressure rise rate (dP/dt) is 3.51 ± 0.66 bar/ms. Its cycle-to-cycle variation is consistent with the fluctuations observed in the combustion duration. The peak wall heat flux is 1.53 ± 0.16 MW/m^2. Both these values will serve as reference for later comparison.

From the different phases of the cycle shown in Figure 4-4, Phase A (intake) and Phase B (combustion) will be analyzed in detail in Section 4.2.2.2 to gain deeper insight into the velocity field and turbulence fluctuation on the spark-ignition mode. The choice of the intake phase (A), depending on the ignition timing and its impact on cycle stability, is discussed in Section 4.3.2. Phase C (cooling) shows potential for further optimization, while Phase D (exhaust) could likely be shortened. These aspects are discussed in Section 4.3.4.

In summary, the spark-ignited cycles obtained from the CV2 set-up operate under near-stoichiometric conditions with moderate dilution, showing good mixture consistency from cycle to cycle. The peak pressure and pressure ratio remain stable, with low variability, reflecting consistent combustion behavior. Although the combustion duration shows higher fluctuations, this can be attributed to the sensitivity of flame development to turbulence, ignition timing and mixture inhomogeneity.

Overall, these results establish a reliable baseline for the present configuration. Their main importance lies in how they affect and interact with other operating parameters, which are further analyzed and discussed in Section 4.3.

4.2.2.2 Chemiluminescence analysis

OH* and CH* chemiluminescence analyses are performed to gain insight into the ignition process, flame development and heat-release characteristics of the spark-ignited cycle. The OH* measurements were conducted first, followed by CH* measurements under identical operating conditions for the referenced spark-ignition case. The camera integration time was adjusted to capture the low luminosity levels associated with spark-ignited flames attenuated by the filters used.

Analysis of fast radical imaging

Figure 4-5 presents the raw OH* and CH* images obtained from cycle 11, illustrating the temporal evolution of the flame from ignition to exhaust valve opening. This cycle was selected as it is representative of the majority of secondary cycles in terms of both OH*-based and CH*-based pressure evolution. As the OH* and CH* measurements were performed separately, direct color visualization was systematically carried out in parallel with each filtered chemiluminescence measurement. This approach allows the overall differences between the two tests to be clearly identified and compared.

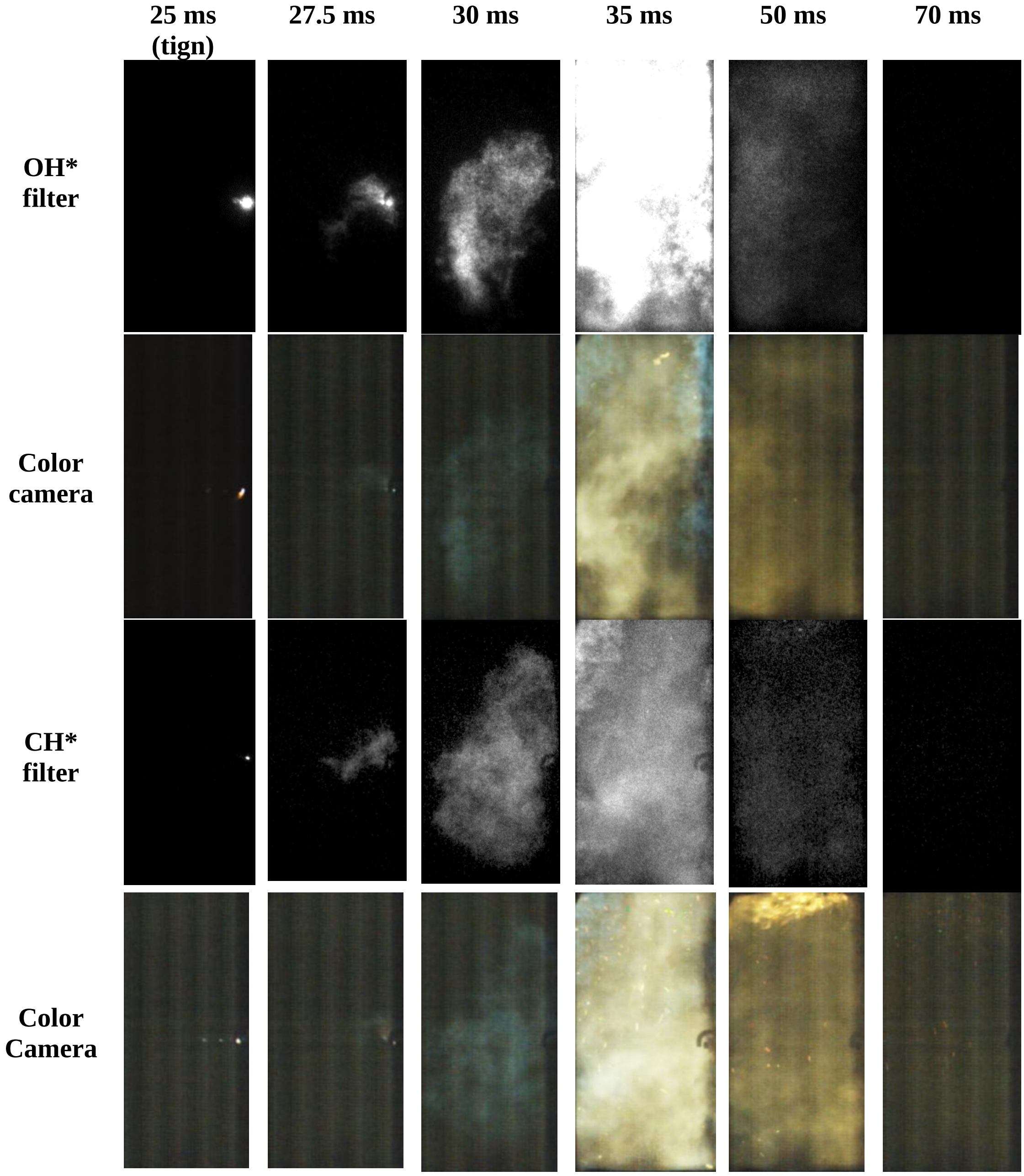

Figure 4-5 Time-resolved OH* and CH* chemiluminescence imaging and corresponding broadband imaging at selected times from ignition to exhaust valve opening.

From Figure 4-5, at 25 ms, corresponding to ignition timing, a small luminous region appears in both the OH* and CH* images, showing the formation of the initial flame kernel near the spark plug.

At 27.5 ms and 30 ms, the flame kernel grows and becomes more visible. The CH* images show an expanding luminous region that marks the propagating flame front and the main reaction zone. At the same time, the OH* emission also increases and fills a large part of the kernel interior, indicating the buildup of high-temperature gases inside the flame. The color images confirm that the flame is still relatively localized in the chamber at these times.

By 35 ms, both OH* and CH* signals intensify as the flame expands to fill the combustion chamber. The CH* emission remains mainly near the advancing flame front, while OH* is more intense inside the flame volume. The observed chemiluminescence validates that CH* highlights the reaction zone close to the front and OH* indicates hotter reaction and product regions inside the flame[74].

At 50 ms, the OH* images show a strong and relatively uniform emission, indicating that the chamber is filled with hot combustion products rather than an actively propagating flame. The CH* signal is still detectable but appears faint and diffuse, consistent with the decay of reaction zones (mainly near the chamber wall) after the main heat-release phase has ended. The color images show a broadly luminous field with no clear flame front, in line with combustion already being essentially completed.

At 70 ms, during the exhaust phase, both OH* and CH* emissions are reduced and close to the background level, which is consistent with decaying radical concentrations as the gases cool with the opening of the exhaust valve.

Overall, the images show CH* closely linked to the flame front during the main propagation phase, while OH* provides a stronger, more global view of the high-temperature products, especially once the combustion is over and the chamber is filled with hot gases.

Quantitative evolution of fast radicals

To gain a closer understanding, the spontaneous radical emissions were analyzed quantitatively. The OH* and CH* images were processed using total pixel intensity, calculated by summing all pixel values in each recorded image. This metric provides a global measurement of radical emission.

Based on the experimental data, 12 secondary cycles were analyzed for OH* and 19 secondary cycles for CH*. The cycle-to-cycle variation in normalized intensity for these secondary cycles is presented in Figure 4-6 while Table 4-3 summarizes the cycle-to-cycle intensity duration (measured at 20% of the normalized intensity) and the combustion duration for the OH* and CH* chemiluminescence.

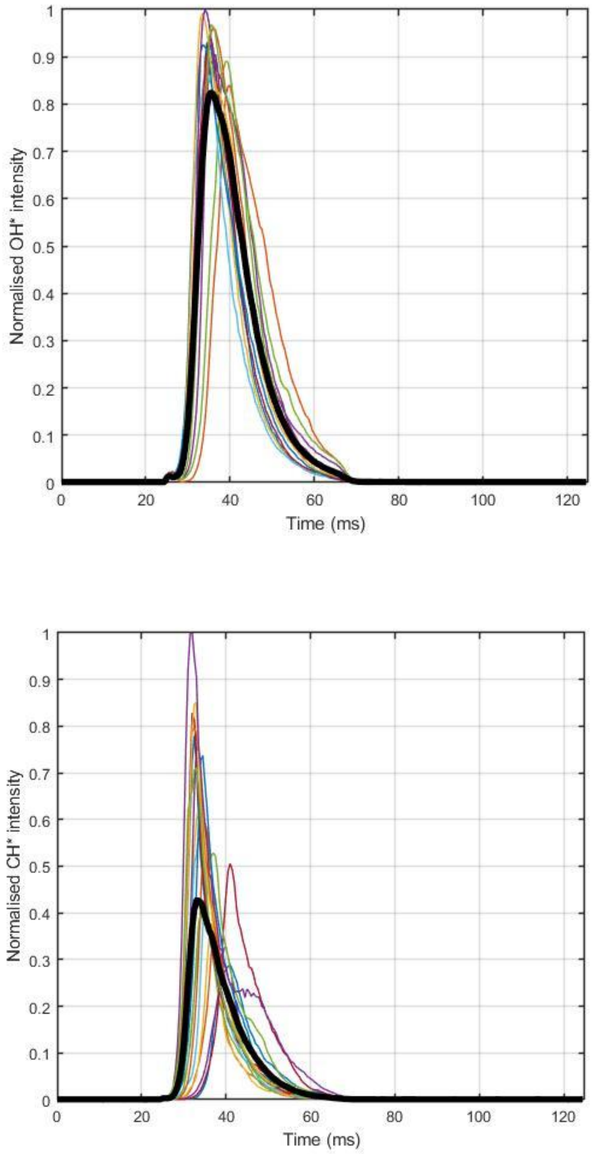

(i)

(ii)

Figure 4-6 Cycle-to-cycle variability of the total intensity of OH* (i) and CH* (ii) secondary cycles of the reference spark-ignition case

Table 4-3. Cycle-to-cycle intensity duration, combustion duration and OER for the OH* and CH* chemiluminescence

Chemiluminescence Type	**OH***	**CH***
Intensity duration$_{20\%}$ (ms)	$18.6 \pm 2.2_{11.8\%}$	$13.4 \pm 2.6_{19.4\%}$
$t_{comb,10\%-90\%}$ (ms)	$3.96 \pm 0.54_{13.6\%}$	$3.91 \pm 0.80_{20.5\%}$
OER	$1.04 \pm 0.04_{3.8\%}$	$1.01 \pm 0.05_{5.0\%}$

The ensemble-averaged total intensity was then computed for the secondary cycles of both OH* and CH*. Figure 4-7 presents the time evolution of the normalized mean total pixel intensity for these two radicals. In the legend, the labels "Pressure OH*" and "Pressure CH*" indicate the chamber pressure signals recorded during the OH* and CH* chemiluminescence experiments, respectively for two equivalent cycles. The intensity traces show the measured chemiluminescence of OH* and CH*, with their corresponding standard deviations shown as dotted lines. Note that the pressure traces originate from separate experiments, since OH* and CH* emissions were not captured simultaneously.

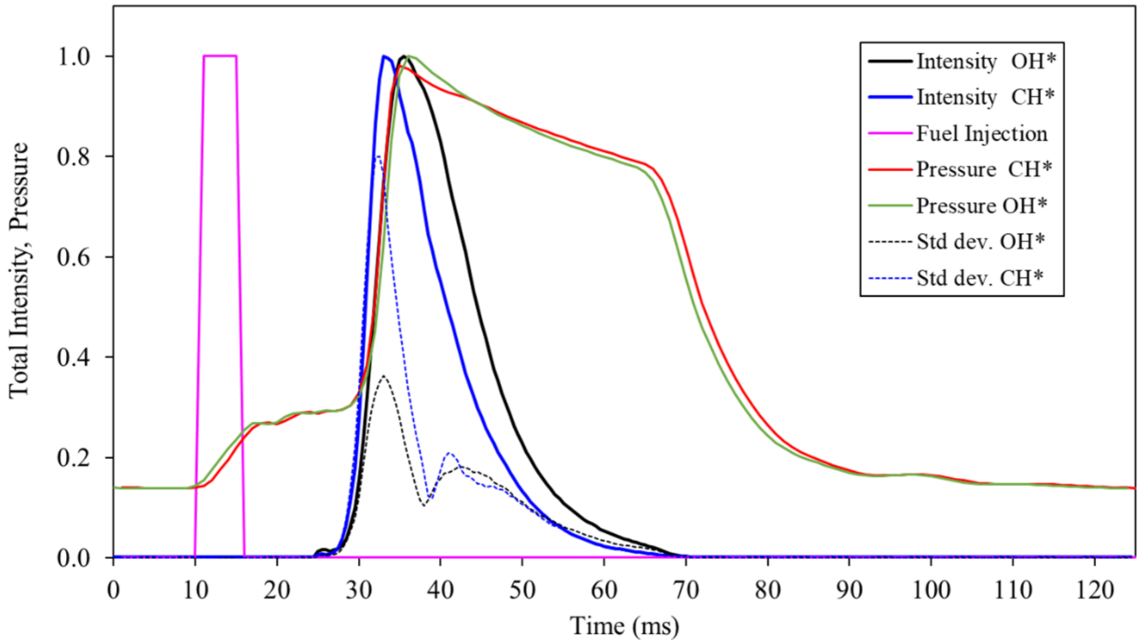

Figure 4-7 Temporal evolution of instantaneous total pixel intensity of OH* and CH*, including their standard deviations (dotted lines) and their corresponding pressure traces

From Figure 4-7, normalized total pixel intensities and normalized chamber pressures are presented to enable comparison of their temporal evolution independent of absolute signal magnitude. Both CH* and OH* exhibit a distinct response following spark ignition and naturally correlate with the pressure rise, confirming that chemiluminescence provides a reliable indicator of combustion progress.

CH* chemiluminescence rises rapidly after ignition and reaches its peak earlier than OH*, consistently with its association with early-stage hydrocarbon oxidation and flame kernel formation at the reaction front. In contrast, OH* increases more gradually and attains its maximum closer to peak chamber pressure, reflecting its link to high-temperature post-flame regions during the main heat-release phase.

In addition to peak timing differences, CH* decays more rapidly than OH* following its maximum. This steep post-peak reduction is characteristic of CH* being confined to the thin reaction zone (13.6±2.6 ms) where changes in local equivalence ratio or temperature quickly suppress the signal. OH*, by comparison, persists for a longer duration (18.6±2.2 ms), consistent with its presence in broader, high-temperature burned-gas regions.

After the opening of the exhaust valve at ~70 ms, pressure decays slowly while both radical signals are close to zero. This shows chemiluminescence cannot track expansion and heat loss phases, as radicals have already recombined into stable combustion products by this point and pressure evolution becomes purely thermodynamic.

Analysis of the normalized standard deviation reveals increased variability around the CH* peak, indicating greater cycle-to-cycle variability during early flame development. In contrast, the lower variability observed for OH* peak intensity implies that the process is more stable once combustion is established.

4.2.2.3 PIV analysis

PIV measurements are performed under the same operating conditions as the reference case (Test 1576) to characterize the chamber flow field and overall aerodynamics. 11 cycles of this test 1630 are retained for analysis. For each cycle, velocity fields are recorded at 10 kHz, providing sufficient temporal resolution to capture the main flow structures and their evolution throughout the cycle. Due to seeding oil combustion during the reactive phase, the analysis is limited to the intake and combustion phase.

4.2.2.3.1 Topology analysis of the velocity field

For the reactive case, an interframe time of *dt* = 25 μs is used. The evolution of the intake and combustion processes of cycle 11 of Test 1630 are presented in Figure 4-8 through tomography images, followed by velocity fields obtained using the multi-pass cross-correlation PIV algorithm described in section 3.4.4

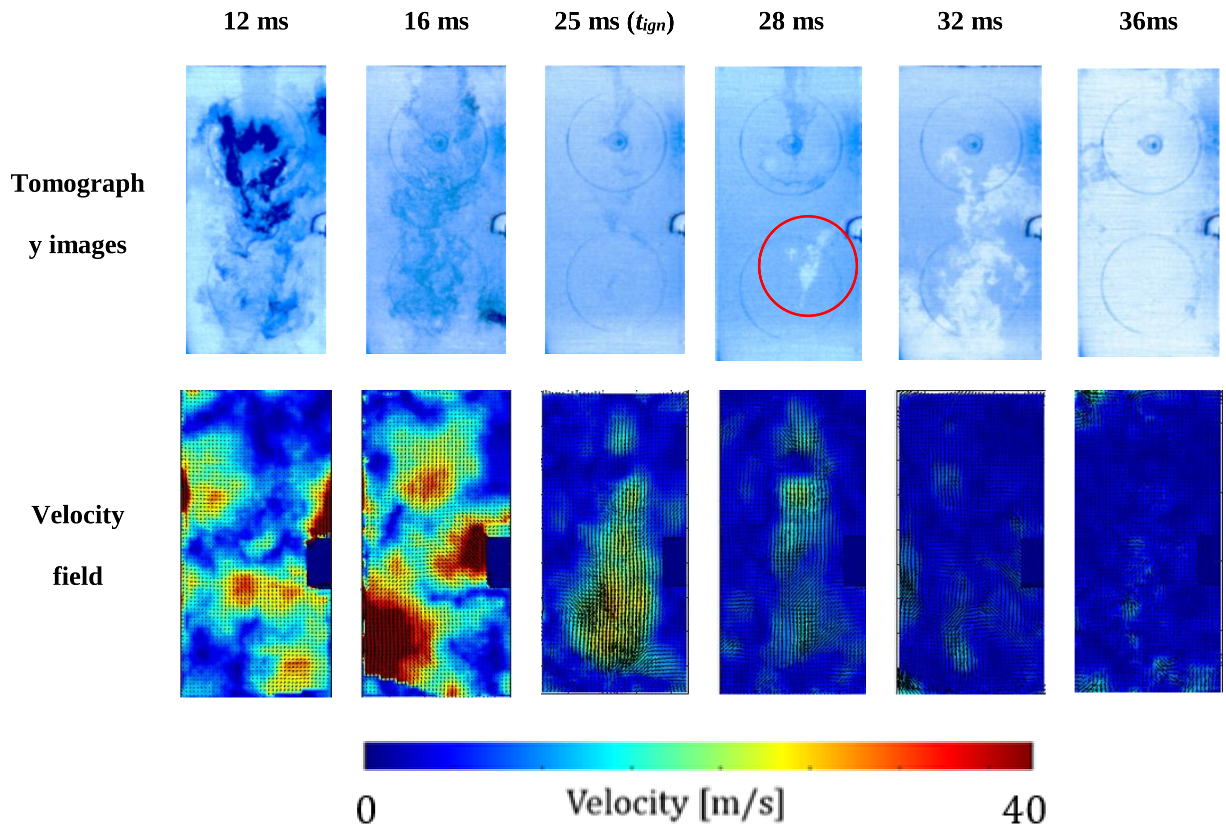

Figure 4-8 Aerodynamics during the intake and combustion phase of the cycle 11 of the spark-ignition Test 1630 sequence.

During the intake phase (t = 12 ms and t = 16 ms), the velocity field exhibits regions exceeding 40 m/s, indicating stronger flow structures during the intake than during the combustion phase (t=25 ms to t=36 ms) as aerodynamics decays prior to ignition. In the tomography images, during the combustion phase, lighter regions correspond to the flame front, where lower velocities are expected due to thermal expansion and reduced local momentum. For the spark-ignited cycles, at t=28 ms, the region circled in red corresponds to the developing flame front originating from the spark-plug kernel. From t=28 ms to t=36 ms, combustion continues, with the flame front, indicated by the white region, progressively propagating across the chamber.

To enable a quantitative comparison, velocity data during the intake and combustion phases were further processed in MATLAB to determine the fields of mean velocity and turbulent fluctuation.

4.2.2.3.2 Quantitative analysis of the velocity field

Using the methodology described in Section 3.4.4.4, a statistical analysis of the flow field is performed over the cycles, which provides sufficient convergence thanks to the low cycle-to-cycle variability between the secondary spark-ignition cycles. The temporal evolution of the spatially-averaged flow velocity and turbulent fluctuation are presented in Figure 4-9. The spatial distribution and temporal evolution of these quantities provide the quantitative basis for characterizing the spark-ignition mode.

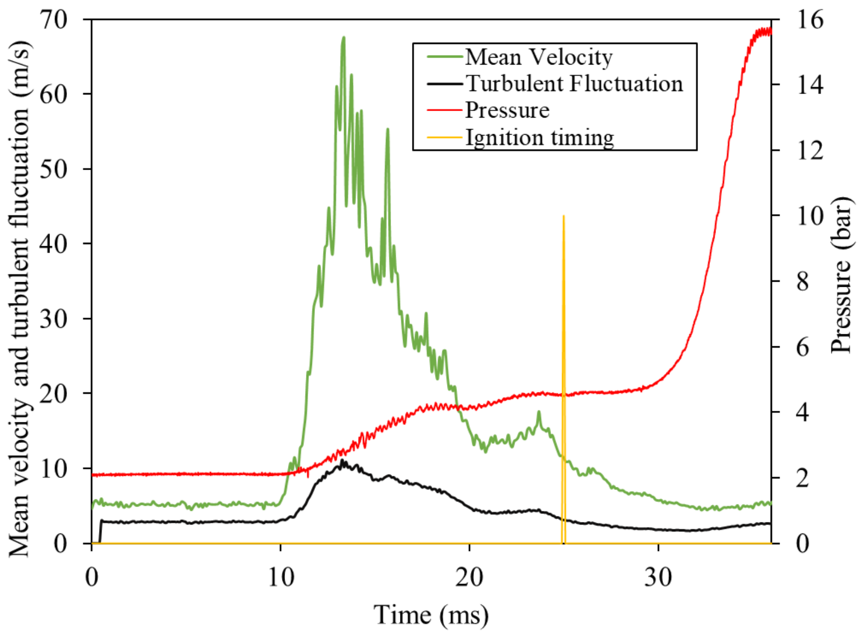

Figure 4-9 Temporal evolution of the mean velocity, turbulent fluctuation and pressure ensemble-averaged across spark-ignited cycles

Air is injected into the chamber from t = 10 ms to t = 18 ms, leading to an increase in mean velocity, turbulent fluctuation and pressure. The mean flow velocity and turbulence are primarily controlled during this intake phase. After intake ends, flow velocity continues to decay while reactants and RBG mix until ignition timing. At spark-ignition timing (t = 25 ms), the ensemble-averaged mean velocity decays to ~10 m/s with turbulent fluctuation ~5 m/s. During combustion, both mean velocity and turbulence decrease further due to gas viscosity increase and thermal expansion from the heat release. The flame thus propagates through a low-velocity field (~10 m/s and lower) with limited interaction with the decaying velocity field.

A representation of the ensemble-averaged fields of mean velocity and turbulent fluctuation at ignition timing (t = 25 ms) is presented in Figure 4-10. The turbulence fluctuation remains high near the wall. This may result from a combination of residual PIV optical artefacts near wall regions and possible flow perturbations induced by the opening and closing of the intake (top) and exhaust (bottom) valves.

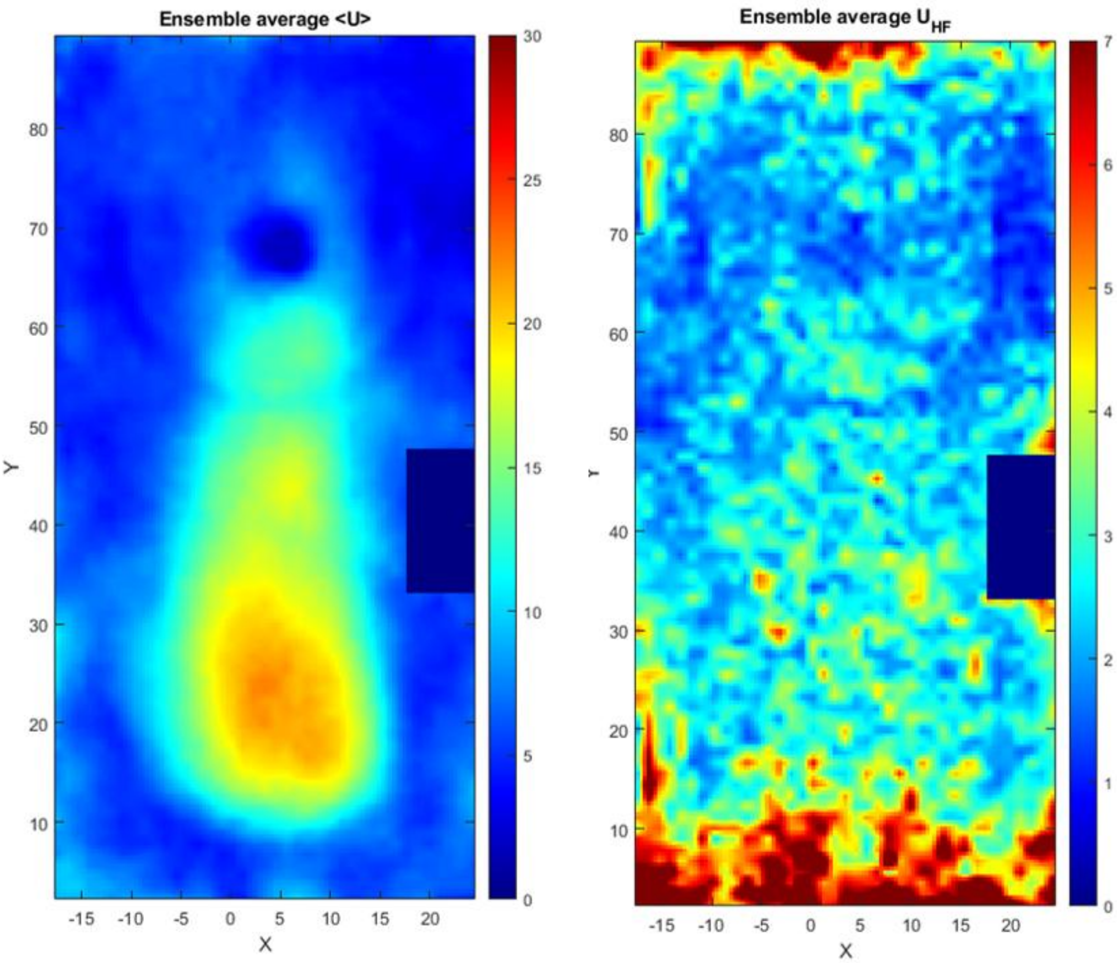

Figure 4-10 Ensemble-average mean velocity and turbulent fluctuation at t= 25 ms

4.2.2.4 Heat loss analysis

A heat loss analysis is carried out on the mean cycle from Figure 4-4 using the 0D/1D model described in Section 3.5.5.2, providing an overall view of the heat losses during the different phases. Figure 4-11 shows the numerical pressure in blue and experimental pressure in red and the different phases of the spark-ignition cycle: intake (A), combustion (B), cooling (C) and exhaust (D) with the heat losses from each phase summarized in Table 4-4.

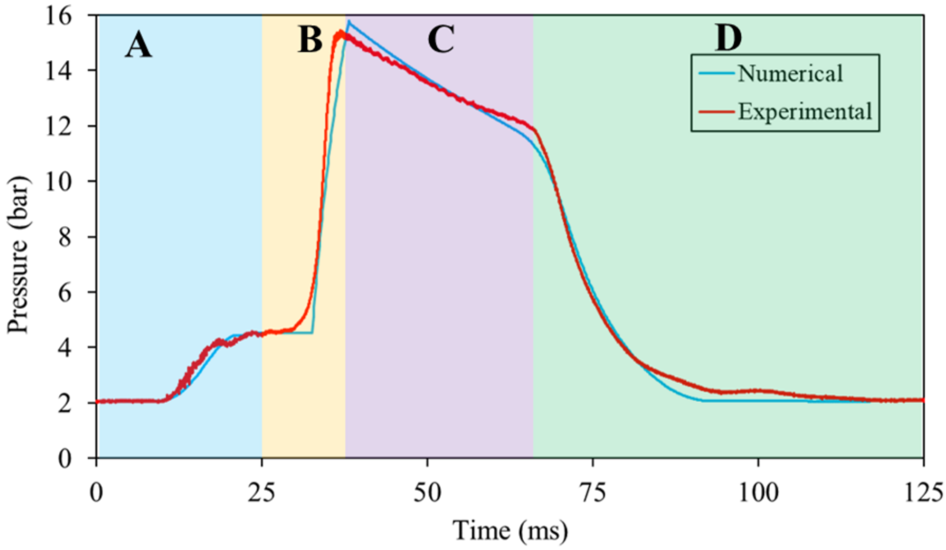

Figure 4-11 Heat loss analysis of the different phases of the spark-ignition cycle using the 0D/1D code

Table 4-4. Contribution of energy losses (% combustion energy) for the different phases of the mean spark-ignited cycle

Phase	A (%)	B (%)	C (%)	D (%)	Total (%)
Ref. cycle	0.6	39.7	20.1	9.0	69.4

Table 4-4 presents the distribution of total energy losses among the different phases of the mean of spark-ignition cycle. The intake phase contributes for the least amount of heat losses. Phase B (combustion and unburnt mass losses) is the major contributor of the energy loss, accounting for nearly 39.7 %. A significant energy loss (20%) is also associated with phase C, corresponding to the isochoric cooling phase, highlighting the non-optimized nature of the cooling process at this type of cycle. This cooling phase will be optimized in section 4.3.4. The exhaust phase has a cooling of 9% which is not as impactful as the combustion and cooling phases.

4.3 Influence of operating parameters

Several parameters obtained from the pressure analysis are interdependent, making it necessary to vary them individually in order to isolate their respective effects. To this end, four separate parametric studies are conducted to evaluate the influence of key operating parameters on combustion behavior and cycle stability.

The first parametric study investigates the influence of the OER, which was varied from 0.6 to 1.5, in order to assess its effect on peak pressure, combustion duration and combustion stability. The second study examines the impact of ignition delay, varied between 10 and 25 ms, on cycle-to-cycle stability. The third parametric study focuses on the effect of exhaust pressure, which was varied from 1 to 2 bar while keeping the initial pressure constant. Finally, a fourth study evaluates the influence of reducing the cycle period from 125 to 80 ms, which corresponds to an attempt of optimizing the cycle frequency for increasing the power delivery.

These variations provide a systematic framework for understanding how individual operating parameters affects the combustion performance.

4.3.1 Effect of fuel/air equivalence ratio

4.3.1.1 Effect of OER on peak pressure

The fuel/air equivalence ratio is a key operating parameter for combustion systems intended for aerospace applications, as it directly affects pressure levels, thermal loading, efficiency and operability. In the context of pistonless constant-volume combustion, controlling the equivalence ratio is essential to ensure stable operation while maintaining pressure characteristics compatible with propulsion requirements. Operating at lean conditions is of particular interest for aeronautical applications, as it enables lower thermal stresses, while also contributing to improved durability of the combustion chamber and turbine components. Moreover, studying a lean mixture also provides insight into less energetic combustion, where the influence of flow on flame dynamics is more pronounced.

This section presents a parametric study of the influence of the fuel/air equivalence ratio on the pressure evolution in the CV2 chamber. This section has three main objectives. The first objective is to look at the effect of the equivalence ratio on the peak pressure during the cycle. This objective is to assess whether the resulting peak pressure behavior remains comparable to that of a conventional internal combustion engine. The second objective is to identify the range of fuel/air equivalence ratios for which stable spark-ignition cycles can be achieved. Particular attention is given to lean operating conditions and their impact on pressure evolution and cycle stability. The third objective is to assess the effect of the OER on the combustion duration of the stable cycles.

To investigate the effect of equivalence ratio, n-heptane–air mixtures are studied over 17 operating points, with equivalence ratios ranging from 0.68 to 1.42.

For comparison, the theoretical peak pressure over the equivalence ratio range from 0.7 to 1.4 is computed using Cantera under idealized isochoric and adiabatic conditions (no dilution with RBG, unlike the 0D/1D model). The resulting secondary peak pressures variation from the experiments and from the ideal Cantera simulations are shown in Figure 4-12.

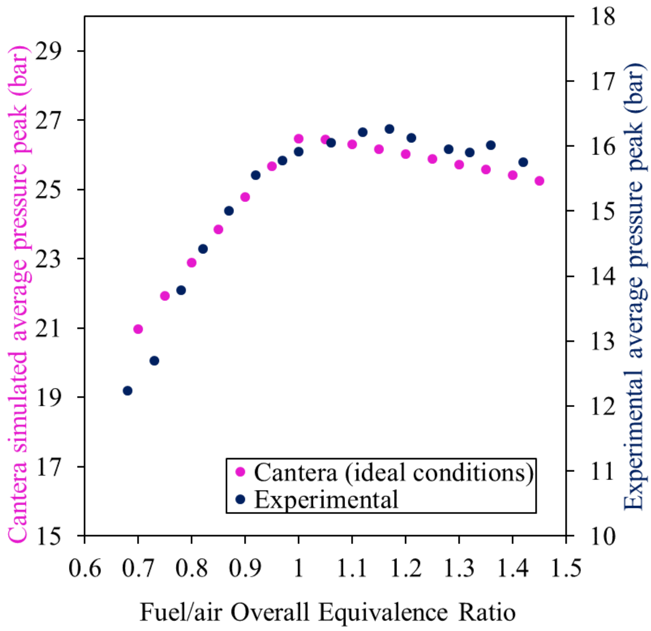

Figure 4-12 Variation of peak pressure with respect to OER for the experimental conditions and non-diluted conditions simulated on Cantera

From Figure 4-12, as expected the peak pressures predicted by Cantera are higher than those measured experimentally. This difference arises because the Cantera simulations assume idealized isochoric and adiabatic conditions (no thermal losses). The experimental pressure is also lower as expected due to the presence of residual burned gases in the secondary cycles, an effect that is not accounted for in the Cantera calculations.

Figure 4-12 also shows that the experimental pressure peaks slightly on the fuel-rich side, between OER = 1.0 and 1.1, where the mixture produces the largest useful pressure rise in the constant-volume chamber and thus the highest effective power output.

In the fuel-lean regime (OER < 1.0), the maximum pressure increases continuously and approximately linearly as OER moves from very lean values toward stoichiometry. This reflects the higher fuel mass fraction in the fresh gases and the corresponding increase in released chemical energy, while product temperatures remain relatively low and dissociation of triatomic species such as CO_2 and H_2O is limited[75].

4.3.1.2 *Effect of OER on cycle stability*

The second objective of this parametric study is to identify the range of equivalence ratios, among the 17 operating points spanning from 0.68 to 1.46, for which stable cyclic spark-ignition is achieved. To this end, an ignition success rate, η_{ign}, is defined based on the percentage of secondary cycles that successfully ignite within each sequence, excluding the first primary cycle and its preceding misfired cycle. Any misfired cycles occurring after the primary cycle are counted in the evaluation.

$$\eta_{\text{ign}} = \frac{N_{\text{ign}}}{N_{\text{total}}} \qquad \text{Equation 4-1}$$

Where N_{ign} is the number of ignited secondary cycles and N_{total} is the total number of cycles following the first primary cycle. The ignition success rate for the different operating points is illustrated in Figure 4-13.

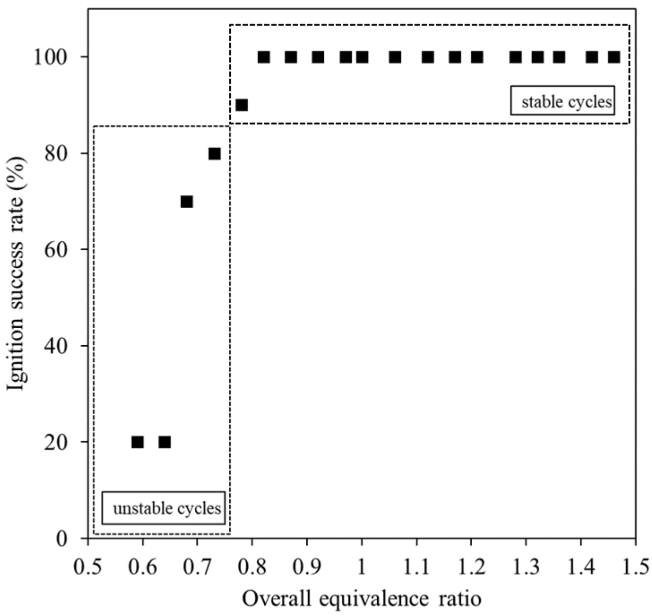

Figure 4-13 Effect of OER on spark-ignition success rate

For a success rate of ignited secondary cycles greater than 90%, the operating points yielding stable cyclic spark ignition are identified in the OER range of 0.78 to 1.46. However, the first criterion is a preference for an OER lesser or equal to stoichiometry. For simplicity, values rounded to one significant figure are preferred. 0.8 thus appears to be a suitable choice over 0.9, as it satisfies the lean condition. But, a second, more important criterion is the maximum combustion pressure.

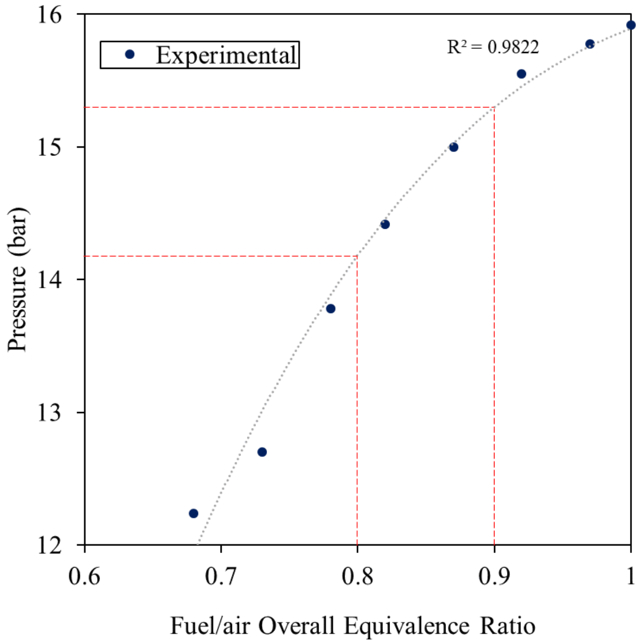

Figure 4-14 Variation of peak pressure with lean Fuel/air OER

Figure 4-14 shows that an OER of 0.9 generates more than 1 bar higher combustion pressure compared to an OER of 0.8. This is because a mixture of OER of 0.9 releases more energy. Similarly, a stoichiometric mixture provides higher combustion pressure, greater energy release when compared to the mixture at OER = 0.9.

As a result, the equivalence ratio defines two distinct operating points, OER = 0.9 and 1.0, in terms of combustion regime for achieving stable cyclic operation in the CV2 setup. The mixture with an OER targeted at 0.9, used in the reference case, therefore represents a good compromise between maintaining slightly fuel-lean operation and achieving a sufficiently high-pressure peak.

4.3.1.3 Effect of OER on combustion duration

The combustion duration is calculated for the OER having at least 80% ignition success rate (cf. Figure 4-13). Figure 4-15 presents the effect of OER on the combustion duration of those stable cycles.

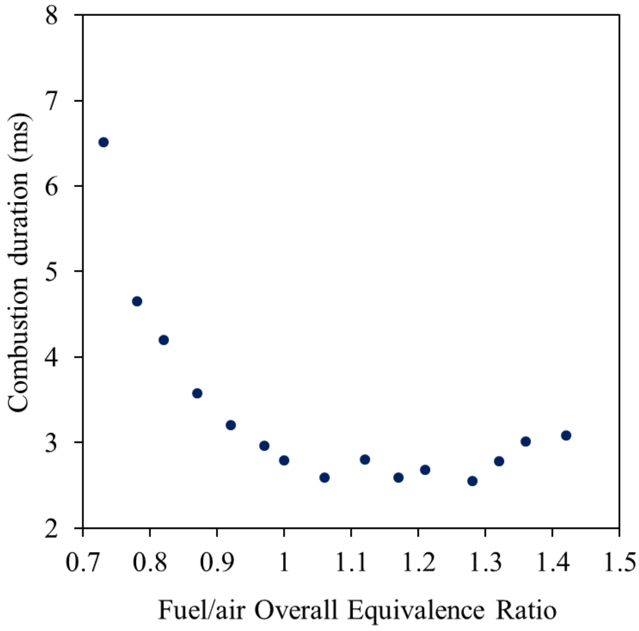

Figure 4-15 Effect of OER on combustion duration

As shown in Figure 4-15, combustion duration decreases sharply from OER ≈ 0.7 to OER ≈ 1, with a minimum for OER = 1.0 – 1.3, then increases again to OER = 1.5. In the CV2 configuration, the flame is turbulent. However, the turbulence characteristics remain unchanged when OER is varied. The observed evolution of combustion duration evolution is analogous to the inverse of the fundamental laminar flame speed of n-heptane, which peaks in the same equivalence ratio range as reported by Chong et al[76]. The turbulence seems to affect turbulence flame speed proportionally to the laminar flame speed. The combustion duration minimum stays where laminar flame speed reaches its maximum[76], indicating that OER primarily governs the mixture reactivity while turbulence provides a multiplicative factor to the laminar flame speed.

4.3.2 Influence of ignition timing on cyclic stability

Like spark-ignition piston engines, the spark-CV2 configuration requires an ignition device to initiate the flame at each cycle. Under partially premixed conditions, the igniter conventionally used in piston engines delivers an electrical discharge of approximately 30 to 100 mJ to the electrodes. In the operating mode considered here, the challenges of endurance and reliability are similar to those in piston engines. However, ignition systems used in gas turbines typically provide higher energies, on the order of 600 mJ[6], which leads to significant erosion of the spark plug electrodes.

For continuous operation of the CV2 chamber during one hour with operating frequency of 40 Hz, 144,000 ignitions are required from the ignition system[6]. A failed ignition would result in an instantaneous loss of power and generates unburnt fuel. This would modify the dilution and the filling of the next cycle, affecting the operating stability of the combustion chamber. To maintain high power density, cycles must be short and combustion sufficiently rapid (allowing the increase of operating frequency and consequently, power output). Therefore, ignition must occur as early as possible in the cycle but must occur successfully. The goal of this parametric study is to determine the minimum ignition timing that ensures stable combustion.

To this end, the ignition timing is varied from 10 ms to 25 ms, while all other parameters of the reference case are kept constant. For each ignition timing, tests consisting of 20 cycles are conducted, with the number of tests adapted based on their relevance. The operating conditions and the number of tests performed for each ignition timing are summarized in Table 4-5.

Table 4-5 Operating conditions and number of tests for each ignition timing

No. of tests	**Targeted OER**	**tign (ms)**	**tex (ms)**	**dt ex (ms)**	**Pex (bar)**
1	0.9	**10**	55	45	2
3	0.9	**12.5**	55	45	2
5	0.9	**15**	55	45	2
5	0.9	**17.5**	55	45	2
5	0.9	**20**	55	45	2
5	0.9	**25**	55	45	2

A visual comparison of the pressure evolution of a representative secondary cycle for the different ignition timings, when achieved, is presented in Figure 4-16. The ignition timing of 10 ms is not shown, as no secondary cycles are produced under this condition.

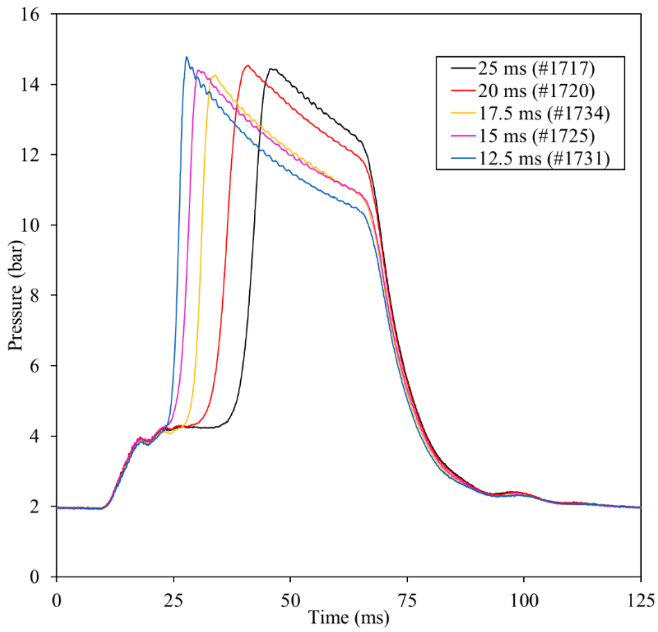

Figure 4-16 Pressure evolution of a secondary cycle for each ignition timing

The combustion duration for the different ignition timings calculated is summarized in Table 4-6.

Table 4-6 Combustion duration measured for each ignition timing

Test No.	tign (ms)	$t_{comb,10\%\text{-}90\%}$ (ms)
#1731	12.5	$1.93 \pm 0.38_{19.7\%}$
#1725	15	$3.38 \pm 0.99_{29.3\%}$
#1734	17.5	$3.43 \pm 0.48_{14.0\%}$
#1720	20	$4.44 \pm 0.92_{20.7\%}$
#1717	25	$4.82 \pm 0.49_{10.1\%}$

As shown in Figure 4-16, ignition timing has little influence on the peak pressure. In addition, Table 4-6 indicates that peak pressure is nearly independent of combustion duration, even though combustion duration becomes shorter with advanced ignition timing.

The main objective of this study is to evaluate ignition reliability in initiating combustion. In this context, particular attention is given to the occurrence of misfired cycles. The occurrence of misfired cycles was evaluated for each operating condition. The probability of misfiring is evaluated using two complementary criteria: one applied to the entire sequence of cycles and another focused specifically on the secondary cycles.

When considering the full sequence, misfires are counted from the start of the sequence. In this case, primary cycles are systematically considered as successful ignitions and are included in the total number of cycles.

Therefore, for a full sequence, the misfiring probability, $P_{\text{misfire,all}}$, is defined as:

$$P_{\text{misfire,all}} = \frac{N_{\text{misfire,all}}}{N_{\text{cycles}}} \qquad \text{Equation 4-2}$$

Where $N_{\text{misfire,all}}$ is the number of misfired cycles counted from the beginning of the sequence and N_{cycles} is the total number of cycles. Primary cycles are considered as successful ignitions and are included in the total cycle count. This implies that a primary cycle followed by a misfire results in a 50% misfire rate for the full sequence analysis. Therefore, the misfire rate for secondary cycles only is defined next.

For the analysis restricted to secondary cycles, a different criterion is applied. Any misfire occurring before the first primary cycle is not considered in the evaluation of the misfiring probability. In addition, primary cycles are excluded from both the total cycle count and the misfire count. Only misfires occurring after the first primary cycle are considered.

Therefore, for the secondary cycles, the misfiring probability, $P_{\text{misfire,sec}}$, is defined as,

$$P_{\text{misfire,sec}} = \frac{N_{\text{misfire,sec}}}{N_{\text{sec}}} \qquad \text{Equation 4-3}$$

Where $N_{\text{misfire,sec}}$ is the number of misfired cycles occurring after the first primary cycle and N_{sec} is the total number of secondary cycles considered. Misfires occurring before the first primary cycle (cycle 2) are excluded from this evaluation and primary cycles are not included in either $N_{\text{misfire,sec}}$ or N_{sec}.

An example illustrating the application of these criteria to the sequence shown above is provided below in Figure 4-17.

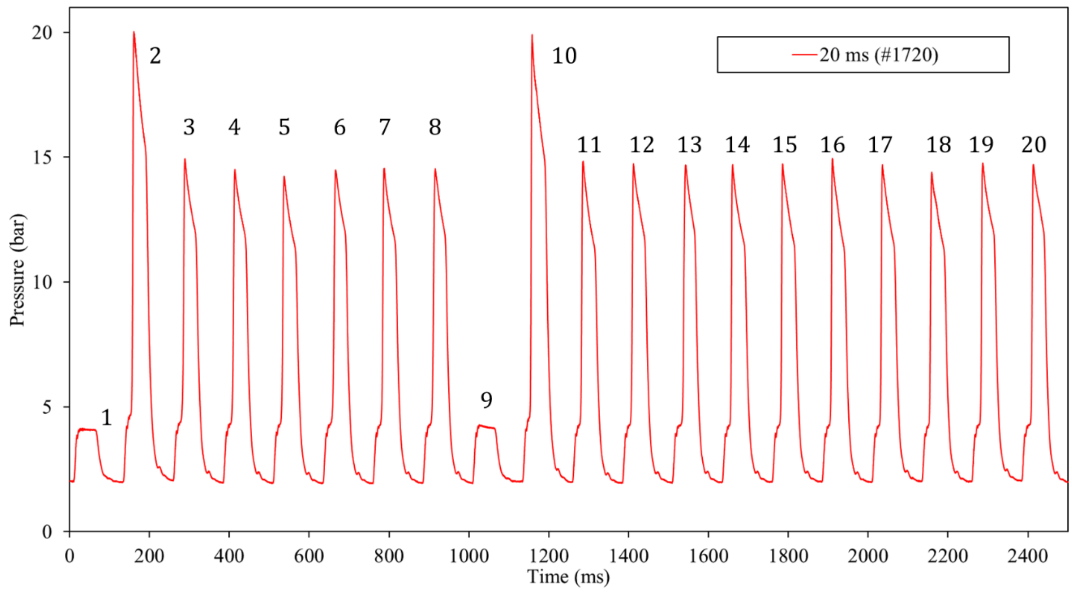

Figure 4-17 Example of a sequence of 20 cycles for evaluation of misfiring probability

The evaluation of the binary matrix corresponding to the sequence example in Figure 4-17 is tabulated in Table 4-7. In the table, a value of 1 indicates a misfired cycle, 0 represents a successfully ignited cycle and "/" denotes cycles that are not counted.

Table 4-7 Example of binary matrix associated with the sequence of Figure 4-17 used for calculating the misfiring probabilities of the whole sequence (denoted as All) and the secondary cycles (denoted as Sec)

Cycle No.	1	2	3	4	5	6	7	8	9	10	11	12	13	14	15	16	17	18	19	20	Tot.	Prob (%)
All	1	0	0	0	0	0	0	0	1	0	0	0	0	0	0	0	0	0	0	0	2	10
Sec	/	/	0	0	0	0	0	0	1	/	0	0	0	0	0	0	0	0	0	0	1	5.9

Figure 4-18 shows the results obtained using the methodology described above, computed across all tests and sequences for the different ignition timing.

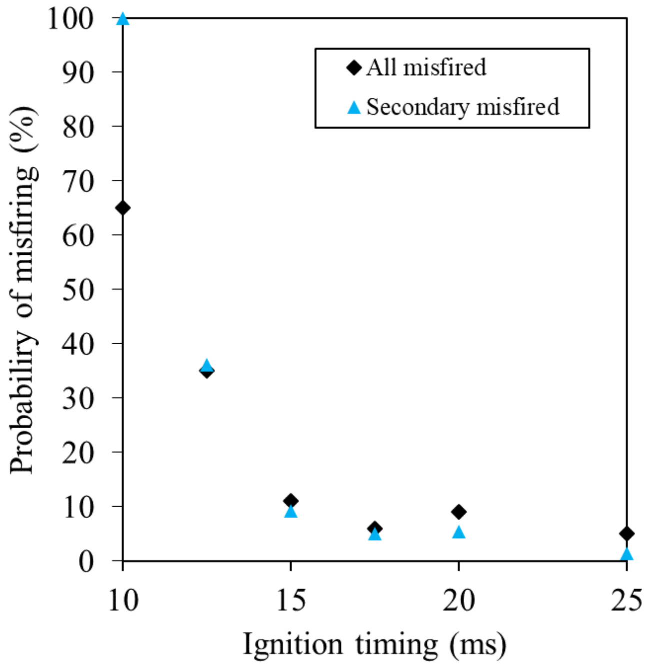

Figure 4-18 Probability of misfiring (whole sequence and secondary cycles) with respect to ignition timing

These results are compared with the mean velocity and turbulence levels at the different ignition timing, derived from the PIV measurements presented in Figure 4-9, in order to assess their influence on combustion stability. The corresponding data are summarized in Table 4-8.

Table 4-8 Spatially-averaged velocity and turbulent fluctuation for each ignition timing (averaged over 11 cycles)

Time (ms)	Mean Velocity (m/s)	Mean turbulent fluctuations (m/s)	Mean turbulence intensity
10	5.72	3.12	0.55
12.5	44.84	9.29	0.21
15	34.84	8.50	0.24
17.5	26.99	7.46	0.28
20	14.86	4.73	0.32
25	11.40	3.11	0.27

At an ignition timing of 10 ms, both the mean velocity and turbulence intensity are relatively low, however, the n-heptane–air mixture does not have sufficient time to mix adequately at the spark-plug position before ignition. As a result, a high misfire rate is observed. While sole primary cycles are obtained ($P_{\text{misfire,all}} = 65\%$), no secondary cycles are successfully ignited $P_{\text{misfire,sec}} = 100\%$).

At 12.5 ms, the mean velocity and turbulence reach their maximum values, corresponding to the intake phase of air and fuel. Although partial premixing has occurred, the high aerodynamic activity leads to unfavorable local conditions at the spark location, resulting in a misfire probability of approximately 35%.

For ignition timings between 15 ms and 20 ms, the misfire probability decreases significantly. This trend indicates that the additional time available for global mixture preparation and flow development, promoting more reliable ignition across the chamber.

At an ignition timing of 25 ms, both the mean velocity and turbulence have decayed substantially. Under these conditions, the overall misfire probability ($P_{\mathrm{misfire,all}}$) is reduced to only a few percent and secondary misfires are nearly eliminated. This behavior suggests that, for most cycles, the local equivalence ratio, dilution level and flow velocity are within the range required for reliable flame kernel formation and propagation.

From this parametric study, it is confirmed that an ignition timing of 25 ms, used for the reference case, represents an optimal condition for secondary cycles. Ignition timings greater than 25 ms may also be suitable, as they minimize misfires while maintaining sufficiently advanced ignition and ensuring adequate fuel–air mixing, together with favorable local thermochemical and aerodynamic conditions for stable combustion.

4.3.3 Effect of exhaust pressure on residual burnt gas dilution for a spark-ignited cycle

The presence of a turbine downstream of the chamber restricts flow at the chamber outlet, which can lead to an increase in the average static pressure upstream of the turbine's high-pressure distributor. This section presents results from a parametric study varying the exhaust pressure from 1 bar to 2 bar, while keeping the initial filling pressure constant at 4.3 bar and the targeted overall equivalence ratio fixed near stoichiometry. The ignition timing is set to 30 ms. Figure 4-19 shows the superposed pressure evolution of representative secondary cycles obtained for exhaust pressures of 1 bar, 1.5 bar and 2 bar along with their respective measured wall heat flux.

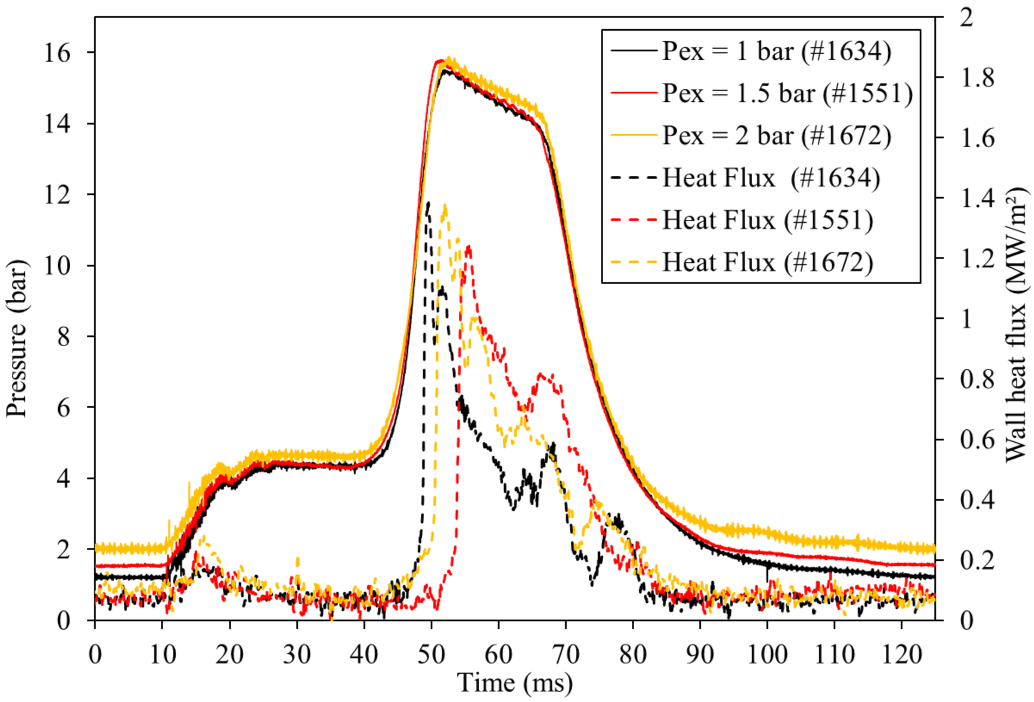

Figure 4-19. Evolution of the pressure signals as a function of the exhaust pressure (1 to 2 bar) at stoichiometry along with their respective wall heat flux

The increase in exhaust pressure shows no noticeable effect on the pressure signals (Figure 4-19). In the heat flux signals, an increase in heat flux is observed during the intake phase (from 10 ms). This rise is associated with the opening of the rapid air intake valve, where the incoming air is preheated and maintained at 150 °C while the combustion chamber temperature is preheated and controlled at 130 °C using a PID regulation system. Key parameters such as initial and peak pressure, combustion duration, wall heat flux, dilution and overall equivalence ratio are compared across cycles (Table 4-9).

Table 4-9. Overall mean and standard deviation of key parameters over the sequences for 18 cycles

Exhaust Pressure	Pex = 1 bar	Pex =1.5 bar	Pex = 2 bar
From experiments:			
OER	0.95 ± 0.06	1.01 ± 0.06	1.08 ± 0.08
Initial pressure (bar)	4.34 ± 0.04	4.37 ± 0.05	4.59 ± 0.07
Maximum pressure (bar)	16.18 ± 0.30	16.07 ± 0.34	16.32 ± 0.19
Pressure ratio	3.73 ± 0.09	3.68 ± 0.09	3.56 ± 0.06
$t_{comb,10\%-90\%}$ (ms)	4.10 ± 0.21	4.75 ± 0.12	4.67 ± 0.08
Maximum wall heat flux (MW/m^2)	1.79 ± 0.41	1.8 ± 0.45	1.52 ± 0.25
From simulations:			
Dilution (%)	22.8 ± 0.4	23.6 ± 0.4	23.8 ± 0.6

The OER is slightly fuel-richer at Pex = 2 bar compared to Pex = 1 bar. This occurs because the initial air intake pressure is kept constant at 4.3 bar. To maintain this pressure, the intake air duration is adjusted slightly. The air intake duration is thus longer when the exhaust pressure is 1 bar than when it is 2 bar, which results in a leaner mixture at 1 bar and a relatively richer mixture at 2 bar. Since the main interest concerns the residual burnt gas dilution, the absolute and relative dispersion value of dilution and combustion duration are tabulated in a second table.

Table 4-10. Absolute versus relative dispersion value for combustion duration and dilution

Exhaust Pressure	1 bar	1.5 bar	2 bar
$t_{comb,10\%-90\%}$: rms/avg (%)	5.12	2.53	1.71
$t_{comb,10\%-90\%}$: difference wrt 2 bar (%)	-12.2	+1.7	0
Dilution: rms/avg (%)	1.75	1.69	2.52
Dilution: difference wrt 2 bar (%)	-4.2	-0.8	0

For a backpressure of Pex = 1 bar, the average dilution was 22.8 ± 0.4%. Increasing the backpressure to 1.5 bar raised the dilution slightly to 23.6± 0.4%, while at 2 bar it was 23.8 ± 0.6%. These variations are minor (relative dilution dispersion less than 5% compared to the reference backpressure of Pex = 2 bar), indicating that the fraction of residual gas in the chamber is largely unaffected by reasonable changes in exhaust pressure, mainly because the initial air intake pressure is controlled. Also, the expansion to lower pressure induces a lower temperature of residual burned gas keeping the density of residual burned gas very little affected.

It can therefore be concluded that, over the range investigated, the residual burnt-gas dilution is weakly dependent on the exhaust backpressure. As a result, a reasonable and arbitrary exhaust backpressure can be selected for spark-ignited mode without significantly affecting the cycle behavior.

4.3.4 Effect of cycle optimization on total energy losses

The objective of this parametric study is to evaluate the ability to increase the power delivery by optimizing the cooling phase and exhaust duration. As a result, the operating frequency is increased. Increasing the operating frequency shortens the time available for heat losses and scavenging, which may influence residual burnt gas accumulation and cycle stability.

Three cycle types are investigated: the reference cycle at 8 Hz, a reduced-cooling cycle (*optimcool*) at 10 Hz and a reduced-exhaust cycle (*optimexhaust*) at 12.5 Hz. The *optimcool* configuration is obtained by advancing the exhaust valve opening in order to reduce the duration of the cooling phase while maintaining the same exhaust duration as in the reference case. This modification allows the cycle frequency to be increased to 10 Hz. In contrast, the *optimexhaust* configuration is derived from the *optimcool* cycle. It maintains the same exhaust valve opening timing but reduces the exhaust duration, thereby optimizing the exhaust phase. This modification allows the cycle frequency to be increased to 12.5 Hz.

For each condition, the operating parameters are applied over 20 cycles, as summarized in Table 4-11. The corresponding pressure evolution for the different operating parameters is presented in Figure 4-20.

Table 4-11. Operating parameters for the different cycle frequencies

Test No.	dt air (ms)	dt fuel (ms)	tign (ms)	tex (ms)	dt ex (ms)	Pex (bar)	Frequency (Hz)
#1576	11	5	25	**55**	**45**	2	**8**
#1577	11	5	25	**30**	**45**	2	**10**
#1578	11	5	25	**30**	**30**	2	**12.5**

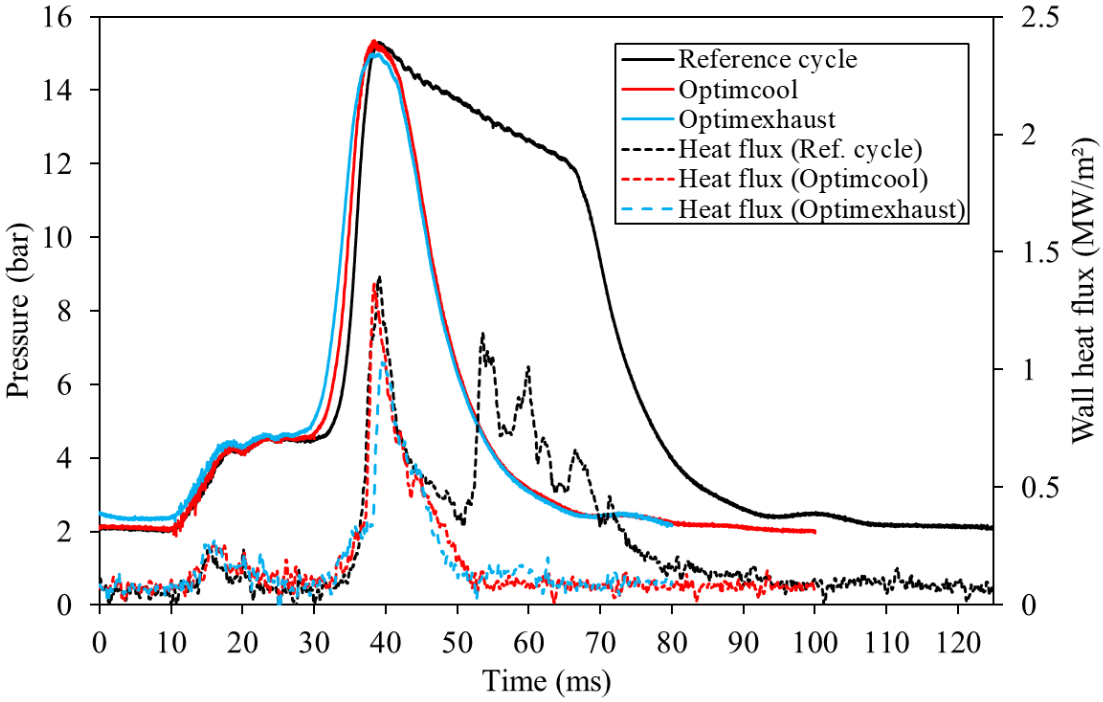

Figure 4-20 Pressure and wall heat flux of the different cycles: reference, optimcool and optimexhaust

For each cycle type, the main thermodynamic and combustion parameters are evaluated over 20 consecutive cycles and averaged to ensure statistical convergence. Table 4-12 summarizes the resulting operating conditions and global cycle characteristics for the three cycle types.

Table 4-12. Overall mean and standard deviation of key parameters for the different cycle frequencies over the sequences for 18 cycles

Cycle type	Reference	Optimcool	Optimexhaust
From experiments			
OER	0.95 ± 0.06	0.93 ± 0.06	0.94 ± 0.05
Initial pressure (bar)	4.49 ± 0.05	4.37 ± 0.05	4.40 ± 0.06
Maximum pressure (bar)	15.51 ± 0.25	15.24 ± 0.35	15.53 ± 0.36
Pressure ratio	3.46 ± 0.06	3.49 ± 0.10	3.46 ± 0.10
$t_{comb,10\%-90\%}$ (ms)	3.79 ±1.17	3.58 ± 0.57	3.47 ± 0.69
Maximum dP/dt (bar/ms)	3.51 ± 0.66	3.45 ± 0.56	3.64 ± 0.84
Maximum wall heat flux (MW/m²)	1.53 ± 0.16	1.62 ± 0.32	1.72 ± 0.40
From simulation			
Dilution (%)	21.9 ± 0.6	21.0 ± 0.4	22.4 ± 0.5
Energy Loss (% of Combustion Energy)	70.5 ± 1.1	57.4 ± 1.4	54.4 ± 1.2

The results show that the global combustion characteristics remain comparable across the three types of spark-ignited cycles. The equivalence ratio, initial pressure, maximum pressure and pressure ratio exhibit only limited variations, indicating that the combustion process remains stable despite the reduction in cycle duration. Similarly, the combustion duration and maximum pressure rise rate are only weakly affected by frequency, suggesting that flame development is not significantly altered within the investigated range.

In contrast, thermal indicators such as the maximum wall heat flux and maximum temperature increase with cycle frequency. At the same time, the total energy loss predicted by the 0D/1D model decreases as the frequency increases, reaching its lowest value at 12.5 Hz, for the *optimexhaust* cycle. The energy loss per cycle is highest at 8 Hz (70.5 ± 1.1 %), lower at 10 Hz (57.3 ± 1.4 %) and lowest at 12.5 Hz (54.3 ± 1.2 %), indicating that the *optimexhaust* cycle reduces energy losses by approximately 16% per cycle. To better understand the origin of these differences, the total energy loss is further decomposed into contributions associated with the different phases of the cycle.

The distinct phases of the spark-ignition cycle, as described in Section 3.5.5.2, are analyzed in detail (Table 4-13) and the corresponding heat losses associated with each phase are evaluated using the 0D/1D model. Intake heat losses are denoted as phase A, phase B accounts for losses related to combustion and unburnt mass, phase C corresponds to heat losses during the isochoric cooling phase and phase D represents exhaust heat losses.

In Figure 4-20, for both *optimcool* and *optimexhaust* cycles, the cooling phase is fully optimized. Under these operating conditions, the isochoric cooling phase is no longer present. Hence, the energy losses associated with phase C become negligible.

Table 4-13. Contribution of energy losses (% combustion energy) for the different phases of the different types of spark-ignited cycle

Phase	A (%)	B (%)	C (%)	D (%)	Total (%)
Ref. cycle	0.6	41.4	19.1	9.3	70.4
Optimcool	0.9	41.4	-	15.1	57.4
Optimexhaust	1.4	37.4	-	15.6	54.4

Table 4-13 presents the distribution of total energy losses among the different phases of the three types of spark-ignition cycle. For the reference cycle, energy losses are distributed over all four phases, with phase B (combustion and unburnt mass losses) being dominant, accounting for nearly 41.4% of the total losses. A significant energy loss (19.1%) is also associated with phase C, corresponding to the isochoric cooling phase, highlighting the non-optimized nature of the cooling process at this type of cycle.

For the *optimcool* and *optimexhaust* cycles, the contribution of phase C disappears, confirming that the cooling phase is fully optimized under these operating conditions. Consequently, the energy losses are mainly associated to phases B and D. Phase B remains the primary source of energy loss, although its relative contribution decreases to 37.4% for the *optimexhaust* cycle. This behavior reflects changes in combustion dynamics and heat transfer resulting from the reduced exhaust duration. The shorter exhaust period limits the time available for the gases to cool before the subsequent cycle.

The contribution of exhaust losses (phase D) increases from 9.3% for the reference cycle to 15.1% and 15.6% for the *optimcool* and *optimexhaus*t cycle respectively. Intake-related losses (phase A) remain negligible for all cases, although a slight increase with frequency is observed.

Overall, the effect of increasing the cycle frequency effectively eliminates cooling-phase losses, leading to a significant reduction in total energy loss (13-16%). These results indicate that the *optimexhaust* cycle is more efficient and better optimized than the reference cycle.

4.4 Conclusion to this chapter

A reference stable cycle was analyzed in detail at 8 Hz (OER = 0.9, tign = 25 ms, Pex = 2 bar), highlighting the key phenomena governing spark-ignited pistonless constant volume combustion. Chemiluminescence measurements showed that the highest cycle-to-cycle variability occurs during the early stages of flame development, as indicated by the CH* signal. As combustion progresses, the process stabilizes, reaching maximum intensity with the OH* signal.

A parametric investigation was conducted to evaluate the influence of the main parameters controlling spark-ignition combustion stability: equivalence ratio, exhaust backpressure, cycle frequency and ignition timing. The study of the equivalence ratio revealed that operating in the range OER = 0.9–1 provides a favorable compromise, ensuring sufficiently high peak pressure while reducing combustion duration. When varying the exhaust backpressure, the initial intake pressure was maintained constant; consequently, the presence of approximately 23% residual burnt gases had only a minor influence on cycle behavior.

The cooling phase of the reference cycle was fully optimized by advancing the exhaust valve opening, allowing the operating frequency to increase to 10 Hz. This configuration was defined as the *optimcool* cycle. Further reduction of the exhaust duration led to the *optimexhaust* cycle, achieving a frequency of 12.5 Hz. A 0D/1D energy analysis demonstrated improved thermal performance at higher frequencies, confirming reduced losses and enhanced efficiency.

The distribution of heat losses across the different phases of the three spark-ignition cycles was also assessed. The combustion phase was identified as the dominant contributor, accounting for approximately 37.4% to 41.4% of total heat losses. 19.1% of the reference cooling cycle was fully optimized for the *optimcool* and *optimexhaust* configurations.

The parametric study of ignition timing showed that 25 ms, used in the reference case, represents an optimal condition for stable secondary cycles. Earlier ignition is strongly influenced by intake-driven turbulence, characterized by mean velocities of approximately 10 m/s and turbulence fluctuation of about 5 m/s, as revealed by PIV analysis. The PIV results further indicate that during combustion, turbulence decays due to increased gas viscosity and thermal expansion. As a result, the flame propagates in a relatively low-velocity flow field with limited aerodynamic interaction.

Overall, the complexity of interacting phenomena makes stable, high-performance operation difficult to achieve. In spark-ignited conditions, combustion initiation strongly depends on the local flow velocity and turbulence level at the moment of ignition, which increases cycle sensitivity. To reduce this dependency and improve robustness, Chapter 5 examines pistonless CVC operation under self-ignition conditions, with the motivation to eliminate the systematic reliance on spark timing.

Chapter 5: Liquid self-ignited cyclic CVC

5.1 Introduction

Spark-plug ignition systems, studied in Chapter 4, present inherent limitations, particularly in terms of durability and lifetime. While automotive igniters are designed for moderate energy deposition (a few tens of mJ per pulse) and can generate hundreds of millions of sparks at frequencies up to 50–60 Hz using high-voltage technology, ignition systems used in gas turbine engines deliver higher energy (up to hundreds of mJ per spark) using high-current technology to ensure reliable discharge under harsh conditions and to comply with electromagnetic compatibility and radiation constraints. In aero-engine applications, these igniters are operated intermittently, primarily during engine start-up and in-flight relight (e.g., adverse weather or high-altitude conditions), rather than in continuous operation, with repetition rates on the order of a few hertz and lifetimes of millions of sparks. All these limitations motivate the exploration of alternative ignition strategies that reduce or eliminate the reliance on spark-plug systems.

The present chapter investigates a multi-chamber combustion concept (see Figure 5-1) intended to deliver sufficient power for practical applications. Within this framework, spark-ignition is still employed, but only to initiate combustion in the first chamber and to establish the initial thermodynamic conditions. Subsequent ignition in the next chambers is then triggered by the transfer of hot burned gases from its N-1 chamber, rather than by a local ignition device. This process is repeated from one chamber to the next one. This operating mode can be referred to as *self-ignition*, in contrast to conventional *spark-ignition*.

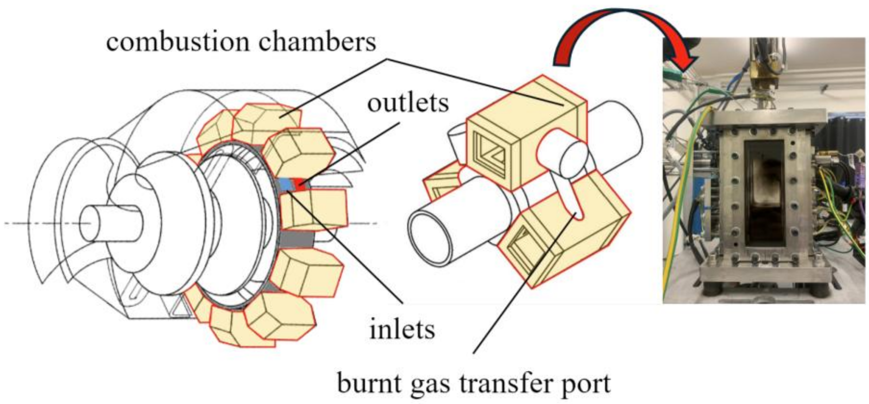

Figure 5-1 Integration of the CV2 chamber into a multi-chamber combustion configuration [6], [39], [77]

In the CV2 set-up, the implementation of self-ignition will be achieved using a single combustion chamber. Although the CV2 configuration involves only one chamber, it is designed to reproduce the thermodynamic conditions, encountered during burned-gas transfer in a multi-chamber system [36], [39], [40]. Self-ignition can be achieved in the CV2 configuration by delaying the ignition timing and by increasing the exhaust pressure or a combination of both as described in the next section.

5.2 Generation of self-ignition events through delayed spark ignition timing

In this section, a first set of 15 tests is carried out, with an air intake valve opening duration of 11 ms (starting at time 11.6 ms) and fuel injection duration of 6 ms (starting at time 10.3 ms), corresponding to a targeted OER at stoichiometry. The cycle frequency is kept at 8 Hz, hence a period of 125 ms, and each sequence contains 20 cycles. The exhaust valve opening time is set to 55 ms and the exhaust valve duration to 45 ms with the exhaust pressure of 1 bar. Ignition timings are delayed from 30 ms to 100 ms to observe the influence of delayed ignition timing on generating self-ignition cycles and the stability of these cycles. The operating conditions are summarized in Table 5-1.

Table 5-1 Operating conditions used for generating self-ignition through delayed spark ignition timing

Targeted OER	tign (ms)	tex (ms)	dt ex (ms)	Pex (bar)	Cycle freq. (Hz)	Cycle period (ms)
1	30 - 100	55	45	1	8	125

The temporal pressure evolution for 8 different ignition times (t_{ign}) is shown in Figure 5-2.

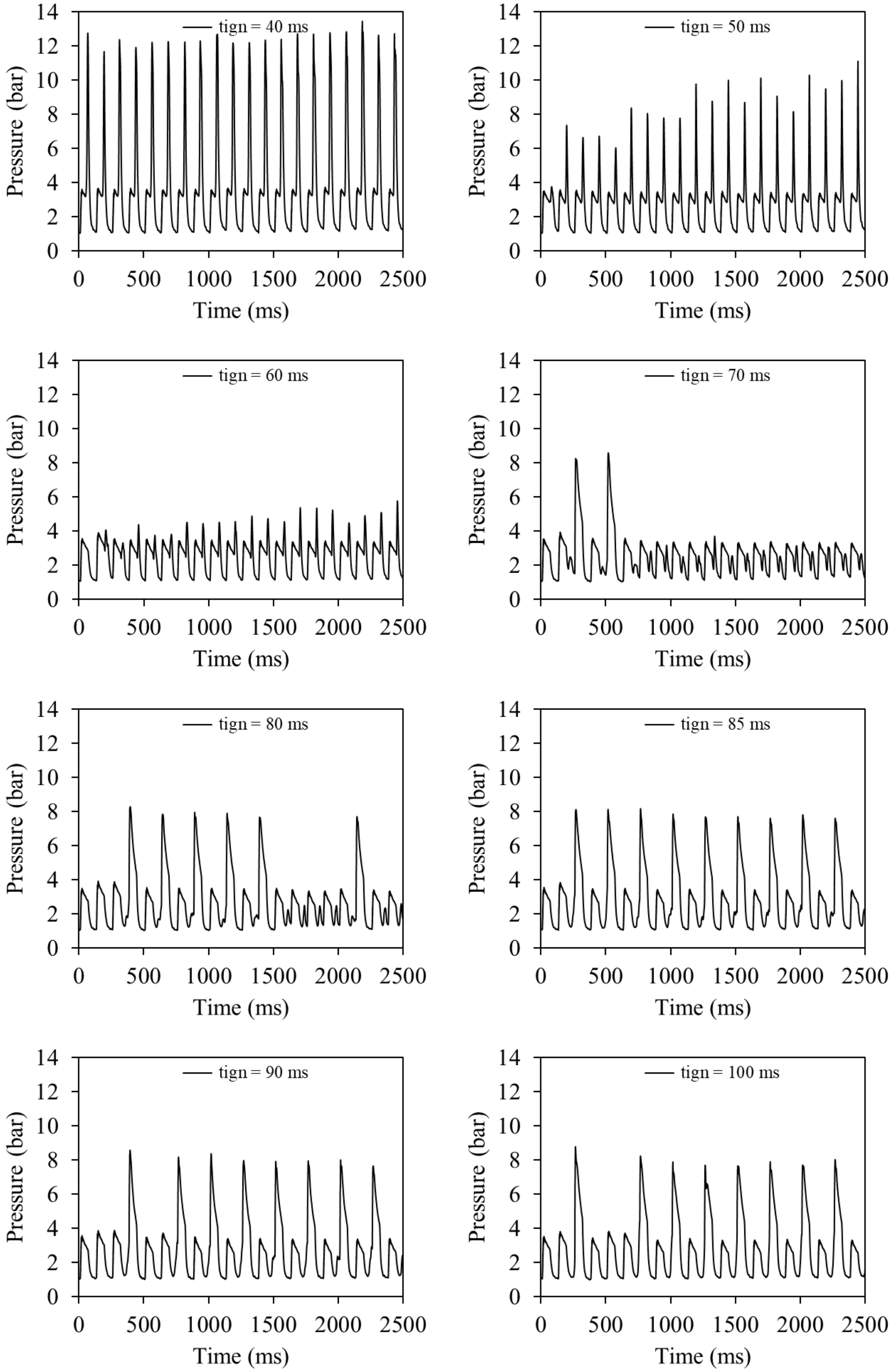

Figure 5-2 Influence of delayed ignition timing in the generation of self-ignited cycles

Delaying the ignition timing strongly affects cycle stability (see Figure 5-2). At a t_{ign} of 40 ms, stable and repeatable spark-ignition cycles are obtained, indicating optimal combustion behavior with high pressure ratio and little to no cycle hysteresis. Under these conditions (see Figure 5-3(i)), no cooling phase at constant volume is observed (between combustion phase and exhaust phase), showing the optimal CVC case for these spark-ignited operating conditions. Moreover, 100% of the cycles are spark-ignited for this ignition timing and repetitive stable cycles are observed.

With ignition timing further delayed at 50 ms, all cycles are still spark-ignited cycle; however, the cycles properties such as the peak pressure are less repeatable. When t_{ign} is increased to 60 ms, the peak pressure is barely noticeable. The combustion process occurs mainly during the exhaust phase and the combustion pressure ratio reaches its minimum, concluding that combustion occurs at constant pressure and not at constant volume.

For t_{ign} = 70 ms, a few self-ignition events are observed. From a t_{ign} of 80 ms, reproducible patterns of self-ignition are observed (one cycle every two cycles). At t_{ign} = 85 ms, the highest number of self-ignition events is observed. Further increasing t_{ign} to 90 ms and 100 ms still yields self-ignition events, but cycles lack repeatability.

Ignition timing affects the thermal state of the residual gases. A later spark shifts combustion in the exhaust phase, reducing the time available for expansion and wall heat losses, which results in higher residual gas temperatures at the end of the cycle. These hotter residual gases are retained in the chamber and provide thermal preconditioning for the following cycle, thereby increasing the likelihood of self-ignition of the next cycle.

A zoomed-in analysis with a clear breakdown of each phase for each cycle type, spark-ignition and self-ignition, is shown in Figure 5-3 and Figure 5-4.

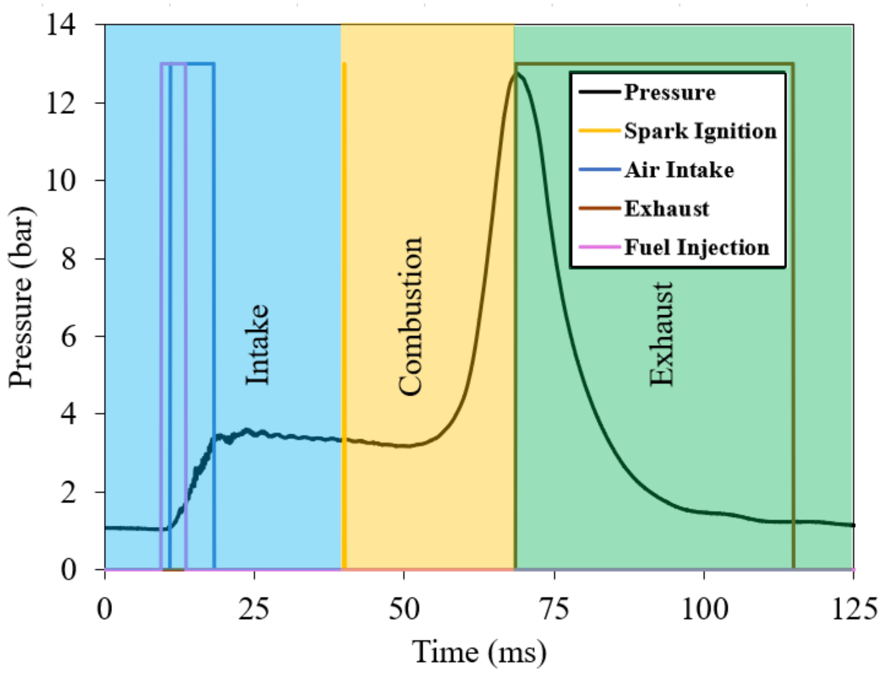

Figure 5-3 The different phases in a spark-ignition cycle (t_{ign} = 40 ms)

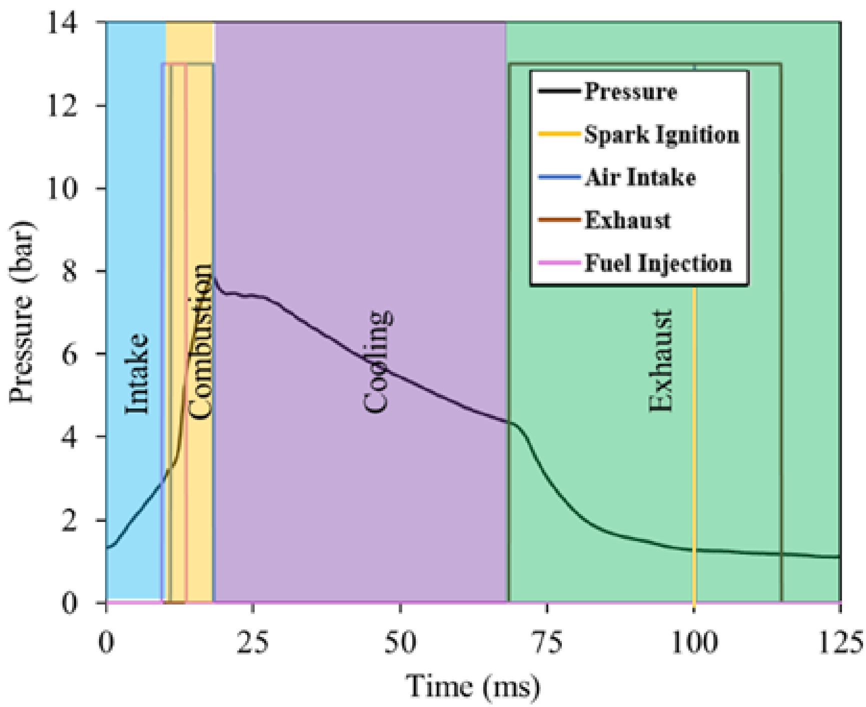

Figure 5-4 The different phases in a self-ignition cycle (t_{ign} = 100 ms)

In a spark-ignited cycle (Figure 5-3), air and fuel are mixed during the intake phase. Spark-ignition initiates the constant-volume combustion, which is then followed by the exhaust phase. The exhaust timing was optimized to minimize any isochoric cooling phase. In contrast, in a self-ignited cycle (Figure 5-4), combustion occurs within the intake phase, with a shorter duration, followed by cooling and exhaust phase prior to the spark timing.

5.2.1 Statistical analysis of self-ignition sequence

A statistical analysis of self-ignition sequence success (RIS) is performed varying the ignition delay for exhaust pressure at 1 bar, 1.5 bar and 2 bar. A RIS is defined as sequences where every alternate cycle re-ignites, excluding any initial misfires. A RIS probability p_{RIS} can then be calculated:

$$p_{RIS} = \frac{2R}{R+S} \qquad \text{Equation 5-1}$$

Where R = number of self-ignited cycles and S = number of spark-ignited cycles.

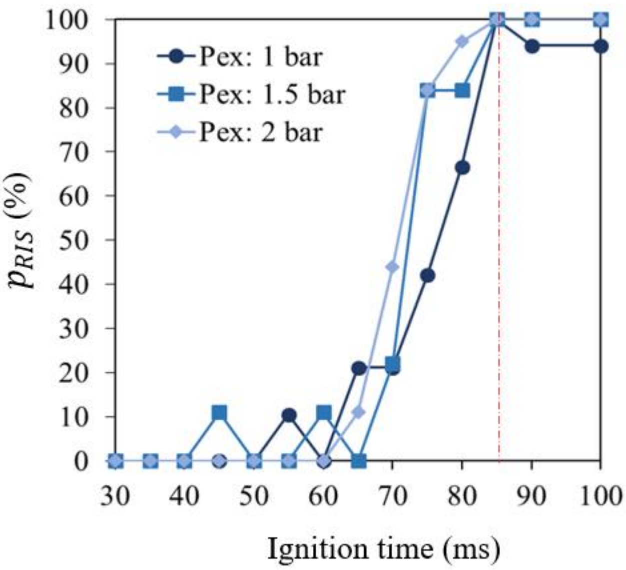

Figure 5-5 Self-ignition probability obtained for different delayed ignition timings at different exhaust pressures

Figure 5-5 shows that a 100% RIS is achieved for an ignition timing of 85 ms across all tested exhaust pressures (denoted as Pex), establishing this ignition timing as the stable point for consistently attaining self-ignition. For a fixed ignition timing, increasing the exhaust pressure results in a higher p_{RIS}, confirming that a larger amount of residual burnt gases helps to promote self-ignition. This demonstrates that both ignition timing and exhaust pressure play a key role in defining the self-ignition operating range.

Based on these results, the reference self-ignition cycle is analyzed in detail. It is defined by an ignition timing of 85 ms and an exhaust pressure of 2 bar, conditions that ensure stable and repeatable self-ignition.

5.3 Presentation and analysis of a typical self-ignition sequence

5.3.1 Self-ignition sequence presentation

A reference case (Test 1579) is selected based on the stability and repeatability criteria. The operating conditions for this reference case are summarized in Table 5-2 and the resulting sequence obtained under these conditions is shown in Figure 5-6.

Table 5-2 Operating conditions for the reference cyclic self-ignition configuration (Test 1579)

dt air (ms)	dt fuel (ms)	tign (ms)	tex (ms)	dt ex (ms)	Pex (bar)	Cycle period (ms)
11	5	85	55	45	2	125

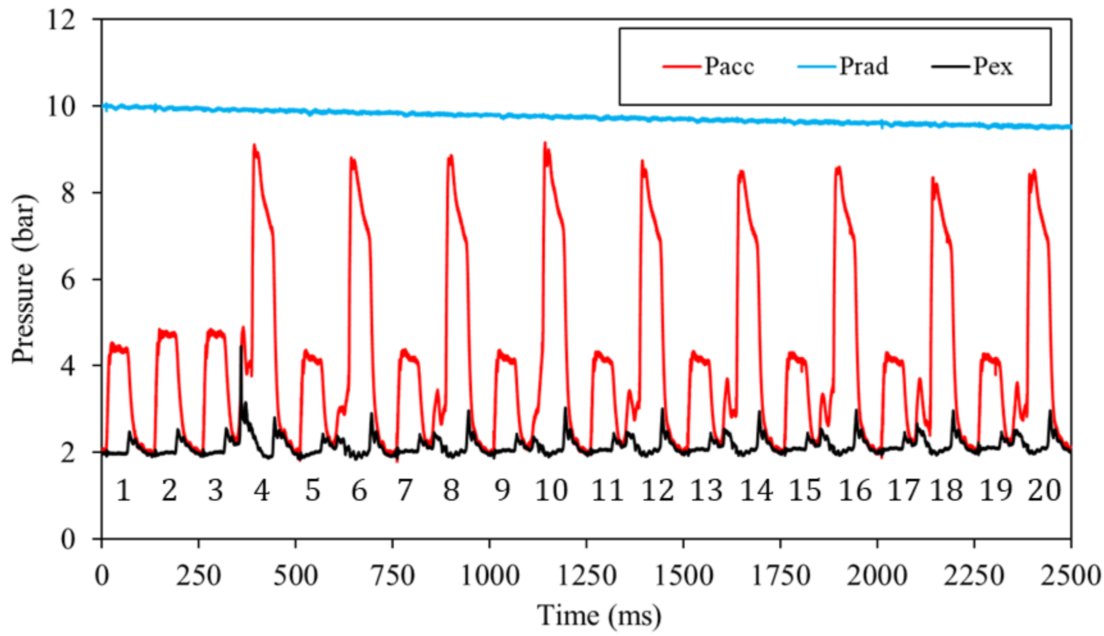

Figure 5-6 Experimental signals of the pressure in tanks and combustion chamber over a sequence of 20 cycles in the reference self-ignition configuration

The reference sequence consists of 20 cycles of which 9 cycles are self-ignited. In this configuration, the OER targeted is equal to 0.9.

Examination of the pressure signal over the 20 cycles within the sequence:
- Cycle 1 and cycle 2 differ from the remainder of the sequence: the initial valve opening is both slower and shorter, resulting in a reduced amount of air being injected into the chamber. As a result, the equivalence ratio during these cycles is modified and may fall outside the flammability limits, similar to the spark-ignition cycles described in the previous chapter. This likely explains why, despite the presence of a spark, combustion rarely occurs during the first cycle (just like in the spark-ignition reference case).

- From Cycle 3 onward, the sequence alternates between spark-assisted ignited cycles (Cycles 3, 5, 7… 19) and self-ignited cycles (Cycles 4, 6, 8… 20).

Each spark-assisted ignited cycle exhibits a delayed ignition timing and precedes a self-ignited cycle. Although combustion is initiated by the spark, this cycle plays a key role in triggering early combustion in the subsequent cycle. It generates the burned gases produced by a second chamber as in the multi-chamber configurations with a burned-gas transfer port (cf.Figure 5-1).

A self-ignited cycle systematically follows a spark-assisted ignited cycle with delayed ignition timing. Prior to the intake phase, the chamber contains burned gases or burning gases, primarily originating from combustion during the preceding spark-assisted ignited cycle. During the intake phase, the fresh gases are diluted by these hot residuals burned gas, leading to an abrupt self-ignition that occurs during this intake phase. Under these reference conditions, the RIS of this sequence is 100%, indicating a stable operating configuration.

The 0D/1D model introduced in Chapter 3.5 allows the simulation of the pressure signal and the determination of overall properties such as mean density inside the combustion chamber and average temperature inside the chamber during each cycle of a sequence (cf. Figure 5-7)

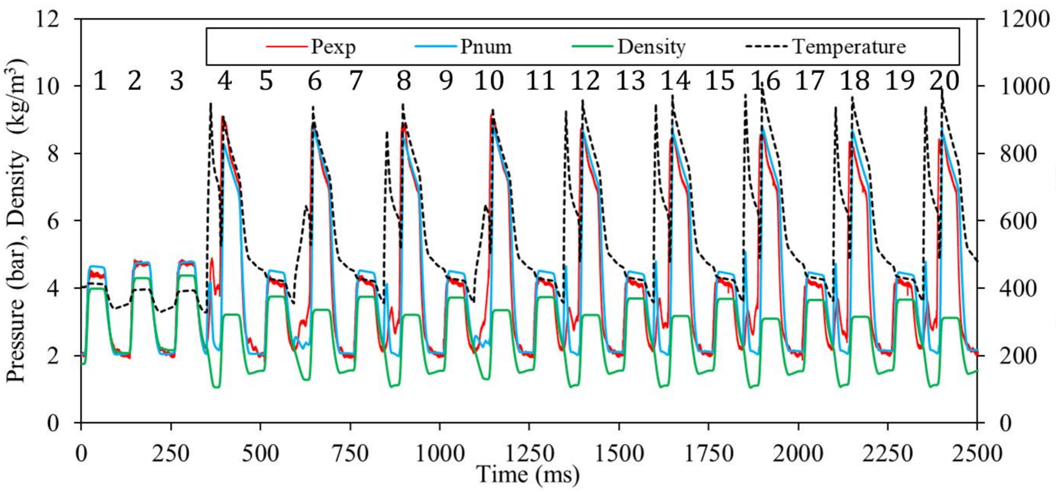

Figure 5-7 0D/1D pressure simulation of the reference self-ignition test and its associated density (0D) and temperature (0D).

5.3.2 Self-ignited cycle analysis

The reference self-ignition cycles are analyzed following the methodology described earlier. Pressure, chemiluminescence and PIV analyses are performed on the secondary cycles (even cycles in Figure 5-7) under the reference conditions. The pressure evolution of a self-ignition cycle and its corresponding intake and exhaust signals of the reference case are shown in Figure 5-8.

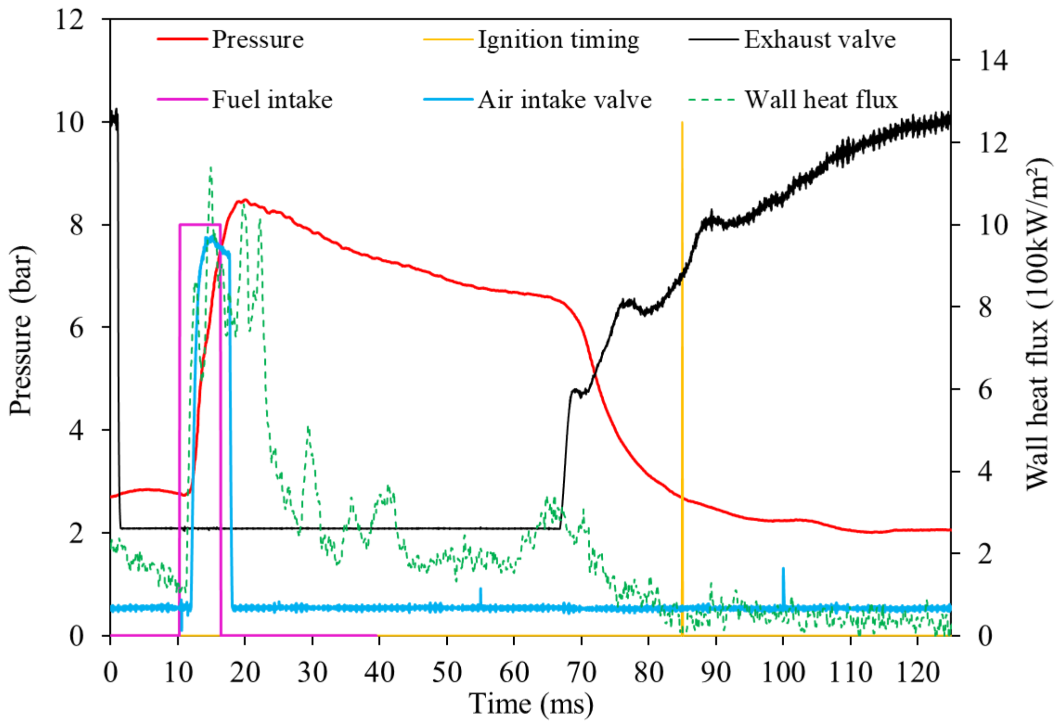

Figure 5-8 Presentation of a self-ignition cycle (reference case – cycle 10): combustion pressure and valve signals

Similar to the spark-ignited cycle, some parameters are directly relevant to specific parametric studies, while others provide a baseline for overall comparison. These results therefore establish a reference condition for the different parameters; their main value of the parameters lies in illustrating their influence on other parameters, as further explored in section 5.4 and 5.5.

5.3.2.1 Pressure analysis

The mean and standard deviation of key parameters obtained from the pressure analysis over the sequence of the 9 self-ignited cycles are summarized in Table 5-3. The RBG dilution computed for a self-ignited cycle is generated from the preceding spark-assisted ignited cycle, analogous to a multi-chamber configuration.

Table 5-3 Overall mean and standard deviation of key parameters over the sequence for 9 self-ignited cycles for the reference case

Parameters	
From experiments:	
OER	$1.23 \pm 0.02_{1.6\%}$
Initial pressure (bar)	$3.59 \pm 0.39_{10.9\%}$
Peak pressure (bar)	$8.74 \pm 0.26_{3.0\%}$
Pressure ratio	$2.25 \pm 0.20_{8.9\%}$
$t_{comb,0\%-100\%}$ (ms)	$6.40 \pm 0.47_{7.3\%}$
Maximum dP/dt (bar/ms)	$1.85 \pm 0.19_{10.3\%}$
Maximum wall heat flux (MW/m²)	$1.03 \pm 0.14_{13.6\%}$
From simulations:	
RBG Dilution (%) generated from preceding spark-assisted	$23.3 \pm 1.1_{4.7\%}$

The pressure analysis indicates that the mixture is rich with an overall equivalence ratio of 1.23 ± 0.02, despite an initial target value of 0.95. This deviation is attributed to combustion occurring during the intake phase, which leads to a rapid pressure rise that limits further air admission into the chamber. In addition, residual burnt gases dilution from the previous cycle is estimated at 23.3 ± 1.1%. They further enrich the mixture by reducing the amount of fresh air, while fuel injection is hardly influenced by chamber pressure and delivers the targeted fuel quantity. The low cycle-to-cycle variability (1.6%) of the equivalence ratio reflects good repeatability of the operating conditions, despite the altered air intake process.

The observed peak pressure of 8.74 ± 0.26 bar aligns with expectations for diluted operation. The reduced amount of fresh reactants (air) and the significant RBG dilution limit the achievable pressure level compared with cycles dominated by fresh mixture. The low standard deviation (~3.0%) indicates stable peak pressure across cycles.

Combustion duration, defined as the interval for 0–100% of energy release, is measured at 6.40 ± 0.47 ms and with a maximum pressure rise rate (dP/dt) of 1.85 ± 0.19 bar/ms. This confirms that the heat release is slower in the case of self-ignition (1.85 bar/ms), compared to spark-ignition (3.51 bar/ms) in comparable conditions. However, a 0-100% combustion duration internal of a spark-ignition cycle is longer than a self-ignition cycle (9.94 ±1.33) ms.

The maximum wall heat flux reaches 1.03 ± 0.14 MW/m^2, which is relatively low compared with spark-ignited cycles (1.53 ± 0.16 MW/m^2). This difference can be attributed to the pressure at which flame-wall interaction occurs. The maximum peak pressure is 15.5 ± 0.25 bar for the spark-ignited cycle and 8.74 ± 0.26 bar for the self-ignited cycle. In premixed combustion, wall heat flux is strongly dependent on pressure[78].

Overall, the reduced wall heat flux reflects a combustion regime dominated by dilution and slower heat release, which collectively mitigate thermal loading on the chamber walls while maintaining stable operation.

In summary, the self-ignited cycles obtained with the CV2 set-up operate under a highly diluted regime, characterized by a reduced peak pressure, a slower heat release and a lower wall heat flux compared to spark-ignited cycles. Combustion occurs partially during the intake phase, with a combined intake and combustion duration of ~ 18 ms, (compared to 25 ms in spark-ignited combustion), followed by a relatively longer cooling phase of ~ 47 ms and an exhaust phase lasting roughly 60 ms. The energy losses associated to these phases are further analyzed in section 5.5. Overall, the cycle exhibits stable behavior with low cycle-to-cycle variability when considering a coupled cycle pair, consisting of a spark-assisted cycle and its self-ignited cycle, providing a consistent reference for analyzing the influence of dilution, combustion phasing and thermal losses.

5.3.2.2 Chemiluminescence analysis of the self-ignited cycles

In the analysis of the self-ignited cycles, it is essential to consider each cycle together with its preceding spark-assisted cycle, since the ignition timing of the latter directly influences the amount of residual burnt gases and the thermodynamic state of the mixture. This coupling is critical for correctly interpreting self-ignition behavior.

Analysis of fast radical imaging

Figure 4-5 presents the raw OH* and CH* images obtained of a spark-assisted and its self-ignited cycle, illustrating the temporal evolution of the flame from ignition timing of spark-assisted cycle to exhaust valve opening of the self-ignited cycle. This cycle was selected as it is representative of the majority of secondary cycles in terms of both OH*-based and CH*-based pressure evolution. As the OH* and CH* measurements were performed separately, broadband color visualization was systematically carried out in parallel with each filtered chemiluminescence measurement. Although the pressure of OH* and CH* remains similar, combustion behavior might differ, thus this approach allows the overall differences between the two tests to be better identified and provide additional qualitative comparison.

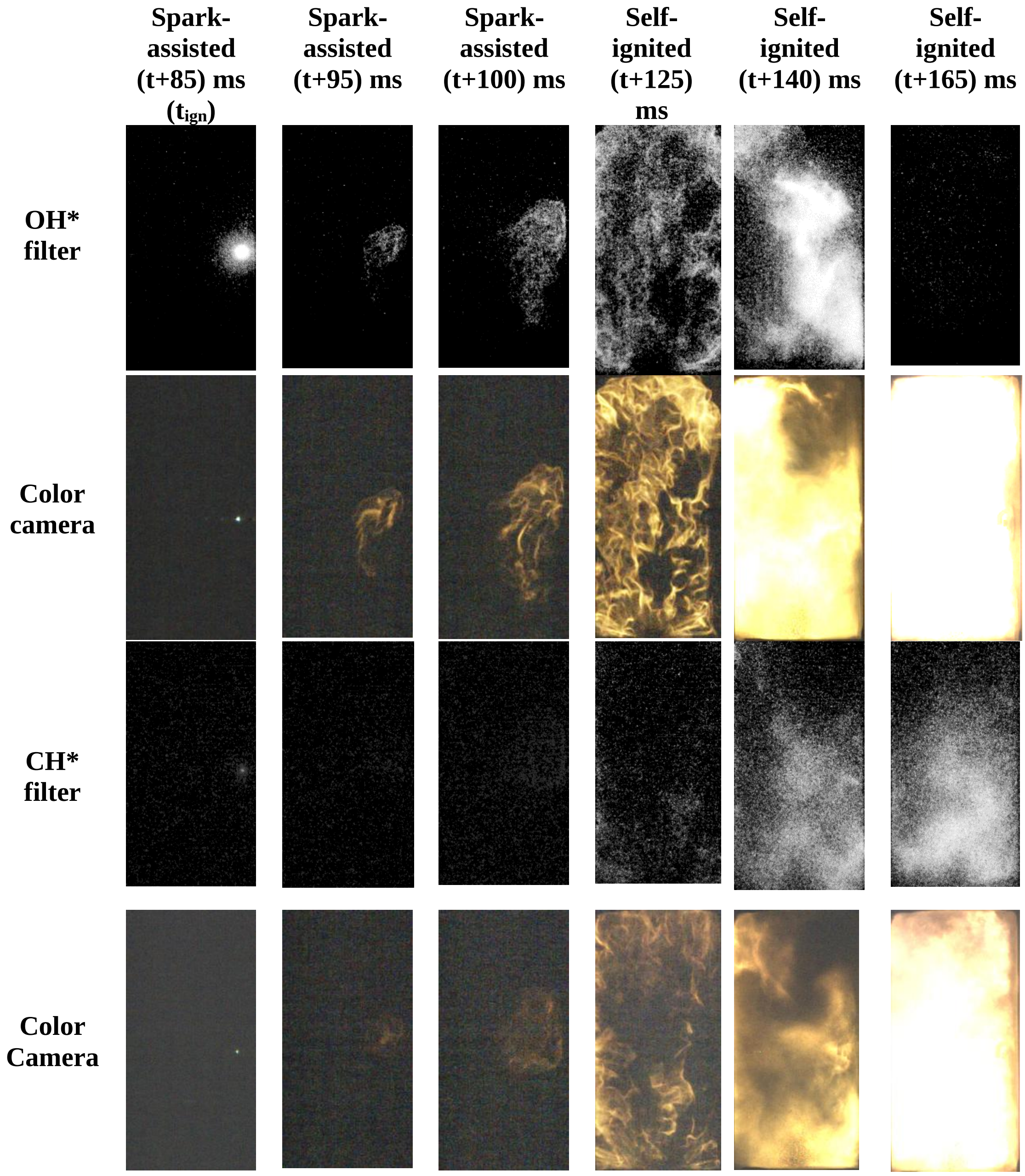

Figure 5-9 Time-resolved OH* and CH* chemiluminescence images and corresponding broadband imaging of a preparatory spark-assisted and self-ignited cycle at selected times from ignition to exhaust valve opening.

From Figure 5-9, t+85 ms corresponds to the ignition timing of the spark-assisted cycle, a small luminous region appears in both the OH* and CH* images, showing the formation of the initial flame kernel near the spark plug. The OH* emission is brighter and more compact, while the CH* signal is weaker and less localized. This suggests that OH* gives a clearer signature of the earliest high-temperature zone, with CH* already present but less intense at this stage.

At t+95 ms and t+100 ms, the flame kernel grows and becomes more visible. The OH* emission increases and fills a large part of the kernel interior, indicating the build-up of high-temperature gases inside the flame. The color images confirm that the flame is still relatively localized in the chamber at these times. The CH* images did not capture much intensity, which may be intrinsic to the CH* cycle itself as the color images are not as bright as the OH* images as well.

In the self-ignited cycle, the OH* and CH* emissions behave much differently (see Figure 5-9). However, both OH* and CH* are more intense in a self-ignition cycle compared to a spark-assisted cycle. Since mixing time is limited in self-ignited cycles, extremely rich pockets are formed and diffusive combustion persists after the main heat release.

At t+125 ms and t+140 ms, the OH* signal is strong and the rich flame occupies a larger portion of the combustion chamber as seen in the color images. The OH* images show a strong and relatively uniform emission, indicating that the chamber is filled with hot combustion products rather than an actively propagating flame. At t+165 ms, the color images show a OH* signal barely captures the intensity of the rich combustion process. The OH* emission is reduced and close to the background level, which is consistent with decaying radical concentrations as the gases cool.

For the CH*, at t+125 ms, the CH* intensity is not apparent despite the rich combustion. However, at t+140 ms and t+160 ms, the CH* intensity increases. This extended CH* emission at t+160 ms is attributed to rich diffusive combustion, which is absent in the spark-assisted cycle. Overall, the images show CH* closely linked to the flame front during the main propagation phase, while OH* provides a stronger, more global view of the high-temperature products.

Quantitative evolution of fast radicals

To gain a closer understanding, the spontaneous radical emissions were analyzed quantitatively. The OH* and CH* images are processed using total pixel intensity, calculated by summing all pixel values in each recorded image. This metrics provide a global measurement of radical emission.

Based on the experimental data, 8 combined spark-assisted and self-ignited cycles are analyzed for OH* and CH*. The cycle-to-cycle variation of normalized intensity for these cycles from the ignition timing of the spark-assisted cycle to the exhaust duration of the self-ignited cycle is presented on Figure 5-10 while Table 5-4 summarizes the cycle-to-cycle intensity duration (measured at 20% of the normalized intensity) and the combustion duration for the OH* and CH* chemiluminescence.

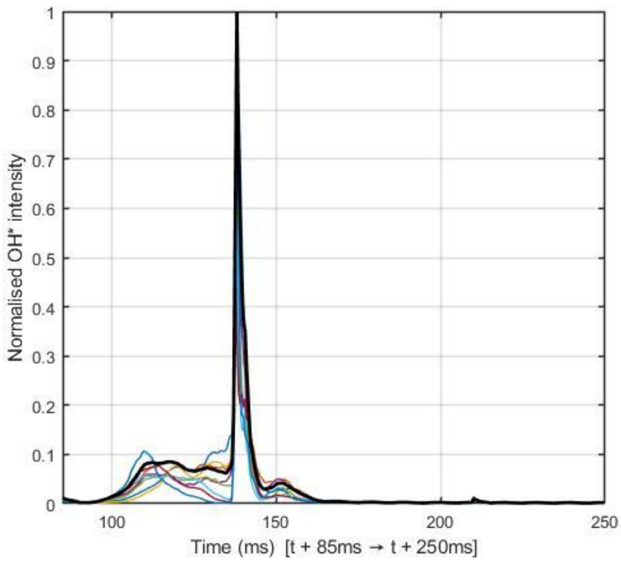

(i)

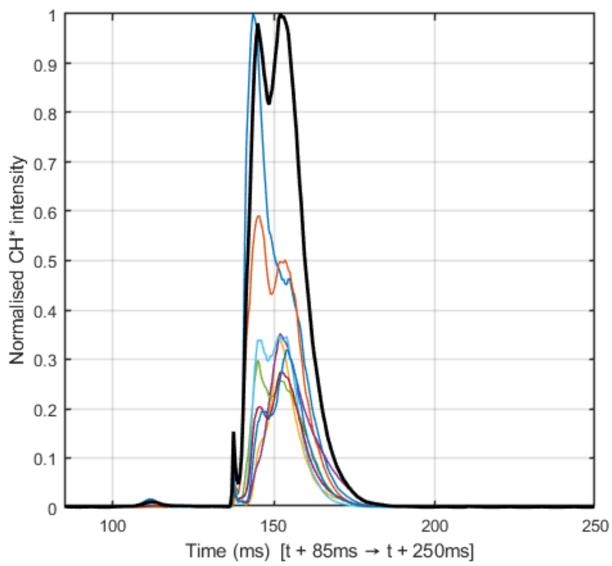

(ii)

Figure 5-10 Cycle-to-cycle variability of the total intensity from ignition timing (85 ms) of the spark-assisted cycle to the exhaust duration of the self-ignited cycle of OH* (i) and CH* (ii) with mean intensity shown in black

Table 5-4. Cycle-to-cycle intensity duration and combustion duration for the OH* and CH* chemiluminescence

Chemiluminescence Type	**OH***	**CH***
Intensity $\text{duration}_{20\%}$ (ms)	$4.2 \pm 0.6_{14.2\%}$	$23.5 \pm 3.3_{14.0\%}$
$t_{comb,0\%\text{-}100\%}$ (ms)	$5.97 \pm 0.39_{6.53\%}$	$6.11 \pm 0.66_{10.8\%}$

The normalized mean total intensity of the OH* and CH* (in black from Figure 5-10) is further analyzed. In the legend, the labels "Pressure OH*" and "Pressure CH*" indicate the chamber pressure signals recorded during the OH* and CH* chemiluminescence experiments, respectively. The intensity traces show the measured chemiluminescence of OH* and CH*, with their corresponding standard deviations shown as dotted lines. Note that the pressure traces originate from separate experiments, since OH* and CH* emissions are not captured simultaneously; the figure includes the representative pressure of OH* and CH* used for analyzing the raw chemiluminescence images.

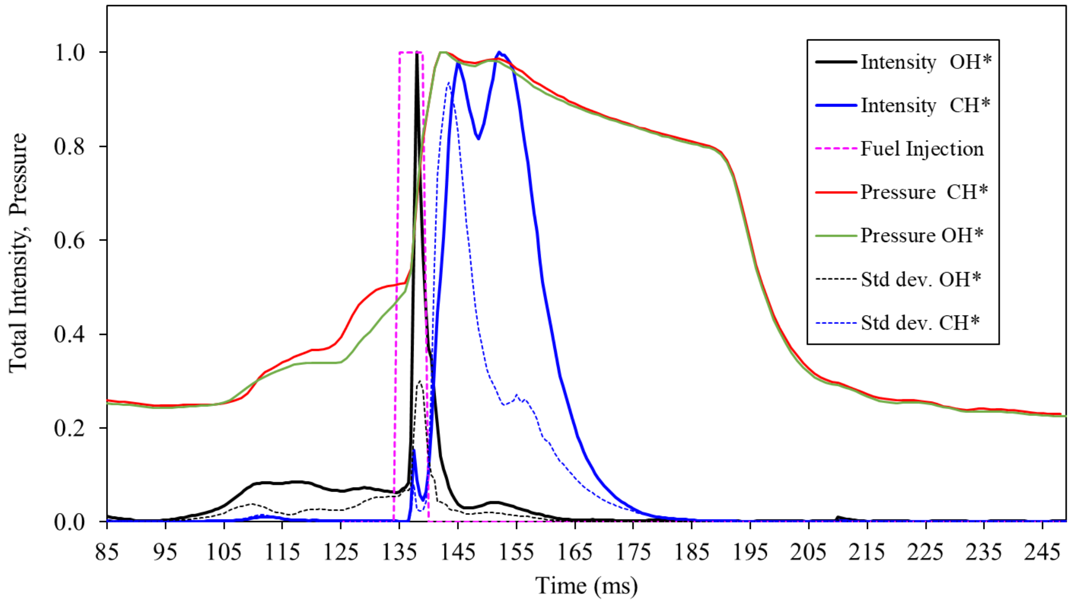

Figure 5-11 Temporal evolution of the instantaneous normalized mean total pixel intensity of OH* and CH*, including their standard deviations (dotted line), for a self-ignited cycled and its preceding spark-assisted cycle (starting from its tign = 85 ms).

From Figure 5-11, normalized mean total pixel intensities and normalized chamber pressures are presented to enable comparison of their temporal evolution independent of absolute signal magnitude.

The observed early rise in CH* and OH* intensity (around 110 ms), together with a slight pressure rise before the air and fuel injection results from the previous spark-assisted cycle that occurs in the cycle prior to the self-ignited cycle. This can be attributed to residual slow combustion from the previous spark ignited cycle that continues into the exhaust (increase from ~95 ms) and early intake phases, as indicated by the OH* intensity. This presence of OH* confirms that hot reactive radicals remain at the beginning of the cycle (125 ms), promoting self-ignition. This mechanism is similar to the pulse jet ignited principle [80], as evidenced by OH* chemiluminescence.

The mixture at the exhaust of from the spark-assisted cycle is fuel-rich. Therefore, when air is injected, this leftover reaction zone produces low chemiluminescence and marginal heat release, which explains the non-zero baseline of both radical signals and the small but noticeable pre-injection pressure increase.

The newly injected air rapidly mixes with this high-temperature, radical-rich environment, hence, this mixture does not require an external spark. Self-ignition occurs once local mixture fractions and temperature become favorable. This transition is marked by a rapid rise in CH* intensity, signaling flame-front establishment, followed by a higher increase in OH* intensity that reflects the growth of high-temperature burned-gas zones and the main heat-release phase, concurrent with the steep pressure rise. OH* peaks before the CH* before the combustion. CH* intensity rises very sharply after the onset of the self-ignition. After their respective peaks, OH* decays more rapidly than CH*.

The OH* and CH* signals in the self-ignition cycle are different from those in the spark-ignition cycle. In spark ignition, the OH* intensity lasts longer (18.6 ms) than the CH* intensity (13.4 ms). In contrast, during self-ignition, the CH* intensity lasts longer (25 ms) while the OH* intensity is much shorter (4.2 ms). This happens because spark ignition creates a flame that spreads gradually, leading to longer high-temperature reactions (OH*), whereas self-ignition occurs more abruptly, which makes CH* last longer while OH* appears more briefly and intensely.

Consequences for the ignition strategy

These observations suggest two complementary approaches for improving self-ignition control. First, chamber design modifications, such as adjusting the geometry, can enhance residual gas distribution and reduce trapped pockets. Second, the modular CV2 design enables mixing strategy optimization, including enhanced turbulence, optimized inlet configuration and recirculation zones. As such, non-linear angled configurations can promote more uniform mixing, limiting over-rich regions and improving cycle stability. A multi-chamber configuration offers a promising solution. Controlled transfer of residual burnt gases from one chamber to another can trigger predictable self-ignition in downstream chambers. Such a configuration not only leverages residual-driven ignition but also improves cycle-to-cycle consistency, operational stability and overall efficiency in liquid-fueled pistonless CVC systems.

5.3.2.3 PIV analysis

PIV measurements are performed under the same operating conditions as the reference case 1579 to characterize the chamber flow field and overall aerodynamics. All the 8 self-ignited of the Test 1632 are retained for analysis. For each cycle, 10 kHz velocity fields are recorded, providing sufficient temporal resolution to capture the main flow structures and their evolution throughout the cycle.

5.3.2.3.1 Topology analysis of the velocity field

For the reactive case, an interframe time of dt = 25 µs is used. The temporal evolution of the intake and combustion processes of cycle 6 of Test 1632 is presented in Figure 5-12 through tomography images, followed by velocity fields obtained using the multi-pass cross-correlation PIV algorithm.

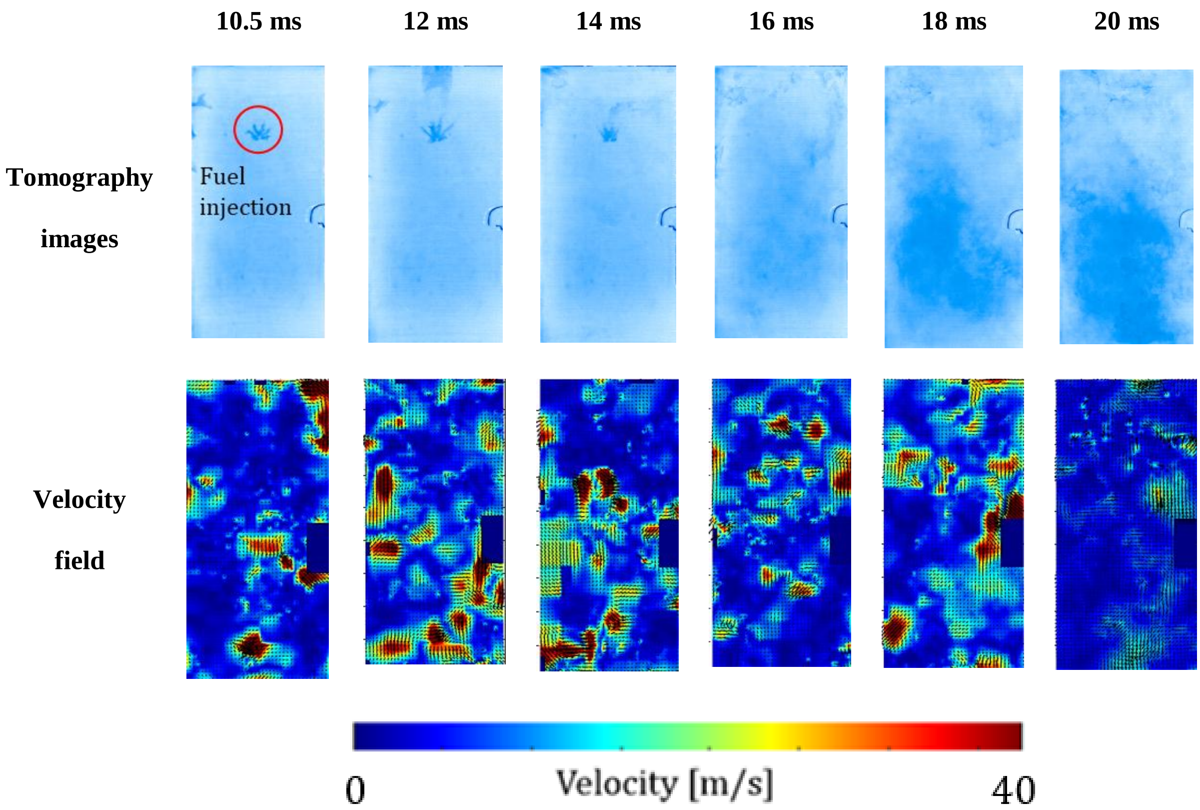

Figure 5-12 Aerodynamics during the intake and combustion phase of the cycle 6 of the self-ignition Test 1632 sequence.

As shown on Figure 5-12, fuel injection begins at 10.5 ms. At this stage, the flow shows localized velocity structures of moderate magnitude, indicating residual motion from the previous cycle, with no clear large-scale patterns. No visible combustion structures are observed. At 12 ms, air injection starts and combustion is triggered through a self-ignition process, as fuel and air mix with the hot surrounding RBG.

By 16 ms, lighter regions appear in the tomographic images, marking the flame front. The tomographic images show a progressive expansion of the reactive zone, with a more diffuse structure occupying a larger portion of the chamber. The velocity maps reveal intensified and more distributed high-velocity regions (yellow–red zones), suggesting an interaction between the flow and reaction. The expansion of burnt gases contributes to local acceleration and redistribution of the flow.

At 20 ms, as combustion nears completion and burned gases fill the chamber, the tomographic image becomes more homogeneous. However, PIV velocity measurements are no longer reliable: seeding particles are consumed, placing the technique outside its validity domain.

Overall, these observations confirm that the flow field plays a key role in mixing and in the propagation of the reaction zone. The interaction between turbulence, residual burnt gases and pressure rise governs the development and spatial distribution of combustion during this phase.

To quantify this, velocity data from the intake and combustion phases are further processed in MATLAB to calculate mean velocity and turbulent fluctuation. The temporal evolution of the mean flow velocity and turbulent fluctuation obtained from the velocity vector field analysis of the self-ignited cycles are presented in Figure 5-13.

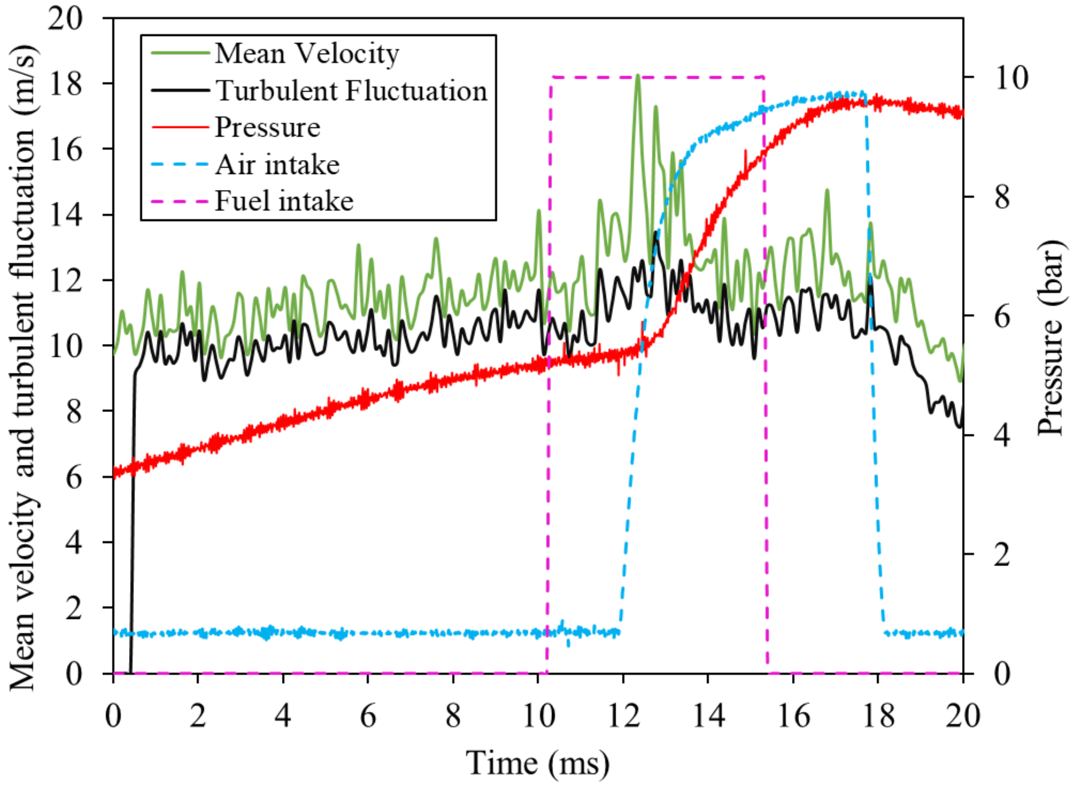

Figure 5-13 Temporal evolution of the mean velocity and turbulent fluctuation across the self-ignited cycles

From Figure 5-13, around t=12 ms, self-ignition occurs shortly following the injection of air and fuel in a pre-heated mixture composed of hot RBG rapidly mixing with fresh gases, leading to a rapid pressure rise, after which the mean velocity decays. At t=12 ms, there are fresh gas and RBG for the self-ignited cycles. However, this fresh mixture has been more diluted with RBG than expected, due to the fact that the air intake gets blocked by the rise of pressure. Because less air gets into the combustion chamber due to this phenomenon, the flow velocity of the self-ignited cycles (~18 m/s) is less than that of the reference spark-ignition cycle (~38 m/s). In the combustion phase (t=12 ms to t = 18 ms), the averaged-mean velocity is ~12 m/s and the combustion phase is mainly driven by turbulence (~10 m/s), with a high turbulence intensity of 0.83. The magnitude of velocity and turbulence in the self-ignited cycle are higher compared to ~5 m/s for both mean velocity and turbulence in spark-ignited cycle. This process becomes much more mixing-limited considering the short time allowed for fuel-air mixing after injection and prior to self-ignition occurring.

A representation of the ensemble-average fields of mean velocity and turbulent fluctuation at the onset of self-ignition (t = 15 ms) is presented in Figure 5-14.

For the ensemble-averaged mean velocity field (U), at *t = 15 ms*, the velocity distribution is relatively smooth and organized, showing the large-scale flow structure with moderate spatial variations.

In contrast, the turbulent fluctuation field (U_{HF}) presents strong local variations, with red and yellow regions indicating high fluctuation intensity. This shows that, during the self-ignition combustion phase, small-scale turbulent structures are superimposed on the mean flow and locally intensify the mixing process.

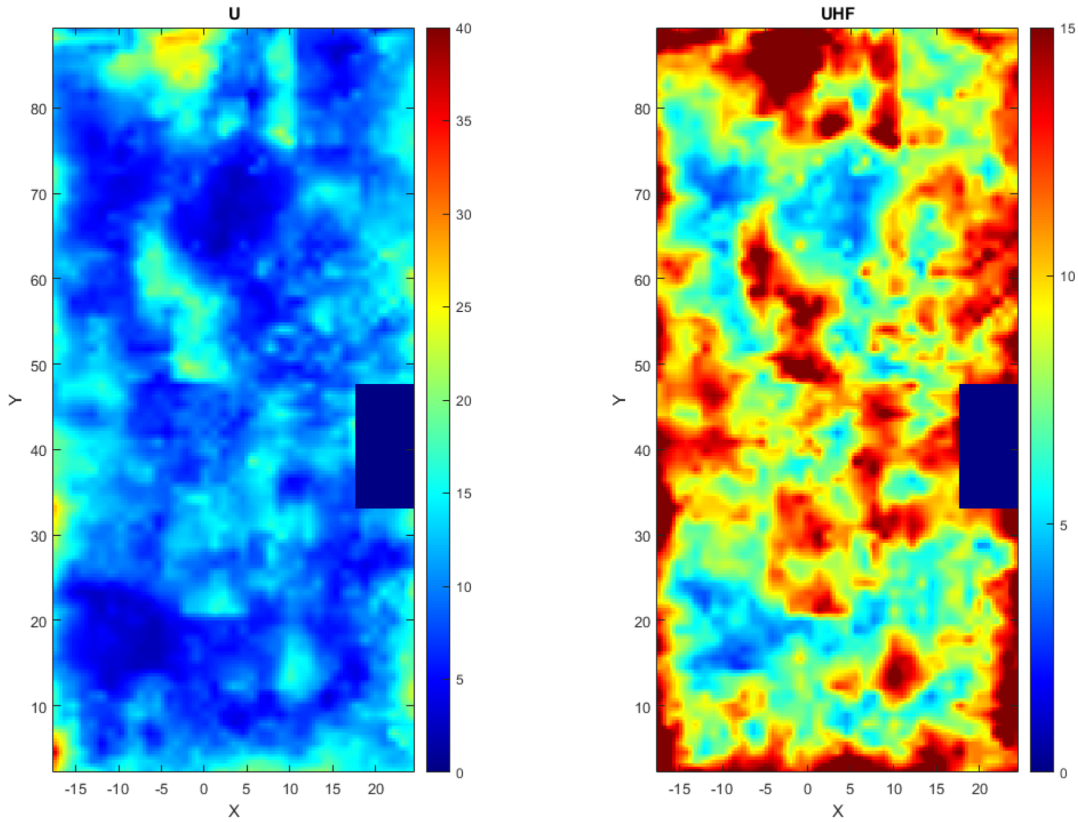

Figure 5-14 Ensemble-averaged mean velocity (U) and turbulent fluctuation (U_{HF}) at t = 15 ms

5.4 Effect of exhaust pressure on the self-ignited cycle properties

This section presents results from a parametric study varying the exhaust pressure from 1 bar to 2 bar, while keeping the initial air intake pressure constant at 4.3 bar and the overall equivalence ratio is targeted at more or less stoichiometry. For each condition, the operating parameters are applied over 20 cycles as summarized in Table 5-5.

Table 5-5. Operating parameters for the different exhaust pressure

Test No.	Targeted OER	dt fuel (ms)	tign (ms)	tex (ms)	dt ex (ms)	Pex (bar)	Cycle Period (ms)
#1703	1	6	85	55	45	**1**	125
#1564	1	6	85	55	45	**1.5**	125
#1279	1	6	85	55	45	**2**	125

Figure 5-15 presents the pressure signal of a self-ignited cycle and its preceding spark-assisted cycle as a function of the exhaust pressure (1 to 2 bar), along with its respective wall heat flux, at stoichiometry.

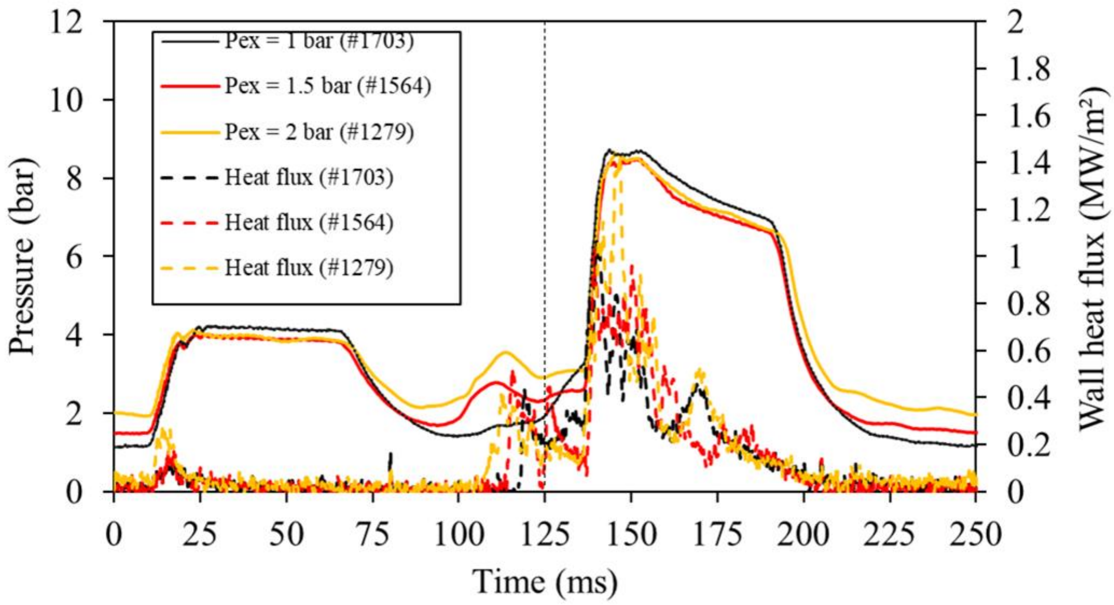

Figure 5-15 Evolution of the pressure signals of the self-ignited cycles and its preceding spark-ignited cycle as a function of the exhaust pressure (1 to 2 bar), along with its respective wall heat flux, at stoichiometry

The increase in exhaust pressure shows no noticeable effect on the peak values of the pressure signals (Figure 5-15). However, higher pressure levels are observed during the exhaust phase of the preceding spark-ignited cycles after 100 ms. Key parameters such as initial and peak pressure, combustion duration, wall heat flux, RBG dilution and overall equivalence ratio are compared across self-ignited cycles (Table 5-6).

Table 5-6. Overall mean and standard deviation of key parameters over the sequences of the self-ignited cycles

Exhaust Pressure	1 bar	1.5 bar	2 bar
From experiments:			
OER	1.31 ± 0.05	1.44 ± 0.07	1.56 ± 0.09
Initial pressure (bar)	2.79 ± 0.59	2.26 ± 0.32	2.90 ± 0.25
Peak pressure (bar)	8.85 ± 0.17	8.50 ± 0.17	8.55 ± 0.18
Pressure ratio	3.32 ± 0.75	3.84 ± 0.57	2.97 ± 0.28
$t_{comb,0\%-100\%}$ (ms)	4.97 ± 0.77	4.61 ± 0.20	4.51 ± 0.34
Maximum wall heat flux (MW/m^2)	1.04 ± 0.14	1.06± 0.12	1.17 ± 0.21
From simulations:			
RBG dilution (%)	25.7 ± 1.3	26.9 ± 0.5	27.2 ± 0.2

Although the mixture is nominally targeted at stoichiometric conditions, variations in the OER are observed. This discrepancy is expected, as the mixture is not perfectly premixed and combustion occurs in the presence of residual gases from the previous cycle and because of air intake limitation induced by chamber pressure. As the exhaust pressure increases from 1 to 2 bar, the OER increases from 1.31 ± 0.05 to 1.56 ± 0.09, reflecting the growing influence of residual burnt gases and reduced fresh air intake. Also, because the initial intake pressure is controlled and kept at 4.3 bar, the air intake duration is slightly varied and longer for the exhaust pressure of 1 bar than the exhaust pressure of 2 bar, leading to a fuel-richer OER at Pex = 2 bar than Pex = 1 bar.

The initial pressure shows moderate variability across operating conditions, while the peak pressure remains relatively stable, with values close to 8.5–8.9 bar for all exhaust pressures. This indicates that self-ignition occurs under comparable thermodynamic conditions despite changes in backpressure. The corresponding pressure ratio varies between 3.0 and 3.8, with a slightly lower value at backpressure 2 bar. The average maximum wall heat flux remains close to 1 MW/m^2 for all conditions, with a slight increase at 2 bar, reflecting the combined effects of dilution and heat capacity of the residual gases.

5.5 Effect of cycle optimization on total energy losses

The energy losses of three self-ignition configurations are evaluated: the reference cycle at 8 Hz, an optimized-cooling cycle (optimcool) at 10 Hz and an optimized-exhaust cycle (optimexhaust) at 12.5 Hz. The same configuration used for spark-ignition analysis is retained, even though it is not optimized for self-ignition cycles. The objective is to assess how reducing the cooling phase and shortening the exhaust duration influence the overall cycle behavior and ignition process.

Following the methodology applied to the spark-ignition cycles in Chapter 4, the optimcool configuration is obtained by advancing the exhaust valve opening in order to reduce the duration of the cooling phase (in spark-ignited cycles) while maintaining the same exhaust duration as in the reference case. In contrast, the optimexhaust configuration is derived from the optimcool cycle. It maintains the same exhaust valve opening timing but reduces the exhaust duration, thereby optimizing the exhaust phase (for spark-ignited cycles). This modification allows the cycle frequency to be increased to 12.5 Hz.

For each condition, the operating parameters are applied over 20 cycles, as summarized in Table 5-7. The corresponding pressure evolution for the different operating parameters is presented in Figure 5-17.

Table 5-7. Operating parameters for the different self-ignition cycles: reference cycle, optimcool, optimexhaust

Cycle Type	**dt air (ms)**	**dt fuel (ms)**	**tign (ms)**	**tex (ms)**	**dt ex (ms)**	**Pex (bar)**	**Cycle freq. (Hz)**	**Cycle period (ms)**
Reference	11	5	85	**55**	**45**	2	**8**	**125**
Optimcool	11	5	70	**30**	**45**	2	**10**	**100**
Optimexhaust	11	5	50	**30**	**30**	2	**12.5**	**80**

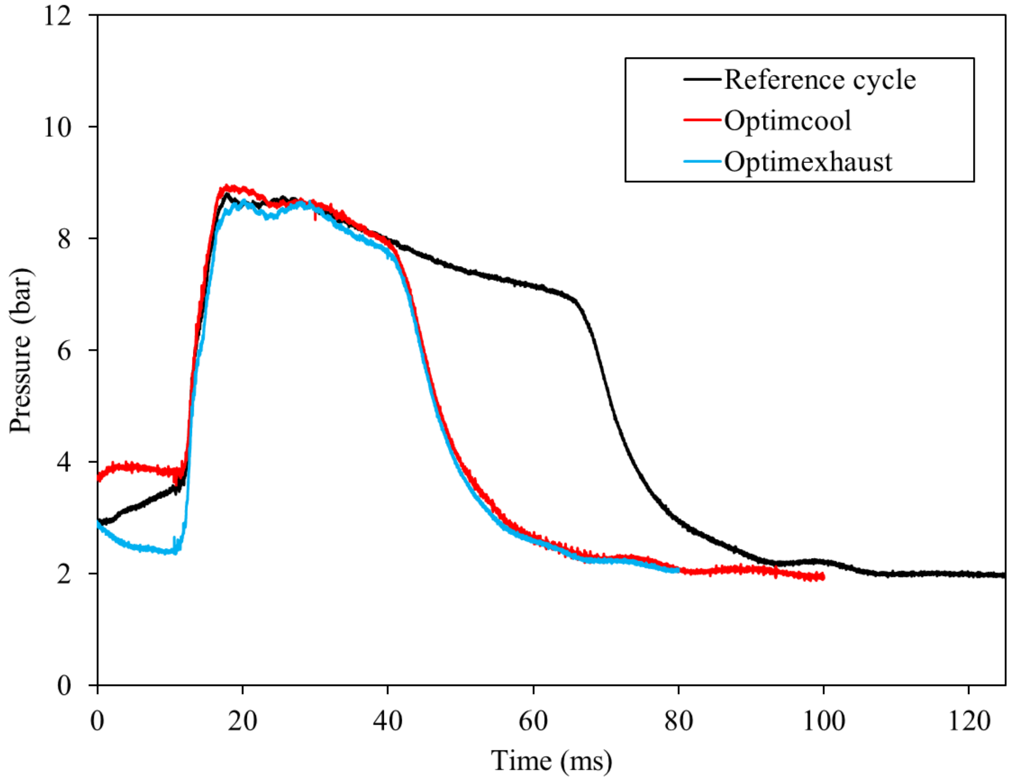

Figure 5-16 Pressure evolution of the different cycles: reference, optimcool and optimexhaust

For each operating frequency, the main thermodynamic and combustion parameters are evaluated over 8 self-ignition cycles and averaged to ensure statistical convergence. Table 5-8 summarizes the resulting operating conditions and global cycle characteristics for the three types of cycle.

Table 5-8. Overall mean and standard deviation of key parameters for the different cycle types over the sequences for 8 cycles

Cycle type	Reference	Optimcool	Optimexhaust
From experiments			
OER	1.23 ± 0.06	1.39 ± 0.17	1.27 ± 0.07
Initial pressure (bar)	3.53 ± 0.38	4.05 ± 0.57	2.89 ± 0.49
Maximum pressure (bar)	8.69 ± 0.24	9.50 ± 0.48	8.88 ± 0.39
Pressure ratio	2.48 ± 0.19	2.40 ± 0.41	3.14 ± 0.44
$t_{comb,0\%-100\%}$ (ms)	4.07 ±0.33	3.52 ± 0.26	4.35 ± 0.21
Maximum dP/dt (bar/ms)	1.83 ± 0.20	2.03 ± 0.55	2.14 ± 0.46
Maximum wall heat flux (MW/m^2)	0.99 ± 0.08	1.16 ± 0.17	0.92 ± 0.21
From simulation			
Dilution (%)	23.7 ± 0.2	24.7 ± 0.1	24.2 ± 0.3
Energy Loss (% of Combustion Energy)	84.9±1.6	77.8 ± 6.8	67.3 ± 10.0

The results show that the global combustion characteristics remain comparable across the three type of cycles. Although the same OER (0.9) is targeted for all the three cycle types, the effective OER is not directly controlled in self-ignited cycles and the mixture remains fuel-rich, due to residual burnt gases and intake–combustion interaction.

The initial pressure varies between the three cases, which contrasts with spark-ignition operation where it is more tightly controlled. This can be explained by the noticeable dispersion prior to the combustion phase in Figure 5-16. This behavior is linked to the self-ignition strategy, which is based on a two-cycle sequence designed to reproduce ignition driven by residual burnt gases. Consequently, variations in the preceding cycle directly influence the conditions of the following one (see Figure 5-9).

The maximum pressure remains within a narrow range (8.69–9.50 bar). The *optimcool* cycle exhibits the highest peak pressure, suggesting slightly improved confinement of the energy release.

Although the *optimcool* case has the highest peak pressure, its higher initial pressure results in a pressure ratio similar to the reference case. In contrast, the *optimexhaust* configuration shows the highest pressure ratio (3.14 ± 0.44), primarily due to its lower initial pressure rather than a substantial increase in peak pressure. This indicates a stronger relative pressure rise during combustion. The *optimcool* cycle also exhibits the shortest combustion duration, indicating slightly faster energy release, while the *optimexhaust* case shows a marginally longer duration.

The dilution level remains relatively close across the three cases, with values of 23.7 ± 0.2%, 24.7 ± 0.1% and 24.2 ± 0.3%. The energy loss per cycle is highest for the reference cycle (84.9± 1.6%), lower at 10 Hz (77.8±6.8%) and lowest at 12.5 Hz (67.3±10.0), indicating that a cycle frequency of 12.5 Hz reduces energy losses by approximately 17.6% per cycle. This is nearly the same value (16.1%) as was obtained in the spark-ignited cycle in Chapter 4. This result is consistent because the differences between the three cycle types depend on the burned-gas phase, which is minimally affected by the combustion phase. However, in the case of the self-ignition cycles, the cooling phase is not fully optimised for the *optimcool* and *optimexhaust* cycles. The total energy loss is, hence, decomposed into contributions associated with the different phases of the cycle to evaluate how to further optimize the self-ignition cycle in the future by reducing the additional cooling phase (zone C in Figure 5-17).

Because combustion occurs during the intake phase, the methodology for evaluating the energy losses in the self-ignited cycles is not the same as the spark-ignited cycles. Hence, the phases are re-introduced as presented in Figure 5-17. The intake and combustion phase are evaluated as a single phase called (A+B), accounting for intake heat losses and losses related to combustion and unburnt mass. Phase C corresponds to heat losses during the isochoric cooling phase (that have to be eliminated in case of optimization) and phase D represents exhaust heat losses. The corresponding heat losses associated with each phase are evaluated using the 0D/1D model.

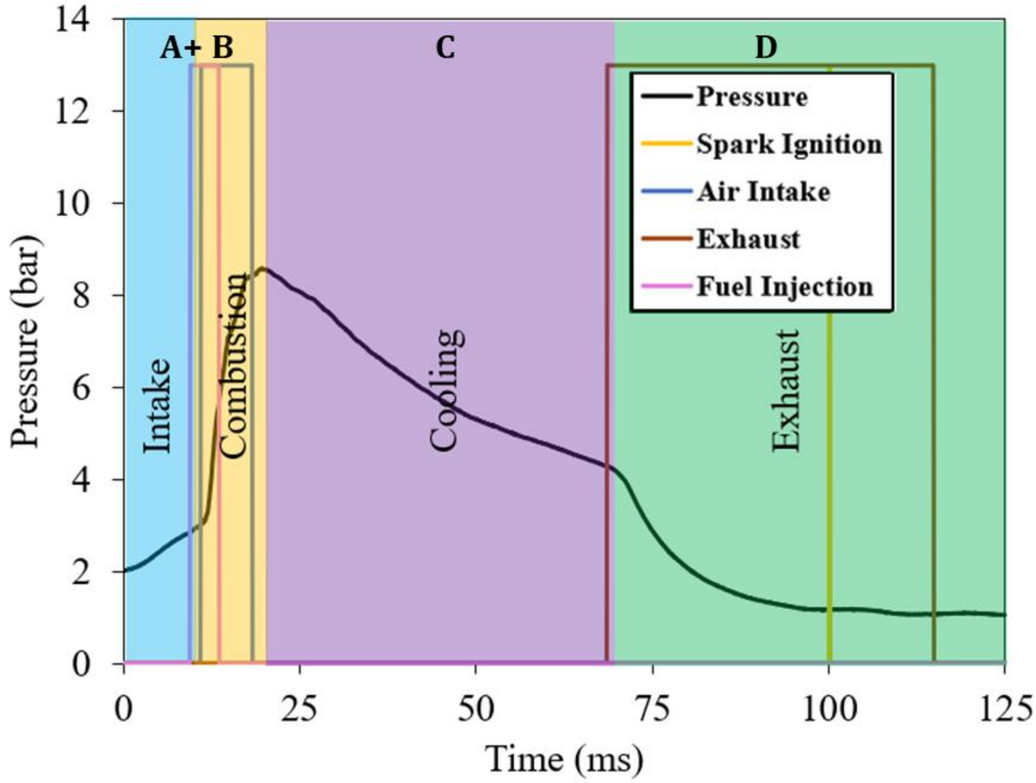

Figure 5-17 Classification of the different heat loss phases in the self-ignited cycle

The distribution of losses associated with each phase of the cycles with respect to the Total Energy Loss (% of Combustion Energy) from Table 5-8 are summarized in Table 5-9:

Table 5-9. Relative contribution of energy losses for the different phases at the different types of self-ignited cycles

Phase	A+B (%)	C (%)	D (%)	Total (%)
Reference cycle	55.7	21.3	7.9	84.9
Optimcool	52.7	14.6	10.5	77.8
Optimexhaust	48.3	11.4	7.6	67.3

For all the three types of cycles, phase A+B is dominant accounting for 48.3–55.7 % of losses, mainly associated to the combustion and unburnt mass. Despite having the same intake conditions, the preceding spark-assisted cycles influence the intake and combustion phases. Advancing the exhaust timing to create an *optimcool* cycle allowed a reduction of at least 6.7% of the cooling phase losses. Reducing further the exhaust duration however did not eventually have an important effect in the exhaust loss evaluation.

11.4% of the *optimexhaust* cycle of the total losses come from phase C, which corresponds to the isochoric cooling phase. This shows that there is still room to improve the cooling process of the self-ignited cycle and potentially increase its operating frequency. If phase C is fully eliminated, the fully optimized self-ignited cycle could reduce total losses to around 55.9%, which remains reasonable considering the pressure ratio used in this study. Moreover, the reduction of the cooling phase allows to reduce the cycle duration by 15ms, increasing the cycle frequency from 12.5 to 15.4 Hz. This increase directly induce an increase of power delivery by 23%.

5.6 Conclusion

Two approaches were identified to generate self-ignition with the CV2 set-up: delaying the ignition timing and increasing the exhaust pressure. Adjusting both together proved to be the most representative way to reproduce the burned-gas transfer expected in a multi-chamber configuration. Under these conditions, a reference stable self-ignition cycle was selected.

This reference cycle was studied at 8 Hz (tign = 25 ms, Pex = 2 bar). It is initiated by a spark-assisted cycle, similar to a secondary chamber in a multi-chamber system. Self-ignition takes place during the combustion phase. PIV measurements show that during the combined intake-combustion phase, the velocity field is lower (about 18 m/s) than in the spark-ignition cycle (about 38 m/s). This is due to the pressure rise during combustion (which happens during the intake phase), blocking the air intake flow. As a result, less air enters the chamber and the mixture becomes more fuel-rich. Therefore, even though the initial target was a lean OER of 0.95, combustion finally takes place at a rich OER (1.27). Unlike the spark-ignition process, self-ignition can succeed under strongly turbulent conditions. Actually, combustion in the self-ignition case is mainly driven by the high turbulent fluctuation (around 10 m/s).

A parametric study was conducted to evaluate the influence of the main parameters controlling self-ignition combustion stability: ignition timing, exhaust backpressure and cycle frequency. Setting the ignition timing during the exhaust phase allowed stable self-ignition. When varying the exhaust backpressure, the initial intake pressure was maintained constant; consequently, the presence of approximately 26% residual burnt gases had only a minor influence on cycle behavior. However, it increased the probability of having successful self-ignition cycles.

The cooling phase of the reference cycle was partly optimized by advancing the exhaust valve opening, allowing the operating frequency to increase to 10 Hz (*optimcool* cycle). Further reduction of the exhaust duration led to the *optimexhaust* cycle, achieving a frequency of 12.5 Hz. A 0D/1D energy analysis demonstrated improved thermal performance at higher frequencies, confirming reduced losses and enhanced efficiency.

The distribution of heat losses across the different phases of the three self-ignition cycles was also assessed. The combined intake-combustion phase was identified as the dominant contributor, accounting for approximately 48.3% to 55.7% of total heat losses. Since the cooling phase was not fully optimized, it offers potential to further improve the self-ignition cycle by about 11.4% and a frequency increase up to 15.4 Hz thanks to cycle duration reduction of 15ms corresponding to cooling phase suppression. This process will allow an increase of power delivery by 23%.

Chapter 6: Conclusion and perspective

In a context marked by continuously increasing air traffic and urgent environmental constraints, the decarbonization of aviation has become a major technological challenge. The objectives set by ACARE, targeting a 75% reduction in CO_2 emissions by 2050 compared to year-2000 aircraft. Current turbomachinery has reached a high level of technological maturity, leaving limited room for further efficiency gains in terms of fuel consumption within the conventional constant-pressure combustion paradigm. Consequently, achieving ambitious low consumption targets requires a profound rethinking of the thermodynamic cycle itself.

Pressure Gain Combustion (PGC) and in particular Constant Volume Combustion (CVC), offers a promising alternative by enabling combustion under nearly constant-volume conditions, thereby recovering the pressure losses inherent to the Brayton cycle and increasing overall cycle efficiency. Within this framework, the present research was conducted as part of the INSPIRE (INSpiring Pressure gain combustion Integration, Research and Education) Marie Skłodowska-Curie Innovative Training Network, which investigates advanced PGC concepts at an integrated level. More specifically, this work contributes to Work Package 2, dedicated to cyclic pistonless constant-volume combustion.

The thesis established the scientific and industrial foundations of PGC (specifically CVC) for air-breathing propulsion. The thermodynamic advantages of the Humphrey and Fickett-Jacobs cycles over the conventional Brayton cycle were discussed, alongside the historical evolution of CVC systems. While early developments demonstrated the theoretical potential of pressure-gain combustion, persistent technical challenges such as thermal loading, mechanical complexity and ignition control, have limited its industrial deployment. Recent research efforts have therefore shifted toward fundamental investigations of pistonless CVC systems, aiming to better understand ignition, flame propagation and the influence of residual gases under highly diluted conditions.

The experimental testbench CV2, previously developed within the CAPA Chair, an ANR–SAFRAN Tech–MBDA France collaborative research program led by the Pprime Institute is used to address the knowledge gap. The CV2 experimental setup provides precise control of intake and exhaust boundary conditions, enabling accurate determination of injected mass, equivalence ratio and residual gas fraction. Comprehensive diagnostics, combining conventional sensors and optical techniques, ensure detailed characterization of combustion dynamics. An inhouse 0D/1D model of the CV2 set-up, previously developed for gaseous fuel, was also adapted for liquid fuel. The 0D/1D model, validated first for all phases of the spark-ignition cycle, offers reliable predictions of mass, energy and pressure evolutions. Its potential has been extended to self-ignition cycle. Together, these tools constitute a robust and consistent methodology for analyzing cyclic combustion phenomena.

Characterization of a reference spark-ignited cycle

A detailed characterization of a reference spark-ignited cycle was documented and analysed. The chemiluminescence OH* and CH* analysis of this type of cycle revealed that the highest cycle-to-cycle variability occurs during early flame development, with combustion stabilization occurring in later stages. A parametric investigation was conducted to evaluate the influence of the main parameters controlling spark-ignition combustion stability: equivalence ratio, exhaust backpressure, cycle frequency and ignition timing. The study of the equivalence ratio revealed that operating in the range OER = 0.9–1 provides a favorable compromise, ensuring sufficiently high peak pressure while reducing combustion duration. When varying the exhaust backpressure, the initial intake pressure was maintained constant; consequently, the presence of approximately 23% residual burnt gases had only a minor influence on cycle behavior.

Increasing the operating frequency from 8 Hz (reference cycle) to 10 Hz (optimcool) and further to 12.5 Hz (optimexhaust) reduced global heat losses and improved thermal performance, as demonstrated by the 0D/1D energy analysis. The combustion phase remained the dominant contributor to total heat losses, accounting for approximately 37.4% to 41.4% of the total losses depending on the configuration. Optimization of the cooling and exhaust phases significantly decreased losses associated with the cooling process (initially about 19.1% in the reference cycle), enabling higher operating frequencies and improved overall efficiency.

The reference spark-ignition cycle ignition timing of 25 ms is identified as optimal for stable secondary cycles. Earlier ignition timings are strongly affected by intake-generated turbulence, characterized by mean flow velocities of approximately 10 m/s and turbulence fluctuations around 5 m/s, as measured by PIV. During combustion, turbulence intensity was observed to decay due to increased gas viscosity and thermal expansion, resulting in a relatively low-velocity flow field during flame propagation. The PIV results highlight a fundamental limitation of spark-ignited pistonless CVC: combustion stability remains strongly dependent on the local flow velocity and turbulence level at the moment of ignition, leading to inherent cycle-to-cycle sensitivity.

Taken together, these findings underline both the potential and the complexity of pistonless constant-volume combustion. While thermodynamic analyses confirm the promise of pressure-gain combustion for efficiency improvement, practical implementation requires overcoming ignition-related instabilities and cycle-to-cycle variability. The strong dependence on spark timing and turbulence intensity motivates the exploration of the self-ignition strategy.

Characterization of a reference self-ignited cycle

The pistonless CV2 set up was investigated under self-ignition conditions, with the objective of overcoming the intrinsic sensitivity observed in spark-ignited cycles. Two complementary strategies were identified to promote self-ignition within the CV2 setup: delaying ignition timing and increasing exhaust backpressure. The combined adjustment of these parameters proved to be the most representative configuration for reproducing the burned-gas transfer expected in a multi-chamber architecture. Under these conditions, a stable reference self-ignition cycle was established.

This reference cycle was studied at 8 Hz (tign = 25 ms, Pex = 2 bar). It is initiated by a spark-assisted cycle, similar to the secondary chamber of a multi-chamber system, while self-ignition effectively occurs during the combustion phase. PIV measurements revealed significant differences compared with spark-ignition operation. During the combined intake–combustion phase, the mean velocity field reached approximately 18 m/s, markedly lower than the 38 m/s observed in spark-ignition cycles. This reduction results from the pressure rise occurring during combustion, which partially blocks the intake flow. Consequently, less air is admitted into the chamber, shifting the mixture from the initial lean target (OER = 0.95) to a rich effective condition (OER = 1.27) at the time of combustion.

In contrast with spark-ignition, self-ignition was shown to remain viable under strongly turbulent conditions. Combustion in this regime is primarily driven by high turbulent fluctuations of approximately 10 m/s, indicating a different stabilization mechanism. The parametric study demonstrated that positioning ignition timing during the exhaust phase enables stable self-ignition. Increasing exhaust backpressure, while maintaining constant intake pressure, led to approximately 26% residual burnt gases, which had limited influence on overall cycle behavior but significantly increased the probability of successful self-ignition events.

As with spark-ignition operation, cycle optimization through reduction of cooling and exhaust durations allowed an increase in frequency from 8 Hz to 10 Hz (optimcool) and further to 12.5 Hz (optimexhaust). The 0D/1D energy analysis confirmed improved thermal performance at higher frequencies. For self-ignition cycles, the combined intake–combustion phase was identified as the dominant source of heat losses, representing approximately 48.3% to 55.7% of total losses. Since the cooling phase was not fully optimized, additional improvements remain possible. Suppressing approximately 15 ms of cooling duration could enable operation up to 15.4 Hz, corresponding to a potential 23% increase in power delivery, while reducing heat losses by an estimated 11.4%.

Perspective

The OER of the self-ignition configuration being fuel-rich, the self-ignition *optimexhaust* (in red in Figure 6-1) cycle can further improved by reducing the fuel intake. An example of this fuel-reduced cycle, leading to a stoichiometric mixture, is shown in purple in Figure 6-1.

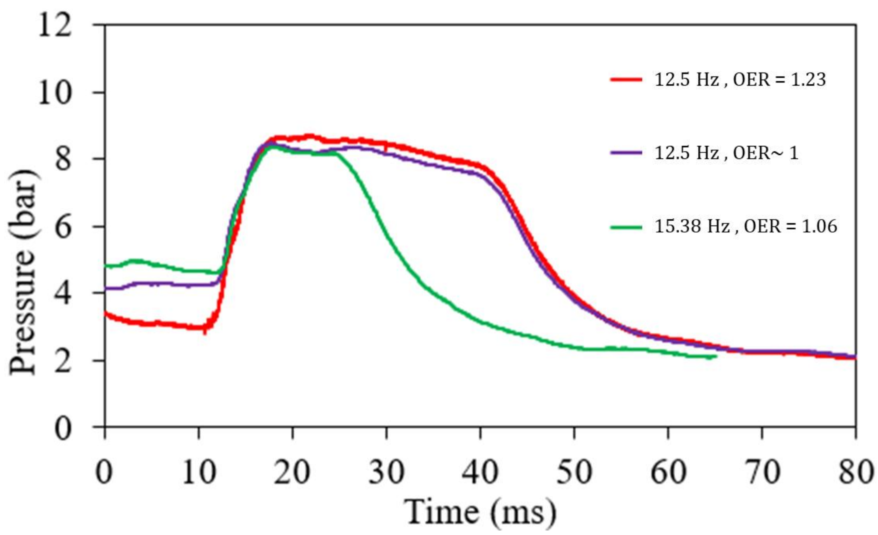

Figure 6-1 Experimental self-ignited optimexhaust cycle (in red), a fuel-reduced cycle at 12.5 Hz (in purple) and a fuel-reduced cycle at 15.38 Hz (in green)

The cooling duration of this new fuel-reduced cycle is then decreased by 15 ms, increasing the cycle frequency to 15.38 Hz (green curve). It can be observed from Figure 6-1 that the cooling phase is still not fully optimized, mainly due to technological limitations of the CV2 set-up. The 0D/1D model can therefore be used as a tool to predict cycle behaviour at higher frequency and investigate operating conditions beyond the current experimental limitations.

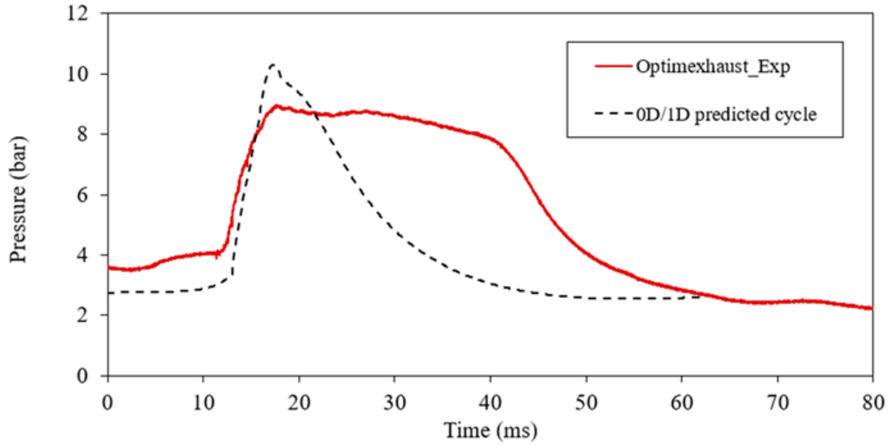

Figure 6-2 An experimental self-ignited optimexhaust (in red) and a 0D/1D fully optimized cooling predicted cycle (in dotted black)

Figure 6-2 presents a predicted fully optimized cooling cycle operating at 15.38 Hz (in dotted black) compared to an experimental *optimexhaust* cycle at a cycle frequency of 12.5 Hz. This result highlights the additional potential of the 0D/1D model for further optimization of the CVC concept through parametric studies that are currently constrained by the CV2 set-up.

In the INSPIRE project, the integration of CVC chambers into a turbomachine was investigated. One of the key challenges in ensuring good overall efficiency lies in reducing the pressure fluctuations seen by the turbine. Indeed, turbine efficiency, whether the turbine is supersonic or not, drops significantly when it is subjected to large upstream pressure variations. As a result, the pressure gains provided by CVC combustion can be partly offset by a decrease in turbine performance. It is therefore important to identify effective ways to damp these pressure fluctuations.

In his PhD thesis, Panos Gallis[79] showed that it was possible to significantly reduce the amplitude of these fluctuations in a prototype CVC chamber operating with spark ignition, by using a properly sized plenum. Operating a CVC chamber in self-ignition mode can further help reduce pressure amplitude while also limiting thermal losses. Combining both approaches appears to be a promising direction for future work.

References

[1] O. Edenhofer *et al.*, *Climate Change 2014 : Mitigation of Climate Change : Summary for Policymakers Technical Summary : Part of the Working Group III Contribution to the Fifth Asessment Report of the Intergovernmental Panel on Climate Change*.

[2] G. Exilard, "Large-Eddy Simulation of constant volume combustion in a ground-breaking new aeronautical engine." [Online]. Available: https://theses.hal.science/tel-02100677v1

[3] M. Bellenoue *et al.*, "Issue 11-June 2016-New Combustion Concepts for Propulsion Engines Challenges in Combustion for Aerospace Propulsion New Combustion Concepts to Enhance the Thermodynamic Efficiency of Propulsion Engines", doi: 10.12762/2016.AL11-12.

[4] P. Stathopoulos, "Comprehensive thermodynamic analysis of the humphrey cycle for gas turbines with pressure gain combustion," *Energies (Basel).*, vol. 11, no. 12, Dec. 2018, doi: 10.3390/en11123521.

[5] F. H. Reynst and M. W. Thring, "Pulsating combustion : the collected works of F.H. Reynst. Ed. by Pergamon. Vol. 6, p. 126," 1961.

[6] Q. Michalski, "Etude expérimentale de la combustion à volume constant pour la propulsion aérobie : influence de l'aérodynamique et de la dilution sur l'allumage et la combustion," École Nationale Superieure De Mecanique et d'Aerotechnique, 2019.

[7] I. Glassman, R. A. Yetter, and N. Glumac, *Combustion.* , 2014th ed. 2014.

[8] P. Wolański, "Detonative propulsion," *Proceedings of the Combustion Institute*, vol. 34, no. 1, pp. 125–158, 2013, doi: 10.1016/j.proci.2012.10.005.

[9] J. Kindracki, "Badania eksperymentalne i symulacje numeryczne procesu inicjacji wiruja̧cej detonacji gazowej, Ph.D. thesis (in Polish), Politechnika Warszawska, Warsaw, Poland, ," 2008.

[10] N. Detomaso, "Simulation aux grandes échelles de la combustion à volume constant : modélisation numérique des flammes turbulentes en expansion dans des mélanges non homogènes." [Online]. Available: https://inspire.cerfacs.fr/en/home/

[11] P. Akbari, E. Szpynda, and R. Nalim, "Recent Developments in Wave Rotor Combustion Technology and Future Perspectives: A Progress Review," in *43rd AIAA/ASME/SAE/ASEE Joint Propulsion Conference & Exhibit*, Reston, Virigina: American Institute of Aeronautics and Astronautics, Jul. 2007. doi: 10.2514/6.2007-5055.

[12] B. C. Bobusch, P. Berndt, C. O. Paschereit, and R. Klein, "Shockless Explosion Combustion: An Innovative Way of Efficient Constant Volume Combustion in Gas Turbines," *Combustion Science and Technology*, vol. 186, no. 10–11, pp. 1680–1689, Nov. 2014, doi: 10.1080/00102202.2014.935624.

[13] C. Smith, P. Snyder, C. Emmerson, and M. Nalim, "Impacts of the Constant Volume Combustor on a Supersonic Turbofan Engine," in *38th AIAA/ASME/SAE/ASEE Joint Propulsion Conference & Exhibit*, Reston, Virigina: American Institute of Aeronautics and Astronautics, Jul. 2002. doi: 10.2514/6.2002-3916.

[14] W. Armbruster *et al.*, "Experimental Investigation of a Small-Scale Oxygen-Hydrogen Rotating Detonation Rocket Combustor," in *AIAA SCITECH 2024 Forum*, Reston, Virginia: American Institute of Aeronautics and Astronautics, Jan. 2024. doi: 10.2514/6.2024-2612.

[15] Q. Xie, Z. Ji, H. Wen, Z. Ren, P. Wolanski, and B. Wang, "Review on the Rotating Detonation Engine and It's Typical Problems," *Transactions on Aerospace Research*, vol. 2020, no. 4, pp. 107–163, Dec. 2020, doi: 10.2478/tar-2020-0024.

[16] G. E. Welch, S. M. Jones, and D. E. Paxson, "Wave-Rotor-Enhanced Gas Turbine Engines," *J. Eng. Gas Turbine. Power*, vol. 119, no. 2, pp. 469–477, Apr. 1997, doi: 10.1115/1.2815598.

[17] R. Nalim, P. Snyder, and M. Kowalkowski, "Experimental Test, Model Validation, and Viability Assessment of a Wave-Rotor Constant-Volume Combustor," *J. Propuls. Power*, vol. 33, 2017.

[18] P. Akbari, R. Nalim, and N. Mueller, "A Review of Wave Rotor Technology and Its Applications," *J. Eng. Gas Turbine. Power*, vol. 128, no. 4, pp. 717–735, Oct. 2006, doi: 10.1115/1.2204628.

[19] G. Jendrassik, "Pressure Exchangers and Applications Thereof," Patent 2946184, 1960

[20] G. Jendrassik, "Jet Reaction Propulsion Units Utilizing a Pressure Exchanger," Patent 2757509, 1956

[21] B. C. Bobusch, P. Berndt, C. O. Paschereit, and R. Klein, "Shockless explosion combustion: An innovative way of efficient constant volume combustion in gas turbines," in *Combustion Science and Technology*, Bellwether Publishing, Ltd., Nov. 2014, pp. 1680–1689. doi: 10.1080/00102202.2014.935624.

[22] L. Cai and H. Pitsch, "Tailoring Fuels for a Shockless Explosion Combustor," 2015, pp. 299–315. doi: 10.1007/978-3-319-11967-0_19.

[23] P. Berndt and R. Klein, "Modeling the kinetics of the Shockless Explosion Combustion," *Combust. Flame*, vol. 175, pp. 16–26, Jan. 2017, doi: 10.1016/j.combustflame.2016.06.029.

[24] T. G. Reichel, J.-S. Schäpel, B. C. Bobusch, R. Klein, R. King, and C. Oliver Paschereit, "Shockless Explosion Combustion: Experimental Investigation of a New Approximate Constant Volume Combustion Process," *J. Eng. Gas Turbine. Power*, vol. 139, no. 2, Feb. 2017, doi: 10.1115/1.4034214.

[25] "Heywood, J. B. (1988). Internal combustion engine fundamentals. New York: McGraw-Hill.".

[26] M. Metghalchi and J. C. Keck, "Burning Velocities of Mixtures of Air with Methanol, Isooctane, and Indolene at High Pressure and Temperature," 1982.

[27] "Holzwarth, H. 1905. Rotary combustion engine. U.S. Patent No. 783,434.".

[28] R. Andriani, U. Ghezzi, and E. Infante, "Thermal Analysis of Constant Volume Combustion Gas Turbine," 2005.

[29] C. A. L. Bosco, "Moteur thermique multicellulaire, à explosion ou à combustion sous volume constant, à détente prolongée et à disposition spéciale d'échange de chaleur," *1006375*, 1948.

[30] P. Canarelli, "Turbine à gaz," *1131310*, 1955.

[31] E. Guenther, "Multi-combustion chamber gas turbine with rotary valving," *US2928242A*, 1960.

[32] M. Kadenacy, "APPARATUS FOR PRODUCING GAS UNDER PRESSURE."

[33] A. G. Forsyth, “Periodically Actuated Jet Motor,” *2427845*, 1947.

[34] J. Semery, “An intermittent combustion gas turbine plant,” *GB2035459A*, 1980.

[35] W. V. Taylor, “Gas turbine engine with rotary regenerator and rotating constant volume combustion chambers,” *3362157*, 1968.

[36] B. Robic, “Chambre de Combustion CVC pour turbomachine d’aeronef comprenant une valve d’admission/d’échappement à tournant sphérique,” *WO2014020275A1*, 2014.

[37] “ B. G. Macarez, ‘Pulsomoteur-Turbomoteur a impulsion-turbine a gaz a chambre de combustion impulsionnelle et a detente de bouffees,’ 2829528, 2001.”.

[38] “G. Taliercio, ‘Constant-volume combustion system for a turbine engine of an aircraft engine,’ WO2016132055, 2016.”.

[39] M. Leyko, “Constant-volume combustion module for a turbine engine, comprising communication-based ignition,” 11066990, Jul. 20, 2021

[40] M. Leyko, P. Moissy-Cramayel, and J. Metge, “Constant-volume combustion system comprising a rotating closure element with segmented apertures,” 2018

[41] C. Tempesti, L. Romani, M. Ciampolini, O. Hakuri, F. Ciccateri, and G. Ferrara, “Experimental methodology for the characterization of a hydrogen-fuelled Pressure Gain Combustor,” in *Journal of Physics: Conference Series*, Institute of Physics, 2023. doi: 10.1088/1742-6596/2648/1/012062.

[42] C. Tempesti, S. Grasa, L. Romani, F. Ciccateri, G. Ferrara, and G. Paniagua, “Numerical modeling of a deflagrative-based pressure gain combustor integrated with an axial turbine,” *Appl. Therm. Eng.*, vol. 290, Apr. 2026, doi: 10.1016/j.applthermaleng.2026.130128.

[43] Q. Michalski, B. Boust, and M. Bellenoue, “Influence of operating conditions and residual burned gas properties on cyclic operation of constant-volume combustion,” in *Notes on Numerical Fluid Mechanics and Multidisciplinary Design*, vol. 141, Springer Verlag, 2019, pp. 215–233. doi: 10.1007/978-3-319-98177-2_14.

[44] Q. Michalski, B. Boust, and M. Bellenoue, “Toward a cyclic self-ignited constant-volume combustion for airbreathing propulsion applications,” in *2018 Joint Propulsion*

Conference, American Institute of Aeronautics and Astronautics Inc, AIAA, 2018. doi: 10.2514/6.2018-4478.

[45] P. Gallis, D. A. Misul, B. Boust, M. Bellenoue, and S. Salvadori, "Development of 1D Model of Constant-Volume Combustor and Numerical Analysis of the Exhaust Nozzle," *Energies (Basel).*, vol. 17, no. 5, Mar. 2024, doi: 10.3390/en17051191.

[46] L. Labarrere, T. Poinsot, A. Dauptain, F. Duchaine, M. Bellenoue, and B. Boust, "Experimental and numerical study of cyclic variations in a Constant Volume Combustion chamber," *Combust. Flame*, vol. 172, pp. 49–61, Oct. 2016, doi: 10.1016/j.combustflame.2016.06.027.

[47] N. Detomaso, D. Laera, P. Pouech, and F. Duchaine, "Large Eddy Simulation of a pistonless constant volume combustor: a new concept of pressure gain combustion." ASME. *J. Eng. Gas Turbines Power*. February 2023; 145(2): 021025. doi: 10.1115/1.4056018

[48] B. Boust, Q. Michalski, and M. Bellenoue, "Experimental investigation of ignition and combustion processes in a constant-volume combustion chamber for air-breathing propulsion," in *52nd AIAA/SAE/ASEE Joint Propulsion Conference, 2016*, American Institute of Aeronautics and Astronautics Inc, AIAA, 2016. doi: 10.2514/6.2016-4699.

[49] B. Boust, M. Bellenoue, and Q. Michalski, "Pressure Gain and Specific Impulse Measurements in a Constant-Volume Combustor Coupled to an Exhaust Plenum," 2022, pp. 3–15. doi: 10.1007/978-3-030-90727-3_1.

[50] P. Gallis, D. Misul, S. Salvadori, M. Bellenoue, and B. Boust, "Development and Validation of a 0-D/1-D Model to Evaluate Pulsating Conditions from a Constant Volume Combustor."

[51] P. Gallis, D. A. Misul, B. Boust, M. Bellenoue, and S. Salvadori, "Numerical Analysis and Design of New Exhaust Section Downstream of Constant Volume Combustor," *J. Eng. Gas Turbine. Power*, vol. 147, no. 2, Feb. 2025, doi: 10.1115/1.4066253.

[52] L. Bonneau, V. Robin, and T. Xavier, "A computational framework combining a basic turbulent combustion model, self-similar chemistry behavior, and a wall thermal law adapted for large-eddy simulations of a cyclically operating constant volume combustion chamber," *Combust. Flame*, vol. 244, p. 112212, Oct. 2022, doi: 10.1016/j.combustflame.2022.112212.

[53] C. Mocquard, D. Laera, J. Dombard, and T. Poinsot, "A two-step chemical scheme for auto-igniting and propagating kerosene flames at reheat conditions," *Combust. Flame*, vol. 248, p. 112558, Feb. 2023, doi: 10.1016/j.combustflame.2022.112558.

[54] Q. Michalski, B. Boust, and M. Bellenoue, "Experimental Investigation of Ignition Stability in a Cyclic Constant-Volume Combustion Chamber Featuring Relevant Conditions for Air-Breathing Propulsion," *Flow Turbul. Combust.*, vol. 102, no. 2, pp. 279–298, Feb. 2019, doi: 10.1007/s10494-019-00015-1.

[55] Q. Michalski, K. Kha, B. Boust, V. Robin, M. Bellenoue, and A. Mura, "Joint Numerical and Experimental Characterization of the Turbulent Reactive Flow within a Constant Volume Vessel," in *2018 Joint Propulsion Conference*, Reston, Virginia: American Institute of Aeronautics and Astronautics, Jul. 2018. doi: 10.2514/6.2018-4964.

[56] M. C. de Jesus Vieira, J. Sotton, M. Bellenoue, and C. Strozzi, "Time-resolved high-speed PIV investigation of minimum ignition energy in propane/air/RBG mixtures under varying flow properties in a constant volume combustion chamber," in *AIAA SCITECH 2024 Forum*, Reston, Virginia: American Institute of Aeronautics and Astronautics, Jan. 2024. doi: 10.2514/6.2024-0397.

[57] Q. Michalski, B. Boust, and M. Bellenoue, "Influence of operating conditions and residual burned gas properties on cyclic operation of constant-volume combustion," in *Active Flow and Combustion Control*, 2018, pp. 215–233.

[58] P. Akbari and M. R. Nalim, "Review of recent developments in wave rotor combustion technology," in *Journal of Propulsion and Power*, American Institute of Aeronautics and Astronautics Inc., 2009, pp. 833–844. doi: 10.2514/1.34081.

[59] J. Duarte *et al.*, "Auto-ignition control in turbocharged internal combustion engines operating with gaseous fuels," *Energy*, vol. 71, pp. 137–147, Jul. 2014, doi: 10.1016/j.energy.2014.04.040.

[60] H.-J. Bauer and E.-4 Rolls-Royce, "New low emission strategies and combustor designs for civil aeroengine applications," 2004.

[61] S. S. Goldsborough, S. Hochgreb, G. Vanhove, M. S. Wooldridge, H. J. Curran, and C.-J. Sung, "Advances in rapid compression machine studies of low-and intermediate-temperature autoignition phenomena," 2017. [Online]. Available: http://www.elsevier.com/open-access/userlicense/1.0/

[62] A. Giusti, J. A. M. Sidey, G. Borghesi, and E. Mastorakos, “Simulations of droplet combustion under gas turbine conditions,” 2017. [Online]. Available: http://www.elsevier.com/open-access/userlicense/1.0/

[63] D. Fredrich and A. Giusti, “Numerical investigation of multi-component droplet evaporation and autoignition for aero-engine applications,” *Combust. Flame*, vol. 241, Jul. 2022, doi: 10.1016/j.combustflame.2022.112023.

[64] O. Hinkeldey, R. Koch, and H. Bauer, “‘Laser Based Study of Spray Auto-Ignition in a Generic Mixing Duct.’ ,” in *Proceedings of the ASME Turbo Expo 2008: Power for Land, Sea, and Air. Volume 3: Combustion, Fuels and Emissions, Parts A and B.* , 2008, pp. 37–46.

[65] Q. Michalski, A. Matino, B. Boust, and M. Bellenoue, “Geometry effects on the pressure, velocity field and operation of an airbreathing constant-volume combustion chamber,” in *AIAA Propulsion and Energy Forum and Exposition, 2019*, American Institute of Aeronautics and Astronautics Inc, AIAA, 2019. doi: 10.2514/6.2019-4211.

[66] A. Padhiary, “Analysis of heat loss during flame wall interaction of premixed propagative flames and diffusive spray flames,” 2022.

[67] Nanmac Specification Sheet, “‘Eroding’ Thermocouple A12D Series-Ultra High Temp Multi-Function Sensors.”

[68] J. Nanigian and D. Nanigian, “A UNIQUE THERMOCOUPLE TO MEASURE THE TEMPERATURES OF SQUIBS, IGNITERS, PROPELLANTS AND ROCKET NOZZLES SPIE Paper 6222-3.”

[69] B. Boust, “ÉTUDE EXPÉRIMENTALE ET MODÉLISATION DES PERTES THERMIQUES PARIÉTALES LORS DE L’INTERACTION FLAMME–PAROI INSTATIONNAIRE,” 2006.

[70] F. V. Tinaut, M. Reyes, B. Giménez, and J. V. Pastor, “Measurements of OH* and CH* chemiluminescence in premixed flames in a constant volume combustion bomb under autoignition conditions,” *Energy and Fuels*, vol. 25, no. 1, pp. 119–129, Jan. 2011, doi: 10.1021/ef1013456.

[71] C. Strozzi, J. Sotton, A. Mura, and M. Bellenoue, “Characterization of a two-dimensional temperature field within a rapid compression machine using a toluene planar laser-

induced fluorescence imaging technique," *Meas. Sci. Technol.*, vol. 20, no. 12, p. 125403, Dec. 2009, doi: 10.1088/0957-0233/20/12/125403.

[72] G. F. Hohenberg, "Advanced Approaches for Heat Transfer Calculations," *Society of Automotive Engineers, Inc.*, 1980.

[73] S. Labuda, M. Karrer, J. Sotton, and M. Bellenoue, "Experimental Study of Single-Wall Flame Quenching at High Pressures," *Combustion Science and Technology*, vol. 183, no. 5, pp. 409–426, Feb. 2011, doi: 10.1080/00102202.2010.528815.

[74] Y. Liu, J. Tan, M. Wan, L. Zhang, and X. Yao, "Quantitative Measurement of OH* and CH* Chemiluminescence in Jet Diffusion Flames," *ACS Omega*, vol. 5, no. 26, pp. 15922–15930, Jul. 2020, doi: 10.1021/acsomega.0c01093.

[75] J. B. . Heywood, *Internal combustion engine fundamentals*. McGraw-Hill Book Company, 1988.

[76] C. T. Chong and S. Hochgreb, "Measurements of laminar flame speeds of liquid fuels: Jet-A1, diesel, palm methyl esters and blends using particle imaging velocimetry (PIV)," *Proceedings of the Combustion Institute*, vol. 33, no. 1, pp. 979–986, 2011, doi: 10.1016/j.proci.2010.05.106.

[77] M. Leyko, "Constant-volume combustion module for a turbine engine, comprising communication-based ignition," 2017

[78] S. Labuda, M. Karrer, J. Sotton, and M. Bellenoue, "Experimental Study of Single-Wall Flame Quenching at High Pressures," *Combustion Science and Technology*, vol. 183, no. 5, pp. 409–426, Feb. 2011, doi: 10.1080/00102202.2010.528815.

[79] P. GALLIS, "Design Solutions for the Coupling of High-Pressure Turbine Vanes to Pressure-Gain Combustors," Politecnico di Torino, 2025.

[80] S. Biswas, S. Tanvir, H. Wang and L. Qiao, "On ignition mechanisms of premixed CH4/air and H2/air using a hot turbulent jet *generated by pre-chamber combustion." Applied Thermal Engineering*, no. 106, pp. 925-937, Aug. 2016.

Appendix A: Characterization of the air intake system

To ensure the proper functioning of the CV2 vessel, the main systems and subsystems of the CV2 must be carefully re-characterized.

The air intake system is responsible for delivering air to the combustion chamber, having a significant impact on the pressure inside the combustion chamber. During the intake process, air is drawn into the combustion chamber through the intake valves. As the air enters the intake system, it undergoes a process of compression due to the decreasing volume of the intake system. This process of compression can lead to an increase in temperature, which can have negative effects on engine performance and efficiency.

To limit the negative effects of adiabatic filling compression and temperature variation, the intake system is slowly pressurized from vacuum to a pressure of approximately 10 bar. By gradually pressurizing the intake system, the air is able to fill the system more uniformly, reducing the impact of compression and temperature changes.

To characterize the air intake and exhaust system, the following parameters were taken into consideration: air intake duration, exhaust duration, exhaust start time for an air intake pressure of 10 bar for a cycle frequency of 8 Hz (Time period: 125 ms). The air intake duration was varied in increments of 0.5 ms from 9 ms to 11 ms while the other two parameters were kept fixed (exhaust duration = 50 ms and exhaust start time = 60 ms). It was found out that the mass of air inside the combustion chamber increases linearly as the intake duration increases; validating the proper functioning of the intake system as seen in Figure A-1.

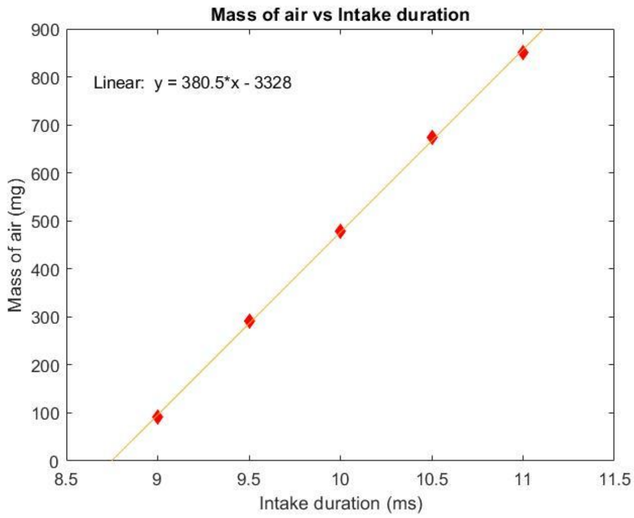

Figure A-1 Mass of air (mg) vs Air Intake Duration (ms)

In conclusion, the intake duration sets the initial pressure, which in turn governs the maximum pressure reached during combustion. With constant volume and adiabatic conditions, the chamber pressure rises in proportion to this starting value. Although the combustion chamber can withstand up to 50 bar, the absolute pressure sensor is limited to 20 bar. To keep within this range and assuming a fivefold increase, the target initial pressure is about 3.5 bar.

Appendix B: Characterization of the liquid fuel (n-Heptane) injection systems

The characterization of the liquid n-heptane is done ex-situ where the liquid injector (Bosch HDEV-5.1) is removed from the CV2 set-up and is suspended over a balance (Fisher Instruments, model PPS413C) placed over a beaker. The distance between the weighing beaker and injector is reduced to avoid splash and it is ensured that the assembly is properly level (i.e. parallel horizontally). The balance has a maximum capacity of 410 g and a precision of 1 mg. The injector is mounted in its original flange and it is at an ambient temperature of 20 °C. The fuel is pressurized to 100 bar.

The air intake duration is set to 0 ms and the fuel injection time is varied from 1 to 10 ms. The exhaust duration and start time are kept constant. At each measurement point, a series of ten injections is performed at a frequency of 8 Hz (corresponding to the typical operating cycle). Each measurement point is repeated three times as seen in Figure B-1. It was found out that the mass of n-heptane injected increases linearly as the intake duration increases; validating the proper functioning of the n-Heptane injection system.

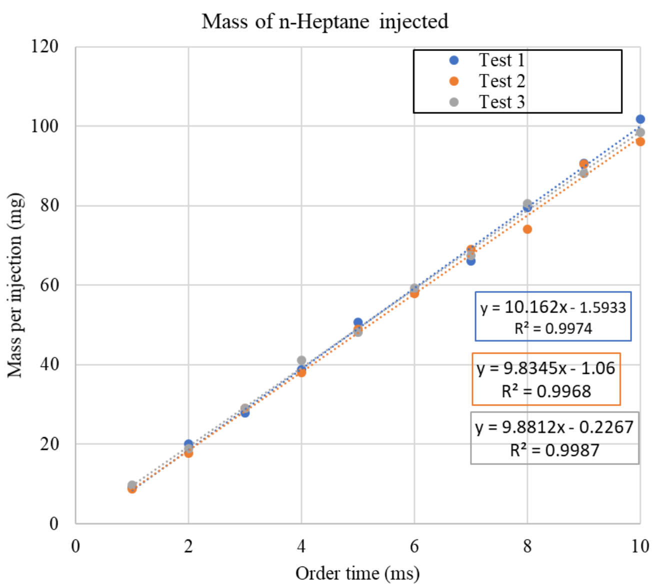

Figure B-1 Mass of n-heptane injected (mg) vs injection duration (ms)

An average value of each points was calculated and the average mass of n-Heptane injected was calculated from this result (plotted in Figure B-2). The average mass flow rate of liquid fuel injector was hence found to be approximately 10 g/s, concluding the Equivalence Ratio can be predicted, enabling control over the experimental conditions.

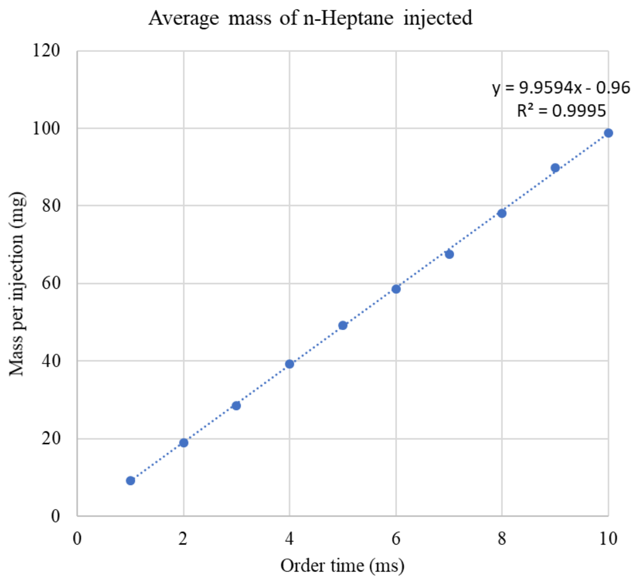

Figure B-2 Average mass of n-heptane injected (mg) vs injection duration (ms)

However, since this characterization has been done ex-situ with the temperature inside the beaker being at ambient temperature, i.e. 20 °C, in the experimental test bench, the combustion chamber is at 130 °C. Considering these factors, the mass flow rate of the liquid fuel injector is found to be around 8.5 g/s. These tests were also carried out for n-decane and n-octane to verify the fidelity of the liquid injection system.

Appendix C: Characterization of the exhaust system

To characterize the exhaust system, the exhaust duration was varied from 30 to 50 ms for the same cycle frequency (8 Hz) as the air intake system in increment of 10 ms while keeping the air intake duration and exhaust start time constant. This experiment determined the proper functioning of the exhaust system, as the air pressure inside the combustion chamber evacuated to return to the same value of the pressure inside the exhaust tank.

In summary, for an intake tank of 10 bar, the intake duration must be at least 10 ms for a cycle duration of 125 ms. An exhaust duration of 50 ms seems convenient in order to have more cycles for a certain duration. While for the exhaust start time, 40 ms is a good value to be noted. Figure C-1 shows the chronogram for an ideal cycle using the conditions stated above where the pressure inside the combustion chamber reached the pressure inside the exhaust pressure (1 bar). This exhaust duration is varied to shorten the cooling phase.

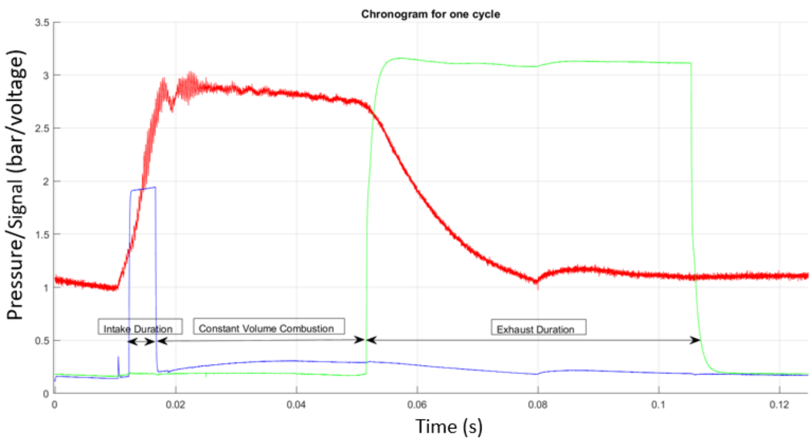

Figure C-1 The intake and exhaust duration of an ideal cycle

Résumé étendu

Chapitre 1 : Introduction

Contexte et objectifs

Au cours des dernières décennies, l'industrie aéronautique a connu des transformations et des avancées majeures, entraînant une véritable révolution du transport aérien. L'une des évolutions clés ayant contribué à cette révolution est l'introduction des moteurs à réaction. Apparues dans les années 1950, ces technologies ont permis des vols plus rapides et plus attractifs. En remplaçant les anciens moteurs à pistons et hélices, elles ont rendu possible le vol à plus haute altitude et à plus grande vitesse, rendant les voyages long-courriers plus courts et plus abordables.

Cependant, l'augmentation du transport aérien s'est accompagnée d'impacts environnementaux significatifs. En 2021, le transport aérien représentait environ 2 % des émissions mondiales de CO_2. Si ce pourcentage peut sembler relativement faible, il correspond en valeur absolue à environ 915 millions de tonnes de CO_2 par an, selon le Groupe d'experts intergouvernemental sur l'évolution du climat (GIEC) [1]. De plus, les émissions aéronautiques exercent une influence supplémentaire car elles sont rejetées à haute altitude, ce qui amplifie leur effet de réchauffant global. Cette contribution pourrait atteindre 3 % d'ici 2050 [2], en raison de l'augmentation de la demande de transport aérien.

Pour répondre à cette problématique complexe, le Conseil consultatif pour la recherche et l'innovation en aéronautique en Europe (ACARE) a fixé des objectifs ambitieux visant à réduire de 75 % les émissions de CO_2 d'ici 2050 par rapport aux niveaux enregistrés en 2000 [3]. Bien que les objectifs chiffrés et leur répartition aient évolué au fil du temps, la conclusion principale reste inchangée : l'amélioration de l'efficacité des avions, de l'efficacité des moteurs, l'utilisation de carburants d'aviation durables (SAF) et l'optimisation de la gestion du trafic aérien constituent les principaux leviers de réduction des émissions.

L'amélioration de l'efficacité des moteurs peut être obtenue par l'augmentation du rendement propulsif ou du rendement thermique. Le rendement propulsif est amélioré par l'optimisation de la conception des moteurs et par l'augmentation du taux de dilution (Bypass Ratio, BPR), ce qui permet une meilleure conversion de l'énergie utile en poussée. Le rendement thermique peut être accru en augmentant le taux de compression global (OPR), ce qui accroît la conversion de l'énergie chimique en énergie utile, ou en modifiant le cycle thermodynamique afin d'autoriser une conversion d'énergie plus efficace de la combustion. Ensemble, ces évolutions permettent aux moteurs de produire davantage de puissance tout en consommant moins de carburant.

Cependant, l'augmentation de l'OPR et de la TET (température entrée turbine) est limitée par des contraintes de taille, de masse et de matériaux. De plus, les conceptions actuelles semblent avoir quasi-atteint un plateau [4]. Parallèlement, un regain d'intérêt se manifeste pour repousser les limites du rendement thermodynamique des turbines à gaz.

Une autre piste prometteuse consiste à repenser le processus de combustion lui-même. Les turbines à gaz traditionnelles fonctionnent avec une combustion isobare. Les analyses exergétiques du cycle de Brayton montrent que la chambre de combustion est responsable de la majorité des irréversibilités et des pertes d'efficacité du système. La combustion à pression constante entraîne une augmentation significative de l'entropie et donc une perte d'énergie disponible. Par conséquent, c'est au niveau du processus de combustion et de la stratégie d'utilisation du carburant que réside le plus grand potentiel pour réaliser un nouveau saut en termes d'efficacité des turbines à gaz.

Ainsi, l'optimisation d'un cycle de combustion alternatif apparaît comme une voie prometteuse pour réduire la production d'entropie et améliorer le rendement global. Dans ce contexte, le programme INSPIRE (INSpiring Pressure Gain Combustion Integration, Research and Education), un réseau européen de formation innovante Marie Skłodowska-Curie (ITN), réunit un consortium d'universités, de laboratoires de recherche et d'industriels afin d'étudier, à un niveau d'intégration innovant, les solutions les plus prometteuses de combustion à gain de pression (PGC), notamment la combustion à volume constant (CVC) et les moteurs à détonation rotative (RDE).

La configuration expérimentale de référence est la chambre CV2 (enceinte de combustion à volume constant). Ce banc d'essai a été développé précédemment dans le cadre de la Chaire CAPA, un programme de recherche collaboratif ANR–SAFRAN Tech–MBDA France dirigé par l'Institut Pprime, afin d'étudier les aspects fondamentaux de la combustion à volume constant [6], sans les contraintes technologiques liées aux systèmes d'admission et d'échappement des chambres de combustion de moteurs réels.

Structure de la thèse

Ce travail est organisé en cinq chapitres.

Le chapitre 1 introduit le sujet de recherche, présente le contexte général et expose les motivations pour l'exploration de cycles de combustion alternatifs dans les applications aérospatiales.

Le chapitre 2 passe en revue les concepts fondamentaux de la combustion à gain de pression, un cycle de combustion alternatif. Il présente également l'état de l'art et les limites des stratégies d'allumage par étincelle en combustion à volume constant, l'une des formes de combustion à gain de pression. En outre, il examine le potentiel des stratégies d'auto-allumage de carburants liquides et définit les objectifs de la présente étude.

Le chapitre 3 décrit le dispositif expérimental, les techniques de diagnostic et la méthodologie d'analyse. Il présente également le modèle interne 0D/1D utilisé pour estimer certains paramètres difficiles à mesurer directement dans le dispositif expérimental, afin d'analyser plus en profondeur le processus de combustion ainsi que les pertes thermiques aux parois au cours d'un cycle.

Le chapitre 4 présente un cas de référence détaillé pour la stratégie d'allumage commandé (par étincelle) et analyse les études paramétriques réalisées à l'aide de la méthodologie décrite au chapitre 3.

Le chapitre 5 explique les mécanismes conduisant à l'auto-allumage dans le dispositif expérimental et propose un cas de référence détaillé. Il discute également des études paramétriques menées afin d'évaluer la sensibilité de cette stratégie d'allumage.

Le manuscrit se conclut par un résumé des principaux résultats et propose des perspectives pour les travaux futurs.

Chapitre 2 : État de l'art – Résumé

Ce chapitre établit les fondements scientifiques et technologiques permettant l'exploration de la combustion à gain de pression (PGC) comme voie vers des systèmes de propulsion aéronautique plus efficaces. Il commence par contextualiser l'impératif environnemental qui motive la recherche en aéronautique, en soulignant les limitations des turbomachines conventionnelles fonctionnant selon le cycle de Brayton et les avantages thermodynamiques offerts par des cycles de combustion alternatifs. La discussion progresse ensuite à travers une revue historique complète des technologies PGC, aboutissant à un examen approfondi de la combustion à volume constant (CVC) dans des configurations sans piston et des défis associés aux stratégies d'allumage commandé (par étincelle).

La combustion à gain de pression englobe tous les processus de combustion qui produisent une augmentation nette de la pression d'arrêt pendant le dégagement de chaleur. Contrairement à la combustion à pression constante en écoulement stationnaire, qui entraîne intrinsèquement des pertes de pression d'arrêt, la PGC est un processus instationnaire dans lequel l'expansion des gaz pendant la combustion est contrainte, permettant l'extraction de travail lorsque l'écoulement se détend jusqu'à une pression désirée. L'obtention de la PGC nécessite de satisfaire plusieurs conditions clés : la combustion doit se produire à volume constant pour maximiser l'augmentation de pression ; la formation d'ondes de choc et les pertes associées doivent être minimisées ; et, idéalement, aucune pièce mobile ne devrait être présente dans le passage principal du flux d'air pour assurer la simplicité et la fiabilité du système. Satisfaire ces exigences a conduit à des générations successives de concepts PGC, tel que les moteurs à détonation pulsée (PDE), les moteurs à détonation rotative (RDE), le Wave rotor, la combustion par explosion sans choc (SEC) et la CVC, chacune présentant des avantages et des inconvénients.

Concernant la CVC, l'application pratique la plus étudiée est le moteur à combustion interne alternatif (ICE), bénéficiant de plus d'un siècle de recherche et développement. Les ICE emploient des pistons se déplaçant entre le point mort haut et le point mort bas. Le comportement thermodynamique approxime le cycle d'Otto, l'efficacité augmentant avec des rapports de compression plus élevés. Malgré ces avantages, les ICE présentent des limitations pour la propulsion aérobie : les pistons imposent des contraintes sur la vitesse de rotation maximale dues à l'inertie et aux limites de vitesse moyenne du piston, les pertes par friction et les contraintes mécaniques limitent les rapports puissance-poids et puissance-cylindrée.

Pour la propulsion aérospatiale, supprimer le piston permet des vitesses de cycle plus élevées, un écoulement plus régulier et une densité de puissance accrue. De nombreux brevets et efforts de recherche ont proposé des architectures sans piston. Les premières tentatives industrielles incluent la turbine à gaz de H. Holzwarth (1905. Les brevets ultérieurs de C.A.L. Bosco (1948), P. Canarelli (1955), E. Guenther (1960), Kadenacy (1948), A.G. Forsyth (1941), J. Semery (1980), W.V. Taylor (1968) et les efforts plus récents de SAFRAN (B. Robic, G. Taliercio, B.G. Macarez) ont exploré diverses configurations de distributeur rotatif et de vannes. En 2016, M. Leyko a breveté un module de combustion visant la combustion à volume constant pour turboréacteurs, turbopropulseurs et configurations à Open-rotor, proposant le transfert de gaz brûlés entre chambres pour déclencher la combustion sans allumeurs à étincelle. Malgré ces efforts, les systèmes CVC précoces n'ont pas atteint la maturité industrielle en raison de défis techniques importants.

La recherche fondamentale sur la CVC sans piston reste limitée, conduite principalement par des groupes de recherche en France et en Italie. L'Université de Florence, le Politecnico di Milano, l'Institut PPrime, le Politecnico di Torino et le CERFACS ont contribué à des études expérimentales et numériques. L'Institut PPrime a développé le banc d'essai CVC doté de vannes rotatives contrôlant l'admission et l'échappement, démontrant la faisabilité d'un fonctionnement à haute fréquence mais observant qu'au-delà d'une certaine fréquence (en l'occurrence environ 40 Hz), la durée de combustion devenait trop longue, conduisant à des variations cycle-à-cycle plus fortes. La modélisation 0D/1D conjointe à ces essais et des simulations numériques 3D ont complété l'étude expérimentale conduite sur ce banc. Un autre banc d'essai de combustion à volume constant (CV2), étudié par Q. Michalski à PPrime, surmonte les principales limitations technologiques du banc CVC, permettant un accès optique complet et une modularité optimale pour des investigations canoniques. Les simulations aux grandes échelles (LES) développées par Bonneau et Detomaso couplent des modèles de combustion turbulente de type flammelettes simplifiés avec des bases de données thermochimiques réduites, reproduisant les signaux de pression mesurés et de flux thermique aux parois tout en identifiant le rôle des gaz brûlés résiduels (RBG).

Le chapitre conclut en identifiant les objectifs de recherche : étudier la faisabilité de remplacer l'allumage commandé (par étincelle) par un auto-allumage contrôlé dans la chambre CV2 sans piston. S'il est correctement contrôlé, l'auto-allumage éliminerait les exigences de bougie, permettrait un fonctionnement à des rapports de compression et températures plus élevés et résulterait en une utilisation plus efficace du carburant. La transition des stratégies d'allumage par étincelle vers l'auto-allumage représente une voie critique vers l'exploitation du plein potentiel thermodynamique de la combustion à volume constant pour les applications de propulsion aérospatiale.

Chapitre 3 : Le dispositif expérimental CV2 et son modèle réduit 0D/1D

Ce chapitre est consacré à la présentation détaillée des matériels, outils et méthodes mobilisés pour la réalisation de l'étude, dont la majorité a été adaptée spécifiquement au cadre expérimental retenu. Il s'articule autour de trois axes principaux : la description du dispositif expérimental CV2, les diagnostics expérimentaux mis en œuvre et le modèle physique 0D/1D développé pour l'analyse phénoménologique.

La première partie présente la structure du banc d'essais CV2 (Constant Volume Combustion Vessel). Ce banc, installé à l'Institut PPRIME, reproduit à l'échelle du laboratoire les conditions thermodynamiques d'une chambre de combustion à volume constant sans piston, avec une séquence de cycles entièrement configurable. Son architecture, ses sous-systèmes tels que le système d'admission, la chambre de combustion et le système d'échappement, et ses conditions aux limites sont détaillés dans ce chapitre. Une attention particulière est portée à la caractérisation précise du système d'admission, qui permet un contrôle rigoureux des masses injectées, le calcul précis de la richesse dans la chambre. Le système d'échappement permet la régulation de la contre-pression à l'échappement. L'ensemble des paramètres pertinents est finement caractérisé et les incertitudes associées sont quantifiées. Cette maîtrise expérimentale constitue un prérequis essentiel au développement et à la validation du modèle 0D/1D, et elle facilite l'interprétation ultérieure des phénomènes physiques observés.

La deuxième partie est consacrée aux diagnostics expérimentaux. Elle décrit en détail les capteurs physiques utilisés (pression, flux thermique, température, masses injectées, etc.) ainsi que les techniques de vélocimétrie et de diagnostics optiques mises en œuvre. Parmi ces diagnostics, on peut citer l'analyse du signal de pression. Cette analyse permet d'identifier les différentes phases du cycle et d'extraire les principaux paramètres thermodynamiques. Parmi ces paramètres figurent la pression initiale et la pression maximale. Ces valeurs permettent notamment de déterminer le taux de compression, ainsi que de caractériser la durée de combustion et le taux de montée maximale pour les deux types de stratégies d'allumage.

La masse d'air admise est déterminée à partir d'un bilan de masse basé sur la chute de pression ΔP mesurée dans le réservoir d'admission. La masse de carburant injectée est quantifiée à partir des paramètres du système d'injection de carburant liquide. Le rapport de richesse est ensuite calculé à partir du rapport entre la masse de carburant injectée et la masse d'air admise dans la chambre de combustion. Le flux de chaleur pariétal local est mesuré à partir du signal de température d'un thermocouple de surface et d'une analyse intégro-différentielle.

Pour l'analyse de vélocimétrie, la PIV rapide (10-20 kHz) utilise un laser bi-cavité 532 nm et une caméra Photron SA-Z, l'air étant ensemencé en particules fluides depuis le réservoir d'admission. Finalement, pour visualiser les front réactifs, l'imagerie de chimiluminescence à haute cadence (OH* à 310 nm, CH* à 430 nm, imagerie couleur large bande) suit en temps réel la formation du noyau d'allumage, la propagation du front de flamme et le dégagement de chaleur. Ces approches permettent d'obtenir une caractérisation complète du comportement de l'écoulement réactif. L'analyse des capacités et des contraintes expérimentales permet ainsi de définir le périmètre d'exploitation fiable des données acquises.

La troisième partie introduit le modèle 0D/1D précédemment développé en interne et adapté à la configuration d'injection directe de carburant liquide et aux conditions d'auto-allumage. Ce code de simulation physique permet de prédire le comportement cyclique de la chambre de combustion à volume constant. Il offre un accès à des grandeurs thermodynamiques difficiles à mesurer expérimentalement, telles que la fraction de gaz brûlés résiduels et les pertes thermiques.

L'architecture de la chambre CV2 couple trois actionneurs (admission air A1, carburant A2, échappement A3) à la chambre de combustion CC via un réseau de volumes parfaits 0D reliés par conduites 1D. La combustion se modélise par "tranchage", en ajustant itérativement la loi de dégagement de chaleur sur la courbe de pression pour l'allumage commandé, et une combustion en continu pour l'auto-allumage. Les hypothèses principales incluent un modèle de gaz parfait, la conservation de la masse et de l'énergie, et un modèle convectif de transfert thermique aux parois. Le modèle a été validé pour l'ensemble des phases du cycle à allumage commandé et à auto-allumage : admission, combustion et échappement ; garantissant ainsi la cohérence et la fiabilité des évolutions prédites. Le modèle 0D/1D validé permet ainsi la quantification précise des pertes thermiques et de la dilution par les RBG.

Ces outils essentiels sous-tendent directement l'analyse comparative entre allumage commandé et auto-allumage développée aux chapitres 4 et 5, assurant la robustesse des résultats et leur interprétation scientifique quantitative.

Chapitre 4 : Combustion cyclique à volume constant par allumage commandé avec injection de carburant liquide

Le présent chapitre introduit des conditions de référence fondées sur l'injection de n-heptane liquide dans le dispositif CV2. Dans le contexte aéronautique, les carburants sont majoritairement stockés et acheminés sous forme liquide, en raison de leur forte densité énergétique et de leur compatibilité avec des systèmes de stockage embarqués compacts. Au sein de l'installation CV2, l'utilisation d'un carburant liquide présente plusieurs avantages déterminants. Elle permet notamment une injection à haute pression (100 bar), rendant le débit massique injecté insensible aux variations de pression dans la chambre, contrairement aux injecteurs basse pression utilisés auparavant pour du carburant gazeux. Cette configuration assure un meilleur contrôle du processus d'injection, une excellente répétabilité et une meilleure représentativité des conditions de fonctionnement pertinentes pour les systèmes de propulsion aéronautique.

L'objectif de ce chapitre est d'identifier les leviers d'optimisation du cycle de combustion et d'évaluer le rendement thermodynamique du processus de combustion à volume constant. Un cycle stable de référence a été analysé en détail à une fréquence de 8 Hz (OER = 0,9 ; tign = 25 ms ; Pex = 2 bar), mettant en évidence les phénomènes-clés gouvernant la combustion à volume constant sans piston, initiée par étincelle.

Les mesures de chimiluminescence ont montré que la variabilité cycle-à-cycle la plus importante apparaît lors des premières phases de développement de la flamme, comme l'indique le signal CH*. À mesure que la combustion progresse, le processus se stabilise et atteint son intensité maximale, mise en évidence également par le signal OH*.

Une étude paramétrique a été menée afin d'évaluer l'influence des principaux paramètres contrôlant la stabilité de la combustion au cours des cycles à allumage commandé: la richesse du mélange, la contre-pression à l'échappement, la fréquence du cycle et l'avance à l'allumage. L'analyse des essais concernant l'influence de la richesse montre que le domaine OER = 0,9–1 constitue un compromis favorable, permettant d'atteindre des pressions maximales élevées tout en réduisant la durée de combustion. Lors de la variation de la contre-pression d'échappement, la pression initiale d'admission a été maintenue constante; la présence d'environ 23 % de gaz brûlés résiduels n'a ainsi exercé qu'une influence limitée sur le comportement global du cycle.

La phase de refroidissement du cycle de référence a été optimisée en avançant l'ouverture de la vanne d'échappement, ce qui a permis d'augmenter la fréquence des cycles à 10 Hz. Cette configuration a été définie comme le cycle *optimcool*. Une réduction supplémentaire de la durée d'échappement a conduit au cycle *optimexhaust*, atteignant une fréquence de cycles de 12,5 Hz. Une analyse énergétique 0D/1D a mis en évidence une amélioration des performances thermiques aux fréquences plus élevées, confirmant une réduction des pertes et une augmentation du rendement.

La répartition des pertes thermiques au cours des différentes phases des trois types de cycle à allumage commandé a également été évaluée. La phase de combustion a été identifiée comme la principale contributrice, représentant environ 37,4 % à 41,4 % des pertes thermiques totales. L'optimisation complète de la phase de refroidissement du cycle de référence a permis de réduire significativement ces pertes dans les configurations *optimcool* et *optimexhaust.*

L'étude paramétrique de l'avance à l'allumage a montré que l'instant d'allumage de 25 ms, retenu dans le cas de référence, correspond à une condition optimale pour assurer la stabilité des cycles secondaires. Un allumage plus précoce est fortement influencé par la turbulence générée lors de l'admission, caractérisée par des vitesses moyennes de l'ordre de 10 m/s et des fluctuations turbulentes d'environ 5 m/s, comme révélé par l'analyse PIV. Les résultats PIV indiquent également qu'au cours de la combustion, la turbulence décroît en raison de l'augmentation de la viscosité des gaz et de leur compression. La propagation de la flamme s'effectue ainsi dans un champ d'écoulement de faible intensité, avec une interaction aérodynamique limitée.

Dans l'ensemble, la complexité des phénomènes couplés rend l'obtention d'un fonctionnement stable et performant particulièrement délicate. En régime d'allumage commandé, l'initiation de la combustion dépend fortement de la vitesse locale d'écoulement et du niveau de turbulence au moment de l'étincelle, ce qui accroît la sensibilité cycle-à-cycle. Afin de réduire cette dépendance et d'améliorer la robustesse du fonctionnement, le chapitre 5 explore le fonctionnement de la combustion à volume constant sans piston en régime d'auto-allumage, avec pour objectif de s'affranchir de la dépendance systématique au calage de l'étincelle.

Chapitre 5 : Combustion cyclique à volume constant par auto-allumage avec carburant liquide

Les systèmes d'allumage par étincelle, étudiés au chapitre 4, présentent des limitations intrinsèques, notamment en termes de durabilité et de durée de vie. Les allumeurs automobiles sont conçus pour des dépôts d'énergie modérés (quelques dizaines de mJ par impulsion) et peuvent générer plusieurs centaines de millions d'étincelles à des fréquences atteignant 50–60 Hz grâce à une technologie de décharge à haute tension. À l'inverse, les allumeurs aéronautiques délivrent des énergies plus élevées (jusqu'à plusieurs centaines de mJ par étincelle), à des fréquences plus faibles (typiquement 2 Hz), avec une durée de vie de l'ordre de quelques millions d'étincelles. Ils reposent sur une technologie à fort courant afin de respecter les contraintes liées à la compatibilité électromagnétique et aux environnements radiatifs sévères. Ces limitations motivent l'exploration de stratégies d'allumage alternatives permettant de réduire, voire de supprimer, la dépendance aux systèmes à bougie.

Le présent chapitre étudie un concept de combustion multi-chambres destiné à fournir une puissance suffisante pour des applications pratiques. Dans cette configuration, l'allumage par étincelle est conservé uniquement pour initier la combustion dans la première chambre et établir les conditions thermodynamiques initiales. L'allumage dans les chambres suivantes est ensuite déclenché par le transfert de gaz brûlés chauds en provenance de la chambre N-1, sans recours à un dispositif d'allumage local. Ce processus, répété d'une chambre à l'autre, correspond à un mode de fonctionnement qualifié d'auto-allumage, par opposition à l'allumage conventionnel par étincelle.

Dans le dispositif CV2, la mise en œuvre de l'auto-allumage est réalisée à l'aide d'une chambre unique. Bien que la configuration CV2 ne comporte qu'une seule chambre de combustion, elle est conçue pour simuler les conditions thermodynamiques associées au transfert de gaz brûlés dans un système multi-chambres. L'auto-allumage peut être obtenu en retardant le moment de l'allumage et/ou en augmentant la pression d'échappement. L'ajustement combiné de ces deux paramètres s'est révélé être l'approche la plus représentative pour reproduire les conditions attendues lors du transfert de gaz brûlés. Dans ce cadre, un cycle stable de référence en auto-allumage a été sélectionné.

Ce cycle de référence a été étudié à 8 Hz (tign = 25 ms, Pex = 2 bar). Il est initié par un cycle assisté par étincelle, analogue au fonctionnement d'une chambre secondaire dans un système multi-chambres. L'auto-allumage se produit ensuite durant la phase de combustion. Les mesures PIV montrent que, durant la phase combinée admission–combustion, le champ de vitesse est plus faible (environ 18 m/s) que dans le cycle à allumage par étincelle (environ 38 m/s). Cette différence s'explique par l'élévation de pression liée à la combustion, qui intervient pendant la phase d'admission et limite l'écoulement d'air entrant. En conséquence, la masse d'air admise est réduite et le mélange devient plus riche. Ainsi, bien que l'objectif initial soit un rapport d'équivalence pauvre (OER = 0,95), la combustion se déroule finalement à un rapport riche (OER ≈ 1,27).

Contrairement au processus à allumage commandé, l'auto-allumage peut se produire avec succès dans des conditions fortement turbulentes. Dans ce cas, la combustion est favorisée par les fluctuations turbulentes élevées (environ 10 m/s), qui accélèrent la propagation de flamme.

Une étude paramétrique a été menée afin d'évaluer l'influence des principaux paramètres contrôlant la stabilité de l'auto-allumage : l'instant d'allumage, la contre-pression d'échappement et la fréquence du cycle. Le positionnement de l'allumage pendant la phase d'échappement a permis d'obtenir un auto-allumage stable. Lors de la variation de la contre-pression, la pression initiale d'admission a été maintenue constante; la présence d'environ 26 % de gaz brûlés résiduels n'a eu qu'une influence modérée sur le comportement global du cycle, tout en augmentant la probabilité de réussite des cycles en auto-allumage.

La phase de refroidissement du cycle de référence a été partiellement optimisée en avançant l'ouverture de la vanne d'échappement, ce qui a permis d'augmenter la fréquence des cycles à 10 Hz (cycle *optimcool*). Une réduction supplémentaire de la durée d'échappement a conduit au cycle *optimexhaust*, de fréquence 12,5 Hz. L'analyse énergétique 0D/1D a démontré une amélioration des performances thermiques aux fréquences plus élevées, confirmant une réduction des pertes et une augmentation du rendement.

La répartition des pertes thermiques au cours des différentes phases des trois types de cycles en auto-allumage a également été évaluée. La phase combinée admission–combustion constitue la principale source de pertes, représentant environ 48,3 % à 55,7 % des pertes thermiques totales. La phase de refroidissement n'ayant pas été entièrement optimisée, elle offre un potentiel d'amélioration supplémentaire d'environ 11,4 %. La suppression de cette phase, correspondant à une réduction de 15 ms de la durée du cycle, permettrait d'augmenter la fréquence jusqu'à 15,4 Hz et d'accroître la puissance délivrée d'environ 23 %.

Dans l'ensemble, ces résultats démontrent le potentiel de l'auto-allumage pour améliorer la robustesse du fonctionnement et réduire la dépendance aux dispositifs d'allumage conventionnels, tout en ouvrant des perspectives significatives d'augmentation de performance et de densité de puissance.

Chapitre 6 : Conclusion générale et perspectives

Dans un contexte marqué par l'augmentation continue du trafic aérien et par des contraintes environnementales de plus en plus strictes, la décarbonation du transport aérien constitue un défi technologique majeur. Les objectifs fixés par l'Advisory Council for Aviation Research and Innovation in Europe (ACARE), visant une réduction de 75 % des émissions de CO_2 d'ici 2050 par rapport aux niveaux de l'an 2000, imposent une rupture dans la conception des systèmes propulsifs. Les turbomachines actuelles ayant atteint un haut degré de maturité technologique, les marges de progression en termes de rendement au sein du paradigme classique de la combustion à pression constante apparaissent désormais limitées. Dans ce contexte, l'amélioration substantielle des performances nécessite une remise en question plus profonde du cycle thermodynamique lui-même.

La combustion à gain de pression (PGC), et plus particulièrement la combustion à volume constant (CVC), représente une alternative prometteuse. En s'approchant d'une combustion à volume quasi constant, elle permet d'augmenter le rendement global du cycle. Les fondements thermodynamiques des cycles de Humphrey et de Fickett-Jacobs, plus performants que le cycle de Brayton conventionnel, ont été discutés, tout comme l'évolution historique des systèmes CVC. Si les premières démonstrations ont confirmé le potentiel théorique de la combustion à gain de pression, des verrous techniques persistants tel que les charges thermiques élevées, la complexité mécanique, la maîtrise de l'allumage, ont freiné leur déploiement industriel. Les recherches récentes se sont ainsi orientées vers l'étude fondamentale de systèmes CVC sans piston, afin de mieux comprendre les mécanismes d'allumage, de propagation de flamme et l'influence des gaz résiduels en conditions fortement diluées.

Les travaux présentés dans cette thèse s'inscrivent dans le cadre du réseau européen INSPIRE (Marie Skłodowska-Curie Innovative Training Network), dédié à l'intégration avancée de concepts de combustion à gain de pression. Le banc expérimental CV2, développé à l'Institut Pprime dans le cadre de la Chaire CAPA (ANR–SAFRAN Tech–MBDA France), a constitué l'outil central de cette étude. Il permet un contrôle précis des conditions aux limites d'admission et d'échappement, une détermination rigoureuse des masses injectées, de la richesse et de la fraction de gaz résiduels. L'instrumentation complète, combinant capteurs conventionnels et diagnostics optiques, assure une caractérisation fine de la dynamique de combustion.

Un modèle interne 0D/1D, initialement développé pour des carburants gazeux, a été adapté à l'injection de carburant liquide et étendu au fonctionnement en auto-allumage. Validé pour l'ensemble des phases du cycle à allumage commandé (admission, combustion, échappement), il fournit des prédictions fiables des évolutions de masse, d'énergie et de pression, et constitue un outil robuste pour l'interprétation physique des phénomènes cycliques.

Apports relatifs à l'allumage commandé par étincelle

La caractérisation détaillée d'un cycle de référence à allumage par étincelle a mis en évidence que la variabilité cycle-à-cycle est maximale lors des premières phases de développement de la flamme, comme révélé par l'analyse des signaux de chimiluminescence CH* et OH*. L'étude paramétrique a montré qu'une richesse comprise entre 0,9 et 1 représente un compromis optimal entre pression de combustion maximale et durée de combustion.

L'augmentation de la fréquence des cycles de 8 Hz à 10 Hz (*optimcool*), puis à 12,5 Hz (*optimexhaust*), a permis de réduire les pertes thermiques globales et d'améliorer les performances énergétiques, comme confirmé par l'analyse 0D/1D. La phase de combustion demeure néanmoins la principale source de pertes (environ 37 à 41 % des pertes totales).

Les mesures PIV ont révélé une dépendance marquée de la stabilité de la combustion à la vitesse locale d'écoulement et au niveau de turbulence au moment de l'étincelle. Cette sensibilité intrinsèque constitue une limite fondamentale du fonctionnement CVC sans piston à allumage commandé.

Apports relatifs à l'auto-allumage

Afin de dépasser ces limitations, le fonctionnement en auto-allumage a été étudié. Deux leviers complémentaires ont été identifiés : l'instant d'allumage et l'augmentation de la contre-pression d'échappement. Leur combinaison permet de reproduire, au sein de la chambre CV2, les conditions thermodynamiques caractéristiques d'un transfert de gaz brûlés comme dans une architecture multi-chambres.

Le cycle de référence en auto-allumage, étudié à 8 Hz, présente des différences notables par rapport au cycle à allumage commandé. L'élévation de pression durant l'admission limite l'entrée d'air et conduit à un mélange effectivement riche (OER ≈ 1,27), malgré une consigne initiale pauvre. La combustion s'avère moins dépendante des conditions aérodynamiques locales et peut se développer en présence d'une forte fluctuation turbulente (~10 m/s), traduisant un mécanisme de stabilisation fondamentalement différent.

L'optimisation des durées de refroidissement et d'échappement a permis d'atteindre 12,5 Hz, avec une amélioration confirmée du rendement thermique. La phase combinée admission–combustion représente la part majoritaire des pertes (48 à 56 %). Des marges d'amélioration subsistent: la suppression d'environ 15 ms de refroidissement permettrait d'atteindre 15,4 Hz, avec un gain potentiel de puissance de 23 % et une réduction estimée des pertes de 11,4 %.

Perspectives

Les résultats combinés des investigations en allumage par étincelle et par auto-allumage offrent une vision complète du fonctionnement CVC sans piston sous contraintes réalistes. Si l'allumage commandé démontre des bénéfices thermodynamiques clairs à haute fréquence, il reste fortement tributaire des conditions locales d'écoulement.

L'auto-allumage, en revanche, repose davantage sur l'état thermochimique du mélange et sur les fluctuations turbulentes que sur un calage précis de l'étincelle. Elle constitue ainsi une voie prometteuse vers des systèmes de combustion à gain de pression plus robustes, notamment dans des architectures multi-chambres où le transfert de gaz brûlés peut naturellement piloter l'initiation de la combustion.

Ce changement de paradigme introduit toutefois de nouveaux défis : la maîtrise fine de la préparation du mélange, de la fraction de gaz résiduels, de la richesse et de la gestion thermique devient essentielle pour garantir la répétabilité et éviter les phénomènes d'auto-allumage incontrôlé.

Dans le cadre du projet INSPIRE, des travaux complémentaires ont étudié l'intégration d'une chambre CVC avec une turbine haute pression conventionnelle, mettant en évidence une modulation de pression importante en régime à étincelle. Le régime en auto-allumage, produisant une amplitude de pression plus modérée, pourrait réduire ces contraintes d'intégration.

En définitive, cette thèse contribue à l'ambition plus large de transformation des cycles propulsifs aéronautiques afin de répondre aux objectifs de réduction de consommation définis par l'ACARE. En combinant diagnostics expérimentaux avancés, caractérisation des écoulements et modélisation 0D/1D validée, ce travail démontre la faisabilité technique d'une combustion à volume constant sans piston contrôlée et apporte des éléments physiques essentiels à l'intégration future de concepts de combustion à gain de pression dans les moteurs aéronautiques de nouvelle génération.

Avec une optimisation approfondie de la gestion thermique, du contrôle du mélange et des stratégies de couplage multi-chambres, l'auto-allumage en combustion à volume constant pourrait constituer un levier technologique crédible pour des systèmes propulsifs à haut rendement, compatibles avec les objectifs de durabilité à long terme du transport aérien

Experimental analysis of cyclic ignition strategies for pistonless constant volume combustion

Abstract:

The continuous growth of air transport has significantly increased its contribution to global CO_2 emissions, highlighting the need for a technological breakthrough in combustion systems. Pressure Gain Combustion (PGC) offers a promising pathway by producing a pressure rise during heat release, thus enhancing thermodynamic efficiency compared with the conventional Brayton cycle. Among PGC concepts, Constant Volume Combustion (CVC), widely exploited in piston engines, is investigated in a pistonless engine concept, aiming to preserve its thermodynamic advantages while reducing mechanical complexity and improving compatibility with aircraft propulsion systems.

Experiments were conducted on the CV2 laboratory-scale combustion vessel operating in cyclic mode. A reference spark-ignition mode was first characterized through pressure measurements, Particle Image Velocimetry (PIV) and high-speed chemiluminescence imaging. An in-house 0D/1D model was adapted to estimate the residual gas fraction and heat losses, providing complementary thermodynamic insight. Subsequently, controlled self-ignition was explored under single-chamber conditions reproducing the thermodynamic environment of ignition by burned-gas transfer in a multi-chamber configuration. Compared to spark-ignition, this controlled self-ignition strategy was shown to be viable under turbulent conditions with velocity fluctuations around 10 m/s. Increasing exhaust backpressure significantly enhanced self-ignition probability. Optimization of cycles allows frequency increase from 8 Hz to 12.5 Hz in spark-ignited cycles, enhancing thermal efficiency. Further shortening the cooling phase during the self-ignited cycle could enable operation up to 15.4 Hz, corresponding to a potential 23% increase in power and an estimated 11.4% reduction in heat losses.

Keywords: Constant volume combustion, pressure gain combustion, turbulent combustion, direct fuel injection, self-ignition, n-heptane, pistonless combustor, turbomachinery

Analyse expérimentale de stratégies d'allumage cyclique appliquées à la combustion à volume constant sans piston pour la propulsion aéronautique

Résumé:

La croissance continue du transport aérien a fortement accru sa contribution aux émissions mondiales de CO_2, soulignant la nécessité de ruptures technologiques dans les systèmes de combustion. La combustion à gain de pression (PGC) qui génère une élévation de pression lors du dégagement de chaleur, améliorant alors le rendement thermodynamique par rapport au cycle de Brayton conventionnel, constitue une voie prometteuse. Parmi les concepts de PGC, la combustion à volume constant (CVC), largement utilisée dans les moteurs à pistons, est appliquée ici à un concept de moteur sans piston. L'objectif est de préserver les avantages thermodynamiques tout en réduisant la complexité mécanique et en facilitant son intégration pour la propulsion aéronautique.

L'étude est menée sur le dispositif CV2 fonctionnant en mode cyclique. Un cycle de référence à allumage commandé a d'abord été caractérisé à l'aide de mesures de pression, de vélocimétrie par images de particules (PIV) et de chimiluminescence à haute vitesse. Un modèle 0D/1D a permis d'estimer la fraction de gaz brûlés résiduels et les pertes thermiques, paramètres difficilement mesurables expérimentalement. L'auto-allumage contrôlé représentative d'un configuration multi-chambre a été étudiée à l'aide du montage mono-chambre en reproduisant les conditions thermodynamiques d'un allumage par transfert de gaz brûlés. Il s'est avéré stable en régime turbulent malgré des fluctuations de vitesse d'environ 10 m/s. L'augmentation de la contre-pression à l'échappement a fortement amélioré la probabilité d'obtention de ce type d'allumage. L'optimisation des cycles à allumage commandé a permis d'accroître la fréquence des cycles de 8 Hz à 12,5 Hz, améliorant notablement le rendement thermique. Une réduction supplémentaire de la phase de refroidissement en mode auto-allumage devrait porter la fréquence à 15,4 Hz, soit un gain potentiel de puissance de 23 % et une diminution estimée de 11,4 % des pertes thermiques.

Mots-clés : combustion à volume constant, combustion à gain de pression, combustion turbulente, injection directe de carburant, auto-allumage contrôlé, n-heptane, chambre de combustion sans piston, turbomachines.